University of Bath

PHD

Structural energy dissipation in extreme loading events using shape memory alloys

Angioni, Stefano

Award date:
2011

Awarding institution:
University of Bath

Link to publication

General rights
Copyright and moral rights for the publications made accessible in the public portal are retained by the authors and/or other copyright owners and it is a condition of accessing publications that users recognise and abide by the legal requirements associated with these rights.

- Users may download and print one copy of any publication from the public portal for the purpose of private study or research.
- You may not further distribute the material or use it for any profit-making activity or commercial gain
- You may freely distribute the URL identifying the publication in the public portal ?

Take down policy
If you believe that this document breaches copyright please contact us providing details, and we will remove access to the work immediately and investigate your claim.

Download date: 23. May. 2019

Structural energy dissipation in extreme loading events using shape memory alloys

submitted by

Stefano Luca Angioni

for the degree of Doctor of Philosophy

of the

University of Bath

Department of Mechanical Engineering

June 2011

COPYRIGHT

Attention is drawn to the fact that copyright of this thesis rests with its author. This copy of the thesis has been supplied on the condition that anyone who consults it is understood to recognise that its copyright rests with its author and that no quotation from the thesis and no information derived from it may be published without the prior written consent of the author.

This thesis may be made available for consultation within the University Library and may be photocopied or lent to other libraries for the purposes of consultation.

Signature of Author ....

Stefano Luca Angioni

Abstract

It is well known that composite materials have a poor resistance to the damage caused by the impact of foreign objects on their outer surface.

There are various methods for improving the impact damage tolerance of composite materials, such as: fiber toughening, matrix toughening, interface toughening, through-the-thickness reinforcements and selective interlayers and hybrids. Hybrid composites with improved impact resistance would be particularly useful in military and commercial civil applications.

Hybridizing composites using shape memory alloys (SMAs) is one solution since SMA materials can absorb the energy of impact through superelastic deformation or recovery stress reducing the effects of the impact on the composite structure. The SMA material may be embedded in the hybrid composites (SMAHC) in many different forms and also the characteristics of the fiber reinforcements may vary, such as SMA wires in unidirectional laminates or SMA foils in unidirectional laminates only to cite two examples. Recently SMA fibers have been embedded in 2-D woven composites.

As part of this PhD work, the existing theoretical models for woven composites have been extended to the case of woven SMAHC using a multiscale methodology in order to predict the mechanical properties and failure behavior of SMAHC plates.

Also several parts of the model have been coded in MATLAB and validated against results extracted from the literature, showing good correlation.

Acknowledgements

My deepest gratitude is to my supervisor, Dr Michele Meo, whose guidance enabled me to develop an understanding of the subject.

The financial support from QinetiQ Limited who funded the research discussed in this thesis is gratefully acknowledged.

I am grateful to Andrew Foreman and Dr Charlotte Meeks of QinetiQ Limited for providing samples, use of their test facilities and assistance for part of the work discussed in chapter 4.

I am also indebted with my friends and colleagues: Francesco Amerini for helping out with the formalities of the submission of this thesis; Dr Ettore Barbieri for invaluable discussions; Francesco Ciampa and Leon Simpson for helpful comments; Captain Giovanni De Angelis for his friendship during the year he spent at the University of Bath; Tieman Postma for reviewing parts of chapters 3 and 5; and Amit Visrolia for contributing to the work discussed in chapter 5.

Finally, I would like to thank my wife, Rosa Orlando, and daughter, Elisabetta, for their constant encouragement throughout the completion of this degree. The final preparation of this thesis coincided with the sudden death of my wife. She has left a void in my life that I will struggle to fill.

In memory of my beloved wife Rosa Orlando who passed away on the 2nd October 2010.

May Lord Almighty rest her soul in eternal peace.

Contents

List of Figures

List of Tables

List of Abbreviations

AEHM	Asymptotic Expansion Homogenization Method
APT	Active Property Tuning
ASET	Active Strain Energy Tuning
BVID	Barely Visible Impact Damage
CCA	Composite Cylinder Assemblage
CFRP	Carbon Fiber Reinforced Plastics
CLT	Classical Lamination Plate Theory
CTE	Coefficient of Thermal Expansion
CZM	Cohesive Zone Model
DL	Discrete Layer Plate Models
DOF	Degrees Of Freedom
ESL	Equivalent Single Layer Plate Models
FBG	Fiber Bragg Grating
FEA	Finite Element Analysis
FEM	Finite Element Modeling or Finite Element Method
FRP	Fiber Reinforced Polymer Composites
FSDT	First-order Shear Deformation Theory
GFRP	Glass Fiber Reinforced Polymers
LWT	Layer-Wise Theory Plate Models
MMC	Metal Matrix Composite

MMSA	Multilevel Mesh Superposition Approach
NiTiNol	Nickel Titanium Naval Ordnance Laboratories
PE	Pseudoelasticity
POF	Plastic Optical Fibers
POM	Preferentially Oriented Martensite
PP	Parallel-Parallel scheme
PS	Parallel-Series scheme
PVDF	Polyvinylidene difluoride
RT	Room Temperature
RUC	Repeating Unit Cell
RVE	Representative Volume Element
SAM	Self-Accommodating Martensite
SIM	Stress-Induced Martensite
SMA	Shape Memory Alloy
SMAHC	Shape Memory Alloy Hybrid Composites
SME	Shape Memory Effect
SP	Series-Parallel scheme
SS	Series-Series scheme
TFA	Transformation Field Analysis
TRIP	Transformation-Induced Plasticity
TWSME	Two-Way Shape Memory Effect
UD	Uni-Directional
VKM	Variable Kinematic Model
XFEM	Extended Finite Element Modeling or Extended Finite Element Method

Chapter 1

Introduction

1.1 Motivation

It is well known that composite materials have a poor resistance to the damage caused by the impact of foreign objects on their outer surface. Impact damage can seriously affect the structural properties of an aircraft. For example, low velocity impacts on composite aircraft structures are particularly dangerous because the impact damage is often hidden beneath the surface of the material generating Barely Visible Impact Damage (BVID) which may go unnoticed during visual inspections. To date the only options are manual repair or replacement of the damaged structures.

Therefore aircrafts are usually built with thicker composites than those required for structural integrity in order to have sufficient reserve to maintain acceptable strength, stiffness and fatigue performance despite the presence of impact damage. This inefficient design process leads to higher structural weight and increased cost in terms of raw materials and fuel consumption.

There are various methods for improving the impact damage tolerance of composite materials, such as: fiber toughening, matrix toughening, interface toughening, through-the-thickness reinforcements and selective interlayers and hybrids. Hybrid composites with improved impact resistance would be particularly useful in military and commercial civil applications.

It is possible to hybridize composites using shape memory alloys (SMA). The SMA materials are able to absorb the energy of impact through superelastic deformation or recovery stress reducing the effects of the impact on the composite structure. These composites are referred to in literature as SMA hybrid composites (SMAHC).

As will be discussed in chapter 2, the use of SMAHCs permits designing structural composites with self-sensing and self-healing properties, bringing greater safety and reduced maintenance costs for aircrafts.

The SMA material may be embedded in the composite materials in many different forms, e.g. SMA wires in unidirectional laminates (e. g. [243]) or SMA foils in unidirectional laminates (e. g. [5]) only to cite two examples. Recently, Foreman et al. [89] have embedded SMA wires in 2-D woven composites.

Woven SMAHC laminates have a greater percentage increase in impact energy absorption compared to uni-directional SMAHC laminates (see section 4.3.3). For this reason the the main focus of this thesis will be on woven SMAHC structures.

1.2 Objectives

The overall objective of this thesis is the experimental-numerical study of the potential use of shape memory alloys (SMA) embedded into woven composite layers (see figure 2-11) for structural energy dissipation.

As will be discussed in chapter 2, the performance of SMAHCs structures is highly dependent on parameters such as pre-strain, volume fraction, orientation and position of the SMA fibers within the laminate, so one of the greatest challenges for designing a woven SMAHCs is the very large design space. This is the reason why it is a challenge to optimize the overall structure relying entirely on expensive experimental tests. Modeling techniques may be both auxiliary and sometimes necessary to the designer in order to optimize composite structures.

Therefore one particular objective of this work is the development of numerical tools for modeling woven SMAHC plates and stiffened panels with different SMA layouts.

Another particular objective is to validate the prediction capabilities of the developed models compared to experimental data and results found in literature.

1.3 Approach

In order to achieve the outlined objectives, this thesis extends to woven SMAHC plates the theoretical models for predicting mechanical properties and failure behavior of two-dimensional (2-D) woven composites by using a multiscale methodology.

The mechanical properties, stresses and strains at the micro- and meso-scales of the Representative Volume Element (RVE) of the SMAHC plate are estimated taking into account their geometrical characteristics and the mechanical properties of the constituents (e.g. matrix, reinforcement fibers and SMA wires) using the two-scale Asymptotic Expansion Homogenization Method (AEHM) [24, 63, 53, 39, 55]. Anisotropic damage mechanics has been integrated with the AEHM to model failure.

Moreover, the AEHM macroscopic problem for SMAHCs has been reformulated using Transformation Field Analysis (TFA) [72, 75] in order to simplify the analysis in order to reduce the computational complexity of the *full* AEHM approach.

At the macro-scale, to achieve a further reduction of the computational burden, the multiple plate models theory for laminated composite plates is proposed for predicting static and dynamic behavior of the SMAHC plate under various loads.

Many different constitutive models have been developed for the SMA. Although in this thesis the three-dimensional (3-D) constitutive model for shape-memory alloys of Sadjadpour and Bhattacharya [212] is used, the approach considered in this thesis is not restricted to this model, but also other existing 3-D models may be employed.

1.4 Thesis Outline

Chapter 2 provides some background information and reviews the literature on the use of SMA materials embedded in composites for impact energy absorption.

Chapter 3 reviews and compares different homogenization methods for 2-D woven composites including the AEHM. This chapter also examines how to integrate anisotropic damage mechanics with the AEHM.

Chapter 4 proposes a multiscale 3-D constitutive modeling approach for SMAHCs based on the the AEHM approach. The use of TFA for reducing the computational cost of the analysis is discussed in this chapter.

Chapter 5 discusses the multiple plate models theory for laminated composite plates.

Chapter 6 presents some conclusions on the work carried out and suggestions for future work.

1.5 Published work

Note that chapters 2, 3 and 5 are based almost entirely on the following published or accepted journal papers

1. Angioni, S.; Meo, M. and Foreman, A. Impact damage resistance and damage suppression properties of shape memory alloys in hybrid composites-a review Smart Materials and Structures, IOP Publishing, 2011, 20, 013001

2. Angioni, S.; Meo, M. and Foreman, A. A comparison of homogenization methods for 2-D woven composites Composites Part B: Engineering, 2011, 42, 181 - 189

3. Angioni, S.; Visrolia, A. and Meo, M. A hierarchical multiple plate models theory for laminated composites including delamination and geometrical nonlinear effects Composite Structures, 2011, 93, 780 - 791

4. Angioni, S.; Meo, M. and Foreman, A. A critical review of homogenization methods for 2D woven composites Journal of Reinforced Plastics and Composites, 2011, Accepted for Publication

5. Angioni, S.; Visrolia, A. and Meo, M. Combining X-FEM and a multilevel mesh superposition method for the analysis of thick composite structures, Composites Part B: Engineering, 2011, Accepted for Publication

Chapter 2

Impact damage resistance and damage suppression properties of shape memory alloys in hybrid composites

2.1 Introduction

Composite materials can support very high loads in the direction of the fibers, but only low loads in the translaminar direction, as all the load is supported only by the matrix. Composite materials have a poor resistance under transverse impact loads, because they dissipate very little impact strain energy (such as plastic yielding in ductile metals) during impact loading.

The effects [202, 96] of the impact on the composite will generally depend upon various factors, such as composite's constituent materials (matrix toughness, fiber surface treatment, moisture content, fiber stiffness and strength), composite's construction, stacking sequence and geometry, and the impact conditions (shape, energy, mass, geometry of the impactor). Bayandor et al. [19] give an overview of each of these different failure modes. In particular composites with woven fiber reinforcements have proven to have superior impact energy absorption capabilities compared to laminates with uni-directional fibers [96, 201].

There are various methods for improving the impact damage tolerance of composite materials, such as: fiber toughening, matrix toughening, interface toughening, through-the-thickness reinforcements and selective interlayers and hybrids. Amongst the through-the-thickness reinforcements methods there are the following: stitching (Mouritz et al. [160]; Greenhalgh and Hiley [96]), braiding [159], z-pinning [158, 96] and 3-D weaving [159], knitting [159, 103]. Selective interlayers and hybrids [96] improve the impact tolerance of the composite material by inserting layers of a secondary reinforcement material at critical locations in the stacking sequence. The tougher secondary reinforcement material is used to increase the impact resistance of the hybrid composite, while the stiffer and stronger primary reinforcement material is used to carry the majority of the load [249]. Hybrid composites with improved impact resistance are particularly useful in military and commercial civil applications.

This chapter reviews the possibility of hybridizing composites using *Shape-Memory Alloys* (SMAs) in their various forms to improve their impact resistance. These materials are capable of absorbing the energy of the impact through superelastic deformation or through recovery stress reducing the effects of the impact on the composite structure.

SMAs are part of the family of the *Shape Memory Materials* (SMMs), which includes also shape-memory ceramics and shape-memory polymers [248]. SMAs owe their name to the *shape memory effect* (SME) . SMAs were know since the 1950s [248], but their usefulness in engineering applications was not evident until the discovery in 1963 [37] of the near-stoichiometric Ti-Ni alloys, the so called NiTiNol (abbreviation for *Nickel Titanium Naval Ordnance Laboratories*) . Broadly speaking SMAs are materials that are able to *remember* their shape. If they are deformed at room temperature, then, after being heated, they return to their original shape. Patoor et al. [191] define more formally SMAs as metallic alloys that can undergo martensitic phase transformations as a result of applied thermo-mechanical loads and are capable of recovering permanent strains when heated above a certain temperature (the *shape memory effect*). SMAs have been discussed extensively in literature. Duerig et al. [70] cover in great detail the properties of SMAs with a particular focus on their applications. Otsuka and Wayman [180] deals more in general with SMMs including alloys and polymers. Bhattacharya [25] discusses the matensitic phase transformation and the crystallographic reasons behind the shape memory effect. A recent reference on SMAs with particular emphasis on modeling is Lagoudas et al. [128].

Moreover, using SMAs it is possible to construct so called *smart* (or *intelligent*) materials and structures (or systems). In most general terms a smart material or structure [248] is one that is able to respond to a change in the environmental conditions in a predefined (known) manner (i.e. time end intensity) and that will return to its original (known) state when the stimulus is removed. Rarely smart materials are single (monolithic) ones, but they are generally the composition or hybridization or integration of several different materials and systems. Although there is not yet a unanimous consensus in the technical community on the terms smart (or intelligent) material and smart (or intelligent) structure (or system), most authors, e.g. Michaud [151] and Wei et al. [248], make a distinction between materials and structures. Following these authors we will define a smart or intelligent material as one that inherently contains sensing, actuating and controlling or information processing capabilities built into its microstructure. While, a smart (or intelligent) structure (or system) is thus an assembly, which presents the previously mentioned characteristics through the combination of various materials, and is usually monitored or controlled using an external microprocessor or computer.

Michaud [151] argues that SMA materials are smart only in a restricted sense because they need to undergo a phase transformation that modifies their physical and mechanical characteristics. However, SMAs are generally considered smart materials, because their various properties allow creating hybrid composites that are able to modify specific material properties in response to environmental changes. Possible applications of SMAs as smart materials, include: tunable stiffness, damping capacity, shape-controllable active surfaces and self-healing capability. Hartl and Lagoudas [97] give various examples of SMAs used as smart materials for aerospace applications.

In the following, different examples of *SMA Hybrid Composites* (SMAHC) will be discussed focusing on the possibility of modifying the stiffness of the material or structure in response to the impact of a foreign object. In particular, section 2.2 will cover the basic properties of the SMAs, while section 2.3 will introduce the generalities of the use of SMAs for improving the impact damage tolerance of hybrid composite materials; section 2.4 will summarize the main modeling techniques adopted for SMAHC; sections 2.5 and 2.6 will describe *passive* and *active* applications, respectively, of SMAHC for damage suppression; finally, section 2.7 provides a discussion and some conclusion on the use of SMAHC for damage suppression.

2.2 Basic Properties of Shape Memory Alloys

SMAs are characterized by two stable phases, a high-temperature phase known as *austenitic phase*, with a highly symmetric (generally cubic) lattice structure, and a low-temperature phase known as *martensitic phase*, with a one or more variants of a very low symmetric lattice structure. In [25] and [191] the martensitic phase transformation is defined by as a shear-dominant displacive (no diffusion) and first-order (abrupt change in the lattice parameter) solid-to-solid phase transformation occurring by nucleation and growth of the martensitic phase from the parent austenitic phase. The martensitic phase transformations in most SMAs, except for some iron based alloys [248], are thermo-elastic transformations, and may be thermally induced or stress- and pressure-induced.

2.2.1 One-Way Shape Memory Effect

In the absence of applied stresses, cooling the solid in the austenitic phase, there is normal thermal contraction until the deformation temperature T_d reaches a critical temperature T_0 where the free energy of Martensite becomes less than the free energy of Austenite and the lattice structure abruptly changes from the austenitic phase into the martensitic phase. This process is called *thermo-elastic (forward) martensitic phase transformation* (*Austenite-to-Martensite*). The temperature T_0 is called *equilibrium temperature* and is the temperature at which the free energies of the two phases are equal. During the martensitic phase transformation, although the crystal structure changes abruptly and the distortion of the cell is significant, there is no diffusion and no change in the relative position of the atoms during this transformation [25]. This type of phase transformation is called *displacive* as the atoms are cooperatively rearranged into a new more stable crystal structure. In contrast, in *diffusional transformations* the new phase can only be formed by moving atoms randomly over relatively long distances [70]. In reality, the transformation does not begin exactly at T_0 , but, in the absence of stress, at a temperature M_s (*Martensite start*), which is less than T_0. The transformation continues to evolve as the temperature T_d is lowered until a temperature, denoted by M_f (*Martensite finish*) is reached and the material is completely in the martensitic phase, as shown in figure 2-1. Cooling the solid in martensitic phase will result only in further thermal contraction. The martensitic phase transformation is crystallographically reversible, in the sense that, in the absence of applied stresses, when the martensitic phase is heated it undergoes thermal expansion until the temperature T_d reaches the equilibrium temperature T_0 where the free energy of Austenite becomes less than the free energy of Martensite and the crystal structure abruptly changes back to the original symmetric lattice of the austenitic phase. This process is called the *thermo-elastic reverse martensitic phase transformation* (*Martensite-to-Austenite*). In reality, the reverse transformation does not begin exactly at T_0 but, in the absence of stress, at a temperature A_s (*Austenite start*), higher than T_0. The reverse transformation continues to evolve as the temperature T_d is increased until a temperature A_f (*Austenite finish*) is reached and the material is entirely in the austenitic phase, as shown in figure 2-1. Heating the solid in austenitic phase will result only in further thermal expansion. The temperatures M_s, M_f, A_s and A_f in figure 2-1 are called *transformation temperatures* of the material. The *equilibrium temperature* T_0 is approximately $(M_s + A_f)/2$ [191]. The transformation temperatures and the differences $M_s - M_f$ and $A_f - A_s$ characterizes the behavior of SMAs. The transformation temperatures depend mainly on the alloy's composition and processing. The interface that separates the Martensite phase from the parent phase is called the *habit plane*. This plane remains unchanged and exhibits neither deformation nor rotation [25]. When a SMA is cooled it will transform into a mixture of different variants of Martensite, which allows the solid to take on a shape that is different from either. During the transformation the solid can not tear itself apart, but the mixture must be coherent with rows of atoms unbroken across the interfaces between the different variants. This process is called *twinning*, and the two different variants are said to be twinned across their interface. The variants must create very complex patterns which constitute the microstructure of the Martensite. The different regions of the solid will transform into different variants of Martensite in such a way that there is no macroscopic change in shape. This transformation of the Austenite into a microstructure of Martensite with no net change in shape of the solid is called *self-accommodation*. SME can be explained [25], linking the symmetry-related variants of Martensite to the energy in the structure as follows, and is visualized in figures 2-1 and 2-2.

($A \rightarrow B$) When a SMA in austenitic phase is cooled, it transforms via the forward martensitic phase transformation from the parent phase into a mixture of twinned (self-accommodated) variants of Martensite.

($B \rightarrow C$) At a temperature below M_f , under stress SMAs in martensitic phase will deform by distorting the crystal structure or by crystallographically reorienting the variants into a single variant microstructure. The second option is preferred, and this process (the condensation of many twin variants into a single favored variant [70]) is called *(stress induced) detwinning*, as the different variants originate from the same parent so they are equivalent in terms of energy, and changing the microstructure allows changing the shape of the solid without changing its energy. Vice versa, distorting the lattice would require energy. De-twinning generates large inelastic strains.

($C \rightarrow D$) When the load is released (always at a temperature below M_f) there is no reason why the solid should return to the self-accommodated state as the deformed state and the self-accommodated are equivalent in terms of energy. The solid stays in the twinned Martensite phase and the inelastic strains are not recovered.

($D \rightarrow F$) If the solid is now heated to a temperature above A_f, whatever the microstructure of Martensite and its shape, the reverse martensitic phase transformation will force the various different variants of Martensite back to the only variant of Austenite, which is also a minimum energy state, forcing the solid to recover its original shape prior to the deformation (*shape recovery*), and recovering the inelastic stains (*strain recovery*) generated during the detwinning process. The inelastic strains are recovered since the Martensite variants were reoriented by stress, then the reversion to Austenite produces large transformational strains with the same amplitude but in opposite direction to the inelastic strains.

2.2.2 Stress-Temperature Diagram

If the temperature range is restricted to include only thermo-elastic transformations and since the martensitic phase transformations do not occur instantaneously, but over a certain range of stresses and temperatures, the uniaxial thermo-mechanical response of SMAs is summarized in the phase diagram called the *stress-temperature diagram* [191], shown in figure 2-2. The diagram shows that SMAs can be in one of the three pure phases: Austenite, twinned (self-accommodated) Martensite and detwinned Martensite. These regions are separated by transformation lines (surfaces in

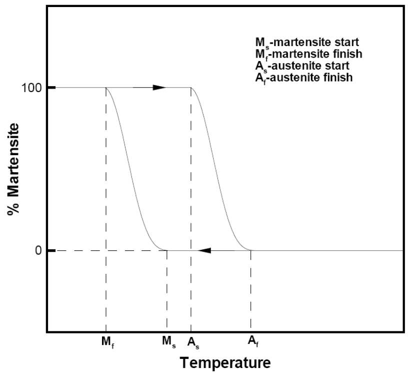

(a) Forward and reverse martensitic phase transformations

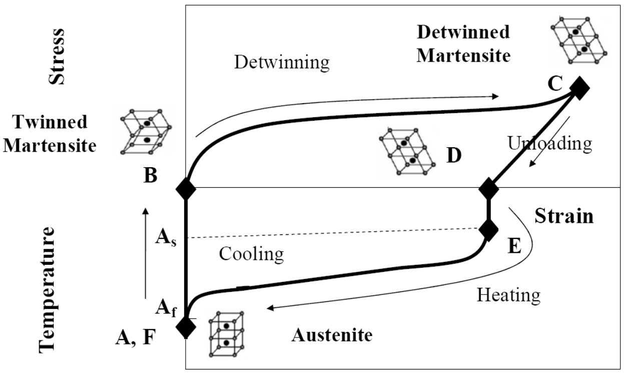

(b) Experimental Niti stress-strain-temperature curve

Figure 2-1: Forward and reverse martensitic phase transformations and experimental Niti stress-strain-temperature curve

multiple dimensions). When the material crosses a transformation surface it undergoes phase transformation (Austenite-to-Martensite) or detwinning (twinned Martensite to detwinned Martensite). During the martensitic phase transformation various physical properties of the material change [81]. Because the martensitic transformations are of the first-order type then the forward transformation (Austenite-to-Martensite) is an *exothermic* phase transformation where latent heat (transformation enthalpy) is released changing in the transformation enthalpy. Vice versa, the reverse martensitic phase transformation (Martensite-to-Austenite) is an *endothermic* phase transformation accompanied where latent heat is absorbed also changing the transformation enthalpy. For a given temperature, the amount of heat is proportional to the volume fraction of the transformed material. A thermal hysteresis is normally present between the forward and the reverse transformations, ranging from several Kelvin to more than 100 Kelvin [248] depending on the material composition and microstructure. The two phases have a different resistance so the phase transformation is also associated with a change in the resistance of the material.

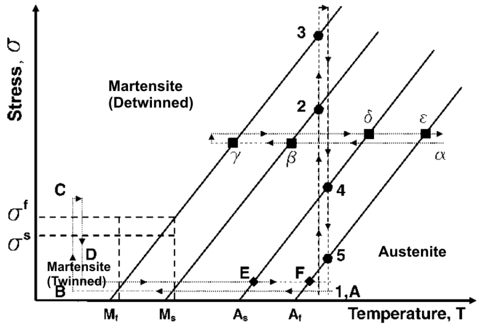

(a) Stress-temperature diagram (reproduced with permission from [97]

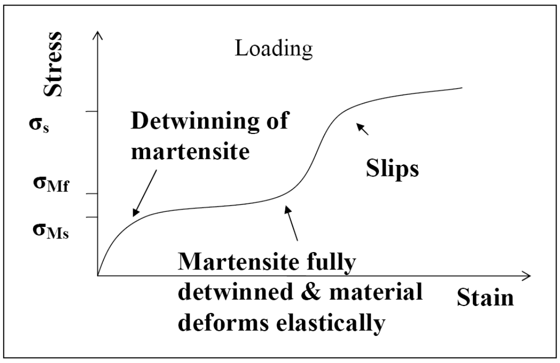

(b) Stress-strain curve for a SMA material

Figure 2-2: Stress-temperature and stress-strain curves for a SMA material

2.2.3 Two-Way Shape Memory Effect

If transformation strains are generated during both heating and cooling, this property is called the *two-way shape memory effect* (TWSME) . The idealized process is described in figure 2-1, but in reality the inelastic strain are partially recovered and a residual strain, called *transformation-induced plasticity* (TRIP) [128] remains after the completion of the heating cycle ($D \to A$). Under repeated heating cycles, the residual strain will increase until saturation. Further cooling of the material in the absence of applied stress ($A \to B$) will generate a macroscopic transformation strain. The transformation hysteresis also stabilizes, as the number of cycles increases. Such repetition until stabilization is often referred to as training effect or cyclic behavior. The two-way shape memory is not an intrinsic but an acquired characteristic produced by cyclic repetition of certain thermo-mechanical loading paths.

2.2.4 Apparent Yield Strength

During the martensitic phase transformation *apparent yield strength* changes significantly. (Here the term *apparent* is used to distinguish the yield strength due to phase transformation, from the yield strength classically used in the context of plastic deformation). The Austenite apparent yield strength is much lower than that of the Martensite, because the former changes its crystal structure via dislocation generation and movement while the latter changes its crystal structure moving the very mobile twin boundaries. Only a certain amount of martensitic deformation can be accommodated by the twinned boundaries, and, once the material is in the fully detwinned phase, then the material will start deforming elastically again. Once the detwinned Martensite has reached the maximum deformation that it is able to be accommodated, if the stress is increased above a value σ_s, then the apparent yield strength changes again because, because the crystal structure of the Martensite will start deforming through a dislocation movement called *(plastic) slip* which is an irreversible process. In summary, as shown in figure 2-2, there are two distinct elastic regions and two distinct stress plateaus, the first due to twin motion (*reversible*) and the second due to slip (*irreversible*). The ratio of resistances to reversible and irreversible deformation (twin movement to slip) should be maximized, so that all deformation can be recovered upon heating.

2.2.5 Stress-Induced Martensite

Martensite starts forming at the temperature M_s in the absence of stress and can also form above M_s in the presence of a stress. In this case the Martensite is called *stress-induced martensite* (SIM) . The cause is mechanical and not thermal as in the case of the SME [70]. Above M_s the critical stress σ_{M_s} required to induce the martensitic transformation increases linearly with temperature, as dictated by the Clausius-Clapeyron equation [154]

$$\frac{\mathrm{d}\sigma_{M_s}}{\mathrm{d}M_s} = \frac{\Delta H}{V T_0 \Delta\epsilon} \tag{2.1}$$

where T_0 is the temperature at which the parent and Martensite phases are in equilibrium at zero stress, ΔH is the transformation latent heat (transformation enthalpy), σ_{M_s} is the applied stress, M_s is the shifted Martensite start temperature, V the molar volume and $\Delta\epsilon$ is the transformation strain in the direction of the applied stress. The critical stress σ_{M_s} required for SIM increases linearly with temperature until a (dislocation) temperature M_d, above which the temperature required to generate SIM is greater than that to produce *dislocations* (plastic slips), i.e. SIM may be generated for temperatures between M_s and M_d. All the transformation temperatures (M_s, M_f, A_s and A_f) follow the Clausius-Clapeyron equation, which can be generalized to the form $\mathrm{d}\sigma/\mathrm{d}T$ which is called *stress rate* of the SMA. Summarizing, for $T_d < M_s$ there is Martensite detwinning, for $M_s < T_d < M_d$ there is SIM and for $T_d > M_d$ there is plastic deformation [70]. In figure 2-3 the stress-strain curves for a SMA at various temperatures is shown.

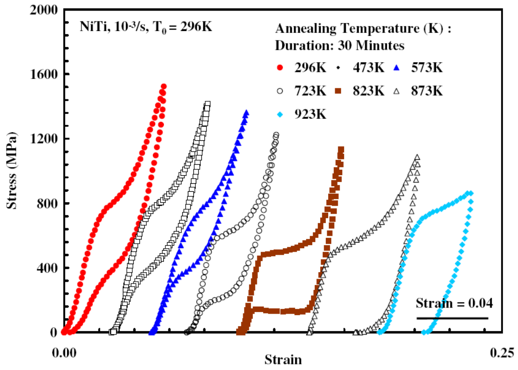

Figure 2-3: Stress-strain curves for a SMA at various deformation temperatures (reproduced with permission from [167])

2.2.6 Pseudoelasticity

With *pseudoelasticity* (PE) we denote any non linearity observed during the unloading in the stress-strain curve [70]. It is due to twinning or by SIM phase transformation. Twinning pseudoelasticity, such as *pseudotwinning* [70] and *rubber-like effect* [191], is caused by the reversible detwinning of twinned Martensite. SIM phase transformation, also called *transformational pseudoelasticity* or simply *pseudoelasticity* by some authors [153, 180, 128, 126] or *superelasticity* by others [70, 191] is observed (see figure 2-2) when the martensitic phase transformation is stress-induced by a uniaxial, isothermal loading (at a deformation temperature T_d above A_f) of the (parent) austenitic phase at zero stress up to a critical stress level σ_{M_s} called the *transformation stress* ($1 \rightarrow 2$). The response is purely elastic up to the critical stress level σ_{M_s} where the material undergoes a (forward) SIM phase transformation ($2 \rightarrow 3$) which produces detwinned Martensite phase directly from the Austenite, during which large inelastic (transformation) strains are developed, represented by the upper plateau on the stress-strain curves in figure 2-4. When the applied stress reaches the value σ_{M_f} the forward transformation is completed and the SMA is in the fully detwinned Martensite phase (point 3). Further loading above σ_{M_f} of the material in the fully detwinned martensitic phase does not produce further phase transformation, although reorientation of the martensitic twins may occur in multiaxial loading conditions, and again only elastic behavior of Martensite is observed. Upon unloading at zero stress the response is purely elastic ($3 \rightarrow 4$) until the reverse SIM phase transformation initiates at the critical stress σ_{A_s} and completes at a stress σ_{A_f} ($4 \rightarrow 5$) during which the large inelastic (transformation) strains are recovered, represented by the lower plateau on the stress-strain curves in figure 2-4. In order to produce isothermal condition the loading must be quasi-static (small strain increments), so that the latent heat generated/absorbed during the forward/reverse martensitic phase transformation has time to dissipate. The transformation process, due to the difference between σ_{M_f} and σ_{A_s} and between σ_{M_s} and σ_{A_f}, results in the loading/unloading stress-strain diagram in a hysteretic loop which reflects the energy dissipated in the cycle. The capability of SMAs of storing large amount of elastic energy is one of the reasons for using superelastic SMAs [70]. The energy is defined as the area under the stress-strain curve. The area under the loading part of the stress-strain curve E_1 in figure 2-4 is the energy per unit volume which is dissipated during one cycle (dissipated energy). The area under the unloading part of the stress-strain curve E_2 is the energy per unit volume which is stored and available upon unloading (elastic energy). Since the total work performed on the material is $(E_1 + E_2)$, the efficiency for energy storage is defined as $E_1/\left(E_1 + E_2\right)$ [153]. This ratio η is a measure of the degree of pseudoelasticity of SMAs. In other words, materials with a higher η ratio behave more pseudo-elastically and have greater capabilities of absorbing impact energy and accommodating deformation with less damage. For a given deformation temperature T_d, E_2 and η increase with increasing the critical stress for inducing Martensite σ_{M_s}. However, in case σ_{M_s} exceeds σ_s, PE becomes incomplete, since a permanent (non recoverable) residual strain ϵ_p is introduced as shown in figure 2-4. If $\sigma_t < \sigma_s$ then both the elastic strain ϵ_{el} and transformation strain ϵ_{tr} is recovered. If $\sigma_t > \sigma_s$, then only the plastic strain, ϵ_p, remains [128, 70]. This property is called the strain dependence of the PE property. The PE property also depends greatly on the (deformation) temperature T_d. Increasing T_d results in an increase of the values of critical transformation stresses, but does not change the general shape of the hysteresis. There is temperature below which upon unloading the inelastic strains are fully recovered (pure superelasticity). Above this temperature recovery upon unloading is incomplete, but heating after unloading will complete the recovery ($\epsilon_f = 0$). As the temperature is increased above the (dislocation) temperature M_d, then also heating after unloading will not cause a complete recovery ($\epsilon_f > 0$). The pseudoelastic behavior is different for single crystal and polycrystalline SMA materials [191, 70]. The stress plateaus are normally quite clear for single crystal SMA material, but are not so evident for polycrystal SMA materials. In single crystal SMA the stress plateaus in figure 2-4 are caused by the growth of a single variant of Martensite which possesses the most favorable orientation with respect to the applied stress. In polycrystalline SMA materials the stress plateaus are caused by the Martensite to form in different variants as in the case of the SME. Here the difference is that the variants are selected during the transformation while in the SME the new variants are generated by consumption of other variants [70]. The recoverable transformation strain for most polycrystalline SMAs can be as much as up to 8%, while for some single-crystalline SMAs may exceed 10%, resulting in a very high elastic energy storage capacity [248]. As for the SME also PE is affected by cycling (training). Only stress cycling and not thermal cycling is of interest for PE. After a certain number of cycles the superelastic properties stabilize. However, when the number of stress cycles exceeds a certain value then the SMA material may experience fatigue failure (pseudoelastic transformation fatigue). An increase in apparent yield strength is also observed with pseudoelasticity. For this reason some authors such as Liu and Galvin [136] talk about two criteria (an increase in apparent yield strength and a deformation temperature exceeding the A_f temperature) being necessary for complete pseudoelasticity, and if either of the two are violated then complete pseudoelastic behaviour is not displayed. The PE is also responsible for increasing the wear resistance of SMA compared to e.g. steel [135].

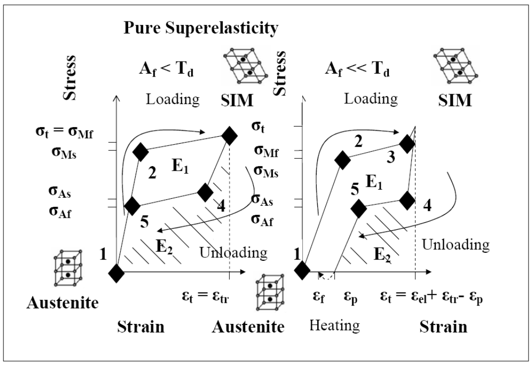

Figure 2-4: Schematic stress-strain curves for single isothermal pseudoelastic loading cycle

2.2.7 Free, Constrained, and Restrained Recovery

In *free recovery* the SMA is heated and it is able to recover all (or at least most of) the inelastic stains gained during deformation. If, in figure 2-5a, T_d is the deformation temperature (in the case $T_d < M_s$), ϵ_t is the total strain imparted to the material, ϵ_p is the apparent plastic strain upon unloading and ϵ_f is the final strain after heating above A'_f the Austenite finish temperature (considering the most general case of irreversible deformations), then the amount of recoverable strain is $\epsilon_r = \epsilon_p - \epsilon_f$. Note that the Austenite start and Austenite finish temperatures A'_s and A'_f in the presence of stress must be distinguished from the Austenite transformation temperatures A_s and A_f in the absence of stress [70]. When free recovery is prevented by an external constraint before temperature A_f is reached, the process is called constrained recovery and a large tensile stress (recovery stress), up to 800 MPa [70], can be generated. If ϵ_c is defined the contact strain, T_c is the contact temperature, i.e. the temperature at which the SMA makes contact with the constraint, and σ_r the recovery stress, then $\epsilon_c - \epsilon_f$ is the unresolved recovery, i.e. the strain that could have been recovered had it been the case of free recovery. From figure 2-5, T_c is temperature at which the stress starts to build up, then continues to build linearly with temperature, with a rate equal to the stress rate $\mathrm{d}\sigma/\mathrm{d}T$, until a maximum value is reached at σ_r defined as *stress recovery.*

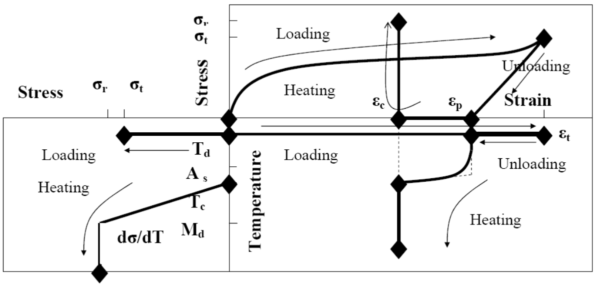

(a) Constrained recovery event

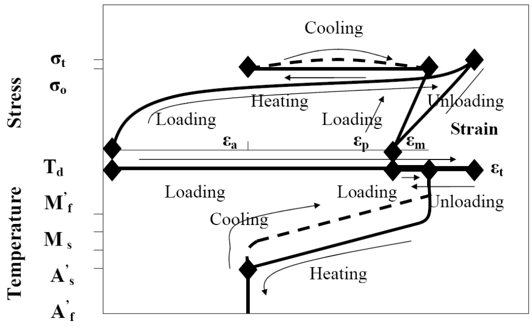

(b) restrained recovery event

Figure 2-5: Stress-Strain-Temperature curve

2.2.8 Hysteresis and Damping Capacity

The difference between the transformation regions A_s to A_f and M_s to M_f is called *hysteresis*, as shown in figure 2-1. Its magnitude depends upon the alloy, but values of 20-40°C are typical for SMAs [70]. Hysteresis can be thought of the friction associated with the movement of the twin boundaries [70]. The damping capacity is the capacity of a material to dissipate mechanical energy into heat and depends on various parameters such as frequency, amplitude and temperature of excitation, and on the difference between the operating and transformation temperatures [191]. In SMAs it is attributed to the observed the internal friction [180] and to various interfaces involved in the martensitic transformation: Austenite and Martensite, those between different variants of Martensite, and the Martensite's twin boundaries. Although the martensitic transformation is theoretically a thermo-elastic transformation, various irreversible events cause dissipation of energy such as defects, movement of dislocations, etc. For temperatures above A_s and stress levels high enough to induce SIM, the damping capacity reaches its maximum. Creation and displacement of Austenite-Martensite interfaces during the loading cycles are accompanied by a strong level of defect production and large thermo-mechanical coupling [191]. In the Austenite phase, the intrinsic damping is relatively small while the martensitic phase offers a high level of energy dissipation due to the movement and reorientation of Martensite twin variants under an applied stress. The hysteresis in pseudoelasticity is also one of the causes of energy dissipation. The greatest level of damping is achieved when the material is in a dual phase domain, [134] i.e. when austenitic and martensitic phases coexist, where internal friction is generated by the movement of interface dislocations between the Austenite and Martensite phases. This mixed-phase domain occurs during both thermally induced martensitic phase transformation or during stress-induced martensitic phase transformation, confirmed analytically in [259] and [260]. Summarizing, damping in SMA [125] is caused by damping resulting from thermally induced martensitic phase transformation, from stress-induced martensitic phase transformation and by intrinsic damping generated by two coexisting phases.

2.3 SMAHC for Damage Suppression

The concept of SMAHC was first proposed in 1988 by Rogers et al. [206, 207, 204].

Commercial SMAs are available in many different forms, such as fibers (or wires) (e.g. uni-directional and woven), short fibers (or whiskers), particles (or particulate) and foils (or sheets or films), allowing the manufacturing of many various types of SMAHC each with different characteristics and properties. The first examples of SMAHC published in literature consist of SMA material in the form of wires, ribbons or strips which have been embedded in an epoxy matrix. SMA materials in the forms of thin films and particulates embedded in an epoxy matrix followed. More recently the SMA material has been embedded into polymer composites (a resin matrix reinforced with commercial fibers such as aramid, carbon or glass) with unidirectional or woven fiber reinforcements.

The SMA material itself may be bulk or porous (e.g. Nemat-Nasser et al. [168] with 12% porosity of volume fraction and Zhao et al. [270] with 13% and 25% porosity of volume fraction).

2.3.1 Fracture Toughening Mechanisms of SMAHC

The impact damage resistance of composites may be improved by hybridizing them with SMA fibers because high-strain SMAs have a relatively high ultimate strength and can absorb and dissipate a large amount of strain energy, first through *Stress-Induced Martensite* (SIM) transformation and then through plastic yielding. SMAs dissipate the strain energy of the order of four times that of high alloy steel and sixteen times that of many graphite/epoxy composites through SIM transformations [249, 123].

The fracture toughness of the SMAHC may be modified both passively and actively. Both methods have been used for improving the impact damage resistance of hybrid composite. When a tensile strain is applied to a SMA fiber or foil before being embedded at room temperature, then it is said to be *pre-strained.* Passively, the embedded pre-strained SMA fibers used to strengthen the matrix can absorb (via SIM transformation) the impact strain energy thereby improving the creep or crack resistance of the material.

Actively, the embedded pre-strained SMA fibers can be activated e.g. by passing an electric current through them, and, because of the heating, they will undergo the reverse martensitic transformation trying to contract to their *normal* length and therefore generating large uniformly distributed shear loads (tension or compression) along their length. These shear loads alter the energy balance within the structure, which in turn may modify the structure's mechanical response.

The mechanical response of the structure may change only because the stiffness (inherent modulus) of the embedded SMA fibers has changed or because of the recovery stress of the plastically elongated SMA fibers. Rogers et al. [204] term these two techniques as *active property tuning* (APT) and *active strain energy tuning* (ASET) , respectively. The best location of the SMA in the composite structure will depend on the desired control technique. In the opinion of Sarip et al. [214], SMA is best situated along the neutral axis of the plates in order to achieve APT. In order to achieve ASET the SMA wires should be located either along the neutral axis of the structure or symmetrically through the thickness of the plate [214]. If the embedded SMA wires are located eccentrically to the natural axis of the composite structure, then the recovery force of the SMA will generate a bending moment that is used to change shape or positions of SMAHC structures [214]. This type of ASET is called the *Active Shape Control* (ASC).

The SMA wires can be embedded directly in the matrix of the SMAHC or through sleeves. The recovery stresses generated by the SMA wires depend, in direct embedding, on the compliance of the surrounding matrix. The lower the compliance, the higher the level of induced force [237]. In the case of overheating, direct embedding has the disadvantage of destroying the matrix, while embedding through sleeves prevents resistive heat to be transferred directly to the matrix. However embedding through sleeves requires the SMA wires to be clamped at both ends in order to get any recovery stress, which is impractical [237].

Passive Fracture Toughening

The SMA fiber or foil reinforcements embedded in the matrix of the composites are pre-strained in the martensitic phase (plastically elongated and constrained from contracting to their *normal* length). During curing to become an integral part of the structure, they are heated to temperatures above the Austenite finish temperature A_f to the austenitic phase and act against the constraining nature of the matrix. During this reverse transformation process from the *soft* Martensite to the parent phase (Austenite), because of the mismatch in the thermal expansion coefficients of the SMA (higher) and the matrix (lower), the SMA fibers will try to recover their original shape and hence tend to shrink. This process introduces in the matrix compressive internal (thermal) residual stresses (*constrained recovery stresses*) [249, 244] which contribute to the tensile properties of the composite and are beneficial to mechanical properties such as the yield stress and fracture toughness.

The impact energy will be absorbed by the SMA wires embedded in the SMAHC during the direct transformation from the Austenite phase to Martensite one. This energy is released afterwards via the reverse martensitic transformation [243].

The improved resistance to fatigue crack propagation of the SMAHC can be attributed to the combination of compressive residual stress, higher stiffness of the composite, the SIM transformation and the dispersion of the mechanical strain energy at the crack tip. Both the ultimate strength and the failure strain of the composite are significantly greater than those of an unreinforced control material with the final failure strain of the hybrid composite exceeding 15% according to Wei et al. [249].

Active Fracture Toughening

When a pre-strained SMA fiber or foil embedded in the laminate is heated, it tends to shrink to it original shape and to instantaneously generate recovery compressive forces along the pre-strained direction in the composite matrix, which are effective at suppressing the initiation and growth of transverse cracks [4, 5, 173]. This compressive force is generated by the martensitic phase transformation from the SIM phase to the Austenite phase.

Ogisu et al. [175] simulated the fabrication and reheating processes of the hybrid composite, and measured the relationship between recovery stresses generated by the pre-strained SMA foils embedded in composite laminates and temperature. This relationship is shown in figure 2-6. The SMA foils were heated while their ends were kept fixed. After pre-straining the recovery stress was zero at room temperature (RT) . Then a recovery stress was generated when the SMA foils were heated (above A_f) up to $180°C$, which was the curing temperature, and it reached 700 MPa. After cooling the SMA foils down to RT, the recovery stress remained at approximately 100 MPa. The recovery stress reached 350 MPa by reheating up to $80°C$ (again above A_f).

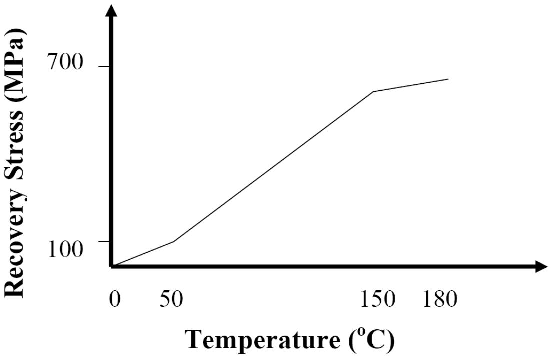

Figure 2-6: Recovery stresses of SMA foils as a function of current heating temperature [175]

In the opinion of Bollas et al. [28] the most efficient SMAHC are those that consist of aramid fibers/NiTiCu wires embedded into an epoxy resin matrix, for the following reasons: (1) fiber reinforcements and SMA wires have similar Young's moduli (Austenite phase); (2) the low negative thermal expansion of the aramid fibers generates relatively small residual thermal stresses within the composite during processing. These authors also note that an epoxy resin matrix with glass transition temperature (T_g) higher than the activation temperature (A_f) of the SMA wires must be selected in order to ensure the generation of recovery stresses. Similar benefits are reported by Zheng et al. [272], but for Kevlar fibers/3% pre-strained TiNiCu wires embedded in an epoxy resin matrix.

Tsoi et al. [240] note that the issues related to fatigue of the SMA fibers and their behavior under cyclic conditions must be addressed, when the fibers need to be continuously activated on and off.

2.3.2 SMAHC Properties

As discussed in Tsoi et al. [243] there is a thermal limit to the generation of SIM and this occurs at temperatures above the dislocation temperature M_d, at which the stress required to form SIM is greater than that needed to move dislocations. Hence, SIM is formed at temperatures T_d between the Martensite start temperature M_s and M_d, i.e. $M_s < T_d < M_d$. Complete superelasticity occurs when SIM is formed above the austenitic transformation temperature, A_f but below M_d.

The levels of compressive residual stresses which are generated in the matrix of the SMAHC during the heating process will vary depending on the fiber pre-treatment, distribution configuration and host matrix material, as well as on the boundary conditions [249].

Effects of the constraining Matrix

The functional properties of the SMAHC are directly related to the constraining behavior that the composite matrix has on the SMA fibers [240]. When the embedded SMA wires are constrained, they operate against the elastic stiffness of the host matrix biasing its strain recovery. Psarras et al. [196] point out that the interface between the wire and the polymer matrix must be sufficiently strong to be able to transmit stresses to the adjacent material.

Various authors [190, 242, 273, 241] explain the effects of the constraining matrix on forward and reverse Martensite transformations in terms of *self-accommodating martensite* (SAM) and *preferentially oriented martensite* (POM) . Tsoi et al. [242] found that there is no significant change in the transformation temperatures of the constrained SMA wires with increasing pre-strain value, but that the measurable transformation heats decrease significantly with increasing pre-strain. Comparing the recovery stress with the heat flow in figure 2-7 (NiTiCu, 3% pre-strain, two cycles shown), it is clear that in the temperature range between $70°C$ and 110°C, where recovery stresses are generated, no indication of a transformation is observed. This indicates that the recovery stress generation is not associated with one or more transformation peaks and vice versa. This observation can be explained by the difference in SAM and POM martensitic variants that can be both present in an SMA.

When there is no stress applied to the alloy and a forward transformation occurs, the strain of one martensitic variant is compensated by the other surrounding variants; so that as the variants grow and shrink self-accommodating groups of martensitic variants (SAM) form at zero net strain. If a stress is applied to an SMA with SAM-variants, the boundaries between adjacent variants move through the growth and compensating contraction of adjacent variants leading to preferentially oriented Martensite (POM) and a net strain is present. Thus, in a first approximation, a specimen containing 100% volume fraction of SAM-variants can be transformed into 100% volume fraction of POM-variants, resulting in the maximum shape memory strain of the alloy. Further straining will induce plasticity. When activated by heating of the SMA, without any external constraint, the SMA will undergo a reverse martensitic transformation of SAM and POM into Austenite and recover the induced shape memory strain. The volume fraction of POM-variants is directly proportional to the amount of shape memory strain.

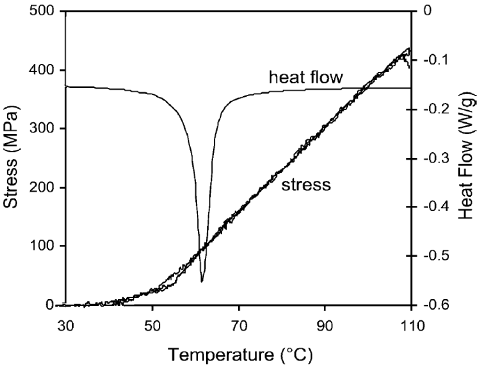

Figure 2-7: The recovery stress build-up and heat flow vs. temperature for a constrained shape memory wire (reproduced with permission from [242])

Pre-strained martensitic SMA wires operate, during heating, against the elastic stiffness of the host matrix, biasing their strain recovery. The reverse transformation of SAM, in a constrained condition, is not impeded by the matrix because no macroscopic shape change occurs during the transformation of SAM. Thus, the constraint has no influence on this transformation. The transformation of POM will be impeded because it generates a net strain that will be constrained. As a result, the shape memory strain associated with the reverse transformation of POM is delayed by the matrix, and recovery stresses are generated gradually by the SMA wires in the composite at a constant rate $d\sigma/dT$ beyond the Austenite finish temperature A_f. After overcoming a temperature hysteresis, the reverse process occurs during cooling. The speed at which the recovery stresses build up is independent of the percentage of POM.

As pointed out by Parthenios et al [190] the ability of an SMA wire to generate recovery stress depends on (a) the initial pre-strain of the SMA wire, (b) the stress rate, $\mathrm{d}\sigma/\mathrm{d}T$, where σ and T are the recovery stress and the activation temperature, and (c) the width of the hysteresis. The stress rate can be considered a material constant, while the width of the hysteresis depends on the SMA wire composition. As the pre-strain increases the amount of POM-variants increases and higher recovery stresses are generated and, thus, the temperature hysteresis size should decrease. In general, the hysteresis observed in a SMA is related to friction produced by the movement of interface boundaries during heating. Thus, if the SMA has a high percentage of SAM-variants there are many boundaries which move when the SMA is heated, therefore, there tends to be a larger hysteresis when compared to a SMA with a large percentage of POM-variants, where there are less boundaries resulting in a smaller hysteresis.

These results were confirmed by Zheng et al. [271] in the case of pre-strained TiNi fibers embedded in a metal matrix. They found that in the case of SMA wires pre-strained between 2% and 6% at the beginning of the reverse transformation, the Martensite volume fraction decreases rapidly, corresponding to the reverse transformation of SAM. When the transformation of SAM is over, POM is still transforming. The total Martensite fraction is not a linear function with temperature. When the specimen is pre-strained to 8%, there is no SAM in the TiNi fiber and the reverse transformation of POM occurs slowly over a large range of temperatures.

Jonnalagadda et al. [115] observe that the restraining effect of the matrix increases with increasing SMA/polymer adhesion, because the increased bond strength reduces the displacement of the SMA wires increasing the interfacial shear stress induced in the matrix.

Effects of Pre-strain and Volume Fraction on the Recovery Force

For a specific SMA material, the constrained recovery stresses will grow in proportion to the pre-strain and the volume fraction of transformed phase within a certain range until optimal values can be found [248, 249, 241].

Tsoi et al. [240] showed that the rate of recovery stress build-up depends on the pre-strain value for a bare SMA wire. The higher the pre-strain value, the slower the recovery stress build-up is. It might be expected that to an increment in volume fraction of SMA wires in the SMAHC (i.e. the more wires are embedded) should correspond a rise in the recovery stress. However, the results in Tsoi et al. [241] show no clear increase in recovery stress with pre-strain. Vice versa, Psarras et al. [196] found that the residual compressive stress decreases as the SMA volume fraction grows. The authors consider this behavior as a direct consequence of the stresses developing during curing. In fact, since the SMA wires are prevented from contracting (during the Martensite-Austenite transformation), as a result of the imposed pre-strain, the tensile stresses which develop during curing are transmitted to the neighboring fibers. The net effect is a reduction of the residual compressive stresses that the fibers would have if the constrained wires were not present.

Tsoi et al. [241] found that the stress-temperature behavior of the SMAHC was similar to that of the bare SMA wires and, in particular, the effect of a difference in the stress rate with temperature. It was found that the SMAHC exhibited a small stress-temperature hysteresis compared to a Kevlar reference specimen. The smaller the hysteresis in the strain-temperature curves, the better are the fibers for being embedded into composites, due to the easier heating capabilities. A small temperature hysteresis also provides better control over the recovery stresses and the temperature range in which they can be activated [240]. Tsoi et al. [240] also showed that at different temperatures the Young's modulus of the hybrid composites changes very little with differing pre-strain. The authors explain this as the effect of the decreasing modulus due to the Kevlar fibers being overcome by the activation of the SMA wires, thus stabilizing the stiffness of the composite.

Interfacial Bonding

Maximum interfacial adhesion between the SMA fibers or foils and the matrix is desirable in the SMAHC because most applications require maximum load transfer, and a strong interfacial bond also increments the structural integrity of the final composites [182, 172].

Various surface treatments of the SMA fibers can be used to improve the interfacial bonding. These surface treatments are normally conducted in order to achieve anchor effects with roughness of the metal surface, to produce a porous oxide layer, or to improve the wetting properties between metal and resin. Ogisu et al. [172] argue that the first factor should be the most effective in improving the bonding properties between SMA and carbon fiber reinforced plastics (CFRP) . According to Wei et al. [249] sand-blasting of SMA fibers increases the bond strength, while hand sanding and acid cleaning actually decrease the bond strength. Paine and Rogers [182] found that plasma coating of the fibers did not significantly alter the adhesive strength. Ogisu et al. [172] checked various methods for improving the bonding properties between SMA foils and CFRP. They performed peel resistance and single lap shear strength tests on SMA foils surface treated with different methods, such as sol-gel method, anodic-oxidation method and spattering method. They found that the treatment by 10% NaOH anodic oxidation was the most effective for improvement of bonding properties. The treated surface was found porous and rough, with improved anchoring effects on the SMA/CFRP interfaces.

Amano et al. [4, 5] also treated the SMA foils with a 10% NaOH anodic oxidation in order to improve the adhesion performance of the epoxy resin. The same authors

[173] cleaned and roughened with 3% fluoride acid-15% nitric acid the SMA (NiTi) foils in order to remove the oxide film created when the material was mechanically rolled. The SMA foils were also cleaned using a solvent when the laminates were manufactured. Amano et al. [4, 5] and Ogisu et al. [173, 175] used an epoxy adhesive film to increase the adhesion between the CFRP laminate and SMA (TiNi) foils. In Jang and Kishi [108] the surfaces of the SMA (TiNi) wires were chemically etched for 10 min in 3% HF+15% HNO3 solution in order to obtain strong adhesion between the SMA wires and a CFRP matrix.

2.4 SMAHC Constitutive Equations and Modeling

Different approaches have been followed for modeling the embodiment of the SMA material in a composite structure.

2.4.1 Using an axial force or elastic foundation

The first simplest approach is to model the effects of the SMA on the composite structure as external axial forces [229, 230]. The amount of recovery stress can be obtained from constrained recovery experiments on shape memory alloy wires or be based on constitutive models of monolithic SMA. A second approach is to model the constrained SMA wires as an equivalent elastic foundation acting on the composite [80]. The elastic foundation stiffness is related to the tension in the shape memory alloy wire. As pointed out by Zhang and Zhao [268], the above approaches amount to neglecting the change in length of the shape memory alloy elements and the interaction between the composite and shape memory alloy deformations.

2.4.2 Modeling only SMA-Composite Interaction

A third modeling approach is to consider the SMA wires and the host structure as separate elements and model their interaction [257, 90, 62]. In Xu et al. [257] the interaction between SMA and the host structure is developed using the Brinson constitutive model. One advantage of this approach is that if SMAHC design parameters change, such as the volume fraction, location and position of the SMA elements in the SMAHC, there is no need to recalculate the constitutive equations of the SMAHC. This simplified approach is not very accurate because it is does not model the interactions between the different constituents in the SMAHC.

2.4.3 Homogenization Techniques

A fourth approach is to model the SMAHC as an equivalent continuum using homogenization techniques. In simpler homogenization techniques the influence of the

SMA on the structure is deduced from the behavior of the monolithic SMA material as predicted by constitutive models model or on the basis of experimental results, assuming perfect bonding and integrating over the beam or plate section [227, 244, 220, 218, 92, 14, 214, 119, 120, 121, 269]. A three-dimensional homogenization technique is developed by Kawai [117].

While such a simplified approach may be satisfactory for structures containing in-sleeve SMA wires, the analysis of structures consisting of active composites, namely polymeric or metallic matrices in which SMA wires are directly embedded, should be based on constitutive relations that have been established by a micromechanical approach. In the framework of such an approach, the detailed interaction of the SMA material with its surrounding is taken into account.

More complex homogenization techniques have also been proposed, involving micro-macro analysis [138, 131, 142, 141, 95, 112]. While Gilat and Aboudi [94] adopted the SMA model of Lagoudas et al. [127] in their micro-macro approach, Marfia and Sacco [142] and Marfia [141] adopted the three-dimensional SMA model developed by Auricchio and Petrini [10, 11]. Jarali et al. [112] extended the model of Marfia and Sacco [142] to include also hygro-thermal effects.

Homogenization techniques are an accurate way of modeling the interaction between the different constituents in the composite, Daghia [62] lists some drawbacks of the homogenization techniques. (a) The non linear behavior of the SMA generates a non linear equivalent continuum, increasing the problem complexity. (b) Some homogenization techniques require three-dimensional SMA model, while SMA wires usually introduced in SMAHC are generally well described by with one-dimensional behavior. The three-dimensional SMA models require greater computational cost respect to one-dimensional models. (c) If the design parameters of the SMAHC change, this approach requires recalculating the homogenized constitutive equations for the SMAHC at an added computational cost.

2.5 Passive Impact Damage Suppression

The passive impact damage suppression mechanism of SMAHC consists in using the energy dissipation properties of the suprelastic (SE) or SIM phase transformations of the SMA material embedded in the composite to dissipate the energy of the impacting object. The passive damage suppression mechanism described above consists simply in increasing the impact damage resistance of the composite through the incorporated SMA material. The SMAHC structure is considered to be *smart*, because it is able to react to stimuli of the external environment, but the suppression mechanism itself is considered to be *passive*, because there is are no activation sensing or functionalities present in the structure.

Passive impact damage suppression will be discussed distinguishing between the different physical forms of SMA material embodied in the hybrid composite and the impact velocities.

2.5.1 SMAHC with uni-directional SMA Wires

Low-velocity Impact Suppression

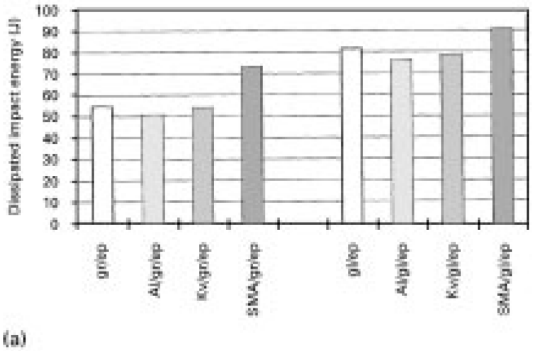

(a) Low-velocity impact tests

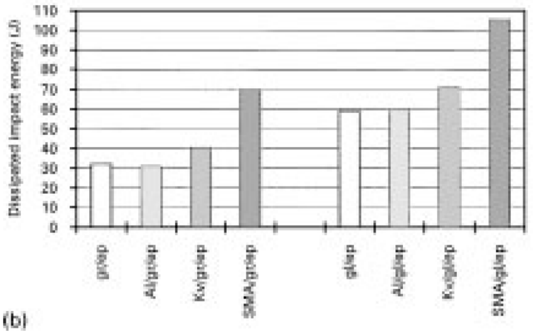

(b) High-velocity impact tests

Figure 2-8: Impact energy absorption for various composite materials [187]. The dissipated energies are volume normalized (reproduced with permission from [249])

SMAHC were first used for improving the impact damage resistance by Paine and Rogers [182, 185, 184, 183, 187, 186]. They performed low-velocity impact tests with velocities lower than 6 m/s using an instrumented drop-weight impact tester on graphite/bismaleimide (gr/bis) and glass/epoxy (gl/ep) composites hybridized using surface layers (to facilitate observation of the failure modes and simplify fabrication) of NiTi fibers/epoxy with 10-25% volume fraction of SMA. Aluminium/epoxy and Kevlar/epoxy hybrid layers were used for comparison. The dissipated impact energy and deflection during impact were determined from force-time data and the ability of various materials to resist the motion of the top during low-velocity perforation can be illustrated from the load versus displacement response (see figure 2-8). From the normalized energy values, which represent the amount of energy per unit volume required to perforate the various materials, it was found that the Ti-Ni/graphite composite produces a rise of 35% for the volume-normalized perforation energy over the monolithic graphite/epoxy (gr/ep) host composite, whereas the aluminium and Kevlar^{TM} hybrids produce little or no increment at all in the energy. Also the monolithic gl/ep composite demonstrated significantly greater impact toughness than the monolithic gr/ep composite. The SMAHC demonstrated a slightly improved perforation toughness and visual inspection showed that they resisted the cutting action through distributing the impact load over a greater surface area, because SMA remained intact during the perforation event. The aluminium and Kevlar^{TM} hybrid composites showed a diminished benefit and failed locally from a punched or cut hole from the local transverse shear stresses at the edge of the impact site.

Paine and Rogers [185] carried out low-velocity tests on a cross-ply layup of $[0^\circ_2, 90^\circ_2, 0^\circ_2]$ of graphite/bismaleimide composite laminates with 2.8% volume fraction of embodied superelastic NiTi fibers of diameter 0.3 mm, with no pre-strain, embedded in the lower $0^\circ/90^\circ$ interface. During the impact tests they found that their specimens were not clamped sufficiently and underwent large deflections and slippage. Using a visual inspection method they compared the amount of impact damage against a reference graphite laminate and found that for high-energy impacts of 18 J and 23 J, the SMA wires in the hybrid laminate prevented complete perforation during the impact. They also found that the all graphite laminate specimens had a larger visible delamination than the hybrid specimens. They then used a special clamping device in order to secure the specimens and to obtain smaller deflections during impact. For these specimens they found that is was more difficult to evaluate the amount of impact damage based only on visual inspection. At the highest impact energy level of 14 J, all graphite laminate specimens underwent complete perforation whereas with the hybrid specimens only the layers above the SMA wire layer were perforated. It was also determined that the peak impact forces of the hybrid specimens were much higher than the all graphite specimens. The delaminations in the center of the laminate were similar in size for both types of specimens.

Kiesling et al. [122, 123] performed quasi-static tests and low velocity (13.9 ft/s) impact tests (resulting in complete penetration) on Graphite/Bismaleimide laminates embodied with uni-directional (3 vol%) and bi-directional (6 vol%) superelastic Ti-Ni fibers. Energy absorption during complete penetration of the hybrid composites was shown experimentally to be significantly improved by low volume fractions of incorporated superelastic SMA fibers. The results showed that although damage initiation and peak loads did not seem to be affected by the SMA fibers (i.e. stiffness and ultimate strength of the composite remained unchanged), the energy absorption after peak loads was greatly increased (41% was observed in bi-directional SMA hybrids and 23% in uni-directional SMA hybrids) suggesting that the SMA fibers distributed the impact load to a greater volume of graphite. However, C-scans of the bi-directional SMA hybrids showed a 22% larger delamination area compared to plain graphite epoxy.

Jia et al. [114, 113] developed a one-dimensional analytical model for studying the impact force and the strain energy absorption of a SMA/graphite/epoxy composite beam under low-velocity impact relating contact deformation, global bending deformation, and transverse shear deformation. The energy absorbed by the SMA hybrid composite is calculated for each contributing factor, and then related to the extent of martensitic phase transformation of the superelastic SMA fibers. They found that at very low velocities, the contact energy absorption is the most effective mechanism, while the shear deformation absorbs most of the impact energy at higher impact velocities and that the total energy absorption of the SMA hybrid composites grows when the stress-induced martensitic transformation occurs. An important result is that the superelastic SMA has better strain-energy absorption capabilities than the martensitic SMA: the maximum strain energy stored in the superelastic SMA being at least twice the maximum strain energy stored in the martensitic SMA.

Tsoi et al. [243] compared the effects of embedding in one layer NiTi superelastic fibers pre-strained to 0, 1.5 and 3% against martensitic NiTi, NiTiCu and steel wires at different through-the-thickness positions within a cross-ply layup of $[0°, 45°, 90°, -45°]_{2s}$ of a glass/epoxy composite. The fibers were aligned along the centre of the plate with a volume fraction of 0.45% (0.5 fibers/mm), 0.89% (1 fibers/mm) and 1.8% (2 fibers/mm) and were placed in the centre, off centre at either 1/2, 1/4 or 3/4 of the through-the-thickness of the plates or in the bottom layer (i.e. 15/16-th). The influence of the wire pre-strain, the wire volume fractions and the wire position on the composite's impact behavior was investigated. It was found that the position of the wires within a laminate is important, in particular between which plies the wires are embodied. The authors' conclusions were that wires should be embedded between 0° plies and any other ply, in order to incorporate them into the matrix leaving no brittle areas. Moreover, embedding the wires in the lower half of the specimen, preferably along the bottom layer, improves the resistance, in particular, to fiber breakage. In fact the wires positioned along the bottom of the specimen (15/16) show an improvement in the energy absorbed of around 25% and 19% for 0.89 vol% and 1.8 vol%, respectively. The projected damage area shows that there is significantly more damage occurring in the plates which contain the wires positioned in the centre. The reason for this is that when the SMA fibers are placed in the centre of the laminate they are placed between 45° plies, and, during curing, the glass and SMA fibers are in different directions, which hinder their joining movement. Because the epoxy matrix runs in between the two types of fibers, a brittle area is formed. During impact, the material is very brittle and susceptible to greater damage.

The volume fraction of the fibers also plays an important role. Samples with different volume fractions of superelastic SMA fibers embodied along the bottom of the specimen were impacted with energies of 6, 12 and 18 J. The results for 6 and 12 J show no significant differences and only at the higher energy level (18 J) the differences are significant. The higher impact energy needs to be dissipated by the specimen and usually goes into damaging the specimen, but as the volume fraction of superelastic SMA fibers grows the amount of energy which goes towards damaging the specimen decreases, since the SMA fibers absorb some of that energy. For the lower impact energies (6 and 12 J), the size of damage of SMA-composites, compared with reference specimens, was equivalent and differs from previously seen results in Paine and Rogers [184]. These differences may be due to the differing layup of the composites. Also due to the limited amount of SMA wire compared to the total volume of the SMAHC the effect of the wire on the impact behavior is limited.

These results are summarized in figure 2-9 using the graph of the *PDA slope* versus the *IEC slope*. The PDA slope is the slope of the damage area versus incident energy and is an indication of the damage resistance of a material. The IEC slope is the slope of the absorbed energy versus incident energy and is a measure of the energy absorption capacity of the material. A high PDA slope is an indication of easier damage accumulation and a high IEC slope suggests a greater capacity for internal damping and impact energy absorption. Of the three different types of volume factions of superelastic SMA fibers, the $0.5fibers/mm$ samples have good damping properties, absorb a lot of energy and have a reasonably low damage accumulation. In general, all three types of superelastic volume fractions show good properties. The choice of wire volume fraction would depend more on the specific application

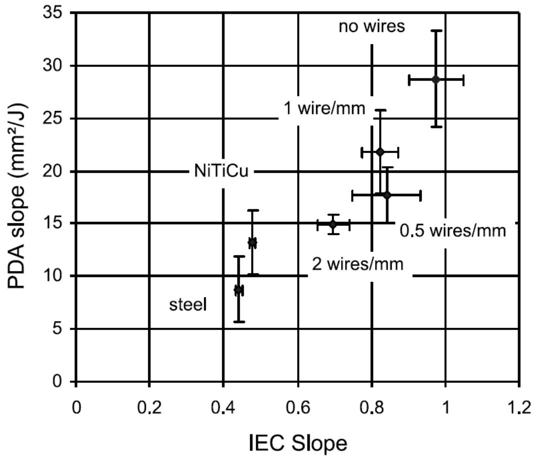

Figure 2-9: Impact performance map (reproduced with permission from [243])

Meo et al. [149] carried out a finite element analysis of carbon fiber/epoxy composite plates incorporated with SMA (NiTi) wires (in the austenitic phase) subjected to low velocity impact with different volume fractions of SMA wires, studying the energy absorbed during the impact, the number of failed plies and the maximum load carrying capability of the studied composite plate. The authors concluded that the influence of the embodied SMA wires on the number of failed plies increased as the impact energy increased. Furthermore, the effect of the SMA wires on the absorption of impact energy was higher as the SMA wires were closer to the impact location.

High and Ballistic-velocity Impact Suppression

High-velocity impact events refer to cases of foreign objects impacting at speeds in the range of 30.48 – 243.84 m/s (100 – 800 ft/s) including situations such as a bird colliding with an airplane. Ballistic impact events refer to cases of foreign objects impacting at speeds exceeding 243.84 m/s (800 ft/s) including situations such as a projectile fired from a gun [79, 78]. Because the high- and ballistic-velocity impact events are characterized by a much more local response of the composite than the low-velocity impact events, these impact results may demonstrate significantly different behavior from the low-velocity test [249].

Chen and Lagoudas [47] modeled the behavior of a semi-infinite rod of SMA material subjected to an end impact load of prescribed constant stress using the thermomechanical constitutive theory developed for bulk SMA by Boyd and Lagoudas [30, 31]. They found that a typical solution is characterized by two wave fronts which are initiated at the impact surface and propagate into the rod. One wave travels at the acoustic speed, separating the tranquil and disturbed regions. The other wave travels at a lower speed, separating the regions of the martensitic and austenitic phases. Furthermore, the stress and temperature are continuous in the transition region when the impact stress is below a certain value, and they become discontinuous above this value. A special feature of the solution is that the temperature jump can be as large as $50^{\circ} K$ under certain conditions.

Meziere and Millett [150] investigated the influence of impact stress on the mechanical behavior of SMA (NiTi) subjected to one-dimensional shock loading using a single stage gas gun. They found that the relationship between shock velocity and particle velocity was strongly nonlinear, and attributed this behavior to irreversible (slip) martensitic transformations within the material. The higher the material is shocked, the more the material changes its crystal structure affecting the dynamic properties of the NiTi, with the effect of reducing the wave velocity in the material. They used a bilinear representation to describe this trend (see figure 2-10).

Paine and Rogers [183, 187] performed high-velocity impact tests at a velocity of up to 152.40 m/s (500 ft/s) by using a non-instrumented gas-gun on composites with the impacted layer hybridized using superelastic NiTi elements. Graphite/BMI and glass/epoxy specimens with the impact side surface layers (hybridized) of NiTi/epoxy, aluminium/epoxy and Kevlar/epoxy were experimentally tested. They found that

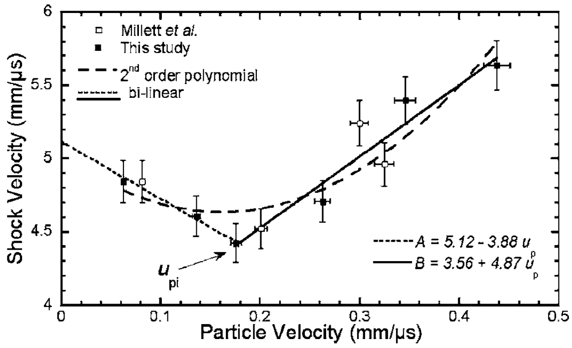

Figure 2-10: Shock velocity versus particle velocity of NiTi (reproduced with permission from [150])

the SMA hybrid composite increased the composite's perforation toughness by 100%, while the glass/epoxy system showed a growth of 67% over comparable monolithic graphite/BMI specimens. In both the systems, the Kevlar hybrid composites demonstrated only a slight improvement to impact energy, while the aluminium hybrid showed little, if any, improvement.

Ellis et al. [78, 79] performed ballistic-impact tests using a 9 mm Beretta handgun with projectiles traveling at velocities greater than 274.32 m/s (900 ft/s) on graphite/epoxy composites with various SMA component configurations. The uni-directional Ti-Ni SMA fiber layer with 1.2% volume fraction was embedded on the front face, in the middle, and on the back face of the host graphite/bismaleimide composite, respectively, to form three hybrid configurations. From visual observation and energy absorption values, it appeared that the back face was the most suitable location of the SMA fibers in the hybrid composite, and no increment in the energy absorption was observed when the SMA fibers were placed on the front and middle locations. In all cases, the SMA fibers were typically pulled through the graphite with-out being strained to their full potential, resulting in a slight, if any, improvement in the high-velocity impact resistance. Increasing the volume fraction of the uni-directional SMA fibers or adding two perpendicular layers of SMA fibers on the back face of the composite yielded no remarkable rise in energy absorption. These facts suggest that the high strain-energy absorption capabilities of SMA were not fully utilized at ballistic velocities because of the high strain-rate effects coupled with a strain mismatch between the relatively tough SMA fibers and the brittle cured epoxy resin [79]. However, the SMA fibers were found to be more effectively used when embodied between layers of the thermo-plastic high performance extended chain polyethylene (ECPE or Kevlar^{TM}) prepreg which were then placed on the back face of the graphite composite: an increment of 23-24% in the energy absorption was achieved when compared to the plain graphite composite. Nevertheless, the SMA fibers were still not fully utilized as evinced by the lack of fibers strained to failure [78].

2.5.2 SMAHC with Woven SMA Wires

The first example of the use of SMA fabrics for composite structures was reported by Boussu et al. [29]. The authors manufactured a fabric of NiTi wires and compared the elastic properties with those of a fabric of stainless steel wires concluding that NiTi has a better aptitude to weaving than stainless steel. No information is provided in this chapter about the practical details of the weaving procedure, but no weaving machine seems to have been utilized.

Masuda et al. [143] produced a fabric of NiTi wires without using a weaving machine, but by hand using simply an apparatus to keep the wires in place during the weaving process. They did not precisely control the pre-strain nor the volume fraction of the SMA wires.

Zhang et al. [265] compared laminated composite plates containing uni-directional fine SMA (NiTi) wires against laminated composite plates with an embodied woven SMA (NiTi) layer and compared their mechanical properties, especially for natural frequency as a function of temperature, after impact vibration tests. The fabric of SMA wires was hand made using an apparatus to align the SMA wires and to maintain proper geometries and restraints on the warp and weft wires. The authors reported that both SMAHC structures seemed very effective in damping the vibrations. They also highlighted the importance of optimizing in the SMA laminated structures the volume fraction and pre-strain of the SMA wires in order to control efficiently the mechanical characteristics of the manufactured hybrid composite.

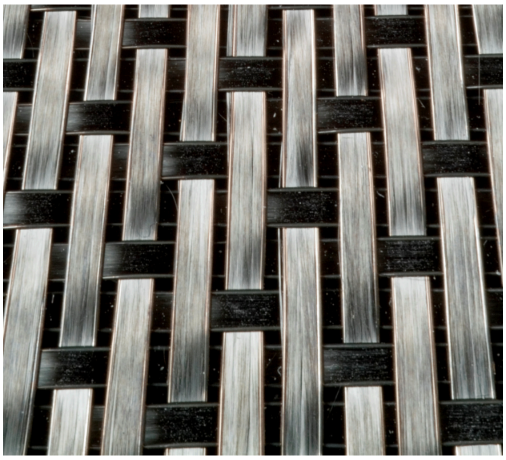

Figure 2-11: Woven SMA carbon fiber fabric (reproduced with permission from [89])

Foreman et al. [89] studied the improved impact resistance properties provided by the SMA-reinforced carbon fiber woven fabrics shown in figure 2-11. The SMAHC were manufactured using an advanced weaving technology that allowed controlling precisely the volume fraction of the embedded SMA (NiTi) by changing the number of SMA wires in the warp and weft directions of the fabrics. The authors performed impact tests using an instrumented falling weight impactor. Two different NiTi alloy types were selected; one was in the martensitic phase at the test temperature, while the other was in the austenitic phase at the test temperature. Different test were performed in order to evaluate the effect of several different material variables, such as SMA type, SMA volume fraction, SMA / carbon fiber weave style and distribution of SMA through the laminate. The results are compared to the baseline composite without SMA wires using energy absorption normalized per unit mass, i.e. the absolute energy absorbed divided by the mass of the clamped region of material during test. The SMAHC shows a performance improvements of 61-227% in the impact energy absorbed compared to baseline in the case of the 10.8% volume fraction SMA. When normalised for mass, this corresponded to a growth from 0.42 for the baseline laminate to 0.97 Joules per gram (see variant 5 in figure 2-12). The authors conclude that the impact energy absorption does not depend on the position of the SMA reinforcement through the thickness of the laminates. They also found that SMA volume fraction and energy absorption vary according to a simple linear relationship. They highlight a significant difference between the impact energy absorption of composite laminates reinforced with SMA alloy in martensitic phase and austenitic phase. This was related to the importance in selecting alloy types which offer similar stress-strain characteristics to the bulk composite, up to the point of its failure in the impact event, in order to achieve the optimal *hybrid* effect from the different materials employed.

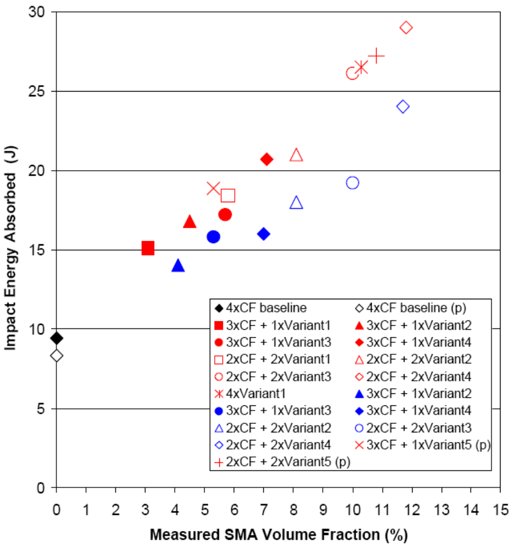

Figure 2-12: Woven SMAHC energy absorption per unit mass for different SMA types and volume fractions (reproduced with permission from [89])

2.5.3 SMAHC with Stitched SMA Wires

While in the previously reported studies the SMA wires were embedded into the hybrid composite during the manufacturing process, Lau et al. [130] studied an alternative approach of using SMA wires (NiTi in full austenitic phase) to stitch a ten layers composite plate of Glass fiber woven fabric and epoxy resin. The authors then subjected stitched and unstitched samples to drop-weight tests and calculated the energy distribution after impact. They found that increasing the volume fraction of SMA resulted in a reduction of the delamination energy and in a rise of the stiffness of the stitched composite plates. Moreover, the natural frequency of the composite plates decreased and the SMA damping energy increased with the increasing of volume fraction of SMA.

2.5.4 SMAHC with SMA Short fibers and Particles

The strengthening of Aluminium metal matrix composite (MMC) using dispersed SMA (TiNi) particles was theoretically studied by Yamada et al. [258]. The strengthening effect is produced by the fact that the SMA filler shrinks in the matrix at the temperature of operation (because of the higher *coefficient of thermal expansion* (CTE) of the filler than that of the matrix) generating a compressive residual stress in the matrix that increases the tensile properties of the composite [250]. The compressive residual stress helps improve certain mechanical properties such as yield strength and fracture toughness.

Murasawa el al. [162] studied the thermo-mechanical properties and damage characteristics of hybrid reinforced composites with short and long SMA (NiTi) wires. In Murasawa el al. [163] the properties of the hybrid fiber reinforced composites with short SMA wires were compared to those with long wires when changing the aspect ratio (i.e. ratio of fiber length to diameter) and volume fraction of the SMA wires. They found that the shrinkage after heating (and in correspondence compressive residual stress) in the matrix increased with the increasing of aspect ratio and volume fraction of the SMA wires. The composite strain history and residual stress history in the matrix varies depending on the aspect ratio and volume fraction of the SMA wires. Quite interestingly, the change of aspect ratio has a small effect on the creation of internal stress in the matrix and deformation of the composite, while the apparent transformation temperature of SMAHC can be changed by changing the aspect ratio. They concluded that for an aspect ratio greater than 25.0 the short and long wires have a very similar performance.

Xie et al. [255] pre-strained the short fibers before embedding them into the matrix and studied the effects of different pre-strain levels. Zhang et al. [266] and Ni et al. [169] studied the effects of dispersing SMA (NiTi) (particles or short fibers) fillers into ER3 epoxy resin. The authors found that by adding 3.5% of SMA fillers to epoxy resin there was a rise of storage modulus as large as six times and of natural frequency as large as 1.26 times that of bulk epoxy resin in the glass transition region; that the loss factor of the short fiber SMA composites grows with the increasing of filler contents; and that the composites with SMA particle fillers exhibit higher loss factors than those with SMA short fiber fillers.

2.6 Active Impact Damage Suppression

The active impact damage suppression mechanism of the SMAHC consists in using the energy dissipation characteristics of the SME phase transformation of the SMA material embedded in the composite to dissipate the energy of the impacting object. Contrary to passive suppression, in this case the phase transformation is stimulated (activated), normally via the application of heat, by the structure itself. One or more types of sensors are used to detect the impact damage on the structure. This is again a *smart* structure, but the suppression mechanism itself is considered to be *active* because of the presence of sensing or activation devices present in the structure. Materials with active impact damage suppression capabilities can be considered examples of *self-healing* materials (e.g. [34, 38]), sometimes called *self-repairing* materials, which are reviewed in general by Kessler [118].

Active impact damage suppression will be discussed distinguishing between the different physical forms of SMA material embodied in the hybrid composite.

2.6.1 SMAHC with uni-directional SMA Wires

Rogers et al. [205] proposed to use SMAs as actuators, because of their good strain energy absorbing capabilities, in order to actively accelerate closure of fatigue cracks and to reduce crack propagation speed. By placing the SMA fibers at the bottom of the notch part where stress concentrates and by applying electric currents in order to heat the SMA fibers thus causing contraction forces within them, it was possible to lower average stress values [205].

Kuang and Cantwell [125] performed a study on the effects of impact on a woven carbon fiber-reinforced epoxy resin beam to which a SMA (NiTi) wire was bonded using an epoxy adhesive. The SMA wire was trained before being attached to the composite beam. Plastic optical fibers (POF) were used as sensors to assess the damage produced by the impacts. The authors first demonstrate theoretically that the damping ratio is inversely proportional to the square of the material stiffness, and then experimentally that increasing the impact energy there is a rise in the measured values of damping ratio, and therefore a reduction of the specimen's stiffness. When the SMAHC beam is impacted with energy of approximately 0.25 J, this being sufficient to provide a vibratory response without damaging the beam, the tests demonstrated that the addition of the

SMA wire has the ability to change the damping response of a composite beam. They showed that when the SMA is activated there is a reduction in the vibration amplitude occurring in the very first cycle compared to when the SMA is deactivated (see figure 2-13). The damping capability of the SMA in the austenitic phase is attributed by the authors to the energy dissipated due to internal friction at the interface of the stress-induced Martensite and the parent phases. They also point out that when high oscillation amplitudes are applied, more energy is available to induce the formation of Martensite resulting in the creation of more interfaces leading to a growth in damping capability of the SMA.

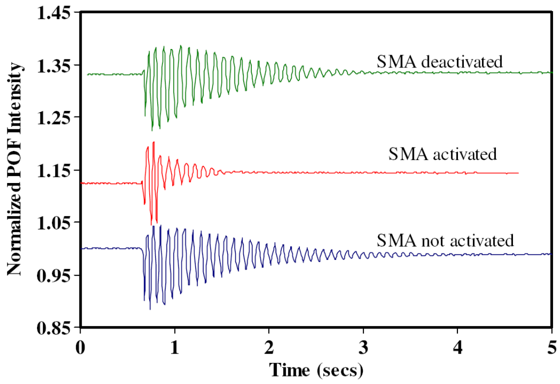

Figure 2-13: Dynamic response of an SMAHC impact-loaded beam (reproduced with permission from [125])

Zhang et al. [267] analyzed the energy absorbing properties of E-glass composite beams reinforced with a 10% volume fraction of incorporated SMA (NiTi alloy) wires (a weight penalty of about 6%). The beams were subjected to tensile tests, and the responses of baseline composite beams was compared with those of SMAHC with no heating, where the SMA wires were in the Martensite phase at room temperature (RT), as well with those of SMAHC with resistive heating, where the SMA wires were in the Austenite phase ($75°C$) at RT. The authors found that when the SMA wires were in the Martensite phase, while there was no significant difference between the hysteresis levels with and without SMA wires, there was a marginal increment in stiffness due to SMA wires of about 5% and the failure stress and failure strain were also higher, resulting in a 50% rise in the strain energy absorption prior to failure. When the SMA wires were in the Austenite phase, there was a significant decrease in the modulus and in the failure load, that the authors attribute to the softening of the epoxy during the heating of the structure required to activate the SMA wires and to failure of the interface between epoxy and SMA wires when the wires contracted due to the reverse martensitic transformation. However, when the SMA wires were in Austenite phase, the composite beam displayed a large hysteresis (and hence damping) compared to the baseline beam, which the authors ascribed to the softening of the epoxy as well as to the large hysteresis associated with the SMA wire response, and the energy absorption prior to failure showed a 600% increase over that for the baseline composite beam, which the authors attributed to the large plastic deformation of the SMA wires.

In Ogihara et al. [170] pre-strained (3.7%) SMA (NiTi) wires were embodied in a symmetrical cross-ply of glass fiber reinforced polymers (GFRP) . The volume fraction of embedded SMA was 10%. The laminates were pre-heated and subjected to tensile loading. The results were compared against various combinations of non preheated samples, non pre-strained samples and samples without the addition of SMA in order to compare the recoverable deformations in the various cases. The authors found that the tensile strength of the GFRP samples that had undergone heat treatment was higher, attributing this behavior to the after cure effect of the heat treatment which enhanced the adhesion between the GFRP plies and the SMA wires. The GFRP with pre-strained SMA wires and heat treatment showed the highest tensile strength. They observed both transverse cracks and delamination in all GFRP laminates during the tensile loading, but only transverse cracks in the GFRP laminates subjected to the heat treatment. In GFRP with pre-strained SMA and heat treatment, the strain at the damage initiation is the highest among the laminates tested. The authors suggested that this implied that the SME of SMA reduced the thermal residual stress in the 90° ply. Moreover, Ogihara and Uehara [171] found that the fracture toughness is higher in acid cleaned SMA wires than in untreated SMA fiber, which implies that the acid cleaning enhances the adhesion between the SMA fiber and the epoxy matrix.

Shimamoto et al. [222, 223] investigated the suppression of crack-tip stress intensity and the change in fracture toughness of composites with an epoxy matrix and incorporated SMA (NiTi) wires with different pre-strain values (0, 1, 3 and 5%) and different crack angles (0°, 15°, 30°, 45°, 60°). They found that the SMA wires were able to suppress the stress intensity factor at the crack tips after heating to the Austenite temperature, and that the suppression effects increased with the increasing of pre-strain levels. Shimamoto et al. [224] verified that there is a retardation in the fatigue crack propagation especially in the region very close to the SMA wires. Araki et al. [8, 7] developed a micromechanics model to study the suppression of crack-tip stress intensity of SMA (NiTi) wires embodied in an epoxy matrix. They conclude that after the activation of the SMA wires via heating, the crack-tip stress intensity decreases gradually, until it reaches a constant value, because of the difference in thermal expansion between SMA wires and matrix. The crack-tip stress intensity decreases with the the increasing of (a) the activation temperature of the SMA wires, (b) the thermal expansion coefficient of the matrix, and (c) the shrinkage of the SMA wires due to the SME.

Jang et al. [111, 109] studied the thermo-mechanical properties of SMAHC composed of pre-strained impregnated SMA (TiNi) wires and CFRP cross-ply laminates. Applying a tensile load the SMA wires were pre-strained between 0.5-7% before being embedded into the CFRP matrix. The authors concluded that the compressive recovery forces generated by shrinkage of the SMA wires increased with the increasing of pre-strain level and number of impregnated SMA wires. They also found that these compressive recovery forces, induced when the pre-strained SMA wires were electrically heated, could heal transverse cracks which formed along the 90° ply CFRP laminate under tensile loading. Furthermore, Jang and Kishi [110] found that the tensile strengths and Young's moduli of the composites decrease as the stacking angle of the carbon fibers grows from 30° to 90°. They put this behavior down to the amount of pores and/or voids that congregate near the embodied SMA wires which were found to rise proportionally with the stacking angle of the carbon fibers.

Kimura et al. [124] analyzed the change in interlaminar fracture toughness and crack propagation rate due to the compressive recovery forces, obtained through heating, generated by SMA (NiTi) wires embedded in CFRP, while performing crack propagation tests under both fatigue and static loading. The results showed that the fracture toughness under mode I static loading increased by 1.7 times. This was attributed to the recovery stress of the SMA wires as well as to the increment in stiffness caused by the embodiment of the SMA wires into the composite. The effect on the fracture toughness of the recovery stress resulted larger than that of the rise in stiffness. The fracture toughness under mode II static loading also increased by 2.3-3.1 times as a result, according to the authors, of (a) the recovery stress of the SMA wires, (b) the rise in stiffness caused by the embodiment of the SMA wires into the composite, and (c) the friction on the fracture surface. Moreover, the fatigue crack propagation tests highlighted a reduction in the crack propagation rate.

Roh and Kim [208, 209] modeled the effects of low velocity impact on SMAHC fiber reinforced plates. The SMA (NiTi) wires are embodied within the layers of a graphite/epoxy composite plate. Three piezoelectric sensors made from polyvinylidene difluoride (PVDF) films are mounted on the opposite side of the impact and used to monitor the impact-induced strains. The deflection and stresses are reduced by employing pre-strained (8%) SMA wires, which are in the martensitic phase when embedded within the plate. The first-order shear deformation theory (FSDT) of plates is used in the analysis and also a finite element formulation is developed to model the dynamic response of the hybrid composite plates. The SMA constitutive used in this study [209] is the Liang and Rogers model [133]. All edges of the plate are clamped and the plate is subjected to an impact with the velocity of 38.1 m/s. The bonded PVDF patches were found to have very little effect on the dynamic response of the plate. The authors imputed this fact to the flexibility of PVDF films, which prove to be ideal sensors. The stiffness of the SMA wires is controlled by the addition of heat (generally obtained by applying a current through the wires), and the resultant in-plane forces adaptively change the structural response of the plate (i.e. ASET). The authors found that, as a result of recovery stress, the maximum deflection of the graphite/epoxy plate was reduced by about 50% with the volume fraction of SMA wires equal to 0.3%. They also found that the orientation of the SMA wires influences the relative deflection. An optimal deflection under the impact can be obtained by considering an appropriate volume fraction of SMA wires and orientation.

Serry et al. [220, 218] propose a sequential solution procedure based of two nonlinear finite-element procedures, the first structural and the second transient electro-thermal, and on the combination of the two after each iteration step. This methodology was then applied to SMAHC composed of SMA wires incorporated into a polymeric matrix for the purpose of investigating the self-healing ability of the SMAHC. The structure uses the variations in the SMA wires as sensor to individuate the presence of a crack (via the reduction of the martensitic volume fraction in the area of the crack, and therefor the rise in resistivity) and the SME induced via heating of the SMA wires is used as actuator to close (*heal*) the crack. The authors then performed a parametric study to evaluate the system. The rise in current density in the SMA wires increases the speed of closure of the crack. It is important to select the proper current density sufficient to close the crack as too much heat might harm the structure. Increasing the wire diameter the amount of heat that can circulate in the SMA wire grows and consequently the recovery forces generated in the wire rises, which speeds up the crack closure. But it was also found that the SMA wire diameter must not be too high because, as the SMA wires have a higher CTE than the matrix, they tend to expand more applying tensile forces on the polymeric matrix that could open the crack instead of closing it. Increasing the volume fraction of SMA wires (i.e. the number of wires per mm^2) was also found to have a positive effect on the crack closure, as now there are more SMA wires near the crack. The summation of the recovery forces of all these wires contribute to closing the crack, and so a smaller force per wire is need. Moreover an increment in number of SMA wires leads to a rise of the sensibility of the system avoiding that small cracks in between the wires remain undetected. The authors found that the SMA wires' pre-strain seemed to have a minor effect on the crack closing recovery process (a part for very small values of pre-strain less than 0.02%), but that sufficient pre-strain is required for obtaining the sufficient volume fraction of detwinned Martensite needed to develop a recovery force strong enough to close completely the crack. Furthermore heat dissipation in the system must be reduced for sufficient heat to be able to reach the SMA wires to generate the recovery forces needed to close completely the crack. Also the initial temperature is important, because as it gets closer to the Austenite start temperature A_s, the reverse Martensite transformation process starts earlier speeding up the crack closure. If the initial temperature is too low, then the longer time required to start the reverse Martensite transformation leads to a growth of the difference in CTE tensile forces and possible harmful effects on the matrix. Serry et al. [219] showed that polymeric matrix materials with similar modulus of elasticity, although their CTE values may be quite different, have similar crack recovery behavior and that the higher the modulus of elasticity is, the faster the crack recovery process tends to be. Finally, the modulus of elasticity of the polymeric matrix also has also an important effect on the SMA wire phase transformation process.

Burton et al. [38] used finite element analysis (FEA) to model the self-healing effect of the recovery stress, obtained through heating, of pre-strained SMA (NiTi) wires embodied in a metal matrix composite. In this study the SMA wires and matrix material are modeled separately in order to allow adapting the method to different types of composites in terms of material properties, locations and positions of SMA wires without reformulation of the constitutive model for the whole composite. The SMA wires were pre-strained to an initial detwinned Martensite fraction of 30%. When unloaded to zero stress, the initial temperature was midway between the Martensite start M_s and Austenite start A_s temperatures and the SMA wires are 100% Austenite. A uniform temperature field is considered during the healing process, neglecting any heat transfer to the matrix. The critical stress to debond the matrix is taken as 60 MPa and the wires transform to a final fraction of 84% detwinned Martensite. Furthermore, the loading of the composite and the subsequent heating are performed quasi-statically. The results show that increasing the density of the wires had the effect of proportionally increasing the closure force upon heating. During heating, the temperature must be raised to well above the Austenite finish temperature A_f to significantly transform the SMA wires to Austenite. The matrix softens during the heating allowing the SMA wires to fully close the crack upon heating. Without sufficient softening, the strong resistance by the matrix would prevent the SMA wires from fully closing the crack.

Khalili et al. [120] divides the effects of embedding SMA fibers on the total stiffness of the composite structure in two different components: *essential* stiffness and *acquired* stiffness. The essential stiffness is the stiffness that a structure gains during the manufacturing process and when it is ready to be used, while the acquired stiffness is the stiffness that a structure gains after its manufacturing process and when it is already in use. Both component contributions are important when SMA wires are used to improve the impact resistance of a hybrid composite structure. Because the SMA wires are embodied in the structure before the manufacturing process of the structure is finished, the presence of these wires changes the essential stiffness component of the structure. When the SMA fibers are activated via heating and they apply positive tensile stresses in the structure this modifies the acquired stiffness component. The authors used an analytical model [119, 120, 121] to study the effects of various parameters on the stiffness components of a hybrid composite structure. See figure 2-14 for some of these parameters.

They considered only cases where the SMA fibers were incorporated in directions

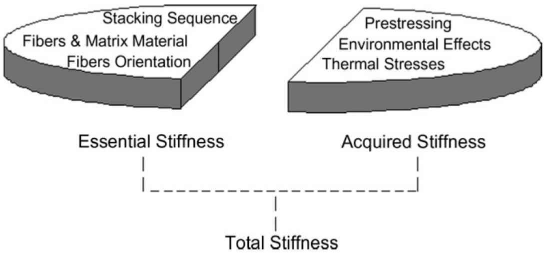

Figure 2-14: The effect of various parameters on the essential stiffness and acquired stiffness of a structure (reproduced with permission from [120])

parallel to the reinforcement fibers of each lamina of the composite, corresponding to the 0° and 90° fiber orientations, simultaneously and in the same volume fraction in each lamina, because they state that if the orientation of the SMA wires is not parallel to the reinforcement fibers of the composite lamina medium, the mismatching of the fibers and the SMA wires might generate some non-fiber spaces which contain only brittle resin, resulting in the reduction of structure properties and eventually causing brittle fracture.

The benefit of embedding the SMA fibers was first studied in relation to increasing the SMA volume fractions in the hybrid composite analyzing two different parameters: (a) the first, the reduction of a non-dimensional transverse deflection w/h, which is the ratio of composite plate deflection to its thickness, is a measure of the benefit to the essential stiffness of the whole structure; (b) the second, the rise in contact force, measures the benefit to the acquired stiffness of the whole structure. There is an interaction between the two stiffness components (*interactive effect*) (see figure 2-15). It was found that the increasing of the volume fraction of SMA fibers more than 40 vol% has only little effect on the reduction of the w/h ratio and so on improving the impact resistance of the structures [119, 120, 121].

The authors find that embedding 40% volume fraction of SMA wires in the composite results in 61% reduction in w/h ratio of the structure, which origins from the increasing of both the essential stiffness and the acquired stiffness of the structure simultaneously (an *interactive effect*). In comparison, embedding 40% volume fraction of steel wires would result instead in only a 7% reduction in w/h ratio of the structure, which origins only from the increasing of the essential stiffness of the structure (a *non-interactive effect*). Although the stiffness of the SMA wires is less than 35% that of the steel wires, they can reduce the w/h ratio of the structure by 54% increasing the essential and the acquired stiffness of the structure together. Note that embedding steel wires instead of the SMA wires would result in a 12.5% increment in the weight of the hybrid composite structure [119, 120, 121].

The authors then studied the effect of the location of the SMA fibers in the through thickness embodied in only two layers of the hybrid composite and keeping a constant

SMA volume fraction equal to 20%. Because the volume fraction of the SMA wires is constant, the positive pre-stress in the structure is the same for all cases, so also the acquired stiffness of the structure is the same for all cases, but the essential stiffness of the structure changes when the location of the SMA wires through the thickness of the structure changes (a *non-interactive effect*). The SMA wires are incorporated in the composite structure within a cross-ply layup of $[0°, 90°, 0°, 90°, 0°]_s$. Embodying the SMA wires parallel to the reinforcement fibers and only in layers 5 and 6 resulted in the lowest value of the w/h ratio of the structure (52%) in comparison with all other cases.

Again for a constant volume fraction of SMA fibers equal to 20%, embedding the SMA wires only in directions parallel or transverse to the reinforcement fibres, but in more than two layers, was more effective than embedding them in only two layers, because, the essential stiffness of the structure is distributed more uniformly so the in-plane strains and stresses on the structure also are distributed in a more uniform way and the impact resistance of the structure improves too. Embedding the SMA wires in the parallel direction was more beneficial than embedding them only in the transvese direction because of the greater negative effect of thermal stresses in the parallel direction, which can be decreased by embedding more SMA fibers in the parallel direction. Increasing the volume fraction to 40%, the negative compression thermal effect of the composite medium decreases, so embedding the SMA wires in direction transverse to the reinforcement fibers improves the impact resistance of the structure a little more, because the volume fraction of the reinforcement fibers of the composite medium in the transverse direction is less than that in the parallel direction. Keeping constant the acquired stiffness and changing only the essential stiffness of the structure (a *non-interactive effect*), the most beneficial properties of the structure are obtained.

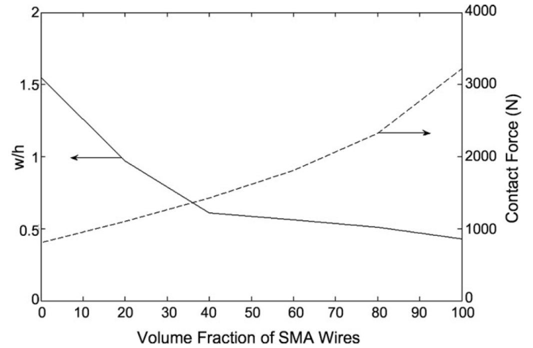

Figure 2-15: Effect of increasing the volume fraction of the SMA wires on non-dimensional deflection (w/h) history and on the contact force history (reproduced with permission from [120])

2.6.2 SMAHC with SMA Foils (Thin Films)

Ogisu et al. [175] studied the best stacking location for the SMA foils using the *strain energy release rate*, G, as an index of edge delamination growth in the laminates. The choice of stacking location of SMA foils affects the overall behavior of smart materials. They found that the best location for suppression of transverse cracks is the 90°-ply in terms of minimum value of the normalized strain energy release rate. For this reason the authors conducted [173, 175, 174] all their tests using the laminates with the stacking sequence of $[+45^\circ/0^\circ/-45^\circ/90^\circ/\mathrm{Ad/SMA/Ad}\ /90^\circ/-45^\circ/0^\circ/+45^\circ]$, where *Ad* is the *adhesive film*. The authors [175] found that the transverse crack onset strain of CFRP laminates with embodied 2% pre-strained SMA increased by 0.22% strain as compared with the conventional CFRP laminates (see figure 2-16). The improvement effect consists of (a) a growth by 0.03% by the incorporated SMA foils, (b) an increment by 0.14% by the recovery stress at RT, and (c) a rise by 0.05% by the recovery stress caused by the heating of 2% pre-strained SMA. The test results confirmed that the onset strain of the transverse crack of CFRP laminates with embodied SMA foils increased by 27% at RT and by 34% at 80°C as compared with the conventional CFRP laminates.

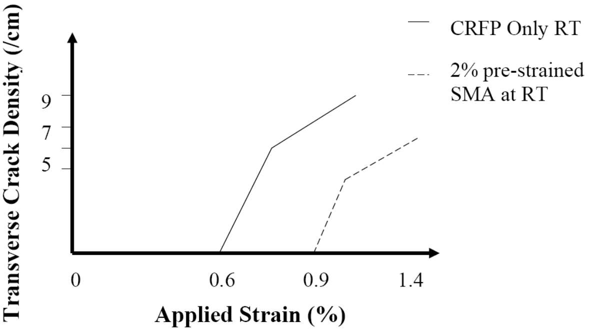

Figure 2-16: Transverse crack density as a function of applied strain of CFRP laminates with or without embedded SMA foils [175]

They [175, 174] also found that the recovery stresses of the embodied 2% pre-strained SMA foils generated by heating up to 80°C were effective for delaying the delamination onset, but the suppression effect for the transverse crack onset was mainly generated by the embedded effects of SMA and the pre-strain of SMA rather than the effects of the recovery stresses of the SMA foils. One of the reasons why the actuation effect by heating the CFRP laminates with embodied 2% pre-strained SMA foils is relatively low when compared with the embedded effect is the low volume fraction of the SMA foils which was used to avoid the increment in density for the SMAHC [174].

Ogisu et al. [173] conducted a technical verification program on a demonstrator test article designed as a 1/3-scale model of a commercial airliner's fuselage structure (B737 class). The purpose of this program was to verify if embodied, pre-strained SMA in CFRP laminates were able to suppress damage growth of transverse cracks and delamination initiating from the transverse cracks when the CFRP laminated structure was subjected to cyclic loads. The comparison in the crack onset strain increase of the CFRP laminate with incorporated pre-strained SMA foils (smart area) with respect to standard CFRP laminates (conventional area) was used as criteria to verify if the damage was suppressed. Both conventional areas and smart areas were integrated on the same evaluation area. The lower side of the demonstrator that is in tension was selected as evaluation area. The conventional area consisted in a $[+45°/0°/-45°/90°]_s$ ply stack-up, while the smart area consisted in a [+45°/0°/−45°/90°/Ad/2% pre-strained SMA/Ad /90°/−45°/0°/+45°] ply stack-up, where *Ad* is the *adhesive film*. Electric current heating was used in the demonstrator test article to generate the recovery stress for the SMA foil. The SMA foils were heated by both electric current heating and a silicon rubber heater in order to avoid over-heating issues in the demonstrator in local areas at the connecting points of SMA foils [173]. The results confirmed that the damage onset and growth strain in the smart area was improved by 30% over that of the conventional area and that the crack multiplication was suppressed, as shown in figure 2-17.

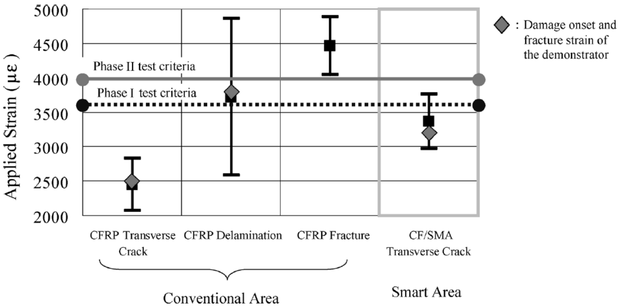

Figure 2-17: Comparison of the demonstrator test data with the prediction of transverse crack, delamination and fracture strain using the previous test data (reproduced with permission from [173])

Amano et al. [4, 5] developed a system for damage detection and suppression based on embedding pre-strained SMA (TiNi) foils and small-diameter fiber bragg grating (FBG) sensors simultaneously in a CFRP cross-ply laminate composite structure. The laminate configuration was a cross-ply [0°/90°/Ad/SMA/Ad/90°/0°], where *Ad* represents an epoxy adhesive film. The small-diameter FBG sensors were embodied into the 0° ply along the reinforcement carbon fibers in contact with the 90° ply, so that it was sensitive to transverse cracks running through the thickness and width of the 90° ply. The pre-strained SMA foils were embedded between two 90° plies. When the small-diameter FBG sensor detects some transverse cracks in the laminates, then the laminate is heated up so that the TiNi SMA foils, acting as actuators, generate the recovery compressive forces to suppress the initiation and growth of transverse cracks. It was proven both experimentally and analytically in Amano et al. [5] that the embodiment of the Ti-Ni SMA foils into CFRP laminates is effective in suppressing the occurrence and growth of the transverse cracks. Figure 2-18 shows a comparison of the rise in the transverse crack density between the predictions of the simulations and the experimental results at the temperatures of 25°C and 90°C.

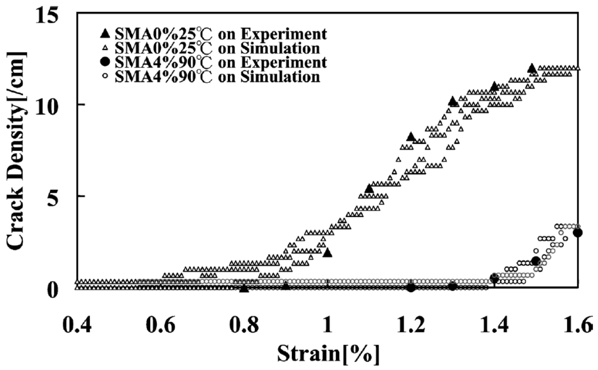

Figure 2-18: Comparison of the increase in transverse crack density between experiment and simulations (reproduced with permission from [5])

The test temperature of 90°C was selected because this temperature is the maximum limit for actual applications of aircrafts and it is also sufficiently beyond the Austenite finish temperature A_f (approximately 61°C) of the TiNi SMA foils. Subsequently Taketa et al. [233] developed an extended Brinson constitutive model in order to characterize the thermo-mechanical behavior of the TiNi foils including also the rhombohedral phase (R-phase) transformation, to which the authors attribute the particular properties of the TiNi foils used as actuators. Experimental tests were performed on the NiTi foils for the determination of the parameters of the constitutive equation. Then several simulations were conducted using this model and the results compared against the experimental results in order to validate the model finding a good agreement. Finally, three-dimensional FEA, using the extended Brinson model of Taketa et al. [233], was conducted by Amano et al. [4] in order to model the behavior the CFRP cross-ply laminate with embodied pre-strained SMA foils confirming that this mechanism is effective in suppressing the occurrence and growth of the transverse cracks.

Takeda et al. [232] proposed a technique for damage detection and suppression (*self-repairing*) mechanism for smart honeycomb sandwich structures. This is based on small-diameter FBG sensors embedded in a reticular pattern in the adhesive layer between the honeycomb core and the facesheet. The density of the sensors is such that unacceptable damage for the structure can be detected. The honeycomb cell walls are made of SMA foils which, heated above the martensitic reverse transformation temperature for shape recovery, are used to repair the BVID, as described in figure 2-19.

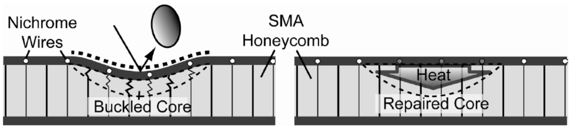

(a) After impact loading. (b) After energization of nichrome wires in damaged area

Figure 2-19: Self repairing technique for BVID in Smart Honeycomb Sandwich Structure (reproduced with permission from [232])

2.6.3 SMAHC with SMA Ribbons

Turner [244] studied the thermo-mechanical properties of SMAHC for glass/epoxy with embodied SMA (NiTi) ribbons performing static and dynamic finite element simulations and comparing the results against experimental results. Brinson et al. [34] studied the self-healing properties of pre-strained SMA actuator ribbons embedded in a polymeric based composite beam. They experimentally found that when heated, first the beam buckles before the SMA ribbons are actuated, then the deflection of the beam is reduced once the ribbons start to generate the recovery stress; finally at a higher temperature it re-buckles due to dominant thermal effects.

Gao et al. [90] studied, using a commercial FEA tool, the self-healing properties of clamped SMAHC beams consisting of a matrix of laminated glass-epoxy layers reinforced with embodied SMA (NiTi) ribbons. The authors found some quantitative differences between experimental data and simulation results, which they attributed to modeling approximations, e.g. amongst the others the assumed constant temperature throughout the model, while in the experiments the SMA ribbons were activated by resistive heating which caused a non uniform temperature distribution in both the SMA ribbons and the composite.

2.7 Conclusions

In this chqpter the state of the art of shape memory alloy hybrid composites (SMAHC) for the purpose of damage suppression has been reviewed. First the general properties of SMAs and SMAHC were considered, with particular emphasis on the fracture toughening mechanism. Then a brief overview of constitutive equations and modeling approaches for SMAHC was given. Finally, both active and passive damage suppression mechanisms were reviewed distinguishing between the different physical forms of SMA materials used, e.g. particles, wires, films, etc.

SMAHC have been particularly successful in achieving damage suppression using both passive and active mechanisms. The active mechanism is not only able to absorb impact energy, but also to accelerate closure of fatigue cracks and to reduce crack propagation speed. Both the ultimate strength and the failure strain of the SMAHC were found to be significantly greater than those of baseline control materials with the final failure strain of the SMAHC exceeding 30% that of the baseline. Normally, the ultimate strain energy was higher for active damage suppression than for passive, but passive damage suppression is in general cheaper and less complex than active.

A critical aspect is the interaction between the SMA material and the matrix in the hybridized composite. Maximum interfacial adhesion between the SMA and the matrix is desirable for obtaining maximum load transfer. Since the structure could get harmed, it is critical that the heating supplied to the SMAHC be not too high when using the active mechanism.

The performance of the SMAHC is highly dependent on parameters such as pre-strain, volume fraction, orientation and position of the SMA fibers within the laminate. Increasing the pre-strain or volume fraction of SMA is generally beneficial for damage suppression until optimal values can be found (after that no further benefit is noticed). The best results are mostly obtained when the SMA material is embedded in the outer layers, and especially in the bottom layer, of the laminate and when the wires are in a direction parallel to that of the reinforcement fibers.

Chapter 3

Homogenization methods for two-dimensional woven composites

3.1 Introduction

The use of composite materials in industrial applications has been increasing over the past years thanks to their very high specific strength, high specific stiffness, fatigue characteristics and moderate cost.

Composite materials can support very high loads in the direction of the fibers, but only low loads in the translaminar direction, as all the load is supported only by the matrix. Composite materials have a poor resistance to the damage caused by the impact of a foreign object on their outer surface, because they dissipate very little impact strain energy (such as plastic yielding in ductile metals) during impact loading.

Composites with woven fiber reinforcements have proven to have superior impact energy absorption capabilities [201] and to have very good properties in mutually orthogonal directions as well as more balanced properties [2] compared to laminates with uni-directional (UD) fibers .

The mechanical properties of the woven composites will depend on the weave architecture and materials used. For this reason the prediction of the mechanical properties for the woven composites assumes a critical role when designing the laminate.

Following the of work of Ishikawa and Chou [105, 106], many methods have been proposed for determining the mechanical properties of two-dimensional (2D) woven composites. For general reviews into modeling for predicting the mechanical properties of textile composites refer to [234] or to [60]. These methods can be broadly categorized in analytical methods based on the mechanics of materials approach (e.g. [2, 165, 3, 68]), methods based on the finite element analysis (e.g. [251, 148]) and methods based on the asymptotic expansion homogenization method (AEHM) approach (e.g. [24, 63, 53, 39, 55]).

Analytical methods based on the mechanics of materials approach use analytical or semi-analytical expressions which are derived based on certain simplifying assumptions, such as iso-strain and iso-stress hypothesis. The designer must select the most appropriate model amongst those available. This selection is thus a critical phase of the design process. Very little information is available in literature in terms of comparison between these different models.

For this reason the present chapter aims to critically compare the analytical methods based on the mechanics of materials approach with regards to their capability in predicting the mechanical properties for different fabric architectures and material constituents. Furthermore the AEHM will be compared with the analytical methods in order to asses its capability in predicting the mechanical properties for different fabric architectures and material constituents.

Furthermore, anisotropic damage mechanics has been integrated with the AEHM to model failure in woven composites by [69, 231].

Section 3.2 reviews the theory behind the analytical methods, the AEHM and anisotropic damage modeling, while sections 3.3.1 and 3.3.2 presents and discusses the numerical results. In section 3.4 we draw some conclusions on the effectiveness of these methods.

3.2 Methods

An orthogonal 2D woven fabric consists of two sets of yarns (or strands) interlaced at 90° to each other. In the following the terms yarns and strands are used interchangeably. The lengthwise yarn is called *warp*, while the crosswise yarn is called *fill* (often also *weft*). The weave patterns repeat every certain number of warp yarns and fill yarns. This basic area, which is the smallest periodic region of the woven composite that repeats itself in the lamina, is a complete *representative volume element* (RVE) of the weave, and is sufficient to estimate its mechanical properties. Note that here the RVE coincides with the *repeating unit cell* (RUC) typical of periodic structures. Refer to Pindera et al. [192] for the definitions of RVE and RUC and a discussion on the most appropriate uses of the two expressions. In the following the term RVE will be used to conform with previous literature.

There are various weave styles of orthogonal 2D woven composites based on the way the yarns are interlaced. The different weave patterns are characterized by the geometrical parameters n_g^f and n_g^w, which represent the n^{th} yarn with which an orthogonal yarn is interlaced. For example a warp yarn is interlaced with every n_g^f fill yarn and a fill yarn is interlaced with every n_g^w warp yarns. Figure 3-1 [238] gives some examples of RVE for some typical 2D weaves. If the yarns have the same size and same undulation length and $n_g^f = n_g^f = n_g$ then the fabric is called *balanced*; otherwise it is called *unbalanced*. Moreover, if the two sets of yarns are of different materials, then the fabric is called a *hybrid* weave [68]. In general, the RVE is characterized by two parameters: (1) the fabric type n_g (see Figure 3-1) and, for the satin fabrics, (2) the satin weave type n_{dec}, which accounts for the position of the interlaced region in the RVE. In the following, $n_{dec} = 1$ is assumed.

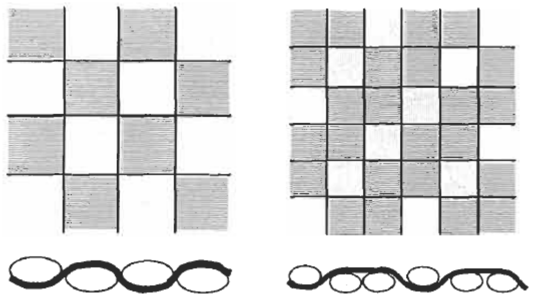

(a) Plain weave ($n_g = 2$) **(b)** Twill weave ($n_g = 3$)

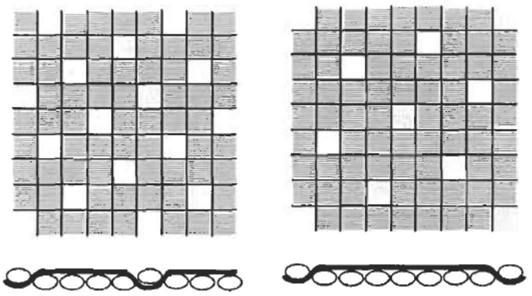

(c) 5-harness satin weave ($n_g = 5$) **(d)** 8-harness satin weave ($n_g = 8$)

Figure 3-1: Representative Volume Elements of typical 2D woven composites (reprinted with permission from [238, p. 71])

3.2.1 Mechanics of materials based approach

The analytical methods employed for predicting the mechanical properties of 2D woven composites (e.g. [164, 216, 217]) are based on the multi-scale modeling approach. The terminology referred to by [129] as *top-down-bottom-up method* will be used in this chapter to describe the homogenization process.

In summary, the top-down-bottom-up method consists of two phases: (1) In the first phase (*top-down*), one must perform a geometrical analysis of the material in order to identify fabric type (and, if applicable, satin weave type), element distribution and fiber volume fraction. (2) In the second phase (*bottom-up*), in order to identify the elastic properties of the woven composite material, one must perform the analysis in the opposite direction (from composite constituents to macroscopic behavior) by determining first the yarn and resin properties, then the basic element properties and finally the homogenized fabric properties.

Once the RVE of the 2D woven lamina has been identified, this area is sub-divided (*top-down* phase) into smaller regions, called *elements*, which in turn can be divided into even smaller sub-regions, called *sub-elements*, based on the undulation of the warp and fill yarns, and the position of the yarns in the element [252]. The mechanical properties of the RVE (*bottom-up* phase) are obtained by homogenizing the properties of the elements (and, in turn, sub-elements) that compose it. In general three different types of sub-elements (in the local co-ordinate system of the fibers) are present in a woven lamina: (1) those composed of both matrix and reinforcement fibers in the fill direction; (2) those composed of both both matrix and reinforcement fibers in the warp direction; and finally (3) those composed only of matrix. Also there is the possibility of a presence of a gap g_f between the fill yarns and a gap g_w between the warp yarns. The presence of gaps will be considered in sections 3.3.1 and 3.3.2.

With regards to notation, the *shorthand* (or *contracted*) notation [226, p. 17] for Cartesian co-ordinates is adopted for stress $\boldsymbol{\sigma}$ and strain $\boldsymbol{\epsilon}$. The co-ordinate axes are an x-y-z system or a 1-2-3 system. The x-y-z system is called the *global* or *off-axis* system, while the 1-2-3 system is the *material* or *on-axis* system. All rotations of co-ordinate axes are assumed to be about the z-axis, so z is coincident with the 3-direction, which is consistent with the assumption that individual lamina are modeled as orthotropic materials. By convention, axis 1 is the direction parallel to the reinforcement fibers, axis 2 is the in-plane direction perpendicular to fibers and axis 3 is the out-of-plane direction perpendicular to fibers.

For the matrix the hypothesis of *isotropic* material will be used, i.e. all planes are planes of material symmetry and are isotropic.

$$\begin{aligned} E_{m_1} &= E_{m_2} = E_{m_3} = E_m \\ G_{m_{12}} &= G_{m_{13}} = E_{m_{23}} = G_m \\ \nu_{m_{12}} &= \nu_{m_{13}} = \nu_{m_{23}} = \nu_m \end{aligned} \tag{3.1}$$

The reinforcement fibers can be assumed to be *isotropic* materials or *transversely isotropic* materials, i.e. the material has an axis of symmetry, e.g. the 1-axis, and any two fibers having symmetrical position to the axis of symmetry have the same stiffness. In this case, the 2-axis and 3-axis can be in any direction (but perpendicular to each other) without altering the value of the compliance and the x-y plane is an isotropic plane. If the reinforcement fibers are *transversely isotropic* materials then the following equations are valid:

$$
\begin{aligned}
E_{f_1} &= E_{f_L} \\
E_{f_2} &= E_{f_3} = E_{f_T} \\
G_{f_{12}} &= G_{f_{13}} = G_{f_{LT}} \\
G_{f_{23}} &= G_{f_{TT}} \\
\nu_{f_{12}} &= \nu_{f_{13}} = \nu_{f_{LT}} \\
\nu_{f_{23}} &= \nu_{f_{TT}} = \frac{E_{f_T}}{2G_{f_{TT}}} - 1
\end{aligned} \tag{3.2}
$$

where L stands for longitudinal direction (along the axis of symmetry), while T stands for transverse direction (perpendicular to the direction of symmetry).

The mechanical properties of the sub-elements composed of two constituents will be derived using micro-mechanical models. Micro-mechanical models are generally used to predict the mechanical properties of *uni-directional* (UD) fiber-reinforced laminae, so the underlaying assumption here is that the yarns (strands) have the same mechanical behavior as in UD laminae.

Various micro-mechanical models can be used to calculate the equivalent mechanical properties of sub-elements composed of matrix plus fiber reinforcements. See e.g. [45] for a review of existing micro-mechanical models. The rules of mixtures model [226] gives very good estimates in the longitudinal direction, but is inaccurate in the transverse direction. Other micro-mechanical models give a better performance in the transverse direction, but at the expense of an increased computational cost. Lamers [129] suggests, as a compromise, using the rules of mixtures only in the longitudinal direction, and a more precise (but more complex) model in the transverse direction.

In particular, (1) the models termed *Chamis* [43] and *Hashin and Rosen* or *Composite Cylinder Assemblage* (CCA) for *anisotropic constituents* [98] are adopted for the sub-elements composed of matrix and transversely isotropic reinforcement fibers; (2) the model termed *Hashin and Rosen* or CCA for *isotropic constituents* [211] is employed for the sub-elements composed of matrix and isotropic reinforcement fibers. These models are summarized in appendix refapp1:microModels.

In all micro-mechanical models one must utilize the fiber volume fraction in the (warp and fill) yarns. As discussed by [164] and [129] the fiber volume fraction in the warp and fill yarns $V_f^{W,F}$ are related to the total fiber volume fraction in the composite V_f as follows:

$$V_f^{W,F} = \frac{\Omega}{\Omega^{W,F}} V_f \tag{3.3}$$

where Ω is the total volume of the composite, and $\Omega^{W,F}$ is the volume of the warp and fill yarns.

V_f is determined by the packing structure, and for square packing is equal to [129, 252]

$$V_f = \frac{\frac{1}{4}\pi d^2}{d^2} = \frac{\pi}{4} \approx 0.785 \tag{3.4}$$

where d is the diameter of the fibers; while for hexagonal packing is [129, 252]

$$V_f = \frac{\frac{1}{8}\pi d^2}{\frac{1}{4}\sqrt{3}d^2} = \frac{\pi}{2\sqrt{3}} \approx 0.907 \tag{3.5}$$

A lamina in a composite laminate is generally assumed to be specially orthotropic with the following stress-strain relationships [226]

$$\boldsymbol{\epsilon} = \boldsymbol{S}\boldsymbol{\sigma} \tag{3.6}$$

$$\boldsymbol{\sigma} = \boldsymbol{S}^{-1}\boldsymbol{\epsilon} = \boldsymbol{Q}\boldsymbol{\epsilon} \tag{3.7}$$

Where $\boldsymbol{S}$ is the *compliance matrix* and $\boldsymbol{Q}$ is the *stiffness matrix* (sometimes referred to in literature as $\boldsymbol{C}$). The compliance matrix can be expressed in terms of elastic modulus E, Poisson's ratio ν and shear modulus G as follows

$$\begin{Bmatrix} \epsilon_1 \\ \epsilon_2 \\ \epsilon_3 \\ 2\epsilon_4 = \gamma_{23} \\ 2\epsilon_5 = \gamma_{31} \\ 2\epsilon_6 = \gamma_{12} \end{Bmatrix} = \begin{bmatrix} \frac{1}{E_1} & -\frac{\nu_{21}}{E_2} & -\frac{\nu_{31}}{E_3} & 0 & 0 & 0 \\ -\frac{\nu_{12}}{E_1} & \frac{1}{E_2} & -\frac{\nu_{32}}{E_3} & 0 & 0 & 0 \\ -\frac{\nu_{13}}{E_1} & -\frac{\nu_{23}}{E_2} & \frac{1}{E_3} & 0 & 0 & 0 \\ 0 & 0 & 0 & \frac{1}{G_{23}} & 0 & 0 \\ 0 & 0 & 0 & 0 & \frac{1}{G_{31}} & 0 \\ 0 & 0 & 0 & 0 & 0 & \frac{1}{G_{12}} \end{bmatrix} \begin{Bmatrix} \sigma_1 \\ \sigma_2 \\ \sigma_3 \\ \sigma_4 = \tau_{23} \\ \sigma_5 = \tau_{31} \\ \sigma_6 = \tau_{12} \end{Bmatrix} \tag{3.8}$$

Betti's reciprocal law of orthotropic material properties states that

$$Q_{ij} = Q_{ji} \qquad i \neq j \tag{3.9}$$

$$\frac{\nu_{ij}}{E_{ii}} = \frac{\nu_{ji}}{E_{jj}} \qquad \frac{\nu_{ji}}{E_{jj}} = \frac{\nu_{ij}}{E_{ii}} \tag{3.10}$$

where E_1 is the elastic modulus in the 1-axis (parallel to the fibers); E_2 is the elastic modulus in the 2-axis (in-plane direction perpendicular to fibers); E_3 is the elastic modulus in the 3-axis (out-of-plane direction perpendicular to fibers); ν_{12} is Poisson's ratio in the 2-axis when the lamina is loaded in the 1-axis; ν_{13} is Poisson's ratio in the 3-axis when the lamina is loaded in the 1-axis; and ν_{23} is Poisson's ratio in the 3-axis when the lamina is loaded in the 2-axis.

The sub-elements composed of matrix or of matrix and reinforcement fibers have the following constitutive equation in local co-ordinates

$$\boldsymbol{\sigma} = \boldsymbol{Q}^{sel}\boldsymbol{\epsilon} \tag{3.11}$$

where the reduced orthotropic stiffness matrix can be written as [217]

$$\boldsymbol{Q}^{sel} = \begin{bmatrix} Q_{11}^{sel} & Q_{12}^{sel} & Q_{13}^{sel} & 0 & 0 & 0 \\ Q_{12}^{sel} & Q_{22}^{sel} & Q_{23}^{sel} & 0 & 0 & 0 \\ Q_{13}^{sel} & Q_{23}^{sel} & Q_{33}^{sel} & 0 & 0 & 0 \\ 0 & 0 & 0 & Q_{44}^{sel} & 0 & 0 \\ 0 & 0 & 0 & 0 & Q_{55}^{sel} & 0 \\ 0 & 0 & 0 & 0 & 0 & Q_{66}^{sel} \end{bmatrix} \tag{3.12}$$

where [226]

$$\begin{aligned}
Q_{11}^{sel} &= \frac{1-\nu_{23}^{sel}\nu_{32}^{sel}}{E_2^{sel}E_3^{sel}\Delta^{sel}} \\
Q_{12}^{sel} = Q_{21}^{sel} &= \frac{\nu_{21}^{sel}-\nu_{31}^{sel}\nu_{23}^{sel}}{E_2^{sel}E_3^{sel}\Delta^{sel}} = \frac{\nu_{12}^{sel}-\nu_{13}^{sel}\nu_{32}^{sel}}{E_1^{sel}E_3^{sel}\Delta^{sel}} \\
Q_{22}^{sel} &= \frac{1-\nu_{31}^{sel}\nu_{13}^{sel}}{E_1^{sel}E_3^{sel}\Delta^{sel}} \\
Q_{23}^{sel} = Q_{32}^{sel} &= \frac{\nu_{32}^{sel}-\nu_{12}^{sel}\nu_{31}^{sel}}{E_1^{sel}E_3^{sel}\Delta^{sel}} = \frac{\nu_{23}^{sel}-\nu_{21}^{sel}\nu_{13}^{sel}}{E_1^{sel}E_2^{sel}\Delta^{sel}} \\
Q_{33}^{sel} &= \frac{1-\nu_{12}^{sel}\nu_{21}^{sel}}{E_1^{sel}E_2^{sel}\Delta^{sel}} \\
Q_{13}^{sel} = Q_{31}^{sel} &= \frac{\nu_{13}^{sel}-\nu_{12}^{sel}\nu_{23}^{sel}}{E_1^{sel}E_2^{sel}\Delta^{sel}} = \frac{\nu_{31}^{sel}-\nu_{21}^{sel}\nu_{32}^{sel}}{E_2^{sel}E_3^{sel}\Delta^{sel}} \\
\Delta^{sel} &= \frac{1-\nu_{12}^{sel}\nu_{21}^{sel}-\nu_{32}^{sel}\nu_{23}^{sel}-\nu_{13}^{sel}\nu_{31}^{sel}-2\nu_{21}^{sel}\nu_{32}^{sel}\nu_{13}^{sel}}{E_1^{sel}E_2^{sel}E_3^{sel}}
\end{aligned} \tag{3.13}$$

and *sel* stands for *sub-element*, and can assume the values W for *Warp*, F for *Fill* and M for *Matrix.*

In order to determine the mechanical properties of the woven lamina in the global co-ordinates the geometrical characteristics and the orientation angles of the reinforcement fibers in the fill and warp strands must be taken into account. Moreover, the mechanical properties of sub-elements have to be combined in order to compute the average properties of the element.

As discussed by various authors [164, 216, 217, 129] in order to calculate the average mechanical properties of an element in the woven lamina one must consider the fill yarn and warp yarn mid-plane functions $m_F^{sel}(x)$, $m_W^{sel}(y)$, and fill yarn and warp yarn cross-sectional shape functions $s_F^{sel}(y)$, $s_W^{sel}(x)$. The shape functions delimit regions in the woven composite with pure matrix material and regions with impregnated yarns.

The height position of the yarn surface h in each sub-element is a sum of the yarn mid-plane shape functions and the cross-sectional yarn shape functions for that sub-element.

$$\begin{aligned} h_{F_T}^{sel}(x,y) &= m_F^{sel}(x) + s_F^{sel}(y) \\ h_{F_B}^{sel}(x,y) &= m_F^{sel}(x) - s_F^{sel}(y) \\ h_{W_T}^{sel}(x,y) &= m_W^{sel}(y) + s_W^{sel}(x) \\ h_{W_B}^{sel}(x,y) &= m_W^{sel}(y) - s_W^{sel}(x) \end{aligned} \tag{3.14}$$

$h_{F_T}^{sel}(x,y)$, and $h_{F_B}^{sel}(x,y)$ define the fill top and bottom surface functions, while $h_{W_T}^{sel}(x,y)$ and $h_{W_B}^{sel}(x,y)$ define the warp top and bottom surface functions for sub-element *sel*.

In defining the mid-plane and surface functions, one might also want to account for the presence of gaps between the fill and warp strands, as will be discussed in sections 3.3.1 and 3.3.2.

The fiber undulation for the fill and warp strands are a function of the yarn mid-plane shape functions as follows

$$\begin{aligned} \theta_F(x) &= \arctan \frac{dm_F^{sel}(x)}{dx} \\ \theta_W(y) &= \arctan \frac{dm_W^{sel}(y)}{dy} \end{aligned} \tag{3.15}$$

These transformation matrices are discussed in appendix B.

Using the stress transformation matrix, the stiffness matrix in the *x-y-z* co-ordinate system (*off-axis* system) can be related to that in the 1-2-3 co-ordinate system (*on-axis* system) as follows [217]

$$\bar{\boldsymbol{Q}}^{sel} = {\boldsymbol{T}^{sel}}^{-1} \boldsymbol{Q}^{sel} \boldsymbol{R} \boldsymbol{T}^{sel} \boldsymbol{R}^{-1} \tag{3.16}$$

where $\boldsymbol{Q}^{sel}$ is the stiffness matrix in the *on-axis* co-ordinate system; $\bar{\boldsymbol{Q}}^{sel}$ is the transformed stiffness matrix in the *off-axis* co-ordinate system; $\boldsymbol{T}^{sel}$ is the stress transformation matrix; $\boldsymbol{R}$ is the Reuter matrix.

The sub-elements composed of matrix and reinforcement fibers in the fill yarn have the following constitutive equation in the global co-ordinates:

$$\boldsymbol{\sigma} = \bar{\boldsymbol{Q}}^{F} \boldsymbol{\epsilon} \tag{3.17}$$

The sub-elements consisting of matrix and reinforcement fibers in the warp yarn have the following constitutive equation in the global co-ordinates:

$$\boldsymbol{\sigma} = \bar{\boldsymbol{Q}}^{W} \boldsymbol{\epsilon} \tag{3.18}$$

For the sub-elements comprised only of matrix, the constitutive equation in global co-ordinates is the following:

$$\boldsymbol{\sigma} = \bar{\boldsymbol{Q}}^{M} \boldsymbol{\epsilon} = \boldsymbol{Q}^{M} \boldsymbol{\epsilon} \tag{3.19}$$

The stiffness matrices for an element *el* can be obtained by integrating the transformed stiffness matrices of the sub-elements $\bar{\boldsymbol{Q}}^{sel}$ through the thickness of the lamina:

$$\left(A_{ij}^{el}\left(x,y\right), B_{ij}^{el}\left(x,y\right), D_{ij}^{el}\left(x,y\right)\right) = \int_{h_B^{el}(x,y)}^{h_T^{el}(x,y)} \left(1, z, z^2\right) \bar{Q}_{ij}^{sel}\left(x,y\right) dz \tag{3.20}$$

where $h_B^{el}\left(x,y\right)$ and $h_T^{el}\left(x,y\right)$ is the height (with respect to the mid-plane of the lamina) of the top and the bottom of the element *el*.

$A_{ij}^{el}\left(x,y\right)$ is termed the *extensional stiffness matrix.* This matrix relates the in-plane loads to in-plane strains. $B_{ij}^{el}\left(x,y\right)$ is called the *extensional-bending coupling* or *in-plane/flexure coupling matrix.* This matrix relates in-plane loads to curvatures and moments to in-plane strains. $D_{ij}^{el}\left(x,y\right)$ is named as the *bending or flexural stiffness matrix.* This matrix relates moments to curvatures.

Using the boundaries of the shape functions [165, 216, 129] the components of the in-plane stiffness matrices for an element can be written according to equations in table 3.1a. The in-plane compliance matrices for an element can be determined using equations in table 3.1b [226].

The mechanical properties of the RVE of the 2D woven lamina are calculated from those of the elements using the averaging approach [165, 217, 129].

There are four different methods for carrying out this operation, depending on how the stiffness and compliance matrices are averaged across the RVE.

In the *Parallel-Parallel (PP) scheme* [216, 217, 129] one assumes iso-strain conditions and averages across the stiffness matrices of the elements as follows:

$$
\begin{array}{rcl}
A_{ij}^{el} & = & \bar{Q}_{ij}^{M}[h_{W_T}^{sel}(x,y) - h_{T}^{el}(x,y) + h_{F_T}^{sel}(x,y) \\
 & - & h_{W_B}^{sel}(x,y) + h_{B}^{el}(x,y) - h_{F_B}^{sel}(x,y)] \\
 & + & \bar{Q}_{ij}^{W}\left(\theta_{W}^{sel}(y)\right)\left[h_{W_B}^{sel}(x,y) - h_{W_T}^{sel}(x,y)\right] \\
 & + & \bar{Q}_{ij}^{F}\left(\theta_{F}^{sel}(x)\right)\left[h_{F_B}^{sel}(x,y) - h_{F_T}^{sel}(x,y)\right] \\
B_{ij}^{el} & = & \frac{1}{2}\bar{Q}_{ij}^{M}[h_{W_T}^{sel}(x,y)^2 - h_{T}^{el}(x,y)^2 + h_{F_T}^{sel}(x,y)^2 \\
 & - & h_{W_B}^{sel}(x,y)^2 + h_{B}^{el}(x,y)^2 - h_{F_B}^{sel}(x,y)^2] \\
 & + & \frac{1}{2}\bar{Q}_{ij}^{W}\left(\theta_{W}^{sel}(y)\right)\left[h_{W_B}^{sel}(x,y)^2 - h_{W_T}^{sel}(x,y)^2\right] \\
 & + & \frac{1}{2}\bar{Q}_{ij}^{F}\left(\theta_{F}^{sel}(x)\right)\left[h_{F_B}^{sel}(x,y)^2 - h_{F_T}^{sel}(x,y)^2\right] \\
D_{ij}^{el} & = & \frac{1}{3}\bar{Q}_{ij}^{M}[h_{W_T}^{sel}(x,y)^3 - h_{T}^{el}(x,y)^3 + h_{F_T}^{sel}(x,y)^3 \\
 & - & h_{W_B}^{sel}(x,y)^3 + h_{B}^{el}(x,y)^3 - h_{F_B}^{sel}(x,y)^3] \\
 & + & \frac{1}{3}\bar{Q}_{ij}^{W}\left(\theta_{W}^{sel}(y)\right)\left[h_{W_B}^{sel}(x,y)^3 - h_{W_T}^{sel}(x,y)^3\right] \\
 & + & \frac{1}{3}\bar{Q}_{ij}^{F}\left(\theta_{F}^{sel}(x)\right)\left[h_{F_B}^{sel}(x,y)^3 - h_{F_T}^{sel}(x,y)^3\right]
\end{array}
$$

(a) In-plane stiffness matrices

If the element is non symmetric:

$$
\begin{array}{rcl}
\boldsymbol{a}^{el}(x,y) & = & \boldsymbol{A}^{*el}(x,y)^{-1} - \boldsymbol{B}^{*el}(x,y)\,\boldsymbol{D}^{*el}(x,y)^{-1}\,\boldsymbol{C}^{*el}(x,y) \\
\boldsymbol{b}^{el}(x,y) & = & \boldsymbol{B}^{*el}(x,y)\,\boldsymbol{D}^{*el}(x,y)^{-1} \\
\boldsymbol{c}^{el}(x,y) & = & -\boldsymbol{D}^{*el}(x,y)^{-1}\,\boldsymbol{C}^{*el}(x,y)\ \text{or} \\
\boldsymbol{c}^{el}(x,y) & = & \boldsymbol{b}^{el}(x,y)^{T} \\
\boldsymbol{d}^{el}(x,y) & = & \boldsymbol{D}^{*el}(x,y)^{-1}
\end{array}
$$

where

$$
\begin{array}{rcl}
\boldsymbol{A}^{*el}(x,y) & = & \boldsymbol{A}^{el}(x,y)^{-1} \\
\boldsymbol{B}^{*el}(x,y) & = & -\boldsymbol{A}^{el}(x,y)^{-1}\,\boldsymbol{B}^{el}(x,y) \\
\boldsymbol{C}^{*el}(x,y) & = & \boldsymbol{B}^{el}(x,y)\,\boldsymbol{A}^{el}(x,y)^{-1} \\
\boldsymbol{D}^{*el}(x,y) & = & \boldsymbol{D}^{el}(x,y) - \boldsymbol{B}^{el}(x,y)\,\boldsymbol{A}^{el}(x,y)^{-1}\,\boldsymbol{B}^{el}(x,y)
\end{array}
$$

Otherwise, if the element is symmetric:

$$
\boldsymbol{a}^{el}(x,y) = \boldsymbol{A}^{el}(x,y)^{-1}
$$

(b) In-plane compliance matrices

Table 3.1: In-plane stiffness and compliance matrices for an element

$$
\left(\tilde{A}_{ij}^{el,PP}, \tilde{B}_{ij}^{el,PP}, \tilde{D}_{ij}^{el,PP}\right) = \frac{1}{l_x}\frac{1}{l_y}\int_0^{l_x}\int_0^{l_y}\left(A_{ij}^{el}(x,y), B_{ij}^{el}(x,y), D_{ij}^{el}(x,y)\right)dxdy \tag{3.21}
$$

where l_x is the length of the RVE across the x direction, while l_y is the length of the RVE across the y direction. The values $\tilde{A}_{ij}^{el,PP}$, $\tilde{B}_{ij}^{el,PP}$, $\tilde{D}_{ij}^{el,PP}$ represent an upper boundary for the stiffness of the RVE. These values are adopted to calculate the compliance matrices $\tilde{a}_{ij}^{el,PP}$, $\tilde{b}_{ij}^{el,PP}$, $\tilde{d}_{ij}^{el,PP}$ which in turn are used to calculate the elastic engineering constants of the woven lamina.

In the *Parallel-Series (PS) scheme* [165] one first assumes iso-strain conditions and averages the stiffness matrices along the x-axis determining the average stiffness matrices along the y-axis.

$$\left(\tilde{A}_{ij}^{el,P}\left(y\right),\tilde{B}_{ij}^{el,P}\left(y\right),\tilde{D}_{ij}^{el,P}\left(y\right)\right)=\frac{1}{l_x}\int_0^{l_x}\left(A_{ij}^{el}\left(x,y\right),B_{ij}^{el}\left(x,y\right),D_{ij}^{el}\left(x,y\right)\right)dx \quad (3.22)$$

The average in-plane stiffness matrices along the y-axis $\tilde{A}_{ij}^{el,P}\left(y\right)$, $\tilde{B}_{ij}^{el,P}\left(y\right)$, $\tilde{D}_{ij}^{el,P}\left(y\right)$ are then employed to calculate the compliance matrices $\tilde{a}_{ij}^{el,P}\left(y\right)$, $\tilde{b}_{ij}^{el,P}\left(y\right)$, $\tilde{d}_{ij}^{el,P}\left(y\right)$ along the y-axis, which, assuming now iso-stress conditions, are then integrated along the y-axis.

$$\left(\tilde{a}_{ij}^{el,PS},\tilde{b}_{ij}^{el,PS},\tilde{d}_{ij}^{el,PS}\right)=\frac{1}{l_y}\int_0^{l_y}\left(\tilde{a}_{ij}^{el,P}\left(y\right),\tilde{b}_{ij}^{el,P}\left(y\right),\tilde{d}_{ij}^{el,P}\left(y\right)\right)dy \quad (3.23)$$

In the *Series-Parallel (SP) scheme* [165] one first assumes iso-stress conditions and averages the compliance matrices along the y-axis determining the average compliance matrices along the x-axis.

$$\left(\tilde{a}_{ij}^{el,S}\left(x\right),\tilde{b}_{ij}^{el,S}\left(x\right),\tilde{d}_{ij}^{el,S}\left(x\right)\right)=\frac{1}{l_y}\int_0^{l_y}\left(a_{ij}^{el}\left(x,y\right),b_{ij}^{el}\left(x,y\right),d_{ij}^{el}\left(x,y\right)\right)dy \quad (3.24)$$

The average compliance matrices along the x-axis $\tilde{a}_{ij}^{el,S}\left(x\right)$, $\tilde{b}_{ij}^{el,S}\left(x\right)$, $\tilde{d}_{ij}^{el,S}\left(x\right)$ are then used to calculate the average stiffness matrices $\tilde{A}_{ij}^{el,S}\left(x\right)$, $\tilde{B}_{ij}^{el,S}\left(x\right)$, $\tilde{D}_{ij}^{el,S}\left(x\right)$ along the x-axis, which, assuming now iso-strain conditions, are then integrated along the x-axis.

$$\left(\tilde{A}_{ij}^{el,SP},\tilde{B}_{ij}^{el,SP},\tilde{D}_{ij}^{el,SP}\right)=\frac{1}{l_x}\int_0^{l_x}\left(\tilde{A}_{ij}^{el}\left(x\right),\tilde{B}_{ij}^{el}\left(x\right),\tilde{D}_{ij}^{el}\left(x\right)\right)dx \quad (3.25)$$

In the *Series-Series (SS) scheme* [129] one assumes iso-stress conditions and then averages across the compliance matrices of the elements as follows:

$$\left(\tilde{a}_{ij}^{el,SS},\tilde{b}_{ij}^{el,SS},\tilde{d}_{ij}^{el,SS}\right)=\frac{1}{l_x}\frac{1}{l_y}\int_0^{l_x}\int_0^{l_y}\left(a_{ij}^{el}\left(x,y\right),b_{ij}^{el}\left(x,y\right),d_{ij}^{el}\left(x,y\right)\right)dxdy \quad (3.26)$$

The values $\tilde{a}_{ij}^{el,SS}$, $\tilde{b}_{ij}^{el,SS}$, $\tilde{d}_{ij}^{el,SS}$ are adopted to calculate the elastic engineering constants of the woven lamina, and to obtain the average stiffness matrices $\tilde{A}_{ij}^{el,SS}$, $\tilde{B}_{ij}^{el,SS}$, $\tilde{D}_{ij}^{el,SS}$, which represent a lower boundary for the stiffness of the RVE.

The effective properties of the woven lamina can be calculated [93] (dropping the super-scripts) as follows:

$$
\begin{aligned}
\tilde{E}_{11} &= \frac{1}{h_t \tilde{a}_{11}} & \tilde{E}_{22} &= \frac{1}{h_t \tilde{a}_{22}} & \tilde{E}_{33} &= \frac{1}{h_t \tilde{a}_{33}} \\
\tilde{G}_{23} &= \frac{1}{h_t \tilde{a}_{44}} & \tilde{G}_{13} &= \frac{1}{h_t \tilde{a}_{55}} & \tilde{G}_{12} &= \frac{1}{h_t \tilde{a}_{66}} \\
\tilde{\nu}_{12} &= -\frac{\tilde{a}_{12}}{\tilde{a}_{11}} & \tilde{\nu}_{13} &= -\frac{\tilde{a}_{13}}{\tilde{a}_{11}} & \tilde{\nu}_{23} &= -\frac{\tilde{a}_{23}}{\tilde{a}_{22}} \\
\tilde{\nu}_{21} &= -\frac{\tilde{a}_{21}}{\tilde{a}_{22}} & \tilde{\nu}_{31} &= -\frac{\tilde{a}_{31}}{\tilde{a}_{33}} & \tilde{\nu}_{32} &= -\frac{\tilde{a}_{32}}{\tilde{a}_{33}}
\end{aligned}
\qquad (3.27)
$$

where h_t is the thickness of the lamina.

3.2.2 Asymptotic Expansion Homogenization Method

As the woven composite has a periodic structure based on the RVE, then it is possible to apply the *asymptotic expansion homogenization method* (AEHM). The mathematical basis of this method were placed by [22, 213]. Recent reviews on the AEHM applied to composites are [116, 61, 177].

The AEHM is characterized by analyzing the material at several scales of analysis. For the woven material it is possible to identify in general three *scales* (or *levels*): (1) the *micro* scale for the constituents (i.e. fibers and matrix); (2) the *meso* scale for the strands and (3) the *macro* scale for the RVE. Some authors [129] refer to macro scale as *mini* scale reserving the term macro scale to the laminate. Here only the two scale analysis will be discussed, specifically the meso (or local) and macro (or global) scales, assuming that the mechanical properties of the strands at the meso scale have been homogenized using micro-mechanics models, as discussed previously in this section. Refer to [39] for the case of three scales analysis applied to woven composites.

The AEHM assumes a small parameter, often called *scale parameter* [55] and referred to here as ϵ, which is the ratio between the two length scales being considered. The two sets of parameters for the macro scale $\boldsymbol{x}$ and meso scale $\boldsymbol{y}$ are then related to by the following equation:

$$\boldsymbol{x} = \frac{\boldsymbol{y}}{\epsilon} \qquad (3.28)$$

The conventional equations of elasticity for a heterogeneous body are given by [116]

$$\frac{\partial \sigma_{ij}^{\epsilon}(\boldsymbol{x})}{\partial x_j^{\epsilon}} + f_i(\boldsymbol{x}) = 0, \tag{3.29}$$

$$\sigma_{ij}^{\epsilon}(\boldsymbol{x}) = a_{ijkl}^{\epsilon}(\boldsymbol{x})\,\epsilon_{kl}(\boldsymbol{u}^{\epsilon}(\boldsymbol{x})), \tag{3.30}$$

$$\epsilon_{ij}(\boldsymbol{u}^{\epsilon}(\boldsymbol{x})) = \frac{1}{2}\left(\frac{\partial u_i^{\epsilon}(\boldsymbol{x})}{\partial x_j^{\epsilon}} + \frac{\partial u_j^{\epsilon}(\boldsymbol{x})}{\partial x_i^{\epsilon}}\right) \tag{3.31}$$

where (3.29) are the *balance equations*, (3.30) are the *constitutive equations* and (3.31) is the *strain definition.* The super-script ϵ is used to indicate that the variables of the problem depend on the true, high-resolution behavior of the material under consideration. The boundary and discontinuity conditions are the following

$$\sigma_{ij}^{\epsilon}(\boldsymbol{x})\,n_j = 0 \text{ on } \partial_1\Omega, \tag{3.32}$$

$$u_i^{\epsilon}(\boldsymbol{x}) = 0 \text{ on } \partial_2\Omega, \tag{3.33}$$

$$[u_i^{\epsilon}(\boldsymbol{x})] = 0 \text{ on } S_J, \tag{3.34}$$

$$\left[\sigma_{ij}^{\epsilon}(\boldsymbol{x})\,n_j\right] = 0 \text{ on } S_J \tag{3.35}$$

Square parentheses denote the jump in the enclosed value. $\boldsymbol{u}$ is the displacement vector, $\epsilon_{ij}(\boldsymbol{u}(\boldsymbol{x}))$ is the strain tensor, $\sigma_{ij}(\boldsymbol{x})$ is the stress tensor, $a_{ijkl}(\boldsymbol{x})$ is the elasticity tensor and $f_i(\boldsymbol{x})$ are the volume forces.

The physical quantities describing the mechanical behavior of the body are approximated with an asymptotic series representation in ϵ given by

$$\boldsymbol{u}^{\epsilon}(\boldsymbol{x}) = \boldsymbol{u}^{(0)}(\boldsymbol{x}) + \epsilon\boldsymbol{u}^{(1)}(\boldsymbol{x}, \boldsymbol{y}) \tag{3.36}$$

$$\boldsymbol{\sigma}^{\epsilon}(\boldsymbol{x}) = \boldsymbol{\sigma}^{(0)}(\boldsymbol{x}) + \epsilon\boldsymbol{\sigma}^{(1)}(\boldsymbol{x}, \boldsymbol{y}) \tag{3.37}$$

$$\boldsymbol{\epsilon}^{\epsilon}(\boldsymbol{x}) = \boldsymbol{\epsilon}^{(0)}(\boldsymbol{x}) + \epsilon\boldsymbol{\epsilon}^{(1)}(\boldsymbol{x}, \boldsymbol{y}) \tag{3.38}$$

Here the expansions have been limited to a two scale approximation. The quantities $\boldsymbol{u}^{(k)}$, $\boldsymbol{\sigma}^{(k)}$ and $\boldsymbol{\epsilon}^{(k)}$ take the same values on opposite sides of the RVE (i.e. *periodic boundary conditions*). Moreover, the introduction of the second coordinate system $\boldsymbol{y}$ means that the derivatives originally with respect to x_i^{ϵ} must now make use of the chain rule of differentiation given by [116]

$$\frac{\partial}{\partial x_i^{\epsilon}} f = \left(\frac{\partial}{\partial x_i} + \frac{1}{\epsilon}\frac{\partial}{\partial y_i}\right) f = \frac{\partial f}{\partial x_i} + \frac{1}{\epsilon}\frac{\partial f}{\partial y_i} \tag{3.39}$$

Substituting the approximations in equations (3.36) to (3.38) into the strain definition equations (3.31) and substituting the resulting strain into the constitutive equations

(3.30) gives an equation dependent on the powers of ϵ. Each coefficient of ϵ is identically zero to ensure that the asymptotic series approximation is valid as $\epsilon \to 0$ [53]. When the first two coefficients are set equal to zero, the equilibrium equations can be reformulated as the following two hierarchical equations

$$\frac{\partial \sigma_{ij}^{(0)}}{\partial y_j}(\boldsymbol{x}, \boldsymbol{y}) = 0 \tag{3.40}$$

$$\frac{\partial \sigma_{ij}^{(0)}}{\partial x_j}(\boldsymbol{x}, \boldsymbol{y}) + \frac{\partial \sigma_{ij}^{(1)}}{\partial y_j}(\boldsymbol{x}, \boldsymbol{y}) + f_i(\boldsymbol{x}) = 0 \tag{3.41}$$

while the constitutive equations takes the form

$$\sigma_{ij}^{\epsilon}(\boldsymbol{x}, \boldsymbol{y}) = a_{ijkl}^{\epsilon}(\boldsymbol{y}) \left(\frac{\partial \epsilon_k}{\partial x_l}\left(\boldsymbol{u}^{(0)}\right) + \frac{\partial \epsilon_k}{\partial y_l}\left(\boldsymbol{u}^{(1)}\right) \right) \tag{3.42}$$

Equation (3.41) is the so-called *micro-equation* as it relates the micro perturbation term $\boldsymbol{u}^{(1)}$ to the zeroth order term $\boldsymbol{u}^{(0)}$.

The solution of the perturbative displacement $\boldsymbol{u}^{(1)}(\boldsymbol{x}, \boldsymbol{y})$ is normally assumed [22, 213] to take the following form with separated variables

$$\boldsymbol{u}_i(\boldsymbol{x}, \boldsymbol{y}) = \frac{\partial \epsilon_p}{\partial x_q}\left(\boldsymbol{u}^{(0)}(\boldsymbol{x})\right) \chi_i^{pq}(\boldsymbol{y}) + C_i(\boldsymbol{x}) \tag{3.43}$$

where the functions $\chi_i^{pq}(\boldsymbol{y})$ are called the *homogenization functions* [116] for the displacement or *characteristic displacements* [61] or *elastic correctors* [55], and $C_i(\boldsymbol{x})$ is a constant of integration.

Given (3.43), the first order component of the equations of equilibrium (3.41) can be formulated as the following boundary value problem

$$\begin{gathered} \text{find } \chi_i^{pq} \in V_Y \text{ such that: } \forall v_i \in V_Y \\ \int_Y a_{ijkl}(\boldsymbol{y}) \left(\delta_{ip}\delta_{jq} + \frac{\partial \chi_i^{pq}}{\partial y_j}(\boldsymbol{y}) \right) \frac{\partial v_k}{\partial y_l}(\boldsymbol{y})\, d\Omega = 0 \end{gathered} \tag{3.44}$$

where V_Y is the set of kinematically admissible functions that contains the functions with equal values on the opposite side of the RVE. The six vectors χ^{pq} depend only on the geometry of the RVE and on the jumps of material coefficients across S_J. Functions $v_i(\boldsymbol{y})$ are test functions defined on the RVE.

In (3.36) the dependence on $\boldsymbol{x}$ alone occurs only on the first term. The functions depending only on $\boldsymbol{x}$ define the *global* behavior o the structure. The global behavior of stresses the following mean values are defined over the RVE

$$\tilde{\sigma}_{ij}^{(0)}(\boldsymbol{x}) = \frac{1}{|Y|}\int_Y \sigma_{ij}^{(0)}(\boldsymbol{x},\boldsymbol{y})\,dY \tag{3.45}$$

which gives rise to the following effective constitutive equation

$$\tilde{\sigma}_{ij}^{(0)}(\boldsymbol{x}) = a_{ijkl}^{h}\epsilon_{kl}^{(0)}(\boldsymbol{x}) \tag{3.46}$$

where

$$a_{ijkl}^{h} = \frac{1}{|Y|}\int_Y a_{ijpq}(\boldsymbol{y})\left(\delta_{kp}\delta_{lq} + \frac{\partial\chi_k^{pq}}{\partial y_l}(\boldsymbol{y})\right)dY \tag{3.47}$$

The woven composite can now be studied as a homogeneous material with the effective properties given by (3.47).

3.2.3 Anisotropic damage modeling using the AEHM

It is very challenging to predict the failure strength of fiber reinforced polymer (FRP) composites because they are by nature heterogeneous in construction and anisotropic. Although there has been a great effort in assessing the damage models for predicting failure strength in FRPs (see e. g. [101]), there is still no conclusive evidence on which is the best approach.

In section 3.2.2 a two-scale AEHM approach for woven composites was adopted. For this resaon here only anisotropic mesoscopic damage models will be considered. Mesoscopic anisotropic damage models have been applied to uni-directional FRPs by [263] and to woven composites by [137, 264] where the stress-strain analysis is carried out using a standard finite element modeling (FEM) approach. Anisotropic damage mechanics has been integrated with the AEHM to model failure in woven composites by [69, 231].

Mesoscopic damage mechanics differentiate themselves on

1. the choice of the damage initiation criteria,
2. the stiffness degradation method, and
3. the algorithm for damage propagation.

The anisotropic damage model for yarns and the isotropic damage model for matrix pockets are utilized to simulate the microscopic damage propagation, and thus to characterize the damage modes.

The Tsai-Wu [239] or Hoffman [102] failure criteria can be used for the yarns. The Von Mieses Failure criterion is used for the matrix. As the yarns can be regarded as transversely isotropic material, then the Tsai-Wu second-order tensor polynomial in equation (3.48) is adopted as failure criterion for each yarn element.

$$\begin{aligned} &F_{11}\sigma_1^2 + F_{22}\sigma_2^2 + F_{33}\sigma_3^2 + F_{44}\tau_{23}^2 + F_{55}\tau_{13}^2 + F_{66}\tau_{12}^2 \\ &\qquad + 2F_{12}\sigma_1\sigma_2 + 2F_{13}\sigma_1\sigma_3 + 2F_{23}\sigma_2\sigma_3 + F_1\sigma_1 + F_2\sigma_2 + F_3\sigma_3 \leq 1 \end{aligned} \tag{3.48}$$

where

$$\begin{aligned} F_{11} &= \frac{1}{\sigma_{1t}\sigma_{1c}}, & F_{22} = F_{33} &= \frac{1}{\sigma_{2t}\sigma_{2c}}, & F_{44} &= \frac{1}{\left(\tau_{23f}\right)^2}, \\ F_{55} = F_{66} &= \frac{1}{\left(\tau_{12f}\right)^2}, & F_{12} = F_{13} &= -\frac{1}{2}\sqrt{F_{11}F_{22}}, & F_{23} &= -\frac{1}{2}\sqrt{F_{22}F_{33}}, \\ F_1 &= \frac{1}{\sigma_{1t}} - \frac{1}{\sigma_{1c}}, & F_2 = F_3 &= \frac{1}{\sigma_{2t}} - \frac{1}{\sigma_{2c}}, \end{aligned}$$

and σ_{1t} and σ_{2t} are the longitudinal tensile and compressive strength of yarn; σ_{1c} and σ_{2c} are the transverse tensile and compressive strength of yarn; τ_{12f} and τ_{23f} are the in-plane and out-of-plane strength of yarn.

As the matrix is an isotropic material, then the Von Mieses failure criterion in equation (3.49) is adopted as failure criterion for each matrix element.

$$(\sigma_1 - \sigma_2)^2 + (\sigma_2 - \sigma_3)^2 + (\sigma_3 - \sigma_1)^2 + 6\left(\tau_{12}^2 + \tau_{23}^2 + \tau_{31}^2\right) - 2\sigma_{1t} \leq 0 \tag{3.49}$$

The anisotropic damage modes for yarns can be classified into four types as shown in figure 3-2. The axes 1, 2 and 3 represent the principle coordinates of the orthotropic material, and correspond to fiber and transverse directions, respectively. The mode 1 represents schematically the fiber breaking, the others represent the transverse and shear cracking. The choice of the damage mode is defined by the stress component corresponding to damaged configuration (normal stress 1, 2 and 3 and shear stress 23, 31 and 12). Damage is registered when one of the stress indices reaches the vale 1.0.

The damage mode of each yarn element can be judged by maximum ratio value of each stress component divided by the strength component as defined in equation (3.2.3), where the direction of maximum ratio value is the direction of the yarn element. For example, if $\sigma_1^2/\sigma_{1t}\sigma_{1c}$ is the maximum ratio in equation (3.2.3), then the damage mode of the yarn element is 1-direction damage.

$$\left\{\frac{\sigma_1^2}{\sigma_{1t}\sigma_{1c}},\quad \frac{\sigma_2^2}{\sigma_{2t}\sigma_{2c}},\quad \frac{\sigma_2^3}{\sigma_{2t}\sigma_{2c}},\quad \left(\frac{\tau_{23}}{\tau_{23f}}\right)^2,\quad \left(\frac{\tau_{31}}{\tau_{12f}}\right)^2,\quad \left(\frac{\tau_{13}}{\tau_{12f}}\right)^2\right\}$$

On the other hand, in order to characterize each one of the damage modes, the second-order Murakamis *damage tensor* [161] is used, which, expressed in the principle

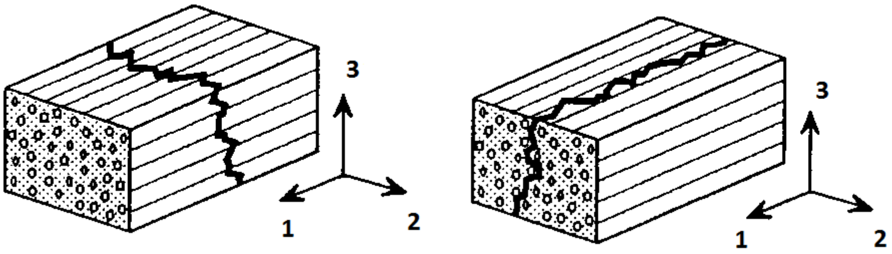

(a) Mode 1 **(b)** Modes 2 and 12

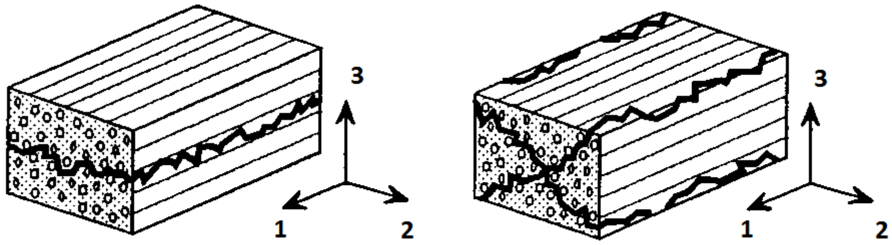

(c) Modes 3 and 31 **(d)** Mode 23

Figure 3-2: Anisotropic damage model for yarns (adapted from [264])

material coordinate system, is defined as follows

$$\boldsymbol{D} = \textstyle\sum_i D_i n_i \otimes n_i \quad (i = 1, 2, 3)$$

D_i and n_i are the principal value and principal unit vector of the damage tensor. In matrix form, this is expressed as follows

$$[D] = \begin{bmatrix} D_1 & 0 & 0 \\ 0 & D_2 & 0 \\ 0 & 0 & D_3 \end{bmatrix}$$

The eigenvalues of the damage tensor $\boldsymbol{D}$ provide a measure of the *fractional reduction* in the original load carrying area. The principle values of the damage tensor D_i may take arbitrary values within the range from 0 to 1. Also a formulation with only two values, 0 for undamaged initial state and 1 for full damaged state, can be used. The corresponding principle values of the damage tensors for the four damage modes are given in table 3.2.

Related to the damage tensor is the second-order *integrity tensor*, which, expressed

Damage Mode	Stress condition	D_1	D_2	D_3
1	$\sigma_1 > 0$	1	0	0
1	$\sigma_1 \leq 0$	0	0	0
2 or 12	$\sigma_2 > 0$	0	1	0
2 or 12	$\sigma_2 \leq 0$	0	0	0
3 or 31	$\sigma_3 > 0$	0	0	1
3 or 31	$\sigma_3 \leq 0$	0	0	0
23	$\sigma_2 > 0$ and $\sigma_3 > 0$	0	1	1
23	$\sigma_2 > 0$ and $\sigma_3 \leq 0$	0	1	0
23	$\sigma_2 \leq 0$ and $\sigma_3 > 0$	0	0	1
23	$\sigma_2 \leq 0$ and $\sigma_3 \leq 0$	0	0	0

Table 3.2: Damage mode and principle values of damage tensor [69]

in the principle material coordinate system, is given by [197]

$$\begin{aligned} \boldsymbol{\Omega} \cdot \boldsymbol{\Omega} &= \boldsymbol{I} - \boldsymbol{D} \\ \boldsymbol{\Omega} &= \sqrt{\boldsymbol{I} - \boldsymbol{D}} \\ \Omega_i &= \sqrt{1 - D_i} \text{ for } i = 1, 2, 3 \end{aligned}$$

In matrix form, this is expressed as follows

$$[\Omega] = \begin{bmatrix} \Omega_1 & 0 & 0 \\ 0 & \Omega_2 & 0 \\ 0 & 0 & \Omega_3 \end{bmatrix}$$

The eigenvalues of the integrity tensor $\boldsymbol{\Omega}$ provide a measure of the original area that is still available to carry load.

The constitutive equation for the damaged composite materials can be derived using the *effective stress* that refers to cross sectional areas that have been reduced due to the presence of damage. The effective stress $\sigma^\star$ is symmetric and related to the *apparent, actual or nominal stress* σ which uses the original undamaged cross sectional area as follows [58]

$$\boldsymbol{\sigma}^\star = \boldsymbol{M}^{-1} \colon \boldsymbol{\sigma} = \left(\boldsymbol{\Omega}^{-1} \otimes \boldsymbol{\Omega}^{-1}\right) : \boldsymbol{\sigma} = \left[\left(\sqrt{\boldsymbol{I} - \boldsymbol{D}}\right)^{-1} \otimes \left(\sqrt{\boldsymbol{I} - \boldsymbol{D}}\right)^{-1}\right] : \boldsymbol{\sigma} \tag{3.50}$$

where $\boldsymbol{M}$ is the fourth-order, doubly symmetric, *damage effect tensor*, i. e. $M_{ijkl} = M_{jikl}$, $M_{ijkl} = M_{ijlk}$ and $M_{ijkl} = M_{jilk}$. Thus as the damage accumulates, i. e. as the D_i increases or as the Ω_i decreases, then the load carrying area decreases which causes the effective stress to increase above the apparent stress.

The components of the *effective* strain tensor $\epsilon^\star$ can be derived using the principle of equivalent strain energy [58]

$$\boldsymbol{\epsilon}^\star = \boldsymbol{M} \colon \boldsymbol{\epsilon} = (\boldsymbol{\Omega} \otimes \boldsymbol{\Omega}) : \boldsymbol{\epsilon} = \left[\left(\sqrt{\boldsymbol{I} - \boldsymbol{D}}\right) \otimes \left(\sqrt{\boldsymbol{I} - \boldsymbol{D}}\right)\right] : \boldsymbol{\epsilon} \tag{3.51}$$

The following expressions are valid for the fourth-order *damaged* compliance tensor

[197]

$$\boldsymbol{S} = \boldsymbol{M}^{-1} : \boldsymbol{S}^{\star} : \boldsymbol{M}^{-1}, \tag{3.52}$$

$$\boldsymbol{S} = \left(\boldsymbol{\Omega}^{-1} \otimes \boldsymbol{\Omega}^{-1}\right) : \boldsymbol{S}^{\star} : \left(\boldsymbol{\Omega}^{-1} \otimes \boldsymbol{\Omega}^{-1}\right), \tag{3.53}$$

$$\boldsymbol{S} = \left[\left(\sqrt{\boldsymbol{I}-\boldsymbol{D}}\right)^{-1} \otimes \left(\sqrt{\boldsymbol{I}-\boldsymbol{D}}\right)^{-1}\right] : \boldsymbol{S}^{\star} : \left[\left(\sqrt{\boldsymbol{I}-\boldsymbol{D}}\right)^{-1} \otimes \left(\sqrt{\boldsymbol{I}-\boldsymbol{D}}\right)^{-1}\right], \tag{3.54}$$

where $\boldsymbol{S}^{\star}$ represents the fourth-order compliance tensor of the undamaged material.

The following expressions are valid for the fourth-order *damaged* stiffness tensor [197]

$$\boldsymbol{C} = \boldsymbol{M} : \boldsymbol{C}^{\star} : \boldsymbol{M}, \tag{3.55}$$

$$\boldsymbol{C} = \left(\boldsymbol{\Omega} \otimes \boldsymbol{\Omega}\right) : \boldsymbol{C}^{\star} : \left(\boldsymbol{\Omega} \otimes \boldsymbol{\Omega}\right), \tag{3.56}$$

$$\boldsymbol{C} = \left[\left(\sqrt{\boldsymbol{I}-\boldsymbol{D}}\right) \otimes \left(\sqrt{\boldsymbol{I}-\boldsymbol{D}}\right)\right] : \boldsymbol{C}^{\star} : \left[\left(\sqrt{\boldsymbol{I}-\boldsymbol{D}}\right) \otimes \left(\sqrt{\boldsymbol{I}-\boldsymbol{D}}\right)\right], \tag{3.57}$$

where $\boldsymbol{C}^{\star}$ represents the fourth-order stiffness tensor of the undamaged material.

For the purpose of the numerical simulation, the damage tensor components D_i usually take the value of 0.99 instead of 1.0 [264].

3.3 Results

3.3.1 A critical review of analytical methods

In this section the equivalent mechanical properties predicted by the analytical models were compared against experimental results found in literature and those from other theoretical models for the same examples. The results for all four averaging schemes (PP, PS, SP and SS), discussed in section 3.2, are reported in the following sections.

Three types of weave fabrics were considered: plain, five-harness (5H) satin weave and eight-harness (8H) satin weave fabrics. Moreover examples of unbalanced weaves, hybrid weaves and weaves with the presence of gaps between the yarns were considered.

It should be noted that while the predicted results are for laminae, the experimental results are normally for the entire laminate. It also should be noted, as pointed out by [3], that not all the mechanical properties are reported in literature because of the difficulties to measure for example the out-of-plane moduli E_3 and G_{13}, measurement that would require very thick test samples which are very difficult to manufacture. Furthermore, Naik and Ganesh [164] studied the sensitivity of the predicted parameters with respect to the height to width ratio a/h of the yarns for a balanced weave. They found that, in the case of transversely isotropic fibers, increasing the ratio a/h corresponds to a decrease in E_1 and an increase in ν_{12}, while G_{12} remains constant; in the case of isotropic fibers, increasing the ratio a/h, all three parameters E_1, E_{12}, G_{12} remain practically constant.

The geometrical parameters in the analyzed examples were normally the average values, within a certain range, determined from measurements using an optical microscope.

If the values of the fiber volume fraction for the fill and warp yarns was available then these values were used in the calculations. Otherwise, the values of the fiber volume fraction for the fill and warp yarns was estimated from the overall fiber volume fraction in the composite, using equation (3.3). Akkerman [3] notes that there is usually a scattering of 1-2% in the fibre volume fractions during the manufacturing of the test samples due to the moulding process, scattering which impacts the predicted results when using analytical models versus the measured ones.

When not directly available, the composite ply thickness was calculated using the following equation [129]

$$h_t = \frac{\rho_w}{V_f^C \rho_f} \tag{3.58}$$

where V_f^C is the composite fiber volume fraction, ρ_f is the fiber density and ρ_w is the areal density of the weave (supplied by the manufacturer). When not directly available, fill yarn width a_f and the warp yarn width a_w were calculated from the values of the fill yarn counts c_f and warp yarn counts c_w according to

$$a_f = \frac{1}{c_f} \qquad\qquad a_w = \frac{1}{c_w} \tag{3.59}$$

As was discussed in section 3.2, the following micro-mechanical models were used to calculate the equivalent mechanical properties of the yarns: (1) the Chamis model [43] and the CCA for anisotropic constituents [98] for the sub-elements composed by matrix and transversely isotropic reinforcement fibers; (2) the CCA model for isotropic constituents [211] for the sub-elements composed by matrix and isotropic reinforcement fibers. These models are summarized in appendix refapp1:microModels. For anisotropic constituents all calculations were repeated for both available models in order to check for differences in the results. Since the differences were found to be very small, only the results using Chamis model are reported.

The sinusoidal functions developed by Scida et al. [216] were used for mid-plane and cross-sectional shape functions. These functions were extended in order to account for the presence of a gaps in the fill yarns (g_f) and in the warp yarns (g_w). Although more complex shape functions are available in literature (e.g. [2, 68]), the ones in [216] provide satisfactory results. Figure 3-3 displays, respectively, the fill and warp mid-plane shape functions, the top and bottom surface functions and the undulation angles for a RVE of 5-harness satin weave fabric.

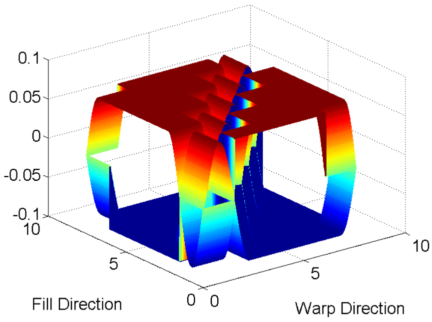

(a) Fill and warp mid-plane shape functions

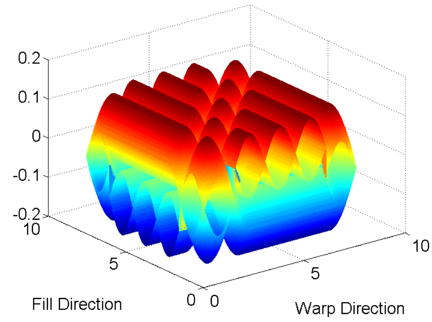

(b) Fill and warp surface functions

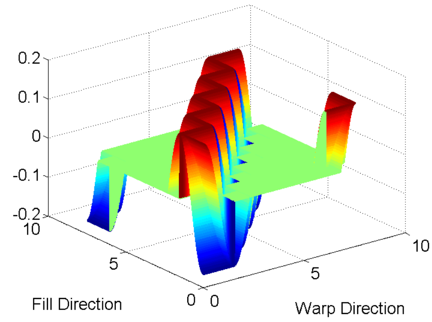

(c) Fill and warp undulation angles

Figure 3-3: RVE of 5-harness satin fabric

In order to calculate the compliance matrix, at present only the equation for symmetric elements in table 3.1b has been implemented in the software. This approximation is valid only for balanced and non-hybrid fabrics. As was discussed in section 3.2, the equations for non symmetric elements in table 3.1b provide more accurate results for unbalanced fabrics or hybrid fabrics.

Two different numerical integration methods were adopted to calculate the average mechanical properties of the RVE in the averaging approach: Simpson's rule and Gauss Quadrature rule. Significant differences were not evident between the two methods, probably because of the high number of integration points utilized (equal to $n_g 100^2$). All the results in the following are based on Gauss Quadrature rule of order 2.

The models were developed in MATLAB.

E-Glass/Vinylester plain weave fabric

Scida el al. [217] reported experimental results for an E-Glass/Vinylester plain weave fabric with elastic properties of fibers and matrix as shown in table 3.3a and geometrical parameters as shown in table 3.3b. No gaps were reported between the yarns. Given that the geometrical parameters of the fill and warp yarns are identical, this is a balanced fabric. It is also a non-hybrid fabric.

Material	E_1 [GPa]	E_2 [GPa]	G_{12} [GPa]	G_{23} [GPa]	ν_{12} [-]
E-Glass/Epoxy	55.7	18.5	6.89	6.04	0.22
EGlass/Vinylester	57.5	18.8	7.44	7.26	0.29

(a) Elastic Properties of fibers and matrix [217]

a_f [mm]	h_f [mm]	g_f [mm]	a_f [mm]	h_f [mm]	g_f [mm]	V_f^C [-]	V_f^S [-]
1.6	0.05	-	0.6	0.05	-	0.55	0.80

(b) Geometrical parameters [217]

Table 3.3: Elastic properties and geometrical parameters for E-Glass/Vinylester plain weave fabric

In table 3.4 the experimental results (*EXP* column) are compared against those predicted by the analytical models and other theoretical results for the same case found in literature.

		EXP [217]	PP	PS	SP	SS	PP [217]
E_1	[GPa]	24.8 ± 1.1	25.42	25.29	24.90	21.46	25.33
E_2	[GPa]	24.8 ± 1.1	25.42	22.13	21.86	21.46	25.33
E_3	[GPa]	8.5 ± 2.6	13.67	13.24	13.21	12.70	13.46
G_{12}	[GPa]	6.5 ± 0.8	5.25	5.11	5.10	4.93	5.19
G_{23}	[GPa]	4.2 ± 0.7	5.30	5.14	5.09	4.94	5.24
G_{13}	[GPa]	4.2 ± 0.7	5.30	5.20	5.12	4.94	5.24
ν_{12}	[-]	0.1 ± 0.01	0.14	0.15	0.15	0.15	0.12
ν_{13}	[-]	0.28 ± 0.07	0.31	0.31	0.31	0.32	0.29

Table 3.4: Results predicted by analytical models compared against experimental ones for E-Glass/Vinylester plain weave fabric

The results from the PP scheme present a very good match with the experimental data, although also the results from the SP and PS are satisfactory. As expected, the in-plane properties are estimated more precisely than the out-of-plane properties, because of the assumption that the individual lamina are modeled as orthotropic materials. Furthermore, note that the elastic properties predicted along directions 1 and 2 by the SP and PS methods are different because these methods are asymmetric as they make different assumptions (iso-stress or iso-strain) along these directions.

T-300 Carbon/PEI 5H satin weave fabric

Akkerman [3] reported experimental results for a T-300 Carbon/PEI 5H satin weave fabric with elastic properties of fibers and matrix as shown in table 3.5a and geometrical parameters as shown in table 3.5b. No gaps were reported between the yarns. Given that the geometrical parameters of the fill and warp yarns are identical, this is a balanced fabric. This fabric is non-hybrid.

Material	E_1 [GPa]	E_2 [GPa]	G_{12} [GPa]	G_{23} [GPa]	ν_{12} [-]
T-300 Carbon	231.0	40.0	24.0	14.4	0.26
PPS	3.8	3.8	1.39	1.39	0.37
PEI	3.0	3.0	1.1	1.1	0.36

(a) Elastic properties of fibers and matrix [252]

a_f [mm]	h_f [mm]	g_f [mm]	a_f [mm]	h_f [mm]	g_f [mm]	V_f^C [-]	V_f^S [-]
1.5	0.16	-	1.5	0.16	-	0.50	–

(b) Geometrical parameters [252]

Table 3.5: Elastic properties and geometrical parameters for T-300 Carbon/PEI 5H satin weave fabric

In table 3.6 the experimental results (*EXP* column) are compared against those predicted by the analytical models and other theoretical results for the same case found in literature. Note that the shape functions used by [3] are different from those used in the present study.

		EXP [3]	PP	PS	SP	SS	PP [3]	SS [252]
E_1	[GPa]	60	64.21	64.07	59.94	41.78	62.0	54.0
E_2	[GPa]	60	64.21	44.25	42.51	41.78	62.0	54.0
E_3	[GPa]	–	14.12	13.42	13.36	12.64	9.4	8.9
G_{12}	[GPa]	3.5	4.96	4.76	4.74	4.50	3.5	3.4
G_{23}	[GPa]	–	4.25	3.93	3.75	3.68	3.8	3.5
G_{13}	[GPa]	–	4.25	4.23	3.97	3.68	3.8	3.5
ν_{12}	[-]	0.05	0.05	0.06	0.07	0.07	0.04	0.04
ν_{13}	[-]	–	0.45	0.44	0.43	0.45	0.44	0.46
ν_{23}	[-]	–	0.45	0.46	0.45	0.45	0.44	0.46

Table 3.6: Results predicted by analytical models compared against experimental ones for T-300 Carbon/PEI 5H satin weave fabric

The results from the PP scheme present a very good match with the experimental data, while the others are not particularly satisfactory. Again the elastic properties predicted along directions 1 and 2 by the SP and PS methods are different.

E-Glass/PPS 8H satin weave fabric

Akkerman [3] reported experimental results for an E-Glass/PPS 8H satin weave fabric with elastic properties of fibers and matrix in table as shown 3.7a and geometrical parameters as shown in table 3.7b. No gaps were reported between the yarns. Given that the geometrical parameters of the fill and warp yarns are not identical, this is an unbalanced fabric. This fabric is non-hybrid.

In table 3.8 the experimental results (*EXP* column) are compared against those

Material	E_1 [GPa]	E_2 [GPa]	G_{12} [GPa]	G_{23} [GPa]	ν_{12} [-]
E-Glass	70.0	70.0	28.45	28.45	0.23
PPS	3.8	3.8	1.39	1.39	0.37

(a) Elastic properties of fibers and matrix [129]

a_f [mm]	h_f [mm]	g_f [mm]	a_f [mm]	h_f [mm]	g_f [mm]	V_f^C [-]	V_f^S [-]
0.45	0.11	-	0.44	0.11	-	0.50	–

(b) Geometrical parameters [129]

Table 3.7: Elastic properties and geometrical parameters for E-Glass/PPS 8H-satin-weave fabric

predicted by the analytical models and other theoretical results for the same case found in literature. Note that the shape functions used by [3] are different from those used in the present study.

	EXP [3]	PP	PS	SP	SS	PP [3]
E_1 [GPa]	25	27.29	26.71	26.16	23.14	27.0
E_2 [GPa]	25	27.32	24.47	24.13	23.19	27.0
E_3 [GPa]	–	18.23	17.45	17.34	16.41	27.0
G_{12} [GPa]	5.1	5.92	5.69	5.68	5.40	5.8
G_{23} [GPa]	–	6.52	6.27	6.19	5.86	6.1
G_{13} [GPa]	–	6.53	6.28	6.15	5.86	6.1
ν_{12} [-]	0.12	0.17	0.19	0.19	0.19	0.15
ν_{13} [-]	–	0.32	0.32	0.32	0.33	0.37
ν_{23} [-]	–	0.32	0.32	0.32	0.33	0.37

Table 3.8: Results predicted by analytical models compared against experimental ones for E-Glass/PPS 8H satin weave fabric

Here the results from the PP and SP schemes give the best match with the experimental ones.

E-Glass/Epoxy plain weave fabric N.1

Naik and Gamesh [164] reported experimental results for an E-Glass/epoxy plain weave fabric with elastic properties of fibers and matrix as shown in table 3.9a and geometrical parameters as shown in table 3.9b. Here gaps were reported between the yarns. Given that the geometrical parameters of the fill and warp yarns are not identical, this is an unbalanced fabric. This fabric is non-hybrid.

Material	E_1 [GPa]	E_2 [GPa]	G_{12} [GPa]	G_{23} [GPa]	ν_{12} [-]
E-Glass	72.0	72.0	27.7	27.7	0.30
Epoxy	3.5	3.5	1.3	1.3	0.35

(a) Elastic properties of fibers and matrix [164]

a_f [mm]	h_f [mm]	g_f [mm]	a_f [mm]	h_f [mm]	g_f [mm]	V_f^C [-]	V_f^S [-]
0.45	0.048	0.30	0.45	0.048	0.30	0.23	0.74

(b) Geometrical parameters [164]

Table 3.9: Elastic properties and geometrical parameters for E-Glass/Epoxy plain weave fabric N.1

In table 3.10 the experimental results are compared against those predicted by the analytical models developed in this work and other theoretical results for the same case found in literature. Only the in-plane shear modulus measured using ±45° off-axis tension tests has been reported. Note that the shape functions used by [164] are different from those used in the present study.

		EXP [164]	PP	PS	SP	SS	SP [164]
E_1	[GPa]	20 ± 0.8	16.46	15.70	15.28	9.14	14.5
E_2	[GPa]	20 ± 0.8	16.46	11.15	10.90	9.14	–
G_{12}	[GPa]	2.95 ± 0.05	3.35	3.05	3.02	2.62	2.96

Table 3.10: Results predicted by analytical models compared against experimental ones for E-Glass/Epoxy Plain Weave Fabric N.1

Here the PP scheme yields the best results. The predicted values are particularly good because the presence of gaps has been accounted for in the model.

E-Glass/Epoxy plain weave fabric N.2

Naik and Gamesh [164] reported experimental results for an E-Glass/epoxy plain weave fabric with elastic properties of fibers and matrix as shown in table 3.9a and geometrical parameters as shown in table 3.11. This is another example of fabric with gaps between the yarns. Given that the geometrical parameters of the fill and warp yarns are not identical, this is an unbalanced fabric. This fabric is non-hybrid.

a_f [mm]	h_f [mm]	g_f [mm]	a_f [mm]	h_f [mm]	g_f [mm]	V_f^C [-]	V_f^S [-]
0.68	0.09	0.04	0.62	0.09	0.10	0.40	0.71

Table 3.11: Geometrical parameters [164]

In table 3.12 the experimental results are compared against those predicted by the analytical models and other theoretical results for the same case found in literature. Only the in-plane shear modulus measured using ±45° off-axis tension tests has been reported. Note that the shape functions used by [164] are different from those used in the present study.

		EXP [164]	PP	PS	SP	SS	SP [164]
E_1	[GPa]	21.5 ± 1.0	21.88	21.36	20.52	16.58	20.2
E_2	[GPa]	21.5 ± 1.0	21.03	16.70	16.35	15.35	–
G_{12}	[GPa]	3.3 ± 0.4	4.04	3.84	3.83	3.61	3.89

Table 3.12: Results predicted by analytical models compared against experimental ones for E-Glass/Epoxy plain weave fabric N.2

Again the PP scheme yields the best results. The predicted values are particularly good because the presence of gaps has been accounted for in the model.

Hybrid plain weave fabric

Donadon et al. [68] reported experimental results for a hybrid plain weave fabric with elastic properties of fibers and matrix as shown in table 3.13a and geometrical parameters as shown in table 3.13b. This is another example of fabric with gaps between the yarns. Given that the geometrical parameters of the fill and warp yarns are not identical, this is also an unbalanced fabric. Moreover, this fabric is hybrid, given that the fibers in the fill and warp yarns are different.

Material	E_1 [GPa]	E_2 [GPa]	G_{12} [GPa]	G_{23} [GPa]	ν_{12} [-]
T-300 Carbon	232.00	23.10	8.96	8.27	0.20
PPG EC09 (Glass)	72.40	72.40	29.27	29.67	0.22
PRIME 20LV	2.97	2.97	1.08	1.08	0.38

(a) Elastic properties of fibers and matrix [68]

a_f [mm]	h_f [mm]	g_f [mm]	a_f [mm]	h_f [mm]	g_f [mm]	V_f^F [-]	V_f^W [-]
2.350	0.329	0.060	1.112	0.116	4.900	0.688	0.580

(b) Geometrical parameters [68]

Table 3.13: Elastic properties and geometrical parameters for hybrid plain weave fabric

In table 3.14 the experimental results are compared against those predicted by the analytical models and other theoretical results for the same case found in literature. Note that the shape functions used by [68] are different from those used in the present study.

		EXP [68]	PP	PS	SP	SS	SP [68]
E_1	[GPa]	100	75.05	75.01	68.08	31.26	114.0
E_2	[GPa]	8.11	8.04	7.42	7.40	6.77	9.11
E_3	[GPa]	–	7.29	7.09	7.08	6.46	14.40
G_{12}	[GPa]	3.88	2.49	2.48	2.48	2.24	4.39
G_{23}	[GPa]	–	1.90	1.88	1.88	1.79	4.23
G_{13}	[GPa]	–	2.77	2.76	2.52	2.28	4.23
ν_{12}	[-]	0.36	0.24	0.26	0.27	0.32	0.38
ν_{13}	[-]	–	0.35	0.34	0.34	0.37	0.43
ν_{23}	[-]	–	0.52	0.53	0.52	0.51	0.43

Table 3.14: Results predicted by analytical models compared against experimental ones for hybrid plain weave fabric

3.3.2 Comparison of analytical methods with the AEHM

In this section the equivalent mechanical properties predicted by the AEHM and analytical model were compared against experimental results found in literature and those from other theoretical models for the same examples. The results for all four averaging schemes (PP, PS, SP and SS), discussed in section 3.2, are reported in the following sub-sections. The models were developed in MATLAB.

Three types of weave fabrics were taken into account: plain weave, five-harness (5H) satin weave and eight-harness (8H) satin weave fabrics. Moreover examples of unbalanced weaves and weaves with the presence of gaps between the yarns were also considered.

It should be noted that while the predicted results are for laminae, the experimental results are normally for laminate. It also should be noted, as pointed out by [3], that not all the mechanical properties are reported in literature because of the difficulties to

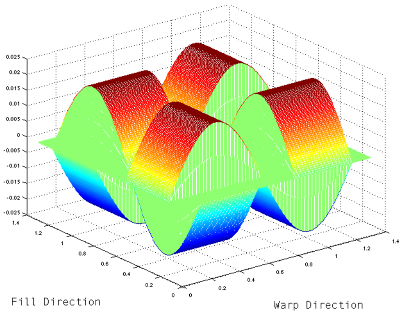

(a) Fill and warp mid-plane shape functions

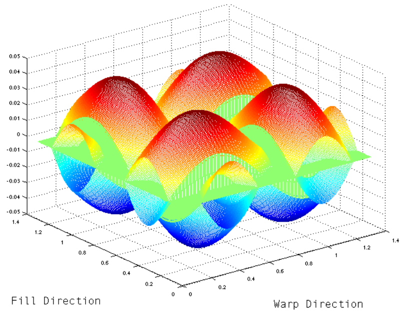

(b) Fill and warp undulation angles

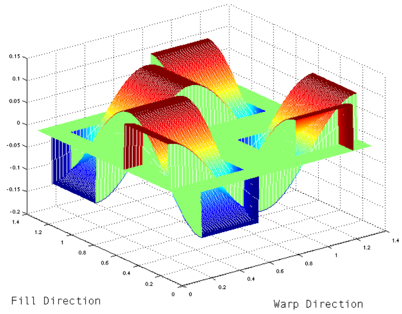

(c) Fill and warp undulation angles

Figure 3-4: RVE of plain weave fabric with gaps

measure for example the out-of-plane stiffnesses E_3 and G_{13}, measurement that would require very thick test samples which are very difficult to manufacture. Furthermore, Naik and Ganesh [164] studied the sensitivity of the predicted parameters with respect to the height to width ratio a/h of the yarns for a balanced weave. They found that, in the case of transversely isotropic fibers, increasing the ratio a/h corresponds to a decrease in E_1 and an increase in ν_{12}, while G_{12} remains constant; in the case of isotropic fibers, increasing the ratio a/h, all three parameters E_1, E_{12}, G_{12} remain practically constant.

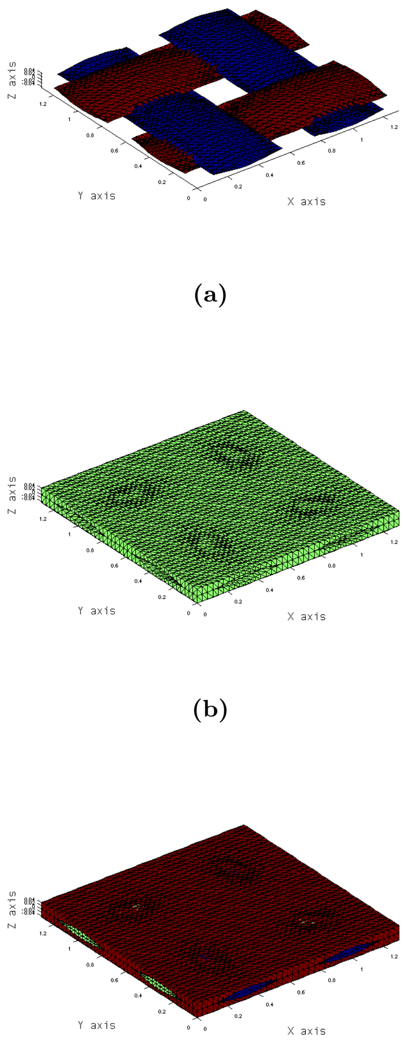

(a)

(b)

(c)

Figure 3-5: Tetrahedral mesh for a RVE of plain weave fabric with gaps : strands (a) , matrix (b) and complete RVE (c)

The geometrical parameters in the analyzed examples were normally the average values, within a certain range, determined from measurements using an optical microscope.

If the values of the fiber volume fraction of fill and warp yarns were available then these values were used in the calculations. Otherwise, the values of the fiber volume fraction of fill and warp yarns were estimated from the overall fiber volume fraction in the composite, using equation (3.3). Akkerman [3] notes that there is usually a scattering of 1-2% in the fibre volume fractions during the manufactures of the test

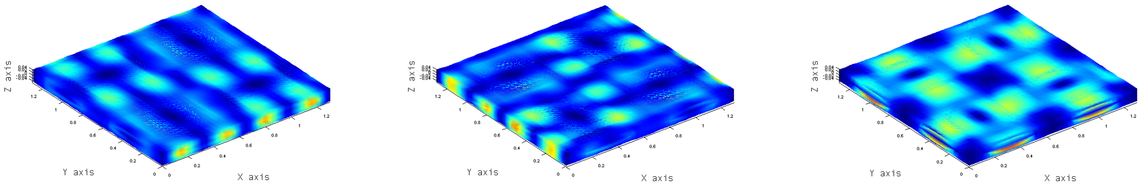

(a) χ_{11} **(b)** χ_{22} **(c)** χ_{33}

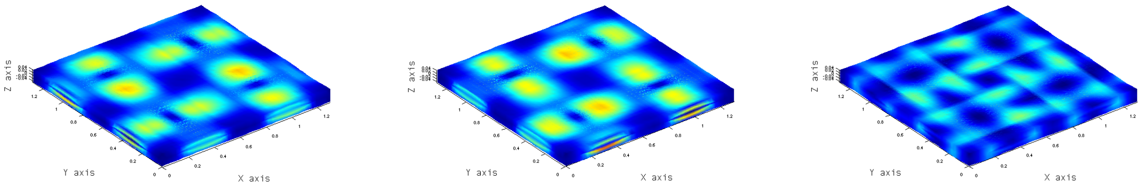

(d) χ_{23} **(e)** χ_{13} **(f)** χ_{12}

Figure 3-6: Microcorrectors for a RVE of plain weave fabric with gaps

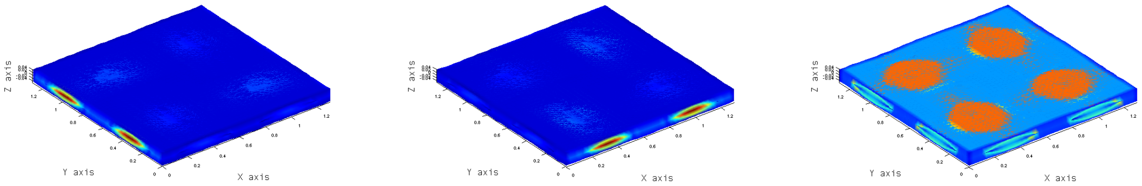

(a) Load for χ_{11} **(b)** Load for χ_{22} **(c)** Load for χ_{33}

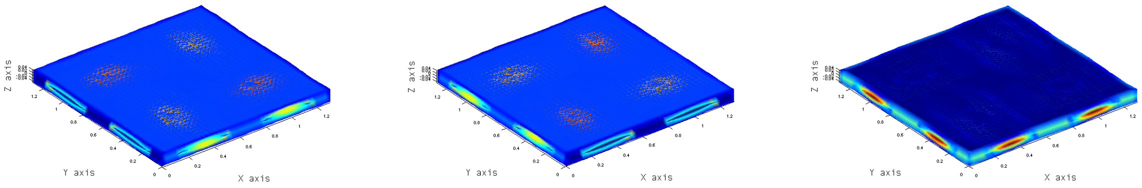

(d) Load for χ_{23} **(e)** Load for χ_{13} **(f)** Load for χ_{12}

Figure 3-7: Characteristic loading vectors for a RVE of plain weave fabric with gaps

samples due to the moulding process, scattering which impacts the predicted results using analytical models versus the measured ones.

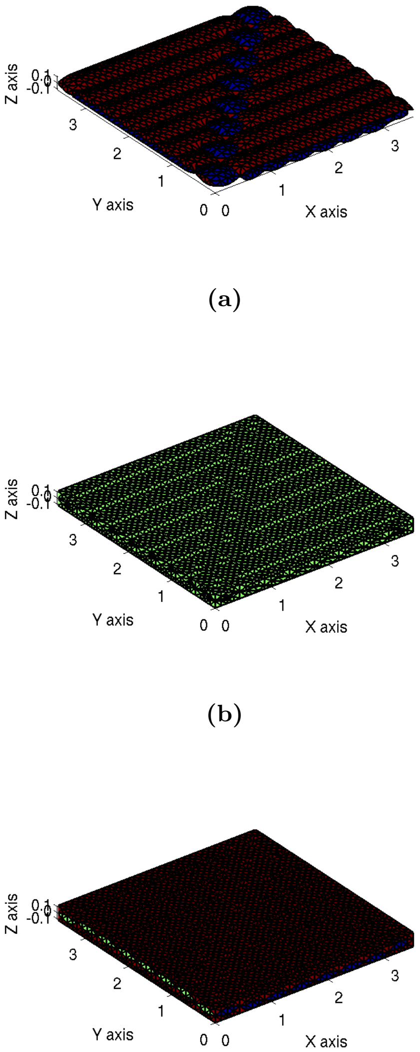

(a)

(b)

(c)

Figure 3-8: Tetrahedral mesh for a RVE of 8-harness satin fabric : strands (a) , matrix (b) and complete RVE (c)

When not directly available, the composite ply thickness was calculated using the following equation [129]

$$h_t = \frac{\rho_w}{V_f^C \rho_f} \tag{3.60}$$

where V_f^C is the composite fiber volume fraction, ρ_f is the fiber density and ρ_w is the areal density of the weave (supplied by the manufacturer). When not directly available, the fill yarn width a_f and the warp yarn width a_w were calculated from the

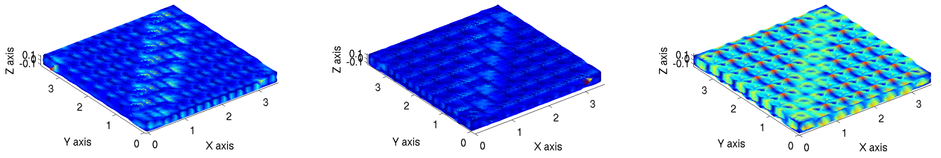

(a) χ_{11} **(b)** χ_{22} **(c)** χ_{33}

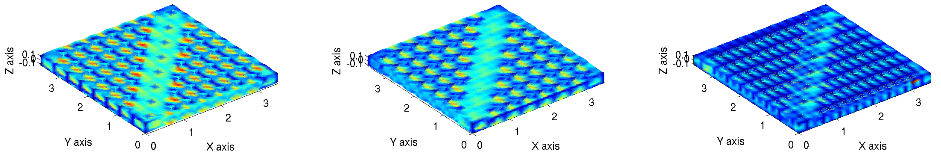

(d) χ_{23} **(e)** χ_{13} **(f)** χ_{12}

Figure 3-9: Microcorrectors for a RVE of 8-harness satin fabric

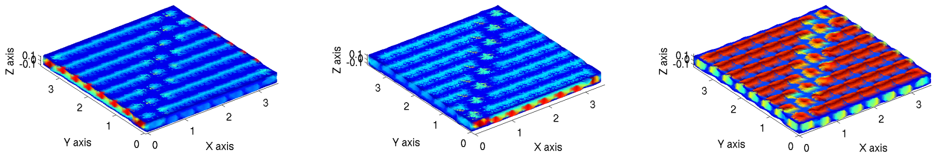

(a) Load for χ_{11} **(b)** Load for χ_{22} **(c)** Load for χ_{33}

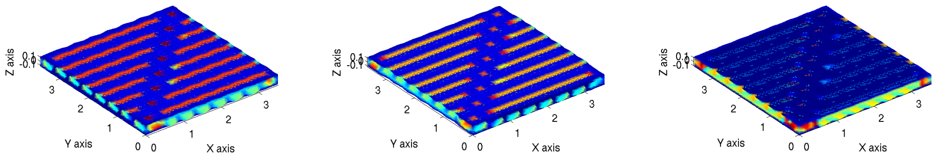

(d) Load for χ_{23} **(e)** Load for χ_{13} **(f)** Load for χ_{12}

Figure 3-10: Characteristic loading vectors for a RVE of 8-harness satin fabric

values of the fill yarn counts c_f and warp yarn counts c_w

$$a_f = \frac{1}{c_f} \qquad\qquad a_w = \frac{1}{c_w} \tag{3.61}$$

As was discussed in section 3.2, the following micro-mechanics models were used to calculate the equivalent mechanical properties of the yarns: (1) the Chamis model [44] and the CCA model for anisotropic constituents [98] for sub-elements composed by matrix and transversely isotropic reinforcement fibers; (2) the CCA model for isotropic constituents [211] for sub-elements composed by matrix and isotropic reinforcement fibers. These models are summarized in appendix refapp1:microModels. For anisotropic constituents all calculations were repeated for both available models in order to check for differences in the results. As only a very small difference was found, only the results using Chamis model are reported.

The sinusoidal functions developed by Scida et al. [216] were used for mid-plane and cross-sectional shape functions. These functions were extended in order to account for the presence of a gaps in the fill yarns (g_f) and in the warp yarns (g_w). Although more complex shape functions are available in literature (e.g. [2, 68]), the ones in [216] provide satisfactory results, as will be shown in the following. Figure 3-4 displays, respectively, the fill and warp mid-plane shape functions, the top and bottom surface functions and the undulation angles for a RVE of plain weave fabric with gaps between the yarns.

In general, as discussed in [139, 23] the asymptotic expansion homogenization can be implemented using two different approaches: the *displacement method* (e.g. [24, 63]) and the *force method* (e.g. [53, 55]). The force method in an ad-hoc code written in MATLAB was used. As explained in [55, 116, 61] this type of approach could have also been easily implemented in a standard finite element code.

For a hexahedral RVE with $y_1 \in \left[0, y_1^0\right]$, $y_2 \in \left[0, y_2^0\right]$ and $y_3 \in \left[0, y_3^0\right]$ the following periodicity conditions [55, 61] were imposed on the surface boundaries of the RVE

$$\begin{aligned}\chi_i^{jk}\left(0, y_2, y_3\right) &= \chi_i^{jk}\left(y_1^0, y_2, y_3\right), \\ \chi_i^{jk}\left(y_1, 0, y_3\right) &= \chi_i^{jk}\left(y_1, y_2^0, y_3\right), \\ \chi_i^{jk}\left(y_3, y_2, 0\right) &= \chi_i^{jk}\left(y_1, y_2, y_3^0\right)\end{aligned} \tag{3.62}$$

An in-house automatic meshing tool was used to discretized the RVE in to tetrahedral elements for computing the results for the AEHM. Nodes on surface boundaries of the RVE can be distinguished in: corners, edges and faces. Furthermore, nodes can be distinguished in master nodes and slave nodes. Corners, edges and face which are slave nodes must be associated to master nodes on parallel faces.

Figure 3-5 displays the tetrahedral mesh for a RVE of a plain weave fabric with gaps, in particular for strands, matrix and complete RVE. Figure 3-8 displays the tetrahedral mesh for a RVE of a 8-harness satin fabric with gaps, in particular for strands, matrix and complete RVE.

As an unstructured mesh was used in this work there is not a one-to-one association between master and slave nodes. For this reason the code is programmed to find the best matching master node for each slave node, as discussed in [61]. Moreover, in order to prevent rigid body motion, the correctors of at least one arbitrary point in the RVE must be fixed. Two different methods were implemented for imposing the periodic boundary conditions: *Lagrange multipliers* and *static condensation* (or simply *condensation*). As only very small differences were found between the two methods, as condensation is more efficient, this method was used for calculating all the results for the AEHM.

Figures 3-6 and 3-7 display, respectively, the microcorrectors and the characteristic loading vectors for a RVE of plain weave fabric with gaps. Figures 3-9 and 3-10 display, respectively, the microcorrectors and the characteristic loading vectors for a RVE of 8-harness fabric with gaps.

E-Glass/PPS Plain Weave Fabric

Akkerman [3] reported experimental results for an E-Glass/PPS plain weave fabric with elastic properties of fibers and matrix in Table 3.15a and geometrical parameters in Table 3.15b. No gaps were reported between the yarns. Given that the geometrical parameters of the fill and warp yarns are not identical, this is an unbalanced fabric. This fabric is non-hybrid.

Material	E_1 [GPa]	E_2 [GPa]	G_{12} [GPa]	G_{23} [GPa]	ν_{12} [-]
E-Glass	70.0	70.0	28.45	28.45	0.23
PPS	3.8	3.8	1.39	1.39	0.37

(a) Elastic Properties of fibers and matrix [129]

a_f [mm]	h_f [mm]	g_f [mm]	a_f [mm]	h_f [mm]	g_f [mm]	V_f^C [-]	V_f^S [-]
0.95	0.11	-	1.04	0.11	-	0.50	–

(b) Geometrical parameters [3]

Table 3.15: Elastic properties and geometrical parameters for E-Glass/PPS Plain Weave Fabric

In Table 3.16 the experimental results are compared against those predicted by the AEHM, the analytical models and other theoretical results for the same case found in literature. Note that the shape functions used by [3] are different from those used in the present study.

		EXP [3]	AEHM	PP	PS	SP	SS	PP [3]
E_1	[GPa]	24	27.56	27.23	26.85	26.38	23.53	25.0
E_2	[GPa]	24	27.99	27.14	24.51	24.18	23.41	–
E_3	[GPa]	–	23.01	18.08	17.43	17.34	16.53	12.0
G_{12}	[GPa]	4.7	6.03	5.87	5.68	5.67	5.44	5.8
G_{13}	[GPa]	–		8.90 6.44	6.24	6.12	5.89	6.8
ν_{12}	[-]	0.12	0.18	0.17	0.19	0.19	0.19	0.14
ν_{13}	[-]	–	0.30	0.32	0.32	0.32	0.33	0.38

Table 3.16: Results from models compared against experimental ones for E-Glass/PPS Plain Weave Fabric

The AEHM gives similar results to the PP method, which is the best of the analytical methods.

T-300 Carbon/PPS 5H-Satin-Weave Fabric

Akkerman [3] reported experimental results for a T-300 Carbon/PPS 5H-satin weave fabric with elastic properties of fibers and matrix in Table 3.17a and geometrical parameters in Table 3.17b. No gaps were reported between the yarns. Given that the geometrical parameters of the fill and warp yarns are identical, this is a balanced fabric. This fabric is non-hybrid.

Material	E_1 [GPa]	E_2 [GPa]	G_{12} [GPa]	G_{23} [GPa]	ν_{12} [-]
T-300 Carbon	231.0	40.0	24.0	14.4	0.26
PPS	3.8	3.8	1.39	1.39	0.37
PEI	3.0	3.0	1.1	1.1	0.36

(a) Elastic Properties of fibers and matrix [252]

a_f [mm]	h_f [mm]	g_f [mm]	a_f [mm]	h_f [mm]	g_f [mm]	V_f^C [-]	V_f^S [-]
1.5	0.15	-	1.5	0.15	-	0.60	–

(b) Geometrical parameters [252]

Table 3.17: Elastic properties and geometrical parameters for T-300 Carbon/PPS 5H-Satin-Weave Fabric

In Table 3.18 the experimental results are compared against those predicted by the AEHM, the analytical models and other theoretical results for the same case found in literature. Note that the shape functions used by [3] are different from those used in the present study.

		EXP [3]	AEHM	PP	PS	SP	SS	PP [3]
E_1	[GPa]	84	76.99	75.18	75.08	70.12	46.91	77.0
E_2	[GPa]	84	81.28	75.18	49.35	47.40	46.91	77.0
E_3	[GPa]	–	21.53	18.14	16.68	16.52	15.28	14.0
G_{12}	[GPa]	4.1	5.51	5.42	5.22	5.20	4.96	5.9
G_{23}	[GPa]	–	5.71	4.42	4.07	3.87	3.83	5.9
G_{13}	[GPa]	–	5.74	4.42	4.41	4.13	3.83	5.9
ν_{12}	[-]	0.02	0.01	0.02	0.03	0.04	0.04	0.05
ν_{13}	[-]	–	0.57	0.56	0.55	0.54	0.59	0.44
ν_{23}	[-]	–	0.57	0.56	0.61	0.61	0.59	0.44

Table 3.18: Results from models compared against experimental ones for T-300 Carbon/PPS 5H-Satin-Weave Fabric

Again, the AEHM gives similar results to the PP scheme, which is the best of the analytical methods.

E-Glass/Epoxy 8H-Satin-Weave Fabric

Scida el al. [217] reported experimental results for an E-glass/epoxy 8H-satin weave fabric with elastic properties of fibers and matrix in Table 3.19a and geometrical parameters in Table 3.19b. No gaps were reported between the yarns. Given that the geometrical parameters of the fill and warp yarns are identical, this is a balanced fabric. This fabric is non-hybrid.

In Table 3.20 the experimental results are compared against those predicted by the analytical model and other theoretical results for the same case found in literature.

The AEHM and the PP scheme yield similar results.

Material	E_1 [GPa]	E_2 [GPa]	G_{12} [GPa]	G_{23} [GPa]	ν_{12} [-]
E-Glass/Epoxy	55.7	18.5	6.89	6.04	0.22
EGlass/Vinylester	57.5	18.8	7.44	7.26	0.29

(a) Elastic Properties of fibers and matrix [217]

a_f [mm]	h_f [mm]	g_f [mm]	a_f [mm]	h_f [mm]	g_f [mm]	V_f^C [-]	V_f^S [-]
0.6	0.09	-	0.6	0.09	-	0.52	0.80

(b) Geometrical parameters [217]

Table 3.19: Elastic properties and geometrical parameters for E-Glass/Epoxy 8H-Satin-Weave Fabric

	EXP [217]	AEHM	PP	PS	SP	SS	PP [217]
E_1 [GPa]	25.6 ± 0.2	27.85	27.52	27.15	26.83	23.13	26.03
E_2 [GPa]	25.6 ± 0.2	28.50	27.52	24.13	23.87	23.13	26.03
E_3 [GPa]	$-$	16.70	21.48	15.98	15.92	15.05	15.65
G_{12} [GPa]	5.7 ± 0.3	6.21	5.94	5.69	5.67	5.36	5.67
G_{23} [GPa]	$-$	5.68	7.84	5.40	5.35	5.12	5.42
G_{13} [GPa]	$-$	5.68	7.89	5.52	5.45	5.12	5.42
ν_{12} [-]	0.13 ± 0.005	0.14	0.13	0.15	0.15	0.15	0.12
ν_{13} [-]	$-$	0.30	0.28	0.30	0.30	0.32	0.28

Table 3.20: Results from models compared against experimental ones for E-Glass/Epoxy 8H-Satin-Weave Fabric

E-Glass/Epoxy plain weave fabric

Naik and Gamesh [164] reported experimental results for an E-Glass/epoxy plain weave fabric with elastic properties of fibers and matrix in Table 3.21a and geometrical parameters in Table 3.21b. This is another example of fabric with gaps between the yarns. Given that the geometrical parameters of the fill and warp yarns are not identical, this is an unbalanced fabric. This fabric is non-hybrid.

Material	E_1 [GPa]	E_2 [GPa]	G_{12} [GPa]	G_{23} [GPa]	ν_{12} [-]
E-Glass	72.0	72.0	27.7	27.7	0.30
Epoxy	3.5	3.5	1.3	1.3	0.35

(a) Elastic Properties of fibers and matrix [164]

a_f [mm]	h_f [mm]	g_f [mm]	a_f [mm]	h_f [mm]	g_f [mm]	V_f^C [-]	V_f^S [-]
0.86	0.11	0.00	0.84	0.11	0.02	0.46	0.74

(b) Geometrical parameters [164]

Table 3.21: Elastic properties and geometrical parameters for E-Glass/Epoxy plain weave fabric

In Table 3.22 the experimental results are compared against those predicted by the analytical model developed in this work and other theoretical results for the same case found in literature. Only the in-plane shear modulus measured using ±45° off-axis tension tests have been reported. Note that the shape functions used by [164] are different from those used in the present study.

	EXP [164]	AEHM	PP	PS	SP	SS	SP [164]
E_1 [GPa]	22.8 ± 1.2	24.26	24.43	23.97	23.19	20.14	22.0
E_2 [GPa]	22.8 ± 1.2	25.21	24.19	20.84	20.42	19.65	$-$
G_{12} [GPa]	5.5 ± 0.1	4.75	4.69	4.51	4.50	4.31	4.55

Table 3.22: Results from models compared against experimental ones for E-Glass/Epoxy plain weave fabric N.3

Here the AEHM and the PP scheme yield the best results. The predicted values are particularly good because the presence of gaps has been accounted for in the model.

3.4 Conclusions

This chapter has reviewed the analytical methods based on the mechanics of materials approach and critically compared their capability in predicting the mechanical properties of 2D woven composites. Four types of averaging schemes were taken into account: the parallel-parallel, the parallel-series, the series-parallel and the series-series schemes. Different types of weave patterns, in particular plain, five-harness satin weave and eight-harness satin weave, as well as different material properties were taken into consideration. Also unbalanced weaves, hybrid weaves and weaves with gaps were analyzed. The results were compared to experimental and numerical results for various cases found in literature.

These methods provide good estimation of the mechanical properties for all the cases, especially for the in-plane properties, while the out-of-plane properties are estimated less precisely, because of the assumption that the individual lamina are modeled as orthotropic materials. The best results were provided by the parallel-parallel scheme compared to the other methods. The precision in the results is greatly improved when the geometry takes in to account the gaps between the yarns. Moreover, the elastic properties predicted along directions 1 and 2 by the parallel-series and the series-parallel methods are different because these methods are asymmetric as they make different assumptions (iso-stress or iso-strain) along these directions.

Furthermore, this chapter has assessed the capability of the asymptotic expansion homogenization method (AEHM) in comparison to analytical methods based on the mechanics of materials approach for predicting the mechanical properties of 2-D woven composites. In terms of analytical methods four types of averaging schemes are taken into account: the parallel-parallel, parallel-series, the series-parallel and the series-series schemes. Different types of weave patterns, in particular plain, five-harness satin and eight-harness satin weave, and material properties were taken into consideration. Also unbalanced weaves and weaves with gaps were analyzed. The results are compared to experimental and numerical results for various cases found in literature.

The AEHM provides a good estimation of the mechanical properties for all the cases especially for the in-plane properties, while the out-of-plane properties are estimated less precisely, because of the assumption that the individual laminae are modeled as orthotropic materials. The AEHM compares well with the best results of the analytical methods which were provided by the parallel-parallel scheme. For all considered methods, the precision in the results is greatly improved when the geometry takes in account of gaps between the yarns. Moreover, although not discussed here, the AEHM is able to provide localization of stresses and strains directly as part of the methodology [55, 116, 61], feature that is not provided by the analytical methods.

Chapter 4

Multiscale three-dimensional constitutive modeling of shape memory alloy hybrid composites

4.1 Introduction

When the shape memory alloy (SMA) material is embedded in the SMA hybrid composites (SMAHCs) in the form of wires the use of a one-dimensional model is a satisfactory approximation (under the hypothesis of small diameter to length ratios).

Many different constitutive models have been developed to describe the thermomechanical behavior of SMA materials, and this topic would be worthy of whole thesis in its own right alone.

Different approaches have been adopted for the solution of the problem, and following Brailovski et al. [32] we will classify them in micro-mechanical, macroscopic and phenomenological. In this chapter we will very briefly review only the macroscopic modeling approach. Moreover, Paiva and Savi [188] classify the macroscopic SMA constitutive models into models with assumed phase transformation kinetics and models based on the elasto-plasticity theory. There authors also provide some numerical results comparing the performance of the later type.

We will first cover the topic of models based on assumed phase transformation kinetics.

Tanaka's [235] one-dimensional (1-D) model is developed starting from the second law of thermodynamics written in terms of the Helmholtz free energy and assuming that the uniaxial strain, temperature, and Martensite volume fraction ξ are the only state variables. This model adopts an exponential expression of ξ is function of stress and temperature. Liang and Rogers' model [133] extended the one-dimensional model developed by Tanaka using a cosine function to describe the Martensite volume fraction

ξ is terms of stress and temperature.

The problem with these models is that they only describe the stress-induced Martensite phase transformation and they do not describe the strain-induced Martensite transformation. As Chopra [49] points out these models can not be applied to model the detwinning of Martensite responsible for the SME at low temperatures.

To overcome this deficiency, the one-dimensional model developed by Brinson [33, 35] follows a different approach to the phase transformation kinetics, in which, besides considering a cosine function to describe the Martensite volume fraction ξ is terms of stress and temperature, the Martensite volume fraction ξ is separated into two contributions. The first contribution ξ_M, called multi-variant Martensite faction, is the part of Martensite induced only by changes in temperature. The second contribution ξ_S, called single variant martensitic fraction, is the part of Martensite induced only by changes in stress. The total volume fraction of Martensite is $\xi = \xi_S + \xi_M$.

The constitutive model developed by Boyd and Lagoudas [30, 31] is derived from the Helmholtz free energy and can cover three dimensional states and non-proportional loading. Other models that are worthwhile remembering are those developed by Sun and Hwang [228] and by Ivshin and Pence [107].

Amongst the SMA constitutive models based on the elasto-plasticity theory firstly proposed for a one-dimensional media we will mention only the Auricchio model, that in the first stage was proposed for the one-dimensional case [9], and that in a second stage was extended to a three-dimensional case [12, 13].

One-dimensional constitutive models are satisfactory for SMAHCs with embedded uni-directional SMA wires, but three-dimensional (3-D) constitutive models are necessary for characterizing the thermo-mechanical behavior of SMAHCs with embedded woven SMA wires.

Recently a 3-D constitutive model has been proposed by Popov and Lagoudas [193, 194] which, developed using a thermodynamics formulation, has three internal variables for the Martensite volume fraction ξ and is capable of modeling simultaneously pseudoelasticity and detwinning of self-accommodated Martensite in polycrystalline SMAs.

The *asymptotic expansion homogenization method* (AEHM) has been previously applied to study the elastic-plastic [56, 88, 221, 246], thermo-viscoelastic creep [54, 52] and elastic-viscoplatic behavior [144, 145, 176] of composite materials.

As discussed by [88, 236] the solution of large scale nonlinear structural problems with accurate resolution of micro-structural fields using the AEHM in not feasible. For linear analysis the microscopic problem over the representative volume element (RVE) has to be solved only one, while for nonlinear structural analysis the microscopic problem over the RVE has to be solved at every increment and for each Gauss point of the macroscopic problem. Moreover, the history data has to be updated at a number of points equal to the number of Gauss points in the microscopic problem times the number of Gauss points in the macroscopic problem.

Different approaches to overcome this issue can be found in literature. Takano et al. [231] in order to reduce the computational complexity of the the nonlinear problem combine the AEHM with anisotropic damage which was discussed in chapter 3 with the the mesh superposition technique [83], also referred to as *s-version* or *s-refinement* of the finite element method, discussed in chapter 5. Fish and Shek [87, 221] develop a two-point homogenization scheme with eigenstrains to compute the overall elastic-plastic response of composite structures, while the microscopic solution is evaluated only in critical points subjecting the unit cells to the macroscopic solution history. Oskay and Fish [179] adapt the method to incorporate failure in both micro-constituents and interfaces between constituents.

The averaging methods developed in [87, 179, 221] are based on the *Transformation Field Analysis* (TFA) developed by Dvorak and co-workers. The mathematical foundations have been posed in [72, 75] while the method was initially applied to elasto-plastic composites in [76, 73, 74].

The AEHM (also referred to as *mathematical homogenization method*) has been applied to the constitutive behavior of Shape Memory Alloys by [99] adapting the methodology developed by Fish and Shek [87, 221] for elasto-plasticity. The authors in [99] study only a two-phase composite consisting of matrix and pseudoelastic shape memory alloy (SMA).

In section 4.2 two constitutive models for SMA will be reviewed: the 1-D Brinson model in subsection 4.2.1 and 3-D Sadjadpour and Bhattacharya model in subsection 4.2.2. Then in subsection 4.2.4 a multiscale approach based on AEHM for modeling the 3-D behavior of SMAHCs will be developed which can easily incorporate TFA. Finally in subsection 4.2.5 the AEHM macroscopic problem for SMAHCs will be reformulated using TFA in order to simplify the analysis, when possible.

In section 4.3 we present some results, while in section 4.4 we draw some conclusions.

4.2 Methods

4.2.1 The Brinson 1-D constitutive model for SMA

Many different one-dimensional constitutive models have been developed for the SMA.

The one-dimensional constitutive model was developed by Brinson to characterize the mechanical behavior of the SMA. This model was initially developed by Brinson [33] and Brinson and Lammering [36] and later simplified by Brinson and Huang [35]. The model of Brinson will be summarized in this section.

The Brinson model belongs to those macroscopic constitutive models which have been developed within the theory of irreversible thermodynamics in a small deformations regime and are called rate-independent. It is assumed that the behavior of the material is a function of stress, strain and temperature, and their corresponding rates of change. The behavior of the material is a non-linear function of these three variables, which are interdependent. The control variables are the stress and the temperature, and the internal variable is the Martensite volume fraction. In this way, the constitutive equation that relates stress, strain, temperature and Martensite volume fraction is obtained.

This model has been extensively used in literature and has been proven to be superior [195, 262, 66, 188] to other one-dimensional models developed by various authors.

The following local forms of the first [140, p. 230] and second law [140, p. 255] of thermodynamics hold at each point of the original configuration C_0

$$\begin{cases} \rho_0 \dfrac{\mathrm{d}u}{\mathrm{d}t} - \boldsymbol{\sigma} : \dot{\boldsymbol{\epsilon}} - \rho_0 r + \nabla_0 \cdot \boldsymbol{F}^{-1} \cdot \boldsymbol{q} = 0 \\ \rho_0 \dfrac{\mathrm{d}s}{\mathrm{d}t} - \rho_0 r T^{-1} + T^{-1} \nabla_0 \cdot \boldsymbol{F}^{-1} \cdot \boldsymbol{q} - T^{-2} \boldsymbol{F}^{-1} \cdot \boldsymbol{q} \cdot \nabla_0 T \geq 0 \end{cases} \tag{4.1}$$

where : operator is the *scalar product* or the *double contracted product* or the *double dot product* of two second-order tensors:

$$A : B = \sum_{i=1}^{3} \sum_{J=1}^{3} A_{ij} B_{ji} \tag{4.2}$$

and $\nabla_0 \cdot$ is the *divergence* operator in the original configuration. $\boldsymbol{\sigma}$ is the *second Piola-Kirchhoff stress* tensor, $\boldsymbol{\epsilon}$ is the *Green-Lagrange strain* tensor, T is the temperature, s is the entropy, r is the heat generated by internal heat sources, $\boldsymbol{q}$ is the heat transferred from the surroundings, $\boldsymbol{F}$ is the *deformation gradient tensor* and u is the internal energy.

The constitutive theory for the SMA is formulated using the *Helmholtz free energy* g, which is related to the entropy s and the internal energy u as follows [140, p. 262]

$$g = u - sT \tag{4.3}$$

In order to express the entropy inequality in terms of the Helmholtz energy, the the last equation is differentiated with respect to time

$$\frac{\mathrm{d}g}{\mathrm{d}t} = \frac{\mathrm{d}u}{\mathrm{d}t} - \frac{\mathrm{d}s}{\mathrm{d}t} T - s \frac{\mathrm{d}T}{\mathrm{d}t} \tag{4.4}$$

and combined with equations (4.1) to obtain

$$\rho_0 \frac{\mathrm{d}g}{\mathrm{d}t} + \boldsymbol{\sigma} : \frac{\mathrm{d}\boldsymbol{\epsilon}}{\mathrm{d}t} + \rho_0 s \frac{\mathrm{d}T}{\mathrm{d}t} + \frac{1}{T} \boldsymbol{F}^{-1} \cdot \boldsymbol{q} \nabla T \geq 0 \tag{4.5}$$

Now the general state variable Λ is defined as

$$\Lambda \equiv (\boldsymbol{\epsilon}, T, \xi) \tag{4.6}$$

and

$$g = g(\Lambda) = g(\boldsymbol{\epsilon}, T, \xi) \tag{4.7}$$

$$\boldsymbol{\sigma} = \boldsymbol{\sigma}(\Lambda) = \boldsymbol{\sigma}(\boldsymbol{\epsilon}, T, \xi) \tag{4.8}$$

$$s = s(\Lambda) = s(\boldsymbol{\epsilon}, T, \xi) \tag{4.9}$$

$$\boldsymbol{q} = \boldsymbol{q}(\Lambda) = \boldsymbol{q}(\boldsymbol{\epsilon}, T, \xi) \tag{4.10}$$

where the independent state variables are the Green-Lagrange strain tensor $\boldsymbol{\epsilon}$, temperature T and the *total volume fraction of Martensite* ξ, which is an internal variable introduced to describe the phase transformation involved in the mechanical behavior of the SMAs.

A basic assumption of continuum mechanics is that every process related through equations (4.7)-(4.10) must satisfy the entropy inequality (4.5). The total derivative of g is

$$\frac{\mathrm{d}g}{\mathrm{d}t} = \frac{\partial g}{\partial \boldsymbol{\epsilon}}\frac{\mathrm{d}\boldsymbol{\epsilon}}{\mathrm{d}t} + \frac{\partial g}{\partial T}\frac{\mathrm{d}T}{\mathrm{d}t} + \frac{\partial g}{\partial \xi}\frac{\mathrm{d}\xi}{\mathrm{d}t} \tag{4.11}$$

and substituting into (4.5) yields

$$\left(\frac{1}{\rho_0}\boldsymbol{\sigma} - \frac{\partial g}{\partial \boldsymbol{\epsilon}}\right) : \frac{\mathrm{d}\boldsymbol{\epsilon}}{\mathrm{d}t} - \left(s + \frac{\partial g}{\partial T}\right)\frac{\mathrm{d}T}{\mathrm{d}t} - \frac{\mathrm{d}\xi}{\mathrm{d}t}\frac{\partial g}{\partial \xi} - \frac{1}{T\rho_0}\boldsymbol{F}^{-1} \cdot \boldsymbol{q}\nabla T \geq 0 \tag{4.12}$$

As a sufficient condition for (4.12) to hold for every choice of $d\boldsymbol{\epsilon}/dt$ and dT/dt, their coefficients must vanish

$$\boldsymbol{\sigma} = \rho_0 \frac{\partial g}{\partial \boldsymbol{\epsilon}} = \boldsymbol{\sigma}(\Lambda) = \boldsymbol{\sigma}(\boldsymbol{\epsilon}, T, \xi) \tag{4.13}$$

$$s = -\frac{\partial g}{\partial T} \tag{4.14}$$

Equation (4.13) is the mechanical constitutive equation of the shape memory alloy material.

As the Brinson model is only a one-dimensional model, from now on the scalar notation will be used for second Piola-Kirchoff stress σ and Green-Lagrange strain ϵ.

Computing the derivative of equation (4.13) with respect to time we have

$$\begin{aligned} \frac{d\sigma}{dt} &= \frac{d\sigma}{d\epsilon}\frac{d\epsilon}{dt} + \frac{d\sigma}{d\xi}\frac{d\xi}{dt} + \frac{d\sigma}{dT}\frac{dT}{dt} \\ \frac{d\sigma}{dt} &= E(\epsilon, T, \xi)\frac{d\epsilon}{dt} + \Omega(\epsilon, T, \xi)\frac{d\xi}{dt} + \Theta(\epsilon, T, \xi)\frac{dT}{dt} \end{aligned} \tag{4.15}$$

where E is the elastic modulus, Ω is the transformation tensor and Θ is the thermo-elastic tensor are

$$E\left(\epsilon, T, \xi\right) = \rho_0 \tfrac{\partial^2 g}{\partial \epsilon^2}; \quad \Omega\left(\epsilon, T, \xi\right) = \rho_0 \tfrac{\partial^2 g}{\partial \epsilon \partial \xi}; \quad \Theta\left(\epsilon, T, \xi\right) = \rho_0 \tfrac{\partial^2 g}{\partial \epsilon \partial T}$$

The model of Brinson separates the total volume fraction of Martensite in two different contributions. The first contribution ξ_M, called *multi-variant martensite faction*, is the part of Martensite induced only by changes in temperature. The second contribution ξ_S, called *single variant martensitic fraction*, is the part of Martensite induced only by changes in stress. The total volume fraction of Martensite is

$$\xi = \xi_S + \xi_M \tag{4.16}$$

With the separation introduced by Brinson, any phase transformation which starts from a phase of 100% Austenite, will produce single variant Martensite (ξ_S) only via variation of stress. If we start from a mixed phase of Austenite and single variant Martensite, then ξ_M will represent the fraction of Martensite only via variation of stress and ξ_S will increase only if the stress applied is sufficient to induce a phase transformation.

Equation (4.15) in virtue of equation (4.16) becomes

$$\frac{d\sigma}{dt} = E\left(\epsilon, T, \xi_S, \xi_M\right)\frac{d\epsilon}{dt} + \Omega_S\left(\epsilon, T, \xi_S, \xi_M\right)\frac{d\xi_S}{dt} + \Omega_M\left(\epsilon, T, \xi_S, \xi_M\right)\frac{d\xi_M}{dt} + \Theta\left(\epsilon, T, \xi_S, \xi_M\right)\frac{dT}{dt}$$

The constitutive equation used in the Brinson model is the following

$$\sigma = E\left(\xi\right)\epsilon + \Omega\left(\xi\right)\xi_S + \Theta\left(T - T_0\right) \tag{4.17}$$

In equation (4.17) T_0 is the *reference temperature* and the transformation tensor is expressed as

$$\Omega\left(\xi\right) = -E\left(\xi\right)\epsilon_L \tag{4.18}$$

where ϵ_L is the *maximal recoverable strain.*

For the relation between the elastic modulus and the total Martensite fraction we use the *Voigt approximation* which considers the material composed by austenitic and martensitic fibers parallel to the external force being applied. In this case the strain on the two phases is identical, and the following equations are valid

$$\begin{aligned}
\epsilon &= \epsilon_M = \epsilon_A \\
\sigma &= \sigma_M \xi + \sigma_A\left(1 - \xi\right) \\
E\epsilon &= \epsilon_M E_M \xi + \epsilon_A E_A\left(1 - \xi\right) \\
E &= E_M \xi + E_A\left(1 - \xi\right) = E_A - \xi\left(E_A - E_M\right)
\end{aligned} \tag{4.19}$$

Another alternative method that can be used is the *Reuss approximation* which will not be discussed here (see e. g. [66]).

Several *laws of evolution* exist for the internal variable in function of the control variables (see figure 4-1).

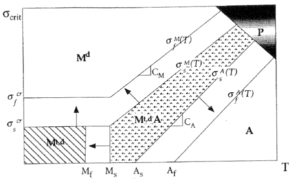

Figure 4-1: The stress-temperature phase diagram for SMA [35, p.109]

These models assumes that tension, temperature and volumetric faction of Martensite (ξ) are related by a state equation $\xi = \xi(\sigma, T)$. This equation can not be directly integrated in closed form because it depends on the actual value of ξ which depends on the integration path in the state space.

The Brinson model has three different evolution laws.

Direct phase transformation to single-variant Martensite ($T > M_s$)

$$\xi_S = \frac{1-\xi_{S0}}{2}\cos\left\{\frac{\pi}{\sigma_s^{CR}-\sigma_f^{CR}}\left[\sigma-\sigma_f^{CR}-C_M\left(T-M_s\right)\right]\right\}+\frac{1+\xi_{S0}}{2} \tag{4.20}$$

$$\xi_M = \xi_{M0}-\frac{\xi_{M0}}{1-\xi_{S0}}\left(\xi_S-\xi_{S0}\right) \tag{4.21}$$

Validity range:

$$T > M_s \quad \text{and} \quad \sigma_s^{CR}+C_M\left(T-M_s\right) < \sigma < \sigma_f^{CR}+C_M\left(T-M_s\right)$$

Direct phase transformation to single-variant Martensite ($T < M_s$)

$$\xi_S = \frac{1-\xi_{S0}}{2}\cos\left\{\frac{\pi}{\sigma_s^{CR}-\sigma_f^{CR}}\left[\sigma-\sigma_f^{CR}\right]\right\}+\frac{1+\xi_{S0}}{2} \tag{4.22}$$

$$\xi_M = \xi_{M0}-\frac{\xi_{M0}}{1-\xi_{S0}}\left(\xi_S-\xi_{S0}\right)+\Delta_{T\xi} \tag{4.23}$$

where

$$\begin{cases}\text{If } M_s < T < M_s \text{ and } T < T_0\text{:} & \Delta_{T\xi} = \frac{1-\xi_{M0}}{2}\left\{\cos\left[a_{ML}\left(T-M_f\right)\right]+1\right\}\\ \text{else:} & \Delta_{T\xi} = 0\end{cases} \tag{4.24}$$

Validity range:

$$T < M_s \quad \text{and} \quad \sigma_s^{CR} < \sigma < \sigma_f^{CR}$$

Reverse phase transformation of single-variant Martensite into Austenite

$$\xi = \frac{\xi_0}{2}\left\{\cos\left[a_{AL}\left(T - A_s - \frac{\sigma}{C_A}\right)\right] + 1\right\} \tag{4.25}$$

$$\xi_S = \xi_{S0} - \frac{\xi_{S0}}{\xi_0}\left(\xi_0 - \xi\right) \tag{4.26}$$

$$\xi_M = \xi_{M0} - \frac{\xi_{M0}}{\xi_0}\left(\xi_0 - \xi\right) \tag{4.27}$$

And substituting equation (4.25) in equations (4.26) and (4.27)

$$\xi_S = \frac{\xi_{S0}}{2}\left\{\cos\left[a_{AL}\left(T - A_s - \frac{\sigma}{C_A}\right)\right] + 1\right\} \tag{4.28}$$

$$\xi_M = \frac{\xi_{M0}}{2}\left\{\cos\left[a_{AL}\left(T - A_s - \frac{\sigma}{C_A}\right)\right] + 1\right\} \tag{4.29}$$

Validity range:

$$T > A_s \quad \text{and} \quad C_A\left(T - A_f\right) < \sigma < C_A\left(T - A_s\right)$$

The constants a_{AL} and a_{ML} in equations (4.22) to (4.29) are defined as follows

$$a_{AL} = \tfrac{\pi}{A_f - A_s} \quad a_{ML} = \tfrac{\pi}{M_s - M_f} \tag{4.30}$$

In all the above equations the subscript 0 refers to the *initial conditions*.
The Brinson model requires the experimental determination of 12 parameters:

1. Young's modulus for Austenite E_A;
2. Young's modulus for Martensite E_M;
3. Martensite finish temperature M_f;
4. Martensite start temperature M_s;
5. Austenite start temperature A_s
6. Austenite finish temperature A_f;
7. Thermo-elastic tensor Θ;
8. Maximal recoverable strain ϵ_L;

9. Stress influence coefficient C_M;
10. Stress influence coefficient C_A;
11. Critical stress at the start for transforming twinned Martensite in detwinned Martensite σ_s^{CR};
12. Critical stress at the finish for transforming twinned Martensite in detwinned Martensite σ_f^{CR}.

As proposed by various authors (e. g. [51] and [91]), Brinsons constitutive model should be extended to properly account for the loading paths through the overlapping transformation regions $[o, t]$ in the phase diagram of the original model (see figure 4-2).

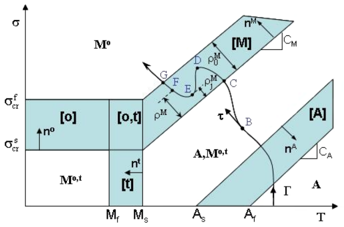

Figure 4-2: One-dimensional phase diagram of SMA where the overlapping transformation region $[o, t]$ is emphasized [91]

Appendix C covers the numerical implementation of this model.

4.2.2 The Sadjadpour and Bhattacharya 3-D constitutive model for SMA

The three-dimensional constitutive model for shape-memory alloys of Sadjadpour and Bhattacharya [212] generalizes the one-dimensional model presented earlier by the same authors [27]. The model of Sadjadpour and Bhattacharya will be summarized in this section.

This model assumes that the Helmholtz free energy density depends on the strain, the temperature and the internal variables

$$g = g\left(\epsilon, \lambda, \epsilon_m, \epsilon_p, T\right) \tag{4.31}$$

where ϵ is the linear strain, λ is the martenstic volume fraction, ϵ_m is the *effective transformation strain*, ϵ_m is the *plastic strain* and T is the temperature.

Neglecting the effects of plasticity, the constitutive equations are

$$\sigma = C\left(\epsilon - \lambda\epsilon_m\right) \tag{4.32}$$

$$d_\lambda = \sigma \colon \epsilon_m - \omega \tag{4.33}$$

$$d_{\epsilon_m} = \lambda\sigma \tag{4.34}$$

where σ is the second Piola-Kirchoff stress tensor, C is the fourth-order stiffness tensor or the elasticity tensor, d_λ, d_{ϵ_m} are the driving forces associated with the rates of change of their conjugate internal variables, λ and ϵ_m, respectively, and ω is the difference in chemical energy between the Austenite and the Martensite.

In terms of Young's modulus E and Poisson's ratio ν (which are assumed to be equal in both the Austenite and the Martensite), Hooke's law for isotropic materials can then be expressed as

$$\epsilon = \frac{1}{E}\sigma - \frac{\nu}{E}\left[\operatorname{tr}(\sigma) I - \sigma\right] \tag{4.35}$$

where tr is the *trace operator* of a second-order tensor:

$$\operatorname{tr}(A) = \sum_{i=1}^{3} a_{ii} \tag{4.36}$$

and I is the second-order *identity tensor.*

Note that the effective transformation strain of the RVE is $\lambda\epsilon_m$ since λ is is the volume fraction of Martensite, ϵ_m is the effective transformation strain of the Martensite and the transformation strain of the Austenite is 0 by choice of reference configuration.

It is assumed [212] that

$$\omega(T) = \frac{\mathcal{L}}{T_{cr}}\left(T - T_{cr}\right) \tag{4.37}$$

where $\mathcal{L}$ is the latent heat of transformation and T_{cr} is the thermodynamic transformation temperature.

The kinetic relation describing the evolution of the martensitic volume fraction λ is taken to be the following

$$\dot{\lambda} = \begin{cases} \dot{\lambda}^{+}\left(1 + \left(d_\lambda - d_\lambda^{+}\right)^{-1}\right)^{-\frac{1}{P}} & d_\lambda > d_\lambda^{+} \text{and} \lambda < 1 \\ \dot{\lambda}^{-}\left(1 + \left(d_\lambda^{-} - d_\lambda\right)^{-1}\right)^{-\frac{1}{P}} & d_\lambda < d_\lambda^{-} \text{and} \lambda > 0 \\ 0 & \textit{otherwise.} \end{cases} \tag{4.38}$$

where $\dot{\lambda}^{\pm}$, $d_\lambda^{\pm}$, p are material parameters.

Note that this law has a stick-slip feature (i.e. it needs a critical driving force before evolution begins and the evolution proceeds in an effectively rate-independent manner) at small rates, but becomes rate-independent at high rates.

The effective transformation strain is the average transformation strain of the different martensitic variants averaged over a representative volume element (RVE) after the material has formed a compatible microstructure [26]. The evolution of the effective transformation strain ϵ_m describes the processes, such as e. g. twinning and detwinning, that convert one martensitic variant to another. Not any arbitrary mixture of martensitic variants can be formed, but ϵ_m is restricted to those average values that are obtained from compatible arrangements.

In summary, the consequences of the microstructure at a material point is specified by two internal variables λ and ϵ_m, which are subject to the following constraints

$$\lambda \in [0,1] \quad \text{and} \quad \epsilon_m \in P = \left[\epsilon_m^c, \epsilon_m^t\right] \tag{4.39}$$

where $\epsilon_m^c < 0$ denotes the largest recoverable compressive strain and $\epsilon_m^t > 0$ denotes the largest recoverable tensile strain.

The set of all possible values of ϵ_m is denoted as the set of effective transformation strains or the set of effective recoverable strains, P . This set P depends on the crystallography of the material and the texture of the specimen.

$$P = \{\epsilon_m | \mathrm{tr}\,(\epsilon_m) = 0, g\,(\epsilon_m) \leq 0\} \tag{4.40}$$

The transformation strain function, $g\,(\epsilon_m)$ can be defined by three principal values of the transformation strain ϵ_m, or its three invariants $I_1\,(\epsilon_m)$, $I_2\,(\epsilon_m)$ and $I_3\,(\epsilon_m)$. Self-accommodation sets the transformation strain ϵ_m to be trace-free [25], which forces $I_1\,(\epsilon_m)$ to vanish, so that the set depends only on the second and third invariants.

$$g\,(\epsilon_m) = (-I_2\,(\epsilon_m))^{\frac{3}{2}} - aI_3\,(\epsilon_m) - b - c\,(\hat{e} \cdot \epsilon_m \hat{e})^3 \tag{4.41}$$

where

$$\begin{aligned} I_2\,(\epsilon_m) &= -\frac{1}{2}\mathrm{tr}\,(\epsilon_m \epsilon_m) \\ I_3\,(\epsilon_m) &= \det\,(\epsilon_m) \end{aligned}$$

where $\hat{e}$ is the *fiber texture vector* or *special direction vector* of the texture.

Shape-memory alloys are often made as wires and tubes by drawing, and as sheets by rolling. These manufacturing processes confer to the material a crystallographic texture: i. e. the grains of the polycrystalline specimen are no longer randomly oriented but show a preferential distribution. It is common to have an uniaxial texture where one crystallographic axis is preferentially oriented along the drawing or rolling direction. So this direction is *special* while all other directions normal to it are equivalent.

The set of transformation strains P is described by three parameters a, b and c. The parameter b scales the set, while parameters a and c describe the asymmetry and anisotropy of the set. The value $a = 0$ corresponds to tension-compression symmetry, and both sets are ellipses. Positive values of a allows large tensile transformation strain, and thus requires smaller tensile stress for transformation. Negative values of a reverse this behavior. The parameter b simply rescales the set of effective transformation strains, and thus also the transformation yield surface. The case $c = 0$ corresponds to the isotropic situation.

The growth rule for the transformation strain is

$$\dot{\epsilon}_m = \begin{cases} \alpha\sigma' & g\left(\epsilon_m\right) < 0 \\ \alpha\left(\sigma' - \sigma' : \frac{\partial g}{\partial \epsilon_m} \frac{\frac{\partial g}{\partial \epsilon_m}}{\left|\frac{\partial g}{\partial \epsilon_m}\right|^2}\right) & g\left(\epsilon_m\right) = 0 \\ 0 & otherwise. \end{cases} \tag{4.42}$$

where σ' is the *deviatoric stress tensor*

$$\sigma' = \sigma - \frac{1}{3}\mathrm{tr}\left(\sigma\right) I$$

and

$$\frac{\partial g}{\partial \epsilon_m} = \frac{3|\epsilon_m|}{\sqrt{8}}\epsilon_m - a\mathrm{cof}\left(\epsilon_m\right)^T - 3c\left(\hat{e}\cdot\hat{e}\right)\left(\hat{e}\cdot\epsilon_m\hat{e}\right)^2 \tag{4.43}$$

where cof is the *cofactor operator* of a second-order tensor. The deviatoric stress tensor can often be seen as difference between the stress and a *mean stress* σ_m, where the latter is often called the *hydrostatic stress* [71].

$$\sigma' = \begin{bmatrix} \sigma_{11} - \sigma_m & \sigma_{12} & \sigma_{13} \\ \sigma_{21} & \sigma_{22} - \sigma_m & \sigma_{23} \\ \sigma_{31} & \sigma_{32} & \sigma_{33} - \sigma_m \end{bmatrix}$$

$$\sigma_m = \frac{\sigma_{11} + \sigma_{22} + \sigma_{33}}{3}$$

Moreover, for adiabatic conditions the following expression can be used

$$T\left(t\right) = T_0 \exp\left(\frac{\left(\lambda\left(t\right) - \lambda_0\right)\mathcal{L}}{c_p T_{cr}}\right) \tag{4.44}$$

where c_p is is the *heat capacity* (assumed to be equal in both the Austenite and the Martensite).

4.2.3 Finite element modeling of shape memory alloy materials

The implementation of nonlinear finite element methods (FEM) for shape memory alloys may be *displacement based* or *force based*. Here the displacement based approach will be considered. For force based finite element models of shape memory alloy materials refer e. g. to [247].

Under small deformation assumption, the strain-displacement relationship is

$$\boldsymbol{\epsilon}\left(\boldsymbol{u}\right) = \frac{1}{2}\left(\nabla\boldsymbol{u} + \nabla\boldsymbol{u}^T\right) \tag{4.45}$$

The generic shape memory alloy constitutive equation can be written as follows

$$\boldsymbol{\sigma} = \boldsymbol{C}\left(\boldsymbol{\epsilon} - \boldsymbol{\epsilon}^{in}\right) \tag{4.46}$$

The *Boundary Value Problem* (BVP) to be solved may be stated as

$$\begin{cases} \nabla \cdot \boldsymbol{\sigma}(\boldsymbol{u}) = -\boldsymbol{f}, & \text{in } \Omega, \\ \boldsymbol{u} = \boldsymbol{u}_D, & \text{in } \partial_1\Omega, \\ \boldsymbol{\sigma} \cdot \boldsymbol{n} = \boldsymbol{g}, & \text{in } \partial_2\Omega. \end{cases} \tag{4.47}$$

The variational formulation of the BVP (4.47) can be written in the following terms

$$\text{Find } \boldsymbol{u} \in V^D \text{ such that: } \int_\Omega \boldsymbol{\epsilon}(\boldsymbol{u}) : \boldsymbol{C}\boldsymbol{\epsilon}(\boldsymbol{v})\, dp = \int_\Omega \boldsymbol{f} \cdot \boldsymbol{v} dp + \int_{\partial_2\Omega} \boldsymbol{g} \cdot \boldsymbol{v} ds, \quad \forall \boldsymbol{v} \in V \tag{4.48}$$

The discrete version of equation (4.48) is

$$\text{Find } \boldsymbol{u}_h \in V_h^D \text{ such that: } \int_\Omega \boldsymbol{\epsilon}(\boldsymbol{u}_h) : \boldsymbol{C}\boldsymbol{\epsilon}(\boldsymbol{v}_h)\, dp = \int_\Omega \boldsymbol{f} \cdot \boldsymbol{v}_h dp, \quad \forall \boldsymbol{v}_h \in V_h \tag{4.49}$$

where spaces V and V^D are replaced by their discrete approximations V_h and V_h^D.

If $\{\phi_j\}$ is the system of piecewise global basis functions of V_h, then the nonlinear finite element analysis of the shape memory alloy material for the static case is reduced to the following first order nonlinear system of ordinary differential equations (ODEs) [199]

$$\boldsymbol{K}(\boldsymbol{U})\boldsymbol{U} = \boldsymbol{F}(\boldsymbol{U}) \tag{4.50}$$

where

$$\begin{aligned} K_{ij}(\boldsymbol{U}) &= \int_{\Omega^e} \boldsymbol{\epsilon}(\phi_i(\boldsymbol{p})) : \boldsymbol{C}\boldsymbol{\epsilon}(\phi_j(\boldsymbol{p}))\, \mathrm{d}\boldsymbol{p} \\ F_i(\boldsymbol{U}) &= \int_{\Omega^e} \boldsymbol{C}\boldsymbol{\epsilon}^{in} \cdot \boldsymbol{\epsilon}(\phi_i(\boldsymbol{p}))\, \mathrm{d}\boldsymbol{p} \end{aligned}$$

and $\boldsymbol{K}$ is the *stiffness matrix*, $\boldsymbol{F}$ is the *force vector* and $\boldsymbol{U} = \{U_1, \ldots U_N\}^T$ is the column vector *of nodal displacements*, and N is the total number of nodes in the problem under analysis (i. e. $N-1$ elements).

The nonlinear problem (4.50) is solved using the iterative Newton-Raphson method by linearizing the right hand side

$$F_i(\boldsymbol{U} + \Delta\boldsymbol{U}) \cong F_i(\boldsymbol{U}) + \sum_{j=1}^{N} \frac{\partial \boldsymbol{F}_i(\boldsymbol{U})}{\partial U_j} \Delta U_j$$

Defining the $k+1$ iteration of the Newton-Raphson formula as follows

$$\boldsymbol{U}^{(k+1)} = \boldsymbol{U}^{(k)} + \boldsymbol{L}^{-1}\left(\boldsymbol{U}^{(k)}\right)\boldsymbol{F}_h\left(\boldsymbol{U}^{(k)}\right)$$

where $\boldsymbol{L}$ is the Jacobian

$$\boldsymbol{L}\left(\boldsymbol{U}^{(k)}\right) := \frac{\partial \boldsymbol{F}_h\left(\boldsymbol{U}^{(k)}\right)}{\partial \boldsymbol{U}}$$

The nonlinear displacement based FEM provides strain increments $\Delta\boldsymbol{\epsilon}$.

Approaches based on return-mapping algorithms similar to those in classical elasto-plasticity [178, 225] are normally adapted to handle the shape memory alloy constitutive equations, so that for a given strain increment $\Delta\boldsymbol{\epsilon}$ and temperature increment ΔT the corresponding stress $\boldsymbol{\sigma}$ is computed from the constitutive equation (e. g. using equation (4.32)).

An increment in strain $\boldsymbol{\epsilon}$ causes increments in both stress $\boldsymbol{\sigma}$ and temperature T as can be seen from the total derivative of stress with respect to strain

$$\frac{\mathrm{d}\boldsymbol{\sigma}}{\mathrm{d}\boldsymbol{\epsilon}} = \frac{\partial \boldsymbol{\sigma}}{\partial \boldsymbol{\epsilon}} + \frac{\partial \boldsymbol{\sigma}}{\partial T}\frac{\partial T}{\partial \boldsymbol{\epsilon}}$$

Appropriate *algorithmic or consistent tangent moduli* have to be computed in order to use iterative procedures such as the Newton-Raphson method to solve the nonlinear system of algebraic equations that arise from the FEM discretization.

Such an implementation utilizes the following incremental form of the SMA constitutive model

$$\mathrm{d}\boldsymbol{\sigma} = \mathsf{L} : \mathrm{d}\boldsymbol{\epsilon} + \Theta \mathrm{d}T \tag{4.51}$$

where L is the *tangent stiffness tensor* and Θ is the *tangent thermal tensor*. The tangent stiffness is a fourth-order tensor while the thermal tangent is a second-order tensor.

Each loading step $(n+1)$ is defined by specifying the values of strain ϵ_{n+1} and temperature T_{n+1}, thus the constitutive equation can be seen as a function of only these variables

$$\boldsymbol{\sigma}_{n+1} = \boldsymbol{\sigma}_{n+1}\left(\boldsymbol{\epsilon}_{n+1}, T_{n+1}\right)$$

The tangent stiffness moduli and tangent thermal moduli are defined as

$$\mathsf{L} := \frac{\partial \boldsymbol{\sigma}_{n+1}\left(\boldsymbol{\epsilon}_{n+1}, T_{n+1}\right)}{\partial \boldsymbol{\epsilon}_{n+1}} \tag{4.52}$$

$$\Theta := \frac{\partial \boldsymbol{\sigma}_{n+1}\left(\boldsymbol{\epsilon}_{n+1}, T_{n+1}\right)}{\partial T_{n+1}} \tag{4.53}$$

Analytical expressions or numerical approximations of the partial derivatives allow to compute equation (4.51).

The Jacobian may be linked to the algorithmic tangent moduli L as follows (e. g.

[193])

$$
\begin{aligned}
\frac{\partial \boldsymbol{F}_h\left(\boldsymbol{U}^{(k)}\right)}{\partial \boldsymbol{U}} &= \int_{\Omega^e} \frac{\partial \boldsymbol{\sigma}\left(\boldsymbol{\epsilon}\left(\boldsymbol{u}_h\right)\right)}{\partial \boldsymbol{U}} : \boldsymbol{\epsilon}\left(\boldsymbol{v}_h\right) \mathrm{d}\boldsymbol{p} \\
&= \int_{\Omega^e} \left(\frac{\partial \boldsymbol{\sigma}\left(\boldsymbol{\epsilon}\left(\boldsymbol{u}_h\right)\right)}{\partial \boldsymbol{\epsilon}\left(\boldsymbol{u}_h\right)} : \frac{\partial \boldsymbol{\epsilon}\left(\boldsymbol{u}_h\right)}{\partial \boldsymbol{U}}\right) : \boldsymbol{\epsilon}\left(\boldsymbol{v}_h\right) \mathrm{d}\boldsymbol{p} \\
&= \int_{\Omega^e} \left(\mathsf{L}\left(\boldsymbol{u}_h\right) : \frac{\partial \boldsymbol{\epsilon}\left(\boldsymbol{u}_h\right)}{\partial \boldsymbol{U}}\right) : \boldsymbol{\epsilon}\left(\boldsymbol{v}_h\right) \mathrm{d}\boldsymbol{p}
\end{aligned}
$$

where

$$
\boldsymbol{L}\left(\boldsymbol{u}_h\right) := \frac{\partial \boldsymbol{\sigma}\left(\boldsymbol{\epsilon}\left(\boldsymbol{u}_h\right)\right)}{\partial \boldsymbol{\epsilon}\left(\boldsymbol{u}_h\right)}
$$

Moreover, as

$$
\frac{\partial \boldsymbol{\epsilon}\left(\boldsymbol{u}_h\right)}{\partial \boldsymbol{U}} = \frac{\partial \boldsymbol{\epsilon}\left(\boldsymbol{U} \cdot \boldsymbol{\phi}\left(\boldsymbol{p}\right)\right)}{\partial \boldsymbol{U}} = \frac{\partial \boldsymbol{U} \cdot \boldsymbol{\epsilon}\left(\boldsymbol{\phi}\left(\boldsymbol{p}\right)\right)}{\partial \boldsymbol{U}} = \boldsymbol{\epsilon}\left(\boldsymbol{\phi}\left(\boldsymbol{p}\right)\right)
$$

then

$$
L_{ij} = \int_{\Omega^e} \boldsymbol{\epsilon}\left(\phi_i\left(\boldsymbol{p}\right)\right) : \mathsf{L}\left(\boldsymbol{U} \cdot \boldsymbol{\phi}\left(\boldsymbol{p}\right)\right) : \boldsymbol{\epsilon}\left(\phi_j\left(\boldsymbol{p}\right)\right) \mathrm{d}\boldsymbol{p} \tag{4.54}
$$

Note that, because of the nonlinear dependence of the stiffness on the displacement, the most time-consuming parts of the FEM procedure are the assembly of the tangent stiffness matrix and the assembly of the force vector at each Newton iteration. These operations require the execution once for each element at each Newton iteration of the stress update procedure via the return-mapping algorithm, which is a computationally expensive operation. When the Reduced Newton-Raphson Method [199] is applied then the update procedure can be limited, in the best case, to each Newton step.

Finally note that computer implementations of finite elements resort to the Voigt notation [21, 71], which consists in expressing the second-order stress $\boldsymbol{\sigma}$ and strain $\boldsymbol{\epsilon}$ tensors as one-dimensional arrays and the fourth-order stiffness tensor $\boldsymbol{C}$ as a two-dimensional array.

$$
\boldsymbol{\sigma} = \begin{bmatrix} \sigma_{xx} & \sigma_{xy} & \sigma_{xz} \\ \sigma_{xy} & \sigma_{yy} & \sigma_{yz} \\ \sigma_{xz} & \sigma_{yz} & \sigma_{zz} \end{bmatrix} \longrightarrow \boldsymbol{\sigma} = \begin{Bmatrix} \sigma_{xx} \\ \sigma_{yy} \\ \sigma_{zz} \\ \sigma_{yz} = \tau_{yz} \\ \sigma_{zx} = \tau_{zx} \\ \sigma_{xy} = \tau_{xy} \end{Bmatrix},
$$

$$\boldsymbol{\epsilon} = \begin{bmatrix} \epsilon_{xx} & \epsilon_{xy} & \epsilon_{xz} \\ \epsilon_{xy} & \epsilon_{yy} & \epsilon_{yz} \\ \epsilon_{xz} & \epsilon_{yz} & \epsilon_{zz} \end{bmatrix} \longrightarrow \boldsymbol{\epsilon} = \begin{Bmatrix} \epsilon_{xx} \\ \epsilon_{yy} \\ \epsilon_{zz} \\ 2\epsilon_{yz} = \gamma_{yz} \\ 2\epsilon_{zx} = \gamma_{zx} \\ 2\epsilon_{xy} = \gamma_{xy} \end{Bmatrix} .$$

In the Voigt notation, the shear strain components are stored as *engineering shears*, which are twice the corresponding tensor shears, and care must be taken when carrying out calculations involving stress and strain using the Voigt notation. Often the Reuter matrix $\boldsymbol{R}$ must be employed to appropriately scale the values of stress and strain (e. g. see equation (3.16)).

$$\boldsymbol{R} = \begin{bmatrix} 1 & 1 & 1 & 1 & 1 & 1 \\ 1 & 1 & 1 & 1 & 1 & 1 \\ 1 & 1 & 1 & 1 & 1 & 1 \\ 1 & 1 & 1 & 2 & 1 & 1 \\ 1 & 1 & 1 & 1 & 2 & 1 \\ 1 & 1 & 1 & 1 & 1 & 2 \end{bmatrix}$$

4.2.4 An AEHM approach to constitutive modeling of SMAHCs

In this section a multiscale approach based on the AEHM will be developed for modeling the constitutive behavior of shape memory alloy hybrid composites.

The Bounday Value Problem (BVP) for small displacements may be witten as follows

$$\frac{\partial \sigma_{ij}}{\partial x_j} + f_i = 0 \text{ , in } \Omega, \tag{4.55}$$

$$\epsilon_{ij}(\boldsymbol{u}) = \frac{1}{2}\left(\frac{\partial u_i}{\partial x_j} + \frac{\partial u_j}{\partial x_i}\right), \tag{4.56}$$

$$\sigma_{ij}(\boldsymbol{u}) = C_{ijkl}\left[\epsilon_{kl}(\boldsymbol{u}) - \epsilon_{kl}^{in}\right], \tag{4.57}$$

$$u_i = 0 \text{ , on } \partial_1\Omega, \tag{4.58}$$

$$\sigma_{ij} n_j = F_i \text{ , on } \partial_2\Omega, \tag{4.59}$$

where (4.55) are the *equilibrium equations*, (4.56) are *strain-displacement relationships*, (4.57) are the *constitutive equations*, (4.58) and (4.59) are the *displacement boundary conditions.* For the development of the AEHM for large displacments refer e. g. to [236].

The elastic constants C_{ijkl} and inelastic strains ϵ_{ij}^{in} (i. e. the eigenstrains) must satisfy the following relationships

$$
\begin{aligned}
C_{ijkl} &= C_{jikl} = C_{ijlk} = C_{klij}, \\
\epsilon^{in}_{ij} &= \epsilon^{in}_{ji}.
\end{aligned}
$$

Recall from chapter 3 that the AEHM assumes that the macro scale $\boldsymbol{x}$ and meso scale $\boldsymbol{y}$ are then related through the *scale parameter* [55] ϵ, which is the ratio between the two length scales being considered:

$$\boldsymbol{x} = \frac{\boldsymbol{y}}{\epsilon} \tag{4.60}$$

and the material properties are periodic in the RVE Y

$$C^{\epsilon}_{ijkl}\left(\boldsymbol{x}\right) = C_{ijkl}\left(\frac{\boldsymbol{x}}{\epsilon}\right) \tag{4.61}$$

Thus the fundamental assumption is that the multiple scales exist only in the spatial variables and no such scaling exists for the time variable [246].

Equations (4.55) to (4.59) can be rewritten as

$$\frac{\partial \sigma^{\epsilon}_{ij}}{\partial x^{\epsilon}_{j}} + f_i = 0 \text{ , in } \Omega, \tag{4.62}$$

$$\epsilon^{\epsilon}_{ij}\left(\boldsymbol{u}^{\epsilon}\right) = \frac{1}{2}\left(\frac{\partial u^{\epsilon}_{i}}{\partial x^{\epsilon}_{j}} + \frac{\partial u^{\epsilon}_{j}}{\partial x^{\epsilon}_{i}}\right), \tag{4.63}$$

$$\sigma^{\epsilon}_{ij}\left(\boldsymbol{u}^{\epsilon}\right) = C^{\epsilon}_{ijkl}\left[\epsilon_{kl}\left(\boldsymbol{u}^{\epsilon}\right) - \epsilon^{in,\epsilon}_{kl}\right], \tag{4.64}$$

$$u^{\epsilon}_{i} = 0 \text{ , on } \partial_1\Omega, \tag{4.65}$$

$$\sigma^{\epsilon}_{ij} n_j = F_i \text{ , on } \partial_2\Omega. \tag{4.66}$$

The $Y-$periodicity of the material requirs that also displacements, strains and stresses be $Y-$periodic.

The displacements and inelastic strains can be approximated with an asymptotic expansion in ϵ as follows

$$u^{\epsilon}_{i}\left(\boldsymbol{x}\right) = u^{(0)}_{i}\left(\boldsymbol{x},\boldsymbol{y}\right) + \epsilon u^{(1)}_{i}\left(\boldsymbol{x},\boldsymbol{y}\right) + \epsilon^2 u^{(2)}_{i}\left(\boldsymbol{x},\boldsymbol{y}\right) + \dots \tag{4.67}$$

$$\epsilon^{in,\epsilon}_{i}\left(\boldsymbol{x}\right) = \epsilon^{in,(0)}_{i}\left(\boldsymbol{x},\boldsymbol{y}\right) + \epsilon\epsilon^{in,(1)}_{i}\left(\boldsymbol{x},\boldsymbol{y}\right) + \epsilon^2\epsilon^{in,(2)}_{i}\left(\boldsymbol{x},\boldsymbol{y}\right) + \dots \tag{4.68}$$

Furthermore, the chain rule must be applied to the derivatives in $\boldsymbol{x}$

$$
\begin{aligned}
\frac{\partial}{\partial \boldsymbol{x}^{\epsilon}} &= \frac{\partial}{\partial \boldsymbol{x}} + \frac{1}{\epsilon}\frac{\partial}{\partial \boldsymbol{y}} \\
\frac{\partial}{\partial x^{\epsilon}_{i}} &= \frac{\partial}{\partial x_i} + \frac{1}{\epsilon}\frac{\partial}{\partial y_i}
\end{aligned}
\tag{4.69}
$$

The strain-displacement relationships (4.56) can be written in expanded form as

$$\begin{aligned}
\epsilon_{ij}\left(\boldsymbol{u}^{\epsilon}\right) &= \frac{1}{2}\left(\frac{\partial u_i^{\epsilon}}{\partial x_j} + \frac{\partial u_j^{\epsilon}}{\partial x_i}\right) \\
&= \frac{1}{2}\Bigg(\frac{\partial u_i^{(0)}}{\partial x_j} + \frac{1}{\epsilon}\frac{\partial u_i^{(0)}}{\partial y_j} + \frac{\partial u_j^{(0)}}{\partial x_i} + \frac{1}{\epsilon}\frac{\partial u_j^{(0)}}{\partial y_i} \\
&+ \epsilon\frac{\partial u_i^{(1)}}{\partial x_j} + \frac{\partial u_i^{(1)}}{\partial y_j} + \epsilon\frac{\partial u_j^{(1)}}{\partial x_i} + \frac{\partial u_j^{(1)}}{\partial y_i} \\
&+ \epsilon^2\frac{\partial u_i^{(2)}}{\partial x_j} + \epsilon\frac{\partial u_i^{(2)}}{\partial y_j} + \epsilon^2\frac{\partial u_j^{(2)}}{\partial x_i} + \epsilon\frac{\partial u_j^{(2)}}{\partial y_i} + \dots\Bigg) \\
&= \frac{1}{2\epsilon}\left(\frac{\partial u_i^{(0)}}{\partial y_j} + \frac{\partial u_j^{(0)}}{\partial y_i}\right) + \frac{1}{2}\left(\frac{\partial u_i^{(0)}}{\partial x_j} + \frac{\partial u_j^{(0)}}{\partial x_i} + \frac{\partial u_i^{(1)}}{\partial y_j} + \frac{\partial u_j^{(1)}}{\partial y_i}\right) \\
&+ \frac{\epsilon}{2}\left(\frac{\partial u_i^{(1)}}{\partial x_j} + \frac{\partial u_j^{(1)}}{\partial x_i} + \frac{\partial u_i^{(2)}}{\partial y_j} + \frac{\partial u_j^{(2)}}{\partial y_i}\right) + \dots
\end{aligned}$$

$$\epsilon_{ij}\left(\boldsymbol{u}^{\epsilon}\right) = \frac{1}{\epsilon}\epsilon_{ij}^{(-1)}\left(\boldsymbol{x},\boldsymbol{y}\right) + \epsilon_{ij}^{(0)}\left(\boldsymbol{x},\boldsymbol{y}\right) + \epsilon\epsilon_{ij}^{(1)}\left(\boldsymbol{x},\boldsymbol{y}\right) + \dots \tag{4.70}$$

The constitutive equation (4.64) can be written in expanded form as

$$\begin{aligned}
\sigma_{ij}^{\epsilon}\left(\boldsymbol{u}^{\epsilon}\right) &= C_{ijkl}^{\epsilon}\left(\boldsymbol{x}\right)\left[\epsilon_{kl}^{\epsilon}\left(\boldsymbol{u}^{\epsilon}\right) - \epsilon_{kl}^{in,\epsilon}\right] \\
&= C_{ijkl}^{\epsilon}\left(\boldsymbol{y}\right)\Bigg[\frac{1}{2\epsilon}\left(\frac{\partial u_i^{(0)}}{\partial y_j} + \frac{\partial u_j^{(0)}}{\partial y_i}\right) + \frac{1}{2}\left(\frac{\partial u_i^{(0)}}{\partial x_j} + \frac{\partial u_j^{(0)}}{\partial x_i} + \frac{\partial u_i^{(1)}}{\partial y_j} + \frac{\partial u_j^{(1)}}{\partial y_i} - \epsilon_{kl}^{in,(0)}\right) \\
&+ \frac{\epsilon}{2}\left(\frac{\partial u_i^{(1)}}{\partial x_j} + \frac{\partial u_j^{(1)}}{\partial x_i} + \frac{\partial u_i^{(2)}}{\partial y_j} + \frac{\partial u_j^{(2)}}{\partial y_i} - \epsilon_{kl}^{in,(1)}\right) + \dots\Bigg]
\end{aligned}$$

$$\sigma_{ij}^{\epsilon}\left(\boldsymbol{u}^{\epsilon}\right) = \frac{1}{\epsilon}\sigma_{ij}^{(-1)}\left(\boldsymbol{x},\boldsymbol{y}\right) + \sigma_{ij}^{(0)}\left(\boldsymbol{x},\boldsymbol{y}\right) + \epsilon\sigma_{ij}^{(1)}\left(\boldsymbol{x},\boldsymbol{y}\right) + \dots \tag{4.71}$$

Replacing equation (4.71) in equation (4.62) generates a set of BVPs relevant to each scale in the multi-scale problem:

$$\begin{aligned}
&\epsilon^{-1}\frac{\partial\sigma_{ij}^{(-1)}}{\partial x_j} + \epsilon^{-2}\frac{\partial\sigma_{ij}^{(-1)}}{\partial y_j} + \epsilon^{0}\frac{\partial\sigma_{ij}^{(0)}}{\partial x_j} + \epsilon^{-1}\frac{\partial\sigma_{ij}^{(0)}}{\partial y_j} \\
&\qquad + \epsilon^{1}\frac{\partial\sigma_{ij}^{(1)}}{\partial x_j} + \epsilon^{0}\frac{\partial\sigma_{ij}^{(1)}}{\partial y_j} + \epsilon^{2}\frac{\partial\sigma_{ij}^{(2)}}{\partial x_j} + \epsilon^{1}\frac{\partial\sigma_{ij}^{(2)}}{\partial y_j} + \dots + f_i = 0
\end{aligned}$$

$$\epsilon^{-2}\frac{\partial\sigma_{ij}^{(-1)}}{\partial y_j}+\epsilon^{-1}\left(\frac{\partial\sigma_{ij}^{(-1)}}{\partial x_j}+\frac{\partial\sigma_{ij}^{(0)}}{\partial y_j}\right)+\epsilon^{0}\left(\frac{\partial\sigma_{ij}^{(0)}}{\partial x_j}+\frac{\partial\sigma_{ij}^{(1)}}{\partial y_j}+f_i\right)$$
$$+\epsilon^{1}\left(\frac{\partial\sigma_{ij}^{(1)}}{\partial x_j}+\frac{\partial\sigma_{ij}^{(2)}}{\partial y_j}\right)+\epsilon^{2}\left(\frac{\partial\sigma_{ij}^{(2)}}{\partial x_j}+\frac{\partial\sigma_{ij}^{(3)}}{\partial y_j}\right)+\cdots=0$$

These equations must valid for all $\epsilon \to 0$ which implies that the first three coefficients must be zero identically.

$$\epsilon^{-2}: \qquad \frac{\partial\sigma_{ij}^{(-1)}}{\partial y_j}=0; \tag{4.72}$$

$$\epsilon^{-1}: \qquad \frac{\partial\sigma_{ij}^{(-1)}}{\partial x_j}+\frac{\partial\sigma_{ij}^{(0)}}{\partial y_j}=0; \tag{4.73}$$

$$\epsilon^{0}: \qquad \frac{\partial\sigma_{ij}^{(0)}}{\partial x_j}+\frac{\partial\sigma_{ij}^{(1)}}{\partial y_j}+f_i=0. \tag{4.74}$$

Substituting equations (4.71) and invoking the symmetry of the material properties, the equations (4.72), (4.73) and (4.74) can be written as

$$\epsilon^{-2}: \qquad \frac{\partial}{\partial y_j}C_{ijkl}\frac{\partial u_k^{(0)}}{\partial y_l}=0; \tag{4.75}$$

$$\epsilon^{-1}: \qquad \frac{\partial}{\partial x_j}C_{ijkl}\frac{\partial u_k^{(0)}}{\partial y_l}+\frac{\partial}{\partial y_j}C_{ijkl}\left(\frac{\partial u_k^{(0)}}{\partial x_l}+\frac{\partial u_k^{(1)}}{\partial y_l}-\epsilon_{kl}^{in,(0)}\right)=0; \tag{4.76}$$

$$\epsilon^{0}: \quad \frac{\partial}{\partial x_j}C_{ijkl}\left(\frac{\partial u_k^{(0)}}{\partial x_l}+\frac{\partial u_k^{(1)}}{\partial y_l}-\epsilon_{kl}^{in,(0)}\right)+\frac{\partial}{\partial y_j}C_{ijkl}\left(\frac{\partial u_k^{(1)}}{\partial x_l}+\frac{\partial u_k^{(2)}}{\partial y_l}-\epsilon_{kl}^{in,(1)}\right)+f_i=0. \tag{4.77}$$

Because $\boldsymbol{u}^{(0)}\left(\boldsymbol{x},\boldsymbol{y}\right)$ is $Y-$periodic and the ellipticity of C_{ijkl}, then

$$\frac{\partial u_k^{(0)}}{\partial y_l}=0$$

and equation (4.76) can be simplified as follows

$$\frac{\partial}{\partial y_j}C_{ijkl}\left(\frac{\partial u_k^{(0)}}{\partial x_l}+\frac{\partial u_k^{(1)}}{\partial y_l}-\epsilon_{kl}^{in,(0)}\right)=0 \tag{4.78}$$

which can be rewritten as

$$\frac{\partial}{\partial y_j}\left(C_{ijkl}\frac{\partial u_k^{(1)}}{\partial y_l}\right) = -\frac{\partial u_k^{(0)}}{\partial x_l}\frac{\partial C_{ijkl}}{\partial y_j} + \frac{\partial}{\partial y_j}\left(C_{ijkl}\epsilon_{kl}^{in,(0)}\right) \tag{4.79}$$

To solve equation (4.79) the following separation of variables is adopted [231, 236, 254]

$$u_i^{(1)} = -\chi_i^{kl^1}\left(\boldsymbol{y}\right)\frac{\partial u_k^{(0)}}{\partial x_l} + \chi_i^2\left(\boldsymbol{y},t\right) + \tilde{u}_i^{(1)}\left(\boldsymbol{x}\right) \tag{4.80}$$

where, as was shown in chapter 3, the functions $\chi_i^{kl^1}$ are called the *homogenization functions* [116] for the displacement or *characteristic displacements* [61] or *elastic correctors* [55], while χ_i^2 are *inelastic correctors*. The function $\tilde{u}_i^{(1)}\left(\boldsymbol{u}\right)$ is a constant of integration independent of $\boldsymbol{y}$. Note that, as pointed out by [254], $\chi_i^{kl^1}$ is a function of only y_j because $\chi_i^{kl^1}$ results from the distibution of C_{ijkl} in Y, while in general χ_i^2 is function of both y_j and t. For homogeneous problems both correctors are identically zero, while in the case where no phase transformation occurs in the shape memory alloy then the problem degenerates to an elastic one.

Substituting equation (4.80) into equation (4.79) gives the following result

$$-\frac{\partial}{\partial y_j}C_{ijkl}\frac{\partial \chi_k^{kl^1}}{\partial y_l}\frac{\partial u_k^{(0)}}{\partial x_l} + \frac{\partial}{\partial y_j}C_{ijkl}\frac{\partial \chi_k^2}{\partial y_l} = -\frac{\partial u_k^{(0)}}{\partial x_l}\frac{\partial C_{ijkl}}{\partial y_j} + \frac{\partial}{\partial y_j}C_{ijkl}\epsilon_{kl}^{in,(0)}$$

or

$$\begin{cases} \frac{\partial}{\partial y_j}C_{ijkl}\frac{\partial \chi_k^{kl^1}}{\partial y_l} = \frac{\partial}{\partial y_j}C_{ijkl} \\ \frac{\partial}{\partial y_j}C_{ijkl}\frac{\partial \chi_k^2}{\partial y_l} = \frac{\partial}{\partial y_j}C_{ijkl}\epsilon_{kl}^{in,(0)} \end{cases}$$

which can be written as

$$\begin{cases} \frac{\partial}{\partial y_j}\left[C_{ijkl}\left(\delta_{ik}\delta_{jl} - \frac{\partial \chi_k^{kl^1}}{\partial y_l}\right)\right] = 0 \\ \frac{\partial}{\partial y_j}\left[C_{ijkl}\left(\frac{\partial \chi_k^2}{\partial y_l} - \epsilon_{kl}^{in,(0)}\right)\right] = 0 \end{cases}$$

where δ_{ij} indicates Kronecker's delta function.

The functions $\chi_i^{kl^1}$ and χ_i^2 are determined by solving the following variational problems:

$$\text{Find } \chi_i^{kl^1} \in V_Y \text{ such that: } \quad \int_Y C_{ijkl}\frac{\partial \chi_k^{kl^1}}{\partial y_l}\frac{\partial v_i}{\partial y_j}\mathrm{d}\boldsymbol{y} = \int_Y v_j\frac{\partial C_{ijkl}}{\partial y_j}\mathrm{d}\boldsymbol{y}, \quad \forall \boldsymbol{v}_i \in V_Y$$

with $Y-$periodicity of $\chi_i^{kl^1}$, and

$$\text{Find } \chi_i^2 \in V_Y \text{ such that: } \quad \int_Y C_{ijkl}\frac{\partial \chi_k^2}{\partial y_l}\frac{\partial v_i}{\partial y_j}\mathrm{d}\boldsymbol{y} = \int_Y v_j\epsilon_{kl}^{in,(0)}\mathrm{d}\boldsymbol{y}, \quad \forall \boldsymbol{v}_i \in V_Y$$

with $Y-$periodicity of χ_i^2.

The strains in the microscopic problem can be obtained substituting equation (4.80) in equation (4.70)

$$\begin{aligned}\epsilon_{ij}^{(0)}(\boldsymbol{x},\boldsymbol{y}) &= \frac{1}{2}\left(\frac{\partial u_i^{(0)}}{\partial x_j} + \frac{\partial u_j^{(0)}}{\partial x_i} + \frac{\partial u_i^{(1)}}{\partial y_j} + \frac{\partial u_j^{(1)}}{\partial y_i}\right)\\ &+ \frac{1}{2}\left(\frac{\partial u_i^{(0)}}{\partial x_j} + \frac{\partial u_j^{(0)}}{\partial x_i} - \frac{\partial \chi_i^{kl^1}}{\partial y_j}\frac{\partial u_k^{(0)}}{\partial x_l} + \frac{\partial \chi_i^2}{\partial y_j} - \frac{\partial \chi_j^{kl^1}}{\partial y_i}\frac{\partial u_k^{(0)}}{\partial x_l} + \frac{\partial \chi_j^2}{\partial y_i}\right)\end{aligned}$$

and because all quantities are symmetric about i and j

$$\epsilon_{ij}^{(0)}(\boldsymbol{x},\boldsymbol{y}) = \left(\delta_{ik}\delta_{jl} - \frac{\partial \chi_i^{kl^1}}{\partial y_j}\right)\frac{\partial u_k^{(0)}}{\partial x_l} + \frac{\partial \chi_i^2}{\partial y_j} \tag{4.81}$$

The stresses in the microscopic problem can be obtained substituting equation (4.80) in equation (4.71)

$$\begin{aligned}\sigma_{ij}^{(0)}(\boldsymbol{x},\boldsymbol{y}) &= C_{ijkl}(\boldsymbol{y})\left(\epsilon_{kl}^{(0)}(\boldsymbol{x},\boldsymbol{y}) - \epsilon_{kl}^{in,(0)}\right)\\ &= C_{ijkl}(\boldsymbol{y})\left(\delta_{ik}\delta_{jl} - \frac{\partial \chi_i^{kl^1}}{\partial y_j}\right)\frac{\partial u_k^{(0)}}{\partial x_l} - C_{ijkl}(\boldsymbol{y})\left(\epsilon_{kl}^{in,(0)} - \frac{\partial \chi_i^2}{\partial y_j}\right)\end{aligned} \tag{4.82}$$

Substituting equation (4.80) into equation (4.77) gives the following result

$$\begin{aligned}&\frac{\partial}{\partial x_j}C_{ijkl}\left(\frac{\partial u_k^{(0)}}{\partial x_l} - \frac{\partial \chi_k^{kl^1}}{\partial y_l}\frac{\partial u_k^{(0)}}{\partial x_l} + \frac{\partial \chi_k^2}{\partial y_l} - \epsilon_{kl}^{in,(0)}\right) +\\ &\frac{\partial}{\partial y_j}C_{ijkl}\left[\frac{\partial}{\partial x_l}\left(-\chi_k^{kl^1}\frac{\partial u_k^{(0)}}{\partial x_l} + \chi_k^2\right) + \frac{\partial \tilde{u}_k^{(1)}}{\partial x_l}(\boldsymbol{u}) + \frac{\partial u_k^{(2)}}{\partial y_l} - \epsilon_{kl}^{in,(1)}\right] + f_i = 0\end{aligned} \tag{4.83}$$

Using the fact that $u_i^{(2)}$ is $Y-$periodic [56], then equation (4.83) admits a unique solution if and only if

$$\int_Y \left[\frac{\partial}{\partial x_j}C_{ijkl}\left(\frac{\partial u_k^{(0)}}{\partial x_l} - \frac{\partial \chi_k^{kl^1}}{\partial y_l}\frac{\partial u_k^{(0)}}{\partial x_l} + \frac{\partial \chi_k^2}{\partial y_l} - \epsilon_{kl}^{in,(0)}\right) + f_i\right]\mathrm{d}\boldsymbol{y} = 0$$

and, after dividing both sides of equation (4.83) by the volume $|Y|$ of the RVE and rearranging, this equation can be written as

$$\begin{aligned}&\frac{\partial}{\partial x_j}\left[\frac{1}{|Y|}\int_Y C_{ijkl}\left(\delta_{ik}\delta_{jl} - \frac{\partial \chi_k^{kl^1}}{\partial y_l}\right)\mathrm{d}\boldsymbol{y}\right]\frac{\partial u_k^{(0)}}{\partial x_l}\\ &-\frac{\partial}{\partial x_j}\left[\frac{1}{|Y|}\int_Y C_{ijkl}\left(\epsilon_{kl}^{in,(0)} - \frac{\partial \chi_k^2}{\partial y_l}\right)\mathrm{d}\boldsymbol{y}\right] + f_i = 0\end{aligned} \tag{4.84}$$

Defining the *homogenized elasticity tensor* as

$$C^h_{ijkl} =< C_{ijkl} >= \frac{1}{|Y|} \int_Y C_{ijkl} \left(\delta_{ik}\delta_{jl} - \frac{\partial \chi_k^{kl^1}}{\partial y_l} \right) \mathrm{d}\boldsymbol{y} \tag{4.85}$$

where the brackets $<>$ are the *volume average operator*

$$<>= \frac{1}{|Y|} \int_Y () \mathrm{d}\boldsymbol{y}.$$

Using definition (4.85) in equation (4.84), this can be recast in the following form

$$\frac{\partial}{\partial x_j} \left\{ C^h_{ijkl} \left[\frac{\partial u_k^{(0)}}{\partial x_l} - \frac{1}{|Y|} \left(C^h_{ijkl} \right)^{-1} \int_Y C_{ijkl} \left(\epsilon_{kl}^{in,(0)} - \frac{\partial \chi_k^2}{\partial y_l} \right) \mathrm{d}\boldsymbol{y} \right] \right\} + f_i = 0 \tag{4.86}$$

Now defining the *homogenized inelastic strain tensor* as

$$\epsilon_{ij}^{in,h} =< \epsilon_{ij}^{in} >= \frac{1}{|Y|} \left(C^h_{ijkl} \right)^{-1} \int_Y C_{ijkl} \left(\epsilon_{kl}^{in,(0)} - \frac{\partial \chi_k^2}{\partial y_l} \right) \mathrm{d}\boldsymbol{y}, \tag{4.87}$$

where

$$\epsilon_{ij}^{in} = C_{ijkl} \left(C^h_{ijkl} \right)^{-1} \left(\epsilon_{kl}^{in,(0)} - \frac{\partial \chi_k^2}{\partial y_l} \right), \tag{4.88}$$

the zero-th order stress, which is also the stress in the macroproblem, is

$$\begin{aligned} < \sigma_{ij}^{(0)} > &= C^h_{ijkl} \left(\frac{\partial u_k^{(0)}}{\partial x_l} - \epsilon_{ij}^{in,h} \right) \\ &= C^h_{ijkl} \left(< \epsilon_{kl}^{(0)} > - \epsilon_{ij}^{in,h} \right). \end{aligned} \tag{4.89}$$

In the absence of inelastic strains, then the stress in the macroproblem can be computed as

$$< \sigma_{ij}^{(0)} >= C^h_{ijkl} < \epsilon_{kl}^{(0)} > ,$$

which is the same result that was found in chapter 3.

The nonlinear homogenized BVP for the shape memory alloy material is

$$\frac{\partial}{\partial x_j} < \sigma_{ij}^{(0)} > + f_i = 0 \text{ in } \Omega \tag{4.90}$$

$$< \epsilon_{kl}^{(0)} >= \frac{\partial u_k^{(0)}}{\partial x_l} \tag{4.91}$$

$$< \sigma_{ij}^{(0)} >= C^h_{ijkl} \left(< \epsilon_{kl}^{(0)} > - \epsilon_{ij}^{in,h} \right) \tag{4.92}$$

$$u_i^{(0)} = 0 \text{ on } \partial_1 \Omega \tag{4.93}$$

$$< \sigma_{ij}^{(0)} > n_j = F_i \text{ on } \partial_2 \Omega \tag{4.94}$$

4.2.5 Reformulation of the AEHM macroscopic problem for SMAHCs using Transformation Field Analysis

In order to reduce the computational complexity of the *full* AEHM approach, this is combined with Transformation Field Analysis (TFA). The AEHM macroscopic problem for SMAHCs is reformulated using TFA and the *full* AEHM approach is applied only to critical regions, defined as those regions where macroscopic stresses or macroscopic inelastic strains exceed certain criteria (refer to section 3.2.3 for more details on how to incorporate damage in the AEHM).

The TFA is characterized by *local fields* and *overall response* (o *average fields*). The overall stress $\bar{\boldsymbol{\sigma}}$, strain $\bar{\boldsymbol{\epsilon}}$ and inelastic strain $\bar{\boldsymbol{\epsilon}}^{in}$ are the average of the local stress, strain and inelastic strain fields which vary pointwise in the RVE.

The average strain $\bar{\boldsymbol{\epsilon}}$, the average stress $\bar{\boldsymbol{\sigma}}$ and the average inelastic strain $\bar{\boldsymbol{\epsilon}}^{in}$ are obtained by integrating equations (4.70), (4.71) and (4.68), respectively, over the RVE under the assumption that $\epsilon \to 0$ [87, 179, 221]

$$\begin{aligned}
\bar{\epsilon}_{ij}\left(\boldsymbol{x},t\right) &= \frac{1}{|Y|}\int_Y \epsilon_{ij}\left(\boldsymbol{x},\boldsymbol{y},t\right)\mathrm{d}\boldsymbol{y} \\
&= \frac{1}{|Y|}\int_Y \epsilon_{ij}^{(0)}\left(\boldsymbol{x},\boldsymbol{y},t\right)\mathrm{d}\boldsymbol{y} + O\left(\epsilon\right) \\
\bar{\sigma}_{ij}\left(\boldsymbol{x},t\right) &= \frac{1}{|Y|}\int_Y \sigma_{ij}\left(\boldsymbol{x},\boldsymbol{y},t\right)\mathrm{d}\boldsymbol{y} \\
&= \frac{1}{|Y|}\int_Y \sigma_{ij}^{(0)}\left(\boldsymbol{x},\boldsymbol{y},t\right)\mathrm{d}\boldsymbol{y} + O\left(\epsilon\right) \\
\bar{\epsilon}_{ij}^{in}\left(\boldsymbol{x},t\right) &= \frac{1}{|Y|}\int_Y \epsilon_{ij}^{in}\left(\boldsymbol{x},\boldsymbol{y},t\right)\mathrm{d}\boldsymbol{y} \\
&= \frac{1}{|Y|}\int_Y \epsilon_{ij}^{in,(0)}\left(\boldsymbol{x},\boldsymbol{y},t\right)\mathrm{d}\boldsymbol{y} + O\left(\epsilon\right)
\end{aligned}$$

Defining the *elastic strain concentrator factor* and the *transformation strain* [72, 75] as

$$\begin{aligned}
A_{ijkl} &= \delta_{ik}\delta_{jl} - \frac{\partial \chi_i^{kl^1}}{\partial y_j}, \\
\mu_{ij} &= \frac{\partial \chi_i^2}{\partial y_j}
\end{aligned}$$

respectively, equation (4.81) can be rewritten as

$$\epsilon_{ij}^{(0)}\left(\boldsymbol{x},\boldsymbol{y},t\right) = A_{ijkl}\frac{\partial u_k^{(0)}}{\partial x_l} + \mu_{ij} \tag{4.95}$$

Defining the *elastic stress concentrator factor* and the *transformation stress* [72, 75] as

$$
\begin{aligned}
B_{ijkl} &= C_{ijkl}\left(\boldsymbol{y}\right)\left(\delta_{ik}\delta_{jl} - \frac{\partial \chi_i^{kl^1}}{\partial y_j}\right), \\
\lambda_{ij} &= C_{ijkl}\left(\boldsymbol{y}\right)\frac{\partial \chi_i^2}{\partial y_j}
\end{aligned}
$$

respectively, equation (4.82) can be rewritten as

$$
\sigma_{ij}^{(0)}\left(\boldsymbol{x},\boldsymbol{y},t\right) = B_{ijkl}\frac{\partial u_k^{(0)}}{\partial x_l} + \lambda_{ij} \tag{4.96}
$$

Note from the above equations that

$$
\begin{aligned}
B_{ijkl} &= C_{ijkl}\left(\boldsymbol{y}\right)A_{ijkl} \\
\lambda_{ij} &= C_{ijkl}\left(\boldsymbol{y}\right)\mu_{ij}
\end{aligned}
$$

In particular, considering a two-scale heterogeneous material composed of n_{ph} phases, the RVE volume will be partitioned into subdomains in such a way that each subdomain Y_r, $r = 1 \ldots Q$, where $\sum Y_r = Y$ and $V_r = |Y_r|/|Y|$ is the volume fraction of subdomain Y_r, belongs to a single homogeneous phase [87, 179, 221], i. e. $\cup_{r=1}^{n_{ph}} Y_r = Y$ and $Y_s \cap Y_t = \emptyset$ for $s \neq t$. Denoting the *characteristic functions* of subdomain Y_r by

$$
\chi_r\left(\boldsymbol{x}\right) = \begin{cases} 1 & \text{if } \boldsymbol{x} \in Y_r, \\ 0 & \text{otherwise,} \end{cases} \qquad\qquad V_r = <\chi_r> ,
$$

then the overall fields are the weighted volume sum of the average fields

$$
\bar{\boldsymbol{\epsilon}} = \sum_{r=1}^{n_{ph}} V_r \boldsymbol{\epsilon}_r, \tag{4.97}
$$

$$
\bar{\boldsymbol{\sigma}} = \sum_{r=1}^{n_{ph}} V_r \boldsymbol{\sigma}_r, \tag{4.98}
$$

If uniform transformation fields are assumed, which involves two levels of approximation [152]

1. the internal variables Λ_r, including the inelastic strain $\boldsymbol{\epsilon}_r^{in}$, are considered to be piecewise constant within each individual phase or subdomain, i. e.

$$
\boldsymbol{\epsilon}^{in} = \sum_{r=1}^{n_{ph}} \boldsymbol{\epsilon}_r^{in} \chi_r\left(\boldsymbol{x}\right);
$$

2. the evolution of the internal variables Λ_r follows exactly the constitutive relations

in phase r, the strain being estimated as the average strain in phase r;

then the local fields in the subdomains are found by superposition of mechanical and transformation field contributions as

$$\bar{\boldsymbol{\epsilon}}_r =< \boldsymbol{\epsilon}_r >= \boldsymbol{A}_r : \bar{\boldsymbol{\epsilon}} + \sum_{s=1}^{n_{ph}} \boldsymbol{D}_{rs} \boldsymbol{\epsilon}_s^{in}, \tag{4.99}$$

$$\bar{\boldsymbol{\sigma}}_r =< \boldsymbol{\sigma}_r >= \boldsymbol{B}_r : \bar{\boldsymbol{\sigma}} + \sum_{s=1}^{n_{ph}} \boldsymbol{F}_{rs} \boldsymbol{\lambda}_s = \boldsymbol{C}_r : \left(\bar{\boldsymbol{\epsilon}}_r - \boldsymbol{\epsilon}_r^{in} \right), \tag{4.100}$$

where $\boldsymbol{A}_r$ and $\boldsymbol{B}_r$ are the strain and stress *concentration factors*, $\boldsymbol{D}_{rs}$ and $\boldsymbol{F}_{rs}$ are the *transformation influence functions*, and $\boldsymbol{C}_r$ is the stiffness tensor for subdomain Y_r. Both the concentration factors and the transformation influence functions depend on the micro-geometry and phase distribution of the RVE.

Under the above assumption, considering a SMA hybrid woven composite of three phases, matrix, yarns and SMA occupying subdomains Y_m, Y_y and Y_{sma}, and with volume fractions $V_m = |Y_m|/|Y|$, $V_y = |Y_y|/|Y|$ and $V_{sma} = |Y_{sma}|/|Y|$, respectively, then $Y_m + Y_y + Y_{sma} = Y$ and $V_m + V_y + V_{sma} = 1$.

The average strain and stress concentration factors can be defined for matrix, yarns and SMA

$$\begin{aligned}
\boldsymbol{A}_m &= \frac{1}{|Y_m|} \int_{Y_m} A_{ijkl} \mathrm{d}\boldsymbol{y}, & \boldsymbol{A}_y &= \frac{1}{|Y_y|} \int_{Y_y} A_{ijkl} \mathrm{d}\boldsymbol{y}, & \boldsymbol{A}_{sma} &= \frac{1}{|Y_{sma}|} \int_{Y_{sma}} A_{ijkl} \mathrm{d}\boldsymbol{y}; \\
\boldsymbol{B}_m &= \frac{1}{|Y_m|} \int_{Y_m} B_{ijkl} \mathrm{d}\boldsymbol{y}, & \boldsymbol{B}_y &= \frac{1}{|Y_y|} \int_{Y_y} B_{ijkl} \mathrm{d}\boldsymbol{y}, & \boldsymbol{B}_{sma} &= \frac{1}{|Y_{sma}|} \int_{Y_{sma}} B_{ijkl} \mathrm{d}\boldsymbol{y};
\end{aligned}$$

and, in the absence of transformation fields, the overall elastic stiffness and compliance, are [100]

$$\begin{aligned}
\bar{\boldsymbol{C}} &= V_m \boldsymbol{A}_m \boldsymbol{C}_m + V_y \boldsymbol{A}_y \boldsymbol{C}_y + V_{sma} \boldsymbol{A}_{sma} \boldsymbol{C}_{sma}, \\
\bar{\boldsymbol{S}} &= V_m \boldsymbol{B}_m \boldsymbol{S}_m + V_y \boldsymbol{B}_y \boldsymbol{S}_y + V_{sma} \boldsymbol{B}_{sma} \boldsymbol{S}_{sma},
\end{aligned}$$

where $\bar{\boldsymbol{S}} = \bar{\boldsymbol{C}}^{-1}$.

Assuming matrix and yarns to have a purely elastic behavior, then equations (4.99) for the matrix, yarns and SMA subdomains can be written as

$$\begin{aligned}\bar{\boldsymbol{\epsilon}}_m &= \boldsymbol{A}_m : \bar{\boldsymbol{\epsilon}},\\ \bar{\boldsymbol{\sigma}}_m &= \boldsymbol{C}_m : \bar{\boldsymbol{\epsilon}}_m;\\ \bar{\boldsymbol{\epsilon}}_y &= \boldsymbol{A}_y : \bar{\boldsymbol{\epsilon}},\\ \bar{\boldsymbol{\sigma}}_y &= \boldsymbol{C}_y : \bar{\boldsymbol{\epsilon}}_y;\\ \bar{\boldsymbol{\epsilon}}_{sma} &= \boldsymbol{A}_{sma} : \bar{\boldsymbol{\epsilon}} + \bar{\boldsymbol{\epsilon}}_{sma}^{in},\\ \bar{\boldsymbol{\sigma}}_{sma} &= \boldsymbol{C}_{sma} : \left(\bar{\boldsymbol{\epsilon}}_{sma} - \bar{\boldsymbol{\epsilon}}_{sma}^{in}\right);\end{aligned}$$

respectively.

For a SMAHCs, equation (4.98) reduces to

$$\bar{\boldsymbol{\sigma}} = V_m \boldsymbol{\sigma}_m + V_y \boldsymbol{\sigma}_y + V_{sma} \boldsymbol{\sigma}_{sma} \tag{4.101}$$

4.3 Results

4.3.1 Brinson-Voigt Model for SMA

Here the results of the Brinson-Voigt model for Nitinol alloy are described. This model was implemented in MATLAB and run for different initial conditions and temperatures.

The thermo-mechanical properties are the following [77, 133, 33]

$$\begin{aligned}E_A &= 67\text{x}10^3 MPa\\ E_M &= 26.3\text{x}10^3 MPa\\ M_f &= 9°C\\ M_s &= 18.4°C\\ A_s &= 34.5°C\\ A_f &= 49°C\\ \Theta &= 0.55\frac{MPa}{°C}\\ \epsilon_L &= 0.067\%\\ C_M &= 8\frac{MPa}{°C}\\ C_A &= 13.8\frac{MPa}{°C}\\ \sigma_s^{CR} &= 100 MPa\\ \sigma_f^{CR} &= 170 MPa\end{aligned}$$

In figure 4-3 the SMA has a super-elastic behavior at $T = 60°C$. The SMA material is initially in 100% Austenite phase (0% Martensite phase), and then during loading, it transforms to 100% single-variant Martensite. After unloading the SMA material transforms back to 100% Austenite phase.

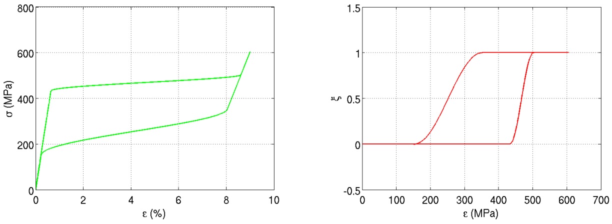

(a) Stress-strain curve **(b)** Total martensitic volume fraction versus stress curve

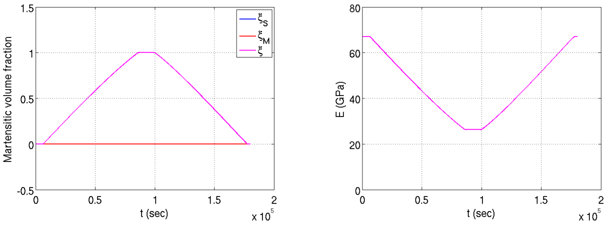

(c) Martensitic volume fraction versus time curve **(d)** Elastic modulus versus time curve

Figure 4-3: Brinson-Voigt Model for NiTi ($T = 60°C$)

In figure 4-4 the SMA has a pseudoelastic behavior at $T = 40°C$, because the initial temperature is lower than A_ff. The SMA material is initially in 100% Austenite phase (0% Martensite phase).

In figure 4-5 ($T = 25°C$) the SMA has SME behavior, because the initial temperature is lower than A_s. Here the hypothesis is that the material comes from a heating process with 0% Martensite phase.

In figure 4-6 ($T = 15°C$) and figure 4-7 ($T = 12°C$) the SMA has SME behavior, because the initial temperatures are lower than M_s. Here the hypothesis is that the initial multi-variant Martensite phase is proportional to the difference between transformation temperatures (i. e. a mixture of Austenite phase and Martensite phase).

In figure 4-8 ($T = 5°C$) the SMA has also SME behavior, because the initial temperatures are lower than M_f. The initial multi-variant Martensite phase is equal to 100%.

4.3.2 3-D isotropic and asymmetric transformation

Stress-controlled tests

In the stress-controlled tests the values of σ_{11}, σ_{12} or both are imposed, while the corresponding values of strain $\boldsymbol{\epsilon}$ are derived.

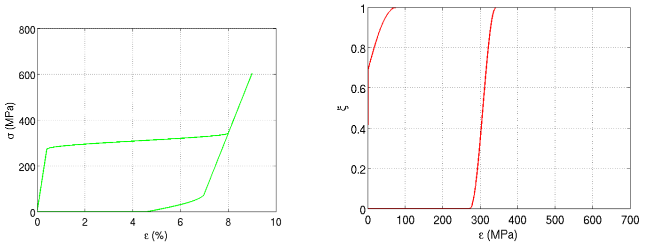

(a) Stress-strain curve **(b)** Total martensitic volume fraction versus stress curve

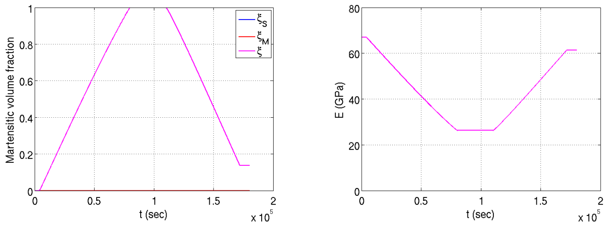

(c) Martensitic volume fraction versus time curve **(d)** Elastic modulus versus time curve

Figure 4-4: Brinson-Voigt Model for NiTi ($T = 40°C$)

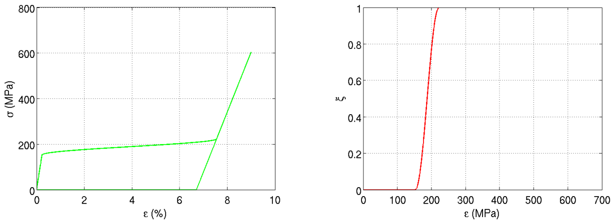

(a) Stress-strain curve **(b)** Total martensitic volume fraction versus stress curve

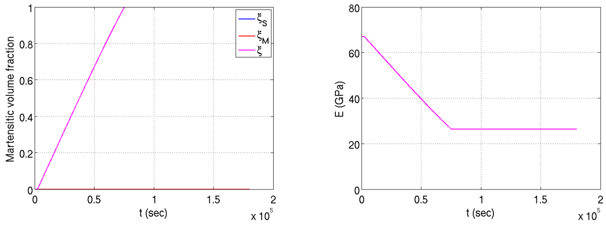

(c) Martensitic volume fraction versus time curve **(d)** Elastic modulus versus time curve

Figure 4-5: Brinson-Voigt Model for NiTi ($T = 25°C$)

For NiTi the following parameters are considered [146]

$$\begin{aligned} M_s = -51.55\,[°C] \quad &\text{and} \quad A_s = -6.36\,[°C] \\ \mathcal{L} = 79\,[\tfrac{MJ}{m^3}] \quad &\text{and} \quad c_p = 5.4\,[\tfrac{MJ}{m^{3}°K}] \\ \epsilon_m^c = -2.5\,[\%] \quad &\text{and} \quad \epsilon_m^t = 5\,[\%] \\ E = 65\,[\text{GPa}] \quad &\text{and} \quad \sigma_y = 1500\,[\text{GPa}] \end{aligned} \tag{4.102}$$

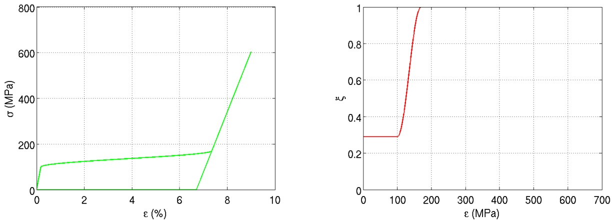

(a) Stress-strain curve **(b)** Total martensitic volume fraction versus stress curve

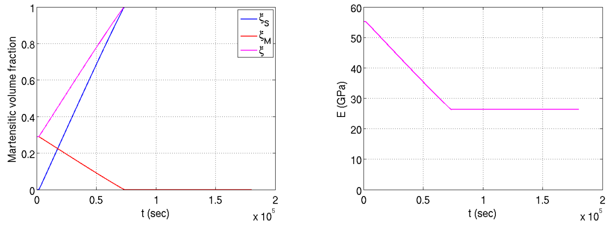

(c) Martensitic volume fraction versus time curve **(d)** Elastic modulus versus time curve

Figure 4-6: Brinson-Voigt Model for NiTi ($T = 15°C$)

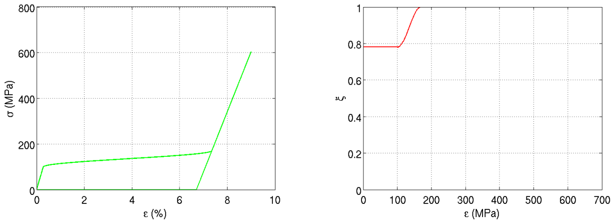

(a) Stress-strain curve **(b)** Total martensitic volume fraction versus stress curve

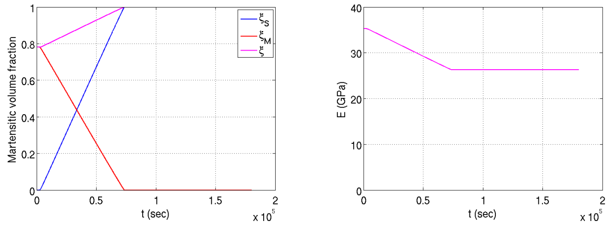

(c) Martensitic volume fraction versus time curve **(d)** Elastic modulus versus time curve

Figure 4-7: Brinson-Voigt Model for NiTi ($T = 12°C$)

where M_s and A_s are the Martensite start and Austenite start temperatures, respectively, and σ_y is the plastic yield stress.

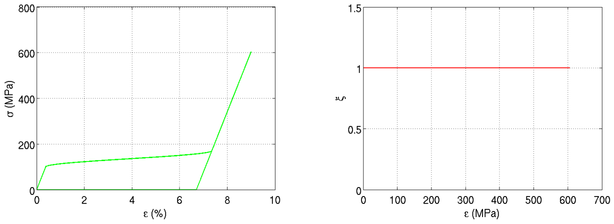

(a) Stress-strain curve **(b)** Total martensitic volume fraction versus stress curve

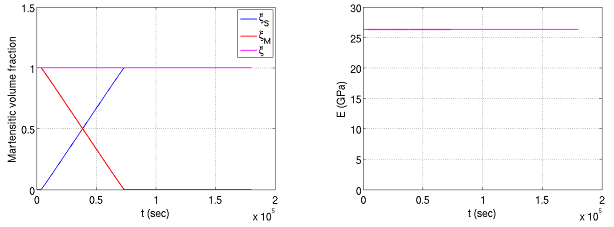

(c) Martensitic volume fraction versus time curve **(d)** Elastic modulus versus time curve

Figure 4-8: Brinson-Voigt Model for NiTi ($T = 5°C$)

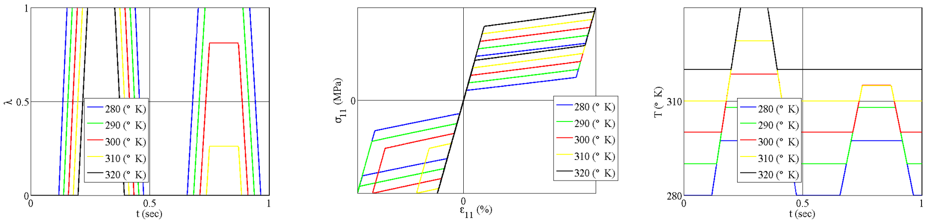

(a) Martensitic volume fraction versus time curve **(b)** Stress-strain curve **(c)** Temperature versus time curve

Figure 4-9: Uniaxial tension-compression stress-strain curves under stress-controlled proportional loading for 3-D isotropic and asymmetric transformation

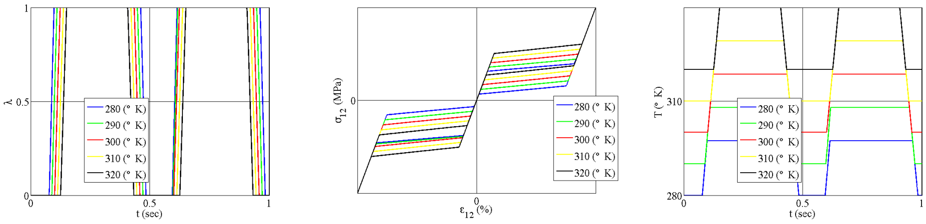

(a) Martensitic volume fraction versus time curve **(b)** Stress-strain curve **(c)** Temperature versus time curve

Figure 4-10: Pure shear stress-strain curves under stress-controlled proportional loading for 3-D isotropic and asymmetric transformation

The following material parameters are assumed [27]

$$\begin{array}{lll} d_\lambda^+ = d_\lambda^- = \mathcal{L}\left(\frac{A_s - M_s}{A_s + M_s}\right), & T_{cr} = \frac{A_s + M_s}{2}, & T_0 = 295^\circ K \\ a = 1.035, & b = 0.000049, & c = 0 \end{array}$$

Moreover, $\hat{e} = [100]$.

The following kinetic coefficients are assumed

$$\dot{\lambda}^+ = \dot{\lambda}^- = 10^4, \quad \alpha = 10^{-3}, \quad p = 2$$

All tests were carried out in adiabatic conditions.

Figure 4-9 shows results of the simulation of the uniaxial tension-compression tests for different initial temperatures T_0.

Figure 4-10 shows the growth of volume fraction of Martensite and temperature as a function of time and the stress-strain response for pure shear tests for different initial temperatures T_0.

Figure 4-11 shows the stress-controlled tension-torsion simulations of the same NiTi sample on four additional stress paths. The material in these tests is stress-loaded axially, followed by a shear stress of equal maximum value.

Strain-controlled tests

In the strain-controlled tests the values of ϵ_{11} and ϵ_{12} are imposed, while the corresponding values of stress $\boldsymbol{\sigma}$ are derived.

The material parameters and kinematic coefficients are the same as those in the stress-driven tests, except for the following material parameters:

$$a = 1.5, \quad b = 0.000049, \quad c = -0.6$$

Figure 4-12 shows the strain-controlled tension-torsion simulations of the same NiTi sample on four different strain paths. The material in these tests is strain-loaded axially, followed by a shear strain of different maximum value.

4.3.3 Comparison of impact testing results for woven and uni-directional SMAHCs

Impact testing on SMA hybrid composites (SMAHCs) was conducted for the purpose of concept-proving and validating the modeling results.

Six samples of SMAHCs were constructed: three woven laminates and three uni-directional laminates.

The three woven laminates were composed of eight plies of five-harness (5H) satin fabric with stacking sequence $[0^\circ/0^\circ/0^\circ/0^\circ]_S$. Note that, as discussed in chapter 3, in

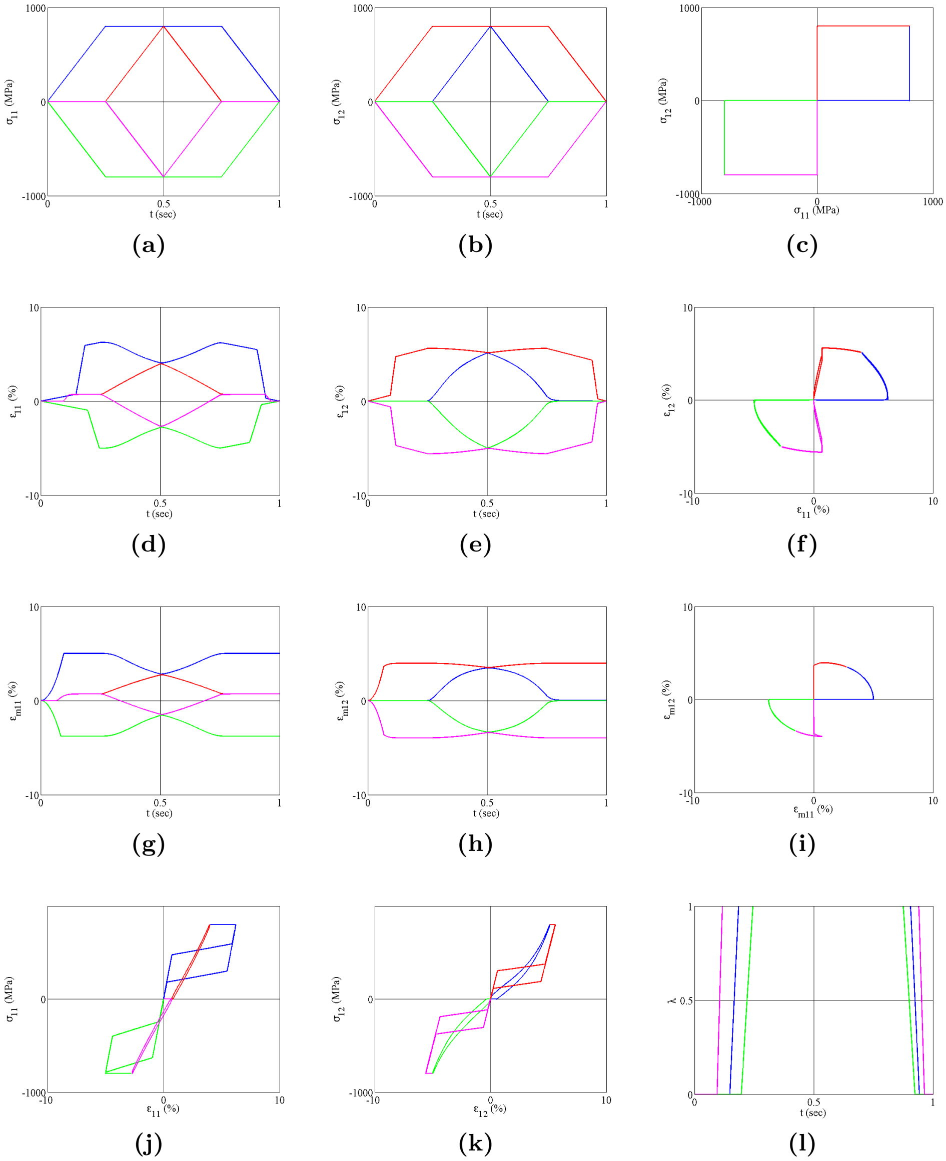

Figure 4-11: Nonproportional stress-controlled loading for 3-D isotropic and asymmetric transformation

each woven ply the warp and fill yarns are interlaced by 90°. The baseline laminate (*laminate n.1* from now on) was made up comprising sixteen plies of conventional woven carbon fiber preform in a matrix of Hexcel® 8552 epoxy resin. The other two laminates were hybridized with NiTi SMA wires: in the first the SMA wires were embedded in only the bottom two plies (*laminate n.2*), while in the second the bottom two and top two plies were hybridized (*laminate n.3*). In particular, the incorporation of SMA wires was carried out in such a way that the warp and fill directions comprised a series of combination threads each comprising a flat tow of carbon fibers and a pair of two SMA wires, one at each lateral edge of the respective tow, as shown in figure 2-11. Please

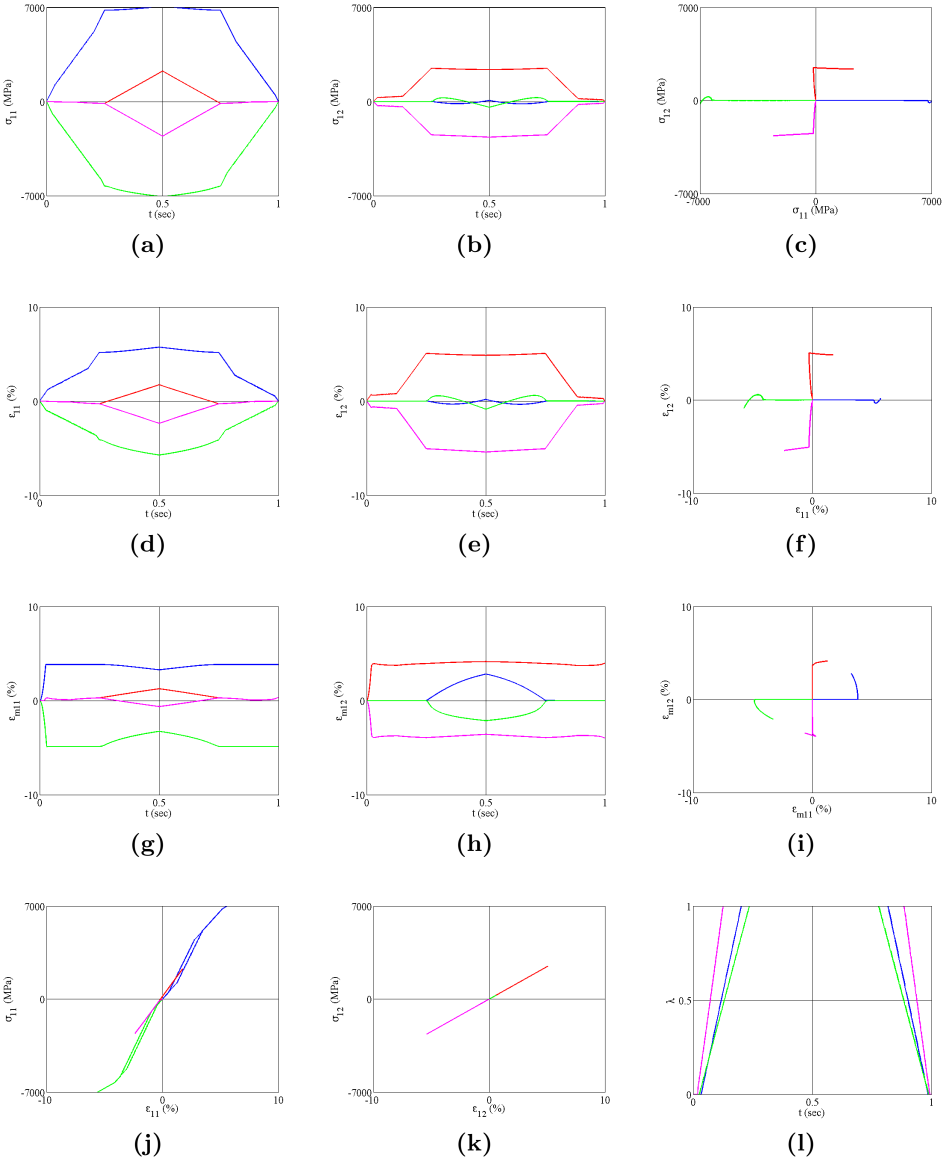

(a) **(b)** **(c)**

(d) **(e)** **(f)**

(g) **(h)** **(i)**

(j) **(k)** **(l)**

Figure 4-12: Nonproportional strain-controlled loading for 3-D isotropic and asymmetric transformation

refer to patent [46] for more details.

For comparing results, the three uni-directional (UD) laminates were composed of sixteen plies with stacking sequence $[0°/90°/0°/90°/0°/90°/0°/90°]_S$. The baseline laminate (*laminate n.4*) was made up comprising sixteen plies of conventional uni-directional carbon fiber preform in a matrix of Hexcel® 8552 epoxy resin. The other two laminates were hybridized using NiTi SMA wires: in the first the SMA wires were incorporated only in the bottom four plies (*laminate n.5*), while in the second the bottom four and top four plies were hybridized (*laminate n.6*). The incorporation of the SMA wires in the uni-directional laminates followed in the same lines that of the woven laminates with one SMA wire at each lateral edge of the respective tow of carbon fibers.

The decision to embed the SMA wires in the outer layers was based on previously published results [243]. The different distribution of SMA wires in the plies of laminates 2, 3, 5 and 6 determines a variation in the volume fraction of SMA between the different samples. Moreover, as highlighted in chapter 2, incorporating the SMA wires in the composite results in an increment in the overall weight, i. e. a weight penalty, which is given in table 4.1 for each SMAHC laminate compared to its baseline.

SMAHC	Increase [%]
UD SMA-TB	55.02
UD SMA-B	26.71
5H SMA-TB	71.58
5H SMA-B	38.19

Table 4.1: Percentage increase in weight of each SMAHC laminate compared to its baseline.

The SMA wires in the structure were designed to function in a purely passive sense, i. e. only the *passive impact damage suppression* properties of the SMA are used here, in contrast to *active impact damage suppression* mechanism where the shape memory effect (SME) is deliberately provoked by supplying heat to the structure, e. g. applying an electrical voltage to the wires. Refer to chapter 2 for a detailed discussion on the differences between the passive and active damage suppression methods. Moreover the SMA wires were not prestrained within the woven preform.

Each sample, held in a $100mm$ diameter Crag ring, was subjected to a full penetration impact energy absorption test in a Rosand® Instrumented Falling Weight Impact Tester, using a $16mm$ hemispherical indenter at a velocity of about $5m/s$ delivering $80J$ impact energy. Because of the asymmetry in samples 2 and 5, these were impacted on both the top and bottom surfaces. Examples of the damage inflicted to the samples can be seen in figure 4-13.

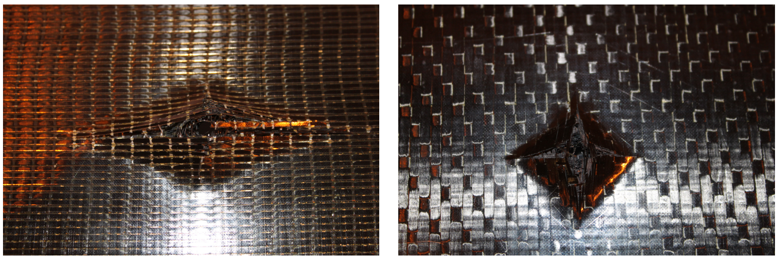
(a) Laminate n.2 **(b)** Laminate n.5

Figure 4-13: Examples of impact damage.

Figures 4-14 and 4-15 display the impact energy absorbed per unit mass and per unit thickness, respectively, for the SMAHC laminates, i. e. the maximum impact energy absorbed divided by the mass and the thickness, respectively, of the clamped region of material during test.

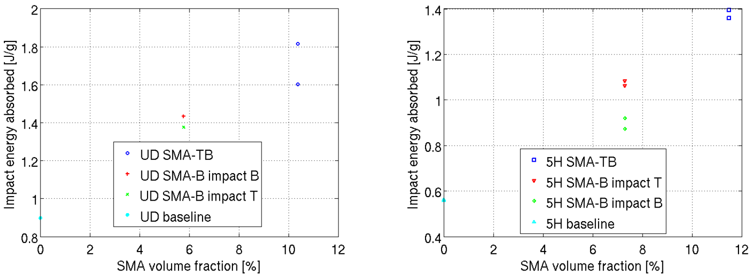

(a) Uni-directional SMAHC laminates **(b)** Five-harness satin weave SMAHC laminates

Figure 4-14: Impact energy absorbed per unit mass.

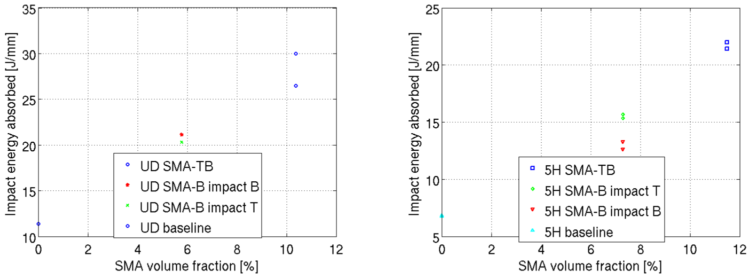

(a) Uni-directional SMAHC laminates **(b)** Five-harness satin weave SMAHC laminates

Figure 4-15: Impact energy absorbed per unit thickness.

Figures 4-14 and 4-15 show that the uni-directional SMAHC laminates have a greater impact energy absorption compared to the five-harness satin weave SMAHC laminates, as the thickness, and therefore stiffness, of the uni-directional laminates is higher.

Moreover, the highest impact energy, compared to the baseline, is absorbed by the SMAHC laminates which incorporate SMA wires in both the top and bottom plies (*UD SMA-TB* and *5H SMA-TB*, in the figures). Next best are the SMAHCs hybridized only in the bottom plies (*UD SMA-B* and *5H SMA-B*, in the figures) when impacted on the top surface, i. e. on the side opposite to the one with the plies containing the SMA wires. Last come the SMAHC laminates hybridized on the bottom plies when impacted on the bottom surface. These findings support previously published results [243].

Table 4.2 gives the percentage increase in impact energy absorption of each SMAHC laminate compared to its baseline. Note that embedding the SMA wires in a five-harness satin weave composite gives a higher percentage increase in impact energy absorption than in the case of uni-directional composites.

SMAHC	Increase [%]
UD SMA-TB	90.33
UD SMA-B impact on T	53.32
UD SMA-B impact on B	59.76
5H SMA-TB	145.67
5H SMA-B impact on T	91.17
5H SMA-B impact on B	59.80

(a) Per unit mass

SMAHC	Increase [%]
UD SMA-TB	147.80
UD SMA-B impact on T	77.90
UD SMA-B impact on B	85.37
5H SMA-TB	219.06
5H SMA-B impact on T	127.49
5H SMA-B impact on B	90.16

(b) Per unit thickness

Table 4.2: Percentage increase in impact energy absorption of each SMAHC laminate compared to its baseline.

4.4 Conclusions

In this chapter first the one-dimensional Brinson constitutive model and the three-dimensional (3-D) Sadjadpour and Bhattacharya constitutive model for shape-memory alloy (SMA) are reviewed. The finite element implementation of these models is also considered. Then a multiscale 3-D constitutive modeling approach for shape-memory alloy hybrid composites (SMAHCs) based on the the AEHM approach is proposed. Finally, the use of transformation field analysis (TFA) for reducing the computational cost of the analysis is discussed.

Results for the Brinson model and the Sadjadpour and Bhattacharya model are given. Moreover, samples of SMAHCs were manufactured and tested in laboratory, and a comparison of impact testing results for woven and uni-directional SMAHCs is presented.

Although the 3-D constitutive model for SMA of Sadjadpour and Bhattacharya is used, the approach considered in this chapter is not restricted to this model, but also other existing 3-D models may be employed.

Chapter 5

Multiple plate models theory for laminated composite plates

5.1 Introduction

5.1.1 Motivation

Key components of primary aircraft structures, such as wing skins, wind turbines etc... are currently being designed using laminated composites. Although the structural designer is interested in the global behavior of the structures, phenomena such as impact loading and relative damage have a localized structural effect. Furthermore, for large 3D scale finite element simulation of thick laminate with complex geometries (tapered geometry, non-uniform ply distribution etc...) using finite element methods (FEM) would result in a high computational and meshing time in order to calculate accurate interlaminar stress. In the following we will use the expressions *plate model* and *assumed displacement field* interchangeably.

5.1.2 Mathematical models for laminated composite plates

Plate models dimensionally reduce the full, three-dimensional elasticity problem by imposing constraints on the through-the-thickness variation of the displacement field. A number of reviews [210, 156, 41, 198] have been conducted into the different plate models available for the analysis of laminated composites. In general, these models can be separated into two categories: (i) *equivalent single layer* (ESL) or *smeared* models; and (ii) *discrete layer* (DL) or *layerwise theory* (LWT) models . The equivalent single layer models (for example the classical lamination plate theory (CLT)) offer a computationally efficient method, whereby the number of degrees-of-freedom in the model is independent of the number of laminae, and, especially in case of thin laminates, can offer accurate modeling of the global displacements. However, using the CLT for the estimation of interlaminar stress would be inaccurate since the theory assumes a state of plane stress within each ply and interlaminar shear stresses are obtained from the three-dimensional equilibrium equations. first-order shear deformation plate theory (FSDT) and higher order plate models take into account transverse shear stresses, but have limited accuracy in predicting interlaminar stresses, can not accurately estimate rapid change of slope of the displacement fields across layer interfaces due to variation of mechanical properties with thickness, known as *zig-zag effect*, and do not satisfy the continuity of the interlaminar stress field. The layerwise models offer a solution for thick laminates, at the cost of increased complexity: in *full* layerwise models the number of degrees of freedom in the model is proportional to the number of laminae in the material. Carrera and Ciuffreda [42] conducted an extensive review of these models using various orders of polynomials, and assess their performance under a variety of transverse loading conditions.

Using a low order plate model throughout the structure would not allow users to obtain accurate interlaminar stresses while a discrete layer approach may be computationally expensive. In this chapter a different approach is proposed to accurately calculate interlaminar stress, by employing hierarchical multiple plate models that offer global-local analysis capabilities where different subregions of laminates are analyzed using different plate models. The total displacement field is represented as the mesh superposition of the displacements of a number of plate models. The displacement field is enriched locally where accurate through-the-thickness stresses are required. In this manner, a computationally efficient low order global model can be used to determine gross displacements, and the enriched models can be used to determine stresses at lamina interfaces for the accurate prediction of localized phenomena such as damage initiation and growth. The proposed modeling technique is implemented by combining an extended FEM (XFEM) and multilevel mesh superposition approach (MMSA) . Extra degrees-of-freedom are added to the model to represent the additional displacement fields, and the meshing process remains independent for each field.

5.1.3 Multiple plate models theories

A number of authors have proposed multiple plate models for laminated composites which *simultaneously* combine various plate models.

Barbero and Reddy created the *generalized plate theory* [16, 15] which combines the CLT plate model with a layerwise expansion for the in-plane displacement components, and is defined as a *partial* layerwise plate model by Reddy [200]. The model can be augmented with a discontinuous field using a step function, as explained in [17], in order to model delamination. Robbins and Reddy [198, 203] proposed a hierarchical multiple plate models approach called the *variable kinematic model* (VKM) that combines a FSDT plate model and a *full* layerwise plate model, as well as a discontinuous field for modeling delamination. This is achieved by superposition of meshes in subregions of the model where more accurate information is required. The VKM is expanded in [261] by making the model automatically adaptive. The VKM is limited to only two specific plate models (i.e. FSDT and layerwise).

In Mohite and Upadhyay [156] a region-by-region modeling strategy is adopted whereby full layerwise, partial layerwise and equivalent plate models are used in different regions of the domain. Any model can be placed in any region of the domain. In each region the plate model is fixed. A three-dimensional mesh is required. Changing the type of model in any region of the domain would require remeshing the whole domain.

The use of Murakami's zig-zag function [67] is always as an enhancement to a simpler model, such as FSDT, and can itself be seen as an example of the unification of two different displacement fields.

5.1.4 Hierarchical plate models

The hierarchical modeling of composite structures is achieved through the use of sequence of plate models, each identified by specific parameters, of which the exact solutions constitute a converging sequence to the solution of the fully three-dimensional model. This modeling approach uses a defined methodology for selecting the model with the appropriate level of sofistication from the sequence.

Cho and Oden [48] applied the concept of hierarchical modeling to ESL and DL plates and shells identifying as relevant parameter the order of the displacement field in the through the thickness direction. However, when they applied this concept to laminated structures, the authors did not take into account the microstructure of the laminae.

As pointed out by Actis et al. [1] the concept of hierarchical plate models must not be confused with that of hierarchical finite element spaces. Hierarchical finite element spaces produce a converging sequence of approximate solutions, the limit of which is the exact solution of the particular mathematical model of interest. Hierarchical plate models provide means for controlling modeling errors while hierarchical finite element spaces provide means for controlling discretization errors. Zienkiewicz and Taylor [274] present a review of hierarchical finite element spaces methods.

Williams [253] proposes a model referred to as a *two length scale* or *global-local approach*, by introducing a coupling between the displacement fields used on the two different length scales. The through the thickness displacement function is of arbitrary selection. Delamination can be incorporated using an arbitrary choice of interfacial constitutive relationships. This global-local strategy is presented in its linear form in [157], and proves to be both accurate and efficient. Its worth noting that most authors (e.g. [116]) speak about *multiscale modeling* only when local information is present in the model along all the axis and not only the z-axis.

5.1.5 Mesh superposition techniques

Of particular interest to this work is the concept of *multilevel mesh superpositioning*, which was first introduced by Fish et al. [83] as the *s-version* or *s-refinement* of the finite element method, where the *s* stands for *superpositioning*.

This technique was first developed for the two level case where a coarse mesh (*global mesh*) is superpositioned by an independent, refined mesh (*overlay mesh* or *local mesh*) in order to form a composite mesh. The total displacement field on the composite mesh is the sum of the displacement field interpolated on the global mesh (*global displacement*) and the displacement field interpolated on the local mesh (*local displacement*). The important aspects of this method is that the original mesh does not need to be changed, global and local meshes do not need compatible discretizations and the local mesh can enhance the global mesh regardless of the original global mesh topology. The mesh superpositioning is called *structured* when the superpositioning elements fit entirely within the domain of the superpositioned element. Otherwise the technique is called *unstructued*. The technique was extended to the multilevel case in [85, 87, 189] and to handle discontinuous fields in [82]. The method was applied to laminated composites in [86, 84]. In these applications the displacement fields at the various levels are all based on the same assumed displacement field, hence the subregions differ only in the level of refinement of the interpolated solution.

The approach used to tackle cracks in the s-version FEM is to mesh the superpositioning elements so that they follow the shape of the crack, and to double the number of nodes within the elements on the crack surface in order to represent the discontinuity.

5.1.6 Modeling of delamination using enrichment methods

Another method for handling discontinuities and cracks is the *extended finite element* (XFEM) or *generalized finite element* [20], which, using the partition of unity property of finite elements [147], allows local enrichment functions to be easily incorporated into a finite element approximation for modeling discontinuities without requiring remeshing.

There are two ways of carrying out the enrichment [155]: enriching the shape functions (*intrinsic enrichment*) or adding to the problem additional unknowns or degrees of freedom associated to the enriched solution (*extrinsic enrichment*).

As discussed by Belytschko et al. [20], the s-version FEM is closely related to the XFEM. Lee et al. [132] combined XFEM and s-version FEM for modeling cracks proposing a hybrid method called XSFEM.

Local enrichment can be used for modeling delamination in laminated composites, as delamination can be considered as a particular form of fracturing in which the planes of fracturing are known a priori [59].

5.1.7 Scope of this work

While previous authors limit the analysis to only two levels of superposition [198, 203] or only to specific plate models [86, 84], this paper proposes a hierarchical multiple plate models approach for modelling structural response of thick laminated composite plates in which any number and type of plate models can be superimposed by using a multilevel mesh superposition approach.

Both equivalent ESL and DL plate models are incorporated into the general framework. Geometric nonlinearities are also included in the form of von Kármán equations. Discontinuous through the thickness displacement fields, such as delaminations, are integrated by performing an extrinsic enrichment of the assumed displacement fields. A cohesive law between laminae is used where appropriate.

In implementation, an adaptive method may be adopted to automatically enhance the model in the appropriate regions to the appropriate level of complexity. When a higher level of precision (accurate stress distribution) is required, then the approximation is enhanced in a hierarchical fashion by adding the extra degrees of freedom needed to represent the additional plate models in the regions of interest.

The outline of the chapter is the following. Section 5.2 outlines the general theory of the hierarchical multiple models theory, while sections 5.3 and 5.4 describe the theory in more detail and the finite element formulation, respectively. Section 5.5 evaluates and discusses the accuracy of this approach in determining displacement and stress for various plate geometries and load cases. Section 5.6 draws some conclusions from the results.

5.2 Overview

The general form for the finite element equations for a single plate model is the following [200]

$$\boldsymbol{M}\ddot{\boldsymbol{U}} + \boldsymbol{K}\boldsymbol{U} = \boldsymbol{F} \tag{5.1}$$

where $\boldsymbol{M}$ is the *system mass* matrix, $\boldsymbol{K}$ is the *system stiffness* matrix, $\boldsymbol{U}$ is the vector of the *nodal degrees of freedom* of the system and $\boldsymbol{F}$ is the *system force* vector.

The authors [6] extend equations (5.1) to any number and type of plate models by calculating the total displacement field $\boldsymbol{u}$ as the multilevel mesh superposition [82, 87, 189] (see figure 5-1) of the displacements $\boldsymbol{u}^{\alpha}$ of the M models being considered.

$$\boldsymbol{u}\left(x, y, z, t\right) = \sum_{\alpha=1}^{M} \boldsymbol{u}^{\alpha}\left(x, y, z, t\right) \tag{5.2}$$

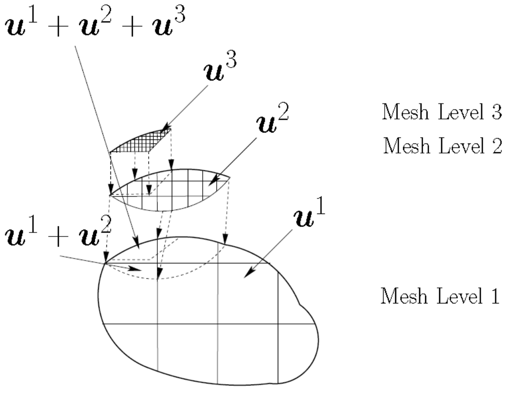

Figure 5-1: Example of multilevel mesh superposition finite element model. The displacement $\boldsymbol{u}^\alpha$ of each plate model being considered is assigned to a different mesh level. Note that the meshing process remains independent for each plate model, which allows the higher mesh levels to be more refined as more localized information is generally needed. In areas where more than one mesh level is present, the total displacement is the superposition of all the displacements in those areas.

As the full, three-dimensional elasticity problem is computationally expensive to solve, plate models dimensionally reduce the problem by constraining the admissible solutions to have a specific dependence on the transverse variable z [215]. The components of the displacement $\boldsymbol{u}^\alpha$ are expressed as follows

$$u_i^\alpha\left(x, y, z, t\right) = U_i^\alpha\left(x, y, t\right) F_i^\alpha\left(z\right) \tag{5.3}$$

where $i = 1, 2, 3$.

For each plate model α the thickness h of the plate is discretized along the z axis (see figure 5-2a) into a number of *mathematical layers* [200, 203] that may consist of several material laminae (*sub-layers*), of a single material lamina (*layer*) or a sub-region of a material lamina (*sub-lamina*). The layers may be assumed to be perfectly bonded together or have displacement steps across interfaces to simulate a delamination event. Each individual lamina and consequently each mathematical layer is assumed to have homogenized mechanical properties.

The displacement $\boldsymbol{u}^\alpha$ is approximated out-of-plane within each mathematical layer using predefined functions, as stylized in figure 5-2b, where for example two plate models are being considered. In this case, model $\boldsymbol{u}^1$ has one equivalent single layer model simulating the three physical layers, while model $\boldsymbol{u}^2$ has one mathematical layer coinciding with only the physical layer in the middle of the plate. Moreover $\boldsymbol{u}^1$ approximates the displacement through-the-thickness of the plate using a linear approximation function, while the displacement is approximated by $\boldsymbol{u}^2$ with a cubic interpolation function. The total displacement field $\boldsymbol{u}$ is the summation (figure 5-2b) of $\boldsymbol{u}^1$ and $\boldsymbol{u}^2$.

When writing the finite element equations, the displacement $\boldsymbol{u}^\alpha$ is further discretized

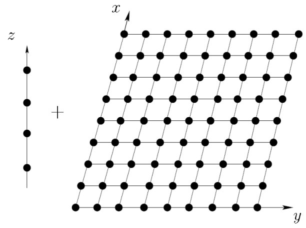

(a) Out-of-plane (z-axis) and in-plane (xy-plane) discretization

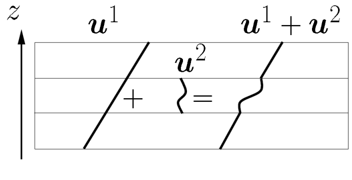

(b) Out-of-plane approximation function

Figure 5-2: Stylized representation of the hierarchical multiple plate models approach. The domain of the plate is discretized both out-of-plane (z-axis) and in-plane (xy-plane). The displacement $\boldsymbol{u}^\alpha$ is approximated out-of-plane within each mathematical layer using predefined functions. The total displacement field $\boldsymbol{u}$ is the summation of $\boldsymbol{u}^1$ and $\boldsymbol{u}^2$.

in the xy-plane (see figure 5-2a). After assembly, the discretized finite element equations for the proposed hierarchical multiple plate model theory are given as follows

$$\boldsymbol{M}_{IJ}^{\alpha\beta}\ddot{\boldsymbol{U}}_I^\alpha + \boldsymbol{K}_{IJ}^{\alpha\beta}\boldsymbol{U}_I^\alpha = \boldsymbol{F}_I^\alpha \tag{5.4}$$

where symbols α and β represent different plate models, while I and J represent different nodes in the out-of-plane discretization of the plate models (or, in equivalent terms, they represent different interfaces between the mathematical layers of the plate models).

In summary, in each node of the 2-D mesh level (in-plane discretization in figure 5-2a) the displacement $\boldsymbol{u}^\alpha$ has a number of degrees of freedom that depends on the number of mathematical layers being considered for model α or, in equivalent terms, on the number of nodes in the out-of-plane discretization (see figure 5-2a) being considered for that model.

It is worth pointing out that using this modeling approach only a 2-D mesh is required instead of a 3-D mesh for a full three-dimensional solid finite element analysis, which simplifies the analysis especially when remeshing is required.

To ensure compatibility of the total displacement field and uniqueness of the solution certain *degrees of freedom* (DOF) should be constrained. For this reason, besides physical boundary conditions additional boundary conditions need to be imposed before

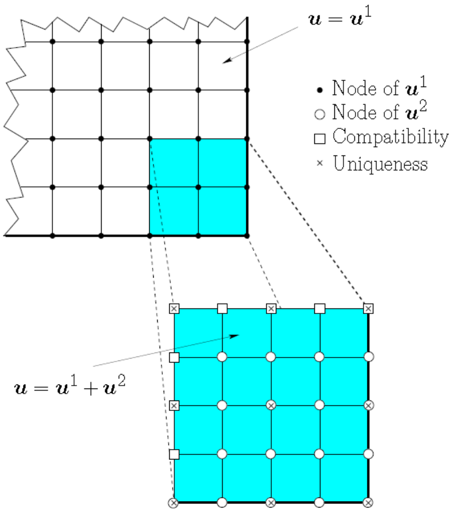

Figure 5-3: Compatibility and uniqueness conditions for the case of structured mesh superposition. Note that the compatibility conditions are not imposed on boundaries that coincide with physical boundaries.

the finite element equations (5.4) can be solved. The additional boundary conditions are generally referred to as *compatibility* and *uniqueness* conditions [261, 189], and are shown in figure 5-3. Note that the compatibility conditions are not imposed on boundaries that coincide with physical boundaries, as displayed in figure 5-3. Here DOF need only to be suppressed in accordance with the physical boundary conditions.

Using an *extended finite element modeling* (XFEM) approach [155], by appropriately defining the boundaries of the *enhancing* displacement fields, the superposition of additional plate models can be used to locally enrich the solution. In this manner, a coarse global plate model can be used to determine gross displacements, and the enriching plate models can be used to determine stresses at lamina interfaces for the accurate prediction of localized phenomena. This is achieved by *extending* the degrees of freedom of the global plate model with the degrees of freedom of the enriching plate models in nodes of the 2-D mesh where accurate interlaminar stresses are required. This technique is normally referred to as *extrinsic enrichment* [155].

5.3 Theory

5.3.1 Notation

Let us consider a open and bounded domain $\Omega \in \Re^3$ with piecewise smooth boundary $\partial\Omega$. The plate is the closure $\overline{\Omega}$ of Ω. The *global* (*laminate*) orthonormal Cartesian co-ordinate system of the plate is denoted as $(x_1, x_2, x_3) = (x, y, z)$ with unit vectors $(\hat{n}_1, \hat{n}_2, \hat{n}_3) = (\hat{n}_x, \hat{n}_y, \hat{n}_z)$. We further assume the z-axis is pointing upward and a right-handed (or positive) system. The boundary $\partial\Omega$ is decomposed as $\partial\Omega = \partial\Omega_u \cup \partial\Omega_t$, where $\partial\Omega_u$ is the boundary where the prescribed displacements are imposed (*Dirichlet boundary conditions*) and $\partial\Omega_t$ is the boundary where the prescribed tractions are imposed (*Neumann boundary conditions*). In general, $\partial\Omega_t$ is a curved surface with a unit normal $\hat{n}_n = n_x\hat{n}_x + n_y\hat{n}_y$ defined to be outward with respect to Ω.

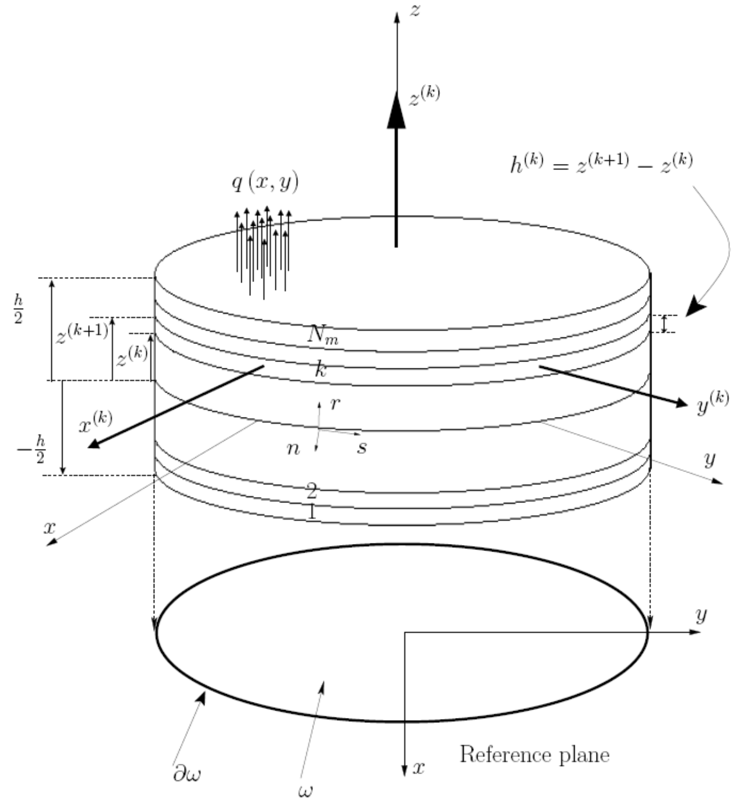

Figure 5-4: Geometry of a laminated plate with curved boundary, including coordinate systems and layer numbering

We will assume the xy-plane (*reference* plane) of the problem to coincide with the midplane ($z = 0$) of Ω and the total thickness of Ω to be h, as shown in Figure 5-4. Moreover, the midplane is assumed to be an open and bounded region $\omega \in \Re^2$ with piecewise smooth boundary $\partial\omega$, so that the total domain $\Omega = \omega \times (-h/2, h/2)$. The boundary $\partial\Omega$ then consists of the union of the plate's top and bottom surfaces $\partial\Omega_u = \omega \times \{-h/2, h/2\}$ and by the lateral surface $\partial\Omega_t = \partial\omega \times (-h/2, h/2)$. A typical point P in Ω is denoted by $\boldsymbol{x} = (\underset{\sim}{x}, x_3) = (\underset{\sim}{x}, z)$, where $\underset{\sim}{x} \in \omega$ and $-h/2 \leq z \leq h/2$.

5.3.2 Total displacement field

The total displacement field $\boldsymbol{u}$ in the proposed hierarchical multiple plate models approach is given in (5.5) by the superposition [85, 87, 189] in Ω of all the individual plate models $\boldsymbol{u}^{\alpha}$ being considered

$$\boldsymbol{u}\left(x,y,z,t\right)=\sum_{\alpha=1}^{M}\boldsymbol{u}^{\alpha}\left(x,y,z,t\right) \tag{5.5}$$

where M is the total number of plate models. A material point occupying the position (x,y,z) in the undeformed laminate moves to the position $(x+u,y+v,z+w)$ in the deformed laminate, where $\boldsymbol{u}=u\hat{e}_x+v\hat{e}_y+w\hat{e}_z$.

5.3.3 Dimensional reduction

As discussed in section 5.1, the full, three-dimensional elasticity problem is computationally expensive to solve. For this reason the problem is dimensionally reduced by semi-discretization. Each plate model α is obtained by constraining the admissible solutions of the three-dimensional problem to have a specific dependence on the transverse variable z. In particular, the problem is discretized only in the transverse direction z [215], while the spatial x and y and time t co-ordinates are left unchanged.

Based on the above assumptions, the components of assumed displacement field for any plate model α can be expressed as follows

$$u_i^{\alpha}\left(x,y,z,t\right)=U_i^{\alpha}\left(\underset{\sim}{x},t\right)F_i^{\alpha}\left(z\right) \tag{5.6}$$

where $i=1,2,3$. U_i^{α} is function only of the variables associated with the midplane $\underset{\sim}{x}$ and time t, while F_i^{α} is function only of the transverse variable z

5.3.4 Material layers

The composite laminated plate is composed of N_m orthotropic material laminae, as shown in Figure 5-4. Each lamina k is of uniform thickness $h^{(k)}=z^{(k+1)}-z^{(k)}$, where $z^{(k)}$ is the co-ordinate of the interface between the k-th and the $(k+1)$-th material layers. The *local* (*layer* or *material*) Cartesian orthonormal co-ordinate system of the k-th layer is denoted as $\left(x_1^{(k)},x_2^{(k)},x_3^{(k)}\right)=\left(x^{(k)},y^{(k)},z^{(k)}\right)$, with $x^{(k)}$ oriented at an angle $\theta^{(k)}$ with respect to the global co-ordinate x. The angle $\theta^{(k)}$ is aligned with the direction of the fibers in the lamina k. The k-th material layer is defined in $z^{(k)}\leq z\leq z^{(k+1)}$. The global and local co-ordinate systems are collinear along the z directions.

5.3.5 Out-of-plane discretization

In order to determine the through the thickness stresses, the microstructure of the laminate, e. g. fibers and matrix constituents and fibers/matrix interface of each lamina, has to be accounted for. We will take into account only of the homogenized mechanical properties of each individual lamina. For each model α the thickness h of the plate can be discretized along the z axis into a number of mathematical layers N_L^α that is independent from the number of material layers N_m. A mathematical layer may consist of several material laminae (*sub-layers*), of a single material lamina or a sub-region of a material lamina (*sub-lamina*). Under the above assumptions, each mathematical layer can be represented by the equivalent homogeneous mechanical properties of the laminae that compose it. The layers may be assumed to be perfectly bonded together or have displacement jumps across interfaces due to delaminations.

Formally, the out-of-plane discretization can be viewed as a partition $\mathcal{P}_z^\alpha$ of the z axis into N_L^α intervals through the thickness of the plate.

$$\mathcal{P}_z^\alpha = \left\{ z \in Z_I^\alpha \mid Z_I^\alpha = \left(z_I^\alpha, z_{I+1}^\alpha\right), Z_I^\alpha \in (-h/2, h/2), I = 1, \ldots, N_L^\alpha \right\} \tag{5.7}$$

where $Z_I^\alpha \bigcap Z_J^\alpha = \emptyset$, if $Z_I^\alpha \in \mathcal{P}_z^\alpha$ and $Z_J^\alpha \in \mathcal{P}_z^\alpha$ and $I \neq J$, and $\bigcup \bar{Z}_I^\alpha = [-h/2, h/2]$.

We define the measure (*length*) of subdomains Z_I^α as $\lambda\left(Z_I^\alpha\right)$. The out-of-plane *discretization step* is then equal to $\lambda\left(Z_I^\alpha\right)$. The exact solution of the semi-discretized problem converges asymptotically to the continuous one [64] as the discretization step along z tends to zero.

5.3.6 Domain of a model

It's useful at this stage to introduce the concept of domain of a model. This concept will be used later for example for imposing compatibility conditions on the assumed displacement fields, i.e. boundary conditions between different models domains.

As we have seen in equation (5.6), the dimensionally reduced displacement field α is the product of an in-plane function and an out of plane function. The domain of a model α is then the product of an in-plane domain and an out-of-plane domain.

If the set of available mathematical models in Ω is defined as $\mathcal{M} = \{1, \ldots, M\}$, then the domain ω can be partitioned into P subdomains ω_i with boundaries $\partial\omega_i$, where within each subdomain ω_i only a subset of models $\mathcal{M}_i \subseteq \mathcal{M}$ are used. This partition is called $\mathcal{P}_\omega$, and can defined formally as follows

$$\mathcal{P}_\omega = \{\omega_i \mid \omega_i \subseteq \omega, 1 \leq i \leq P\} \tag{5.8}$$

where $\omega_i \bigcap \omega_j = \emptyset$, if $\omega_i \in \mathcal{P}_\omega$, $\omega_j \in \mathcal{P}_\omega$ and $i \neq j$, and $\bigcup \bar{\omega}_i = \bar{\omega}$.

The number of elements of $\mathcal{M}_i$ is called the *cardinality* of $\mathcal{M}_i$ and is denoted $|\mathcal{M}_i|$. The *greatest element* S_i of $\mathcal{M}_i$ is the element of $\mathcal{M}_i$ which is greater than or equal to any other element of $\mathcal{M}_i$.

We define the in-plane domain ω^α with boundary $\partial\omega^\alpha$ of a model α as a subdomain of ω which is the union of all subdomains ω_i where the model α is utilized. Formally we can write, $\omega^\alpha = \bigcup \omega_i$ for all subdomains ω_i such that $\alpha \in \mathcal{M}_i$. The elements of the in-plane domain are $\underset{\sim}{x} \in \omega^\alpha$.

We define the out-of-plane domain of a model α as any subset of intervals $\left\{Z_1^\alpha, Z_2^\alpha, \ldots, Z_{N_I^\alpha}^\alpha\right\}$ within the partition $\mathcal{P}_z^\alpha$, with $N_I^\alpha \leq N_L^\alpha$, where the model α is utilized. Some of these intervals may be contiguous, but in general this is not a requirement for the intervals. The elements of the out-of-plane domain are $z^\alpha \in \left\{Z_1^\alpha, Z_2^\alpha, \ldots, Z_{N_I^\alpha}^\alpha\right\}$ and $z_I^\alpha \in Z_I^\alpha$.

The domain of a model α then is $\omega^\alpha \times \left\{Z_1^\alpha, Z_2^\alpha, \ldots, Z_{N_I^\alpha}^\alpha\right\}$, which in general is equal to one or more disjoint volumes.

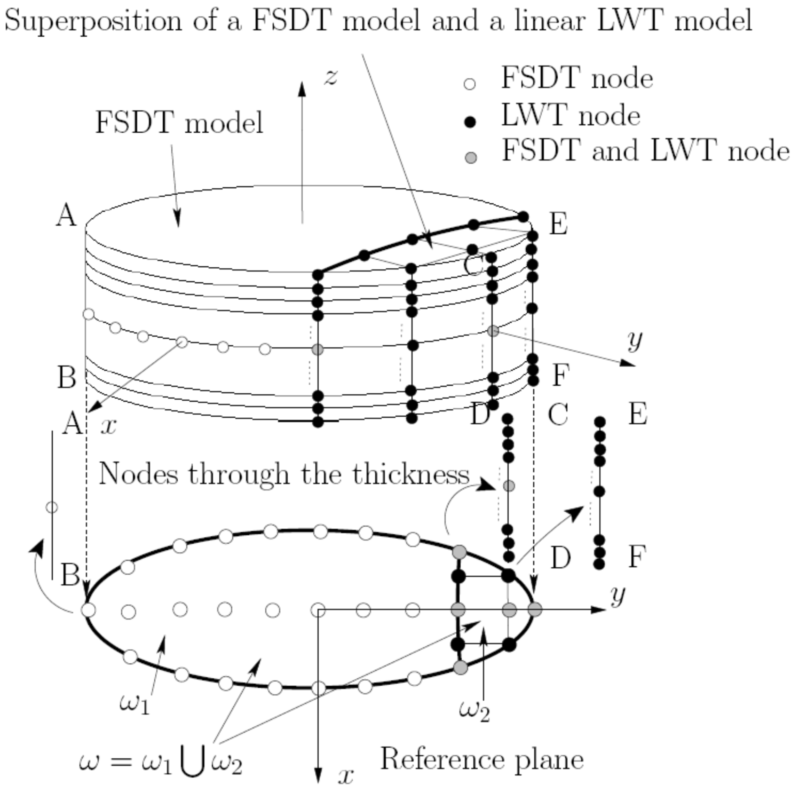

Figure 5-5: Superposition of a FSDT model with a linear LWT model

For example, in the case of the superposition of a FSDT with a linear LWT model displayed in Figure 5-5, as the FSDT theory can be represented by the superposition of two assumed displacement fields $\{1, 2\}$ and we refer to the linear LWT as model 3, the set of available mathematical models in Ω is $\mathcal{M} = \{1, 2, 3\}$. In subdomain ω_1 only the FSDT model is available, so $\mathcal{M}_1 = \{1, 2\}$. In subdomain ω_2 both FSDT and linear LWT models are available, so $\mathcal{M}_2 = \{1, 2, 3\}$. The in-plane domain of the FSDT model coincides with ω, while the in-plane domain of the linear LWT model equal to ω_2.

5.3.7 Out-of-plane approximation functions

In each interval Z_I^α the displacement variables $U\overset{\alpha}{\underset{i}{I}}$ can be approximated using a predefined approximation function $F\overset{\alpha}{\underset{i}{I}}$ of degree $L\overset{\alpha}{\underset{i}{I}}$. For simplicity, if we assume that the components of the displacement are approximated using the same functions then we can drop the index i and write

$$F^{\alpha}_{I}\left(z^{\alpha}_{I}\right) = \sum_{l=0}^{L^{\alpha}_{I}} F^{\alpha}_{\underset{l}{I}}\left(z^{\alpha}_{I}\right)^{l} \tag{5.9}$$

for $z^{\alpha}_{I} \in Z^{\alpha}_{I}$. Note that here l is the exponential operator.

5.3.8 Number of nodes through the thickness

The number of nodes through the thickness of the plate in each point $\underset{\sim}{x}$ for a model α is equal to

$$N^{\alpha}_{p} = \sum_{I=1}^{N^{\alpha}_{I}} \left(L^{\alpha}_{I} + 1\right) \tag{5.10}$$

if all N^{α}_{I} intervals are contiguous. Otherwise the expression in (5.10) is increased by one for every non contiguous intervals.

For example, in the case of the superposition of a FSDT with a linear LWT model displayed in Figure 5-5, there is one node through the thickness for the FSDT model in ω, while there are $N_m + 1$ nodes through the thickness for the linear LWT model in ω_2, if a number of subdivisions through the thickness equivalent to the number of material layers N_m is used for the LWT.

5.3.9 Layer semidiscretized displacement fields

Now, introducing the concept of mathematical layers into definition (5.6), we can write

$$u^{\alpha}_{i}\left(\underset{\sim}{x}, z, t\right) = \sum_{I=1}^{N^{\alpha}_{p}} U^{\alpha}_{\underset{i}{I}}\left(\underset{\sim}{x}, t\right) F^{\alpha}_{\underset{i}{I}}\left(z\right) \tag{5.11}$$

where $i = 1, \ldots, 3$, $\underset{\sim}{x} \in \omega^{\alpha}$ and $z \in \left\{Z^{\alpha}_{1}, \ldots, Z^{\alpha}_{N^{\alpha}_{I}}\right\}$.

In equation (5.11) the variables $\boldsymbol{U}^{\alpha}_{I}$ are called the *generalized displacements* or *kinematic variables* for the assumed displacement field α, and are the unknowns of the problem. In the global coordinate system (x, y, z) the components of $\boldsymbol{U}^{\alpha}_{I}$ are $(U^{\alpha}_{I}, V^{\alpha}_{I}, W^{\alpha}_{I})$.

$\boldsymbol{F}^{\alpha}_{I}$ are 1-D *a-priori* selected approximation functions that are continuous within one or more contiguous mathematical layers. Here, for simplicity, the functions are assumed to have the same components $(F^{\alpha}_{I}, F^{\alpha}_{I}, F^{\alpha}_{I})$ along the x-, y- and z-directions, then the same number of points through the thickness N^{α}_{p} can be used for the components of displacement field α

Equation (5.11) can be written as

$$u^{\alpha} = \sum_{I=1}^{N_p^{\alpha}} U_I^{\alpha} F_I^{\alpha} \qquad v^{\alpha} = \sum_{I=1}^{N_p^{\alpha}} V_I^{\alpha} F_I^{\alpha} \qquad w^{\alpha} = \sum_{I=1}^{N_p^{\alpha}} W_I^{\alpha} F_I^{\alpha} \tag{5.12}$$

5.3.10 Functional degrees of freedom

The *functional degrees of freedom* (FDOF) or *nodal degrees of freedom* of the multiple models theory can be very useful when comparing different combinations of models. This parameter has the following definition

$$FDOF = 3 \left(\sum_{\alpha=1}^{M} N_p^{\alpha} \right) \tag{5.13}$$

and is in general a function of $\underset{\sim}{x}$.

5.3.11 Displacements and strains

The nonlinear strains associated with the total displacement field in equations (5.3.2) and (5.11) can be calculated using the von Kármán equations [57]. The nonlinear strains are given in equations (5.14).

$$\varepsilon_{xx} = \sum_{\alpha=1}^{M} \left(\sum_{I=1}^{N_p^{\alpha}} \frac{\partial U_I^{\alpha}}{\partial x} F_I^{\alpha} \right) + \frac{1}{2} \sum_{\alpha,\beta=1}^{M} \left[\left(\sum_{I=1}^{N_p^{\alpha}} \frac{\partial W_I^{\alpha}}{\partial x} F_I^{\alpha} \right) \left(\sum_{J=1}^{N_p^{\beta}} \frac{\partial W_J^{\beta}}{\partial x} F_J^{\beta} \right) \right] \tag{5.14a}$$

$$\varepsilon_{yy} = \sum_{\alpha=1}^{M} \left(\sum_{I=1}^{N_p^{\alpha}} \frac{\partial V_I^{\alpha}}{\partial y} F_I^{\alpha} \right) + \frac{1}{2} \sum_{\alpha,\beta=1}^{M} \left[\left(\sum_{I=1}^{N_p^{\alpha}} \frac{\partial W_I^{\alpha}}{\partial y} F_I^{\alpha} \right) \left(\sum_{J=1}^{N_p^{\beta}} \frac{\partial W_J^{\beta}}{\partial y} F_J^{\beta} \right) \right] \tag{5.14b}$$

$$\varepsilon_{zz} = \sum_{\alpha=1}^{M} \left(\sum_{I=1}^{N_p^{\alpha}} W_I^{\alpha} \frac{dF_I^{\alpha}}{dz} \right) \tag{5.14c}$$

$$\gamma_{yz} = \sum_{\alpha=1}^{M} \left(\sum_{I=1}^{N_p^{\alpha}} V_I^{\alpha} \frac{dF_I^{\alpha}}{dz} + \sum_{I=1}^{N_p^{\alpha}} \frac{\partial W_I^{\alpha}}{\partial y} F_I^{\alpha} \right) \tag{5.14d}$$

$$\gamma_{zx} = \sum_{\alpha=1}^{M} \left(\sum_{I=1}^{N_p^{\alpha}} U_I^{\alpha} \frac{dF_I^{\alpha}}{dz} + \sum_{I=1}^{N_p^{\alpha}} \frac{\partial W_I^{\alpha}}{\partial x} F_I^{\alpha} \right) \tag{5.14e}$$

$$\gamma_{xy} = \sum_{\alpha=1}^{M}\left[\sum_{I=1}^{N_p^\alpha}\left(\frac{\partial U_I^\alpha}{\partial y} + \frac{\partial V_I^\alpha}{\partial x}\right)F_I^\alpha\right] + \sum_{\alpha,\beta=1}^{M}\left[\left(\sum_{I=1}^{N_p^\alpha}\frac{\partial W_I^\alpha}{\partial x}F_I^\alpha\right)\left(\sum_{J=1}^{N_p^\beta}\frac{\partial W_J^\beta}{\partial y}F_J^\beta\right)\right] \tag{5.14f}$$

5.3.12 Equations of motion

The equations of motion can be derived using the dynamic version of the principle of virtual displacements

$$0 = \int_0^T (\delta U + \delta V - \delta K)\,\mathrm{d}t \tag{5.15}$$

where δU is the virtual strain energy, δV is the virtual work done by the applied forces, δK is the virtual kinetic energy and T is the time interval.

The virtual strain energy can be expressed as

$$\delta U = \int_\Omega \Big\{\sigma_{xx}\delta\varepsilon_{xx} + \sigma_{yy}\delta\varepsilon_{yy} + \sigma_{zz}\delta\varepsilon_{zz} + \sigma_{yz}\delta\gamma_{yz} + \sigma_{zx}\delta\gamma_{zx} + \sigma_{xy}\delta\gamma_{xy}\Big\}\mathrm{d}\Omega \tag{5.16}$$

The virtual work done by the applied forces, in the case of a distributed load, is

$$\delta V = -\int_\Omega q\delta w \mathrm{d}\Omega \tag{5.17}$$

The virtual kinetic energy is

$$\delta K = \int_\Omega \Big\{\rho_0\Big(\dot{u}\delta\dot{u} + \dot{v}\delta\dot{v} + \dot{w}\delta\dot{w}\Big)\Big\}\mathrm{d}\Omega \tag{5.18}$$

where ρ_0 is the density of the plate material and a dot on the variable indicates time derivative.

For laminated plate structures the following relation stands true

$$\int_\Omega \Big\{\Big\}\mathrm{d}\Omega = \int_\omega \Big\{\int_{-\frac{h}{2}}^{\frac{h}{2}} \Big\{\Big\}\mathrm{d}z\Big\}\mathrm{d}x\mathrm{d}y = \int_\omega \Big\{\sum_{k=1}^{N_m}\int_{z_b^{(k)}}^{z_t^{(k)}} \Big\{\Big\}\mathrm{d}z\Big\}\mathrm{d}x\mathrm{d}y \tag{5.19}$$

where N_m is the number of material layers in the laminate, $z_b^{(k)} = z^{(k)}$ and $z_t^{(k)} = z^{(k+1)}$ are the co-ordinates of the bottom and top of the k-layer.

Defining the *force resultants*, the *moment resultants* and the *mass moments of* *inertia* as

$$
\begin{aligned}
\left\{ \underset{1}{N^{\alpha}_{I}} \quad \underset{2}{N^{\alpha}_{I}} \quad \underset{4}{N^{\alpha}_{I}} \quad \underset{5}{N^{\alpha}_{I}} \quad \underset{6}{N^{\alpha}_{I}} \right\}^{T} &= \sum_{k=1}^{N_m} \int_{z_b^{(k)}}^{z_t^{(k)}} \left\{ \sigma_{xx} \quad \sigma_{yy} \quad \sigma_{yz} \quad \sigma_{zx} \quad \sigma_{xy} \right\}^{T} F^{\alpha}_{I} \mathrm{d}z \\
\left\{ \underset{3}{\tilde{N}^{\alpha}_{I}} \quad \underset{4}{\tilde{N}^{\alpha}_{I}} \quad \underset{5}{\tilde{N}^{\alpha}_{I}} \right\}^{T} &= \sum_{k=1}^{N_m} \int_{z_b^{(k)}}^{z_t^{(k)}} \left\{ \sigma_{zz} \quad \sigma_{yz} \quad \sigma_{zx} \right\}^{T} \frac{dF^{\alpha}_{I}}{\mathrm{d}z} \mathrm{d}z \\
\left\{ \underset{nn}{\hat{N}^{\alpha}_{I}} \quad \underset{ns}{\hat{N}^{\alpha}_{I}} \quad \underset{nz}{\hat{N}^{\alpha}_{I}} \right\}^{T} &= \sum_{k=1}^{N_m} \int_{z_b^{(k)}}^{z_t^{(k)}} \left\{ \hat{\sigma}_{nn} \quad \hat{\sigma}_{ns} \quad \hat{\sigma}_{nz} \right\}^{T} F^{\alpha}_{I} \mathrm{d}z \\
\left\{ \underset{1}{Q^{\alpha\beta}_{IJ}} \quad \underset{2}{Q^{\alpha\beta}_{IJ}} \quad \underset{6}{Q^{\alpha\beta}_{IJ}} \right\}^{T} &= \sum_{k=1}^{N_m} \int_{z_b^{(k)}}^{z_t^{(k)}} \left\{ \sigma_{xx} \quad \sigma_{yy} \quad \sigma_{xy} \right\}^{T} F^{\alpha}_{I} F^{\beta}_{J} \mathrm{d}z \\
I^{\alpha\beta}_{IJ} &= \sum_{k=1}^{N_m} \int_{z_b^{(k)}}^{z_t^{(k)}} \rho_0^{(k)} F^{\alpha}_{I} F^{\beta}_{J} \mathrm{d}z
\end{aligned}
\tag{5.20}
$$

and integrating through the thickness of the laminate, we can write

$$
\begin{aligned}
\delta U = &\int_{\omega} \sum_{\alpha=1}^{M} \Bigg\{ \sum_{I=1}^{N_p^{\alpha}} \Bigg[\underset{1}{N^{\alpha}_{I}} \frac{\partial \delta U^{\alpha}_{I}}{\partial x} + \underset{2}{N^{\alpha}_{I}} \frac{\partial \delta V^{\alpha}_{I}}{\partial y} + \underset{4}{N^{\alpha}_{I}} \frac{\partial \delta W^{\alpha}_{I}}{\partial y} + \underset{5}{N^{\alpha}_{I}} \frac{\partial \delta W^{\alpha}_{I}}{\partial x} + \underset{6}{N^{\alpha}_{I}} \left(\frac{\partial \delta U^{\alpha}_{I}}{\partial y} + \frac{\partial \delta V^{\alpha}_{I}}{\partial x} \right) \\
&\qquad + \underset{3}{\tilde{N}^{\alpha}_{I}} \delta W^{\alpha}_{I} + \underset{4}{\tilde{N}^{\alpha}_{I}} \delta V^{\alpha}_{I} + \underset{5}{\tilde{N}^{\alpha}_{I}} \delta U^{\alpha}_{I} \Bigg] \Bigg\} \mathrm{d}x \mathrm{d}y \\
+ &\int_{\omega} \sum_{\alpha,\beta=1}^{M} \Bigg\{ \sum_{I=1}^{N_p^{\alpha}} \sum_{J=1}^{N_p^{\beta}} \Bigg[\underset{1}{Q^{\alpha\beta}_{IJ}} \frac{\partial \delta W^{\alpha}_{I}}{\partial x} \frac{\partial W^{\beta}_{J}}{\partial x} + \underset{2}{Q^{\alpha\beta}_{IJ}} \frac{\partial \delta W^{\alpha}_{I}}{\partial y} \frac{\partial W^{\beta}_{J}}{\partial y} + \underset{6}{Q^{\alpha\beta}_{IJ}} \left(\frac{\partial \delta W^{\alpha}_{I}}{\partial x} \frac{\partial W^{\beta}_{J}}{\partial y} + \frac{\partial W^{\alpha}_{I}}{\partial x} \frac{\partial \delta W^{\beta}_{J}}{\partial y} \right) \Bigg] \Bigg\} \mathrm{d}x \mathrm{d}y
\end{aligned}
\tag{5.21}
$$

$$
\delta V = -\int_{\omega} \left[q_b(\underset{\sim}{x}) \delta w(\underset{\sim}{x}, -h/2) + q_t(\underset{\sim}{x}) \delta w(\underset{\sim}{x}, h/2) \right] \mathrm{d}x \mathrm{d}y - \int_{\partial\Omega_t} \int_{-\frac{h}{2}}^{\frac{h}{2}} \left(\hat{\sigma}_{nn} \delta u_n + \hat{\sigma}_{ns} \delta u_s + \hat{\sigma}_{nz} \delta w \right) \mathrm{d}z \mathrm{d}s
$$

$$
\delta V = -\int_{\omega} \sum_{\alpha=1}^{M} \left(q_b \delta W^{\alpha}_{1} + q_t \delta W^{\alpha}_{N_p^{\alpha}} \right) \mathrm{d}x \mathrm{d}y - \int_{\partial\Omega_t} \sum_{\alpha=1}^{M} \left[\sum_{I=1}^{N_p^{\alpha}} \left(\underset{nn}{\hat{N}^{\alpha}_{I}} \underset{n}{\delta U^{\alpha}_{I}} + \underset{ns}{\hat{N}^{\alpha}_{I}} \underset{s}{\delta U^{\alpha}_{I}} + \underset{nz}{\hat{N}^{\alpha}_{I}} \delta W^{\alpha}_{I} \right) \right] \mathrm{d}s
\tag{5.22}
$$

$$
\delta K = \int_{\omega} \sum_{\alpha,\beta=1}^{M} \left[\sum_{I=1}^{N_p^{\alpha}} \sum_{J=1}^{N_p^{\beta}} I^{\alpha\beta}_{IJ} \left(\dot{U}^{\alpha}_{I} \delta \dot{U}^{\beta}_{J} + \dot{V}^{\alpha}_{I} \delta \dot{V}^{\beta}_{J} + \dot{W}^{\alpha}_{I} \delta \dot{W}^{\beta}_{J} \right) \right] \mathrm{d}x \mathrm{d}y
\tag{5.23}
$$

where $q_b(\underset{\sim}{x})$ and $\delta w(\underset{\sim}{x}, -h/2)$ are respectively the distributed stress and the component along z of the displacement on the bottom of the plate $\left(z = -\frac{h}{2}\right)$, $q_t(\underset{\sim}{x})$ and

$\delta w\big(\underset{\sim}{x}, h/2\big)$ are respectively the distributed stress and the component along z of the displacement on the top of the plate $\left(z = \frac{h}{2}\right)$ and $q = q_b + q_t$. $\mathrm{d}s$ is the arc-length of an infinitesimal line element along the boundary. $(\hat{\sigma}_{nn}, \hat{\sigma}_{ns}, \hat{\sigma}_{nz})$ are the specified stress components on the portion $\partial\Omega_t$ of the boundary, where n is the normal direction and s is the tangential direction on $\partial\Omega$, as shown in Figure 5-4. Note that if the unit outward normal vector is oriented at an angle θ from the x-axis with cosine directors $n_x = \cos\theta$ and $n_y = \sin\theta$, then the transformation between the coordinate systems (x, y, z) and (n, s, r) is

$$\begin{aligned}
\hat{n}_x &= \cos\theta \hat{n}_n + \sin\theta \hat{n}_s \\
\hat{n}_y &= -\cos\theta \hat{n}_n + \sin\theta \hat{n}_s \\
\hat{n}_z &= \hat{n}_r
\end{aligned} \tag{5.24}$$

In virtue of equations (5.24) the displacements $\big(\underset{n}{U^{\alpha}_{I}}, \underset{s}{U^{\alpha}_{I}}\big)$ are related to $\big(U^{\alpha}_{I}, V^{\alpha}_{I}\big)$ by

$$\underset{n}{U^{\alpha}_{I}} = n_x U^{\alpha}_{I} + n_y V^{\alpha}_{I} \tag{5.25}$$

$$\underset{s}{U^{\alpha}_{I}} = -n_x U^{\alpha}_{I} + n_y V^{\alpha}_{I} \tag{5.26}$$

Substituting the expressions of δU, δV and δK in equations (5.21), (5.22) and (5.23) in equation (5.15), collecting the coefficients of each generalized displacement $(\delta U^{\alpha}_{I}, \delta V^{\alpha}_{I}, \delta W^{\alpha}_{I})$ and setting these coefficients to zero separately over ω, we obtain the following Euler-Lagrange equations of the theory

$$\begin{aligned}
\delta U^{\alpha}_{I}: &\quad \frac{\partial \underset{1}{N^{\alpha}_{I}}}{\partial x} + \frac{\partial \underset{6}{N^{\alpha}_{I}}}{\partial y} + \underset{5}{\tilde{N}^{\alpha}_{I}} = \sum_{\beta=1}^{M} \left(\sum_{J=1}^{N^{\beta}_{p}} I^{\alpha\beta}_{IJ} \frac{\partial U^{\beta}_{J}}{\partial t^2} \right) \\
\delta V^{\alpha}_{I}: &\quad \frac{\partial \underset{2}{N^{\alpha}_{I}}}{\partial y} + \frac{\partial \underset{6}{N^{\alpha}_{I}}}{\partial x} + \underset{4}{\tilde{N}^{\alpha}_{I}} = \sum_{\beta=1}^{M} \left(\sum_{J=1}^{N^{\beta}_{p}} I^{\alpha\beta}_{IJ} \frac{\partial V^{\beta}_{J}}{\partial t^2} \right) \\
\delta W^{\alpha}_{I}: &\quad \frac{\partial \underset{4}{N^{\alpha}_{I}}}{\partial y} + \frac{\partial \underset{5}{N^{\alpha}_{I}}}{\partial x} + \underset{3}{\tilde{N}^{\alpha}_{I}} - q_b - q_t + \sum_{\beta=1}^{M} \left\{ \sum_{J=1}^{N^{\beta}_{p}} \left[\frac{\partial}{\partial x} \left(\underset{1}{Q^{\alpha\beta}_{IJ}} \frac{\partial W^{\beta}_{J}}{\partial x} + \underset{6}{Q^{\alpha\beta}_{IJ}} \frac{\partial W^{\beta}_{J}}{\partial y} \right) \right.\right. \\
&\quad \left.\left. + \frac{\partial}{\partial y} \left(\underset{2}{Q^{\alpha\beta}_{IJ}} \frac{\partial W^{\beta}_{J}}{\partial y} + \underset{6}{Q^{\alpha\beta}_{IJ}} \frac{\partial W^{\beta}_{J}}{\partial x} \right) \right] \right\} = \sum_{\beta=1}^{M} \sum_{J=1}^{N^{\beta}_{p}} I^{\alpha\beta}_{IJ} \frac{\partial W^{\beta}_{J}}{\partial t^2}
\end{aligned} \tag{5.27}$$

Note that in the equations above integration-by-parts (spatial and time) was used to relieve the generalized displacements of any differentiation of the variational operator δ, in order to use the fundamental lemma of calculus. Also the terms in ω evaluated at $t = 0$ were set to 0 because the generalized displacements are zero there.

The *essential* (*geometric*) boundary conditions for the theory are imposed on U_I^α, V_I^α and W_I^α. The *natural* (*force*) boundary conditions for the theory are

$$\begin{aligned}
N\overset{\alpha}{\underset{nn}{I}} - \hat{N}\overset{\alpha}{\underset{nn}{I}} &= 0\\
N\overset{\alpha}{\underset{ns}{I}} - \hat{N}\overset{\alpha}{\underset{ns}{I}} &= 0\\
N\overset{\alpha}{\underset{nz}{I}} - \hat{N}\overset{\alpha}{\underset{nz}{I}} &= 0
\end{aligned} \tag{5.28}$$

where

$$\begin{aligned}
N\overset{\alpha}{\underset{nn}{I}} &= N\overset{\alpha}{\underset{1}{I}}\, n_x + N\overset{\alpha}{\underset{6}{I}}\, n_y\\
N\overset{\alpha}{\underset{ns}{I}} &= N\overset{\alpha}{\underset{6}{I}}\, n_x + N\overset{\alpha}{\underset{2}{I}}\, n_y\\
N\overset{\alpha}{\underset{nz}{I}} &= N\overset{\alpha}{\underset{5}{I}}\, n_x + N\overset{\alpha}{\underset{4}{I}}\, n_y + \sum_{\beta=1}^{M}\left[\sum_{J=1}^{N_p^\beta}\left(Q\overset{\alpha\beta}{\underset{1}{IJ}}\,\frac{\partial W_J^\beta}{\partial x} + Q\overset{\alpha\beta}{\underset{6}{IJ}}\,\frac{\partial W_J^\beta}{\partial y}\right)n_x + \left(Q\overset{\alpha\beta}{\underset{2}{IJ}}\,\frac{\partial W_J^\beta}{\partial y} + Q\overset{\alpha\beta}{\underset{6}{IJ}}\,\frac{\partial W_J^\beta}{\partial x}\right)n_y\right]
\end{aligned}$$

The *primary* variables (displacements) and *secondary* variables (forces) for the hierarchical multiple plate models theory are

$$\text{Primary variables:} \qquad U\overset{\alpha}{\underset{n}{I}}, U\overset{\alpha}{\underset{s}{I}}; W_I^\alpha \tag{5.29}$$

$$\text{Secondary variables:} \qquad N\overset{\alpha}{\underset{nn}{I}}, N\overset{\alpha}{\underset{ns}{I}}; N\overset{\alpha}{\underset{nz}{I}} \tag{5.30}$$

5.3.13 Laminate Constitutive Equations

For the k-th (orthotropic) mathematical layer we have the following 3-D stress-strain relationships

$$\begin{Bmatrix} \sigma_{xx}\\ \sigma_{yy}\\ \sigma_{zz}\\ \sigma_{yz}\\ \sigma_{zx}\\ \sigma_{xy} \end{Bmatrix}^{(k)} = \begin{bmatrix} \bar{C}_{11}^{(k)} & \bar{C}_{12}^{(k)} & \bar{C}_{13}^{(k)} & 0 & 0 & \bar{C}_{16}^{(k)}\\ \bar{C}_{21}^{(k)} & \bar{C}_{22}^{(k)} & \bar{C}_{23}^{(k)} & 0 & 0 & \bar{C}_{26}^{(k)}\\ \bar{C}_{31}^{(k)} & \bar{C}_{32}^{(k)} & \bar{C}_{33}^{(k)} & 0 & 0 & \bar{C}_{36}^{(k)}\\ 0 & 0 & 0 & \bar{C}_{44}^{(k)} & \bar{C}_{45}^{(k)} & 0\\ 0 & 0 & 0 & \bar{C}_{54}^{(k)} & \bar{C}_{55}^{(k)} & 0\\ \bar{C}_{61}^{(k)} & \bar{C}_{62}^{(k)} & \bar{C}_{63}^{(k)} & 0 & 0 & \bar{C}_{66}^{(k)} \end{bmatrix}^{(k)} \begin{Bmatrix} \varepsilon_{xx}\\ \varepsilon_{yy}\\ \varepsilon_{zz}\\ \gamma_{yz}\\ \gamma_{zx}\\ \gamma_{xy} \end{Bmatrix}^{(k)} \tag{5.31}$$

where $\bar{C}_{ij}^{(k)}$ are the transformed elastic coefficients in the global (laminate) co-ordinates, which are related to the elastic coefficients in the local (layer) co-ordinates $C_{ij}^{(k)}$ by the following relationship

$$\bar{\boldsymbol{C}} = \boldsymbol{T}\boldsymbol{C}\boldsymbol{T}^T \tag{5.32}$$

where $\boldsymbol{T}$ is the transformation tensor with components

$$T_{ij} = \begin{bmatrix} cos^2\theta^{(k)} & sin^2\theta^{(k)} & 0 & 0 & 0 & -sin2\theta^{(k)} \\ sin^2\theta^{(k)} & cos^2\theta^{(k)} & 0 & 0 & 0 & sin2\theta^{(k)} \\ 0 & 0 & 1 & 0 & 0 & 0 \\ 0 & 0 & 0 & cos\theta^{(k)} & sin\theta^{(k)} & 0 \\ 0 & 0 & 0 & -sin\theta^{(k)} & cos\theta^{(k)} & 0 \\ sin\theta^{(k)}cos\theta^{(k)} & -sin\theta^{(k)}cos\theta^{(k)} & 0 & 0 & 0 & cos^2\theta^{(k)} - sin^2\theta^{(k)} \end{bmatrix} \tag{5.33}$$

The laminate stiffnesses are defined as follows

$$\begin{aligned} \underset{ij}{A^{\alpha\beta}_{IJ}} &= \sum_{k=1}^{N_m} \int_{z_b^{(k)}}^{z_t^{(k)}} \bar{C}^{(k)}_{ij} F^{\alpha}_{I} F^{\beta}_{J} \mathrm{d}z & \underset{ij}{\bar{A}^{\alpha\beta}_{IJ}} &= \sum_{k=1}^{N_m} \int_{z_b^{(k)}}^{z_t^{(k)}} \bar{C}^{(k)}_{ij} F^{\alpha}_{I} \frac{dF^{\beta}_{J}}{dz} \mathrm{d}z \\ \underset{ij}{\bar{\bar{A}}^{\alpha\beta}_{IJ}} &= \sum_{k=1}^{N_m} \int_{z_b^{(k)}}^{z_t^{(k)}} \bar{C}^{(k)}_{ij} \frac{dF^{\alpha}_{I}}{dz} \frac{dF^{\beta}_{J}}{dz} \mathrm{d}z & \underset{ij}{B^{\alpha\beta\gamma}_{IJK}} &= \sum_{k=1}^{N_m} \int_{z_b^{(k)}}^{z_t^{(k)}} \bar{C}^{(k)}_{ij} F^{\alpha}_{I} F^{\beta}_{J} F^{\gamma}_{K} \mathrm{d}z \\ \underset{ij}{\bar{B}^{\alpha\beta\gamma}_{IJK}} &= \sum_{k=1}^{N_m} \int_{z_b^{(k)}}^{z_t^{(k)}} \bar{C}^{(k)}_{ij} F^{\alpha}_{I} F^{\beta}_{J} \frac{dF^{\gamma}_{K}}{dz} \mathrm{d}z & \underset{ij}{D^{\alpha\beta\gamma\delta}_{IJKL}} &= \sum_{k=1}^{N_m} \int_{z_b^{(k)}}^{z_t^{(k)}} \bar{C}^{(k)}_{ij} F^{\alpha}_{I} F^{\beta}_{J} F^{\gamma}_{K} F^{\delta}_{L} \mathrm{d}z \end{aligned} \tag{5.34}$$

The laminate constitutive equations can be written as

$$\begin{aligned} \underset{i=1,2,6}{N^{\alpha}_{I}} &= \sum_{\beta=1}^{M} \left\{ \sum_{J=1}^{N_p^{\beta}} \left[\underset{i1}{A^{\alpha\beta}_{IJ}} \frac{\partial U^{\beta}_{J}}{\partial x} + \underset{i2}{A^{\alpha\beta}_{IJ}} \frac{\partial V^{\beta}_{J}}{\partial y} + \underset{i3}{\bar{A}^{\alpha\beta}_{IJ}} W^{\beta}_{J} + \underset{i6}{A^{\alpha\beta}_{IJ}} \left(\frac{\partial U^{\beta}_{J}}{\partial y} + \frac{\partial V^{\beta}_{J}}{\partial x} \right) \right] \right\} \\ &+ \sum_{\beta,\gamma=1}^{M} \left[\sum_{J=1}^{N_p^{\beta}} \sum_{K=1}^{N_p^{\gamma}} \left(\frac{1}{2} \underset{i1}{B^{\alpha\beta\gamma}_{IJK}} \frac{\partial W^{\beta}_{J}}{\partial x} \frac{\partial W^{\gamma}_{K}}{\partial x} + \frac{1}{2} \underset{i2}{B^{\alpha\beta\gamma}_{IJK}} \frac{\partial W^{\beta}_{J}}{\partial y} \frac{\partial W^{\gamma}_{K}}{\partial y} + \underset{i6}{B^{\alpha\beta\gamma}_{IJK}} \frac{\partial W^{\beta}_{J}}{\partial x} \frac{\partial W^{\gamma}_{K}}{\partial y} \right) \right] \end{aligned} \tag{5.35a}$$

$$\underset{i=4,5}{N^{\alpha}_{I}} = \sum_{\beta=1}^{M} \left[\sum_{J=1}^{N_p^{\beta}} \left(\underset{i4}{\bar{A}^{\alpha\beta}_{IJ}} V^{\beta}_{J} + \underset{i4}{A^{\alpha\beta}_{IJ}} \frac{\partial W^{\beta}_{J}}{\partial y} + \underset{i5}{\bar{A}^{\alpha\beta}_{IJ}} U^{\beta}_{J} + \underset{i5}{A^{\alpha\beta}_{IJ}} \frac{\partial W^{\beta}_{J}}{\partial x} \right) \right] \tag{5.35b}$$

$$\begin{aligned} \underset{3}{\tilde{N}^{\alpha}_{I}} &= \sum_{\beta=1}^{M} \left\{ \sum_{J=1}^{N_p^{\beta}} \left[\underset{31}{\bar{A}^{\beta\alpha}_{JI}} \frac{\partial U^{\beta}_{J}}{\partial x} + \underset{32}{\bar{A}^{\beta\alpha}_{JI}} \frac{\partial V^{\beta}_{J}}{\partial y} + \underset{33}{\bar{\bar{A}}^{\beta\alpha}_{JI}} W^{\beta}_{J} + \underset{36}{\bar{A}^{\beta\alpha}_{JI}} \left(\frac{\partial U^{\beta}_{J}}{\partial y} + \frac{\partial V^{\beta}_{J}}{\partial x} \right) \right] \right\} \\ &+ \sum_{\beta,\gamma=1}^{M} \left[\sum_{J=1}^{N_p^{\beta}} \sum_{K=1}^{N_p^{\gamma}} \left(\frac{1}{2} \underset{31}{\bar{B}^{\beta\gamma\alpha}_{JKI}} \frac{\partial W^{\beta}_{J}}{\partial x} \frac{\partial W^{\gamma}_{K}}{\partial x} + \frac{1}{2} \underset{32}{\bar{B}^{\beta\gamma\alpha}_{JKI}} \frac{\partial W^{\beta}_{J}}{\partial y} \frac{\partial W^{\gamma}_{K}}{\partial y} + \underset{36}{\bar{B}^{\beta\gamma\alpha}_{JKI}} \frac{\partial W^{\beta}_{J}}{\partial x} \frac{\partial W^{\gamma}_{K}}{\partial y} \right) \right] \end{aligned} \tag{5.35c}$$

$$\underset{i=4,5}{\tilde{N}\overset{\alpha}{\underset{I}{}}} = \sum_{\beta=1}^{M}\left[\sum_{J=1}^{N_p^{\beta}}\left(\underset{i4}{\bar{\bar{A}}{}^{\beta\alpha}_{JI}}\,V_J^{\beta} + \underset{i4}{\bar{A}{}^{\beta\alpha}_{JI}}\,\frac{\partial W_J^{\beta}}{\partial y} + \underset{i5}{\bar{\bar{A}}{}^{\beta\alpha}_{JI}}\,U_J^{\beta} + \underset{i5}{\bar{A}{}^{\beta\alpha}_{JI}}\,\frac{\partial W_J^{\beta}}{\partial x}\right)\right] \tag{5.35d}$$

$$\begin{aligned}\underset{i=1,2,6}{Q\overset{\alpha\beta}{\underset{IJ}{}}} = &\sum_{\gamma=1}^{M}\left\{\sum_{K=1}^{N_p^{\gamma}}\left[\underset{i1}{B^{\alpha\beta\gamma}_{IJK}}\,\frac{\partial U_K^{\gamma}}{\partial x} + \underset{i2}{B^{\alpha\beta\gamma}_{IJK}}\,\frac{\partial V_K^{\gamma}}{\partial y} + \underset{i3}{\bar{B}^{\alpha\beta\gamma}_{IJK}}\,W_K^{\gamma} + \underset{i6}{B^{\alpha\beta\gamma}_{IJK}}\left(\frac{\partial U_K^{\gamma}}{\partial y} + \frac{\partial V_K^{\gamma}}{\partial x}\right)\right]\right\}\\ &+ \sum_{\gamma,\delta=1}^{M}\left[\sum_{K=1}^{N_p^{\gamma}}\sum_{L=1}^{N_p^{\delta}}\left(\frac{1}{2}\underset{i1}{D^{\alpha\beta\gamma\delta}_{IJKL}}\,\frac{\partial W_K^{\gamma}}{\partial x}\frac{\partial W_L^{\delta}}{\partial x} + \frac{1}{2}\underset{i2}{D^{\alpha\beta\gamma\delta}_{IJKL}}\,\frac{\partial W_K^{\gamma}}{\partial y}\frac{\partial W_L^{\delta}}{\partial y} + \underset{i6}{D^{\alpha\beta\gamma\delta}_{IJKL}}\,\frac{\partial W_K^{\gamma}}{\partial x}\frac{\partial W_L^{\delta}}{\partial y}\right)\right]\end{aligned} \tag{5.35e}$$

Sometimes it is useful to express the equations of motion (5.27) in terms of generalized displacements $(U_I^{\alpha}, V_I^{\alpha}, W_I^{\alpha})$. This can be achieved by substituting the expressions for the force and moment resultants from equations (5.35) in to equation (5.27).

5.4 Finite element formulation

5.4.1 In-plane discretization

The in-plane discretization is based on the multilevel mesh superposition approach [83], which is shown in Figure 5-6. In the multilevel mesh superposition finite element analysis, the domain $\bar{\omega}$ is discretized into a collection of elements such that each in-plane model domain ω^{α} is discretized independently with its own mesh

$$\bar{\omega}^{\alpha} \approx \bigcup_{e=1}^{N_e^{\alpha}} \bar{\omega}_e^{\alpha} \tag{5.36}$$

$$\bar{\omega}^{\alpha} = \omega^{\alpha} \bigcup \partial\omega^{\alpha} \tag{5.37}$$

$$\bar{\omega}_e^{\alpha} = \omega_e^{\alpha} \bigcup \partial\omega_e^{\alpha} \tag{5.38}$$

We define the measure (*area*) of subdomain ω_e^{α} as $\lambda\left(\omega_e^{\alpha}\right)$. In each subdomain ω_i there will be $|\mathcal{M}_i|$ non overlapping meshes, where each level of mesh is more refined than the previous ones in the hierarchy, i. e. $\lambda\left(\omega_e^{\alpha+1}\right) \leq \lambda\left(\omega_e^{\alpha}\right)$. In general the boundaries of the models in $\mathcal{M}_i$ do not coincide.

The highest level of mesh in ω_i is the one for model S_i. This mesh will be referred to [261] as the *top* mesh, while the meshes of the remaining plate models within $\mathcal{M}_i$ are referred to as *non-top* meshes.

The representative element domain ω^e of this mesh will be used to derive the weak forms of the equations for the theory, under the assumptions that each element has a known shape and associated interpolation functions.

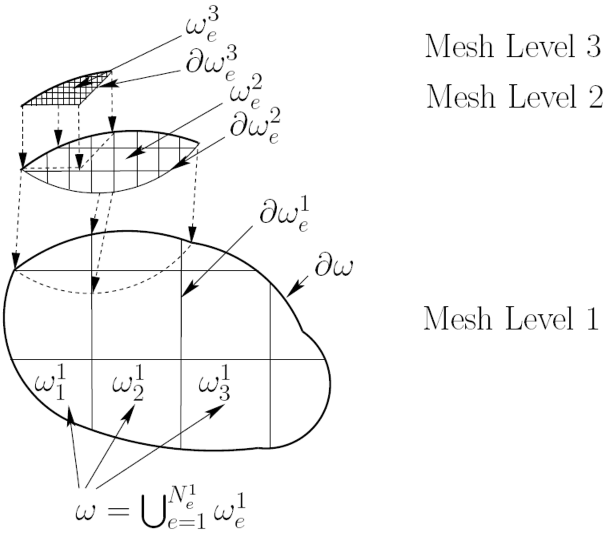

Figure 5-6: Multilevel mesh superposition finite element model

5.4.2 Weak forms

Multiplying the three equations in (5.27) by δU_I^α, δV_I^α and δW_I^α, respectively, then integrating over the representative element domain ω^e and finally integrating per parts using the component forms of the *Green-Gauss* theorem (*gradient* or *divergence* theorem) to weaken the differentiability of U_I^α, V_I^α and W_I^α results in the following equations

$$0 = \int_{\omega^e} \left[\frac{\partial \delta U_I^\alpha}{\partial x} N_{\underset{1}{I}}^{\alpha} + \frac{\partial \delta U_I^\alpha}{\partial y} N_{\underset{6}{I}}^{\alpha} + \tilde{N}_{\underset{5}{I}}^{\alpha} \delta U_I^\alpha - \delta U_I^\alpha \sum_{\beta=1}^{M} \sum_{J=1}^{N_p^\beta} I_{IJ}^{\alpha\beta} \frac{\partial U_J^\beta}{\partial t^2} \right] \mathrm{d}x\mathrm{d}y - \oint_{\partial\omega^e} \left(N_{\underset{1}{I}}^{\alpha} n_x + N_{\underset{6}{I}}^{\alpha} n_y \right) \mathrm{d}s \tag{5.39a}$$

$$0 = \int_{\omega^e} \left[\frac{\partial \delta V_I^\alpha}{\partial y} N_{\underset{2}{I}}^{\alpha} + \frac{\partial \delta V_I^\alpha}{\partial x} N_{\underset{6}{I}}^{\alpha} + \tilde{N}_{\underset{4}{I}}^{\alpha} \delta V_I^\alpha - \delta V_I^\alpha \sum_{\beta=1}^{M} \sum_{J=1}^{N_p^\beta} I_{IJ}^{\alpha\beta} \frac{\partial V_J^\beta}{\partial t^2} \right] \mathrm{d}x\mathrm{d}y - \oint_{\partial\omega^e} \left(N_{\underset{6}{I}}^{\alpha} n_x + N_{\underset{2}{I}}^{\alpha} n_y \right) \mathrm{d}s \tag{5.39b}$$

$$
\begin{aligned}
0 = {} & \int_{\omega^e} \left[\frac{\partial \delta W_I^\alpha}{\partial y} \underset{4}{N_I^\alpha} + \frac{\partial \delta W_I^\alpha}{\partial x} \underset{5}{N_I^\alpha} + \underset{3}{\tilde{N}_I^\alpha}\, \delta W_I^\alpha - q_b \delta W_I^\alpha - q_t \delta W_I^\alpha \right] \mathrm{d}x\mathrm{d}y + \int_{\omega^e} \left\{ \sum_{\beta=1}^{M} \left[\sum_{J=1}^{N_p^\beta} \underset{1}{Q_{IJ}^{\alpha\beta}} \frac{\partial \delta W_I^\alpha}{\partial x} \frac{\partial W_J^\beta}{\partial x} \right. \right. \\
& + \underset{6}{Q_{IJ}^{\alpha\beta}} \left(\frac{\partial \delta W_I^\alpha}{\partial x} \frac{\partial W_J^\beta}{\partial y} + \frac{\partial W_I^\alpha}{\partial x} \frac{\partial \delta W_J^\beta}{\partial y} \right) + \left. \underset{2}{Q_{IJ}^{\alpha\beta}} \frac{\partial \delta W_I^\alpha}{\partial y} \frac{\partial W_J^\beta}{\partial y} \right] - \delta W_I^\alpha \sum_{\beta=1}^{M} \sum_{J=1}^{N_p^\beta} I_{IJ}^{\alpha\beta} \frac{\partial W_J^\beta}{\partial t^2} \Bigg\} \mathrm{d}x\mathrm{d}y \\
& - \oint_{\partial\omega^e} \left\{ \sum_{\beta=1}^{M} \left[\sum_{J=1}^{N_p^\beta} \left(\underset{1}{Q_{IJ}^{\alpha\beta}} \frac{\partial W_J^\beta}{\partial x} + \underset{6}{Q_{IJ}^{\alpha\beta}} \frac{\partial W_J^\beta}{\partial y} \right) n_x + \left(\underset{2}{Q_{IJ}^{\alpha\beta}} \frac{\partial W_J^\beta}{\partial y} + \underset{6}{Q_{IJ}^{\alpha\beta}} \frac{\partial W_J^\beta}{\partial x} \right) n_y \right] \right\} \mathrm{d}s
\end{aligned}
\tag{5.39c}
$$

where (n_x, n_y) are the cosine directors of the unit normal on the element boundary $\partial\omega^e$ and $\mathrm{d}s$ is the arc-length of an infinitesimal line element along the boundary. Integration-by-parts is performed on the terms containing moment resultants in equation (5.39c), so that the resulting weak form is symmetrical. This leads to symmetrical mass and linear stiffness matrices in the finite element model.

5.4.3 In-plane spatial discretization

For simplicity, we will use in the following the same interpolation functions for the components of the generalized displacements. Because each in-plane model domain ω^α has its own mesh, then in each element domain ω_e^α an approximation of the following form shall be assumed

$$
\underset{i}{U_I^\alpha}\left(\underset{\sim}{x}, t\right) = \sum_{m=0}^{L_e^\alpha} \underset{im}{U_{\alpha I}^{e}}\left(t\right) \underset{im}{\psi^{\overset{\alpha}{e}}}\left(\underset{\sim}{x}\right) \tag{5.40}
$$

where $i = 1, \ldots, 3$ and $L_e^\alpha + 1$ is the number of nodes per 2-D element domain ω_e^α used to approximate the generalized displacements for model α and interface I and $\underset{im}{\psi^{\overset{\alpha}{e}}}\left(\underset{\sim}{x}\right)$ are two-dimensional interpolation functions in ω_e^α.

5.4.4 Order of a model

We will assume the models within $\mathcal{M}$ to be defined in a hierarchical fashion. In particular, we will assume that the properties of the models determining their hierarchal nature are the following

$$
\begin{aligned}
\lambda\left(Z_I^1\right) \geq \cdots \geq \lambda\left(Z_I^\alpha\right) \geq \cdots \geq \lambda\left(Z_I^M\right) \\
L_I^1 \leq \cdots \leq L_I^\alpha \leq \cdots \leq L_I^M \\
\lambda\left(\omega_e^1\right) \geq \cdots \geq \lambda\left(\omega_e^\alpha\right) \geq \cdots \geq \lambda\left(\omega_e^M\right) \\
L_e^1 \leq \cdots \leq L_e^\alpha \leq \cdots \leq L_e^M
\end{aligned}
\tag{5.41}
$$

The order of a model α within the hierarchy $\mathcal{M}$ is identified by parameters

$(\lambda(Z_I^\alpha), L_I^\alpha, \lambda(\omega_e^\alpha), L_e^\alpha)$. A higher order model can be added to a sequence of models by creating a new model where any one of the above parameters is increased with respect to greatest element in the set $\mathcal{M}$.

5.4.5 Finite element model

Substituting equation (5.40) in to the weak forms in equations (5.39) we obtain the *semidiscrete* finite element model of the hierarchical multiple plate models theory.

$$\underset{IJ}{\overset{e}{\boldsymbol{K}^{\alpha\beta}}}\,\underset{I}{\overset{e}{\boldsymbol{U}^{\alpha}}} + \underset{IJ}{\overset{e}{\boldsymbol{M}^{\alpha\beta}}}\,\underset{I}{\overset{e}{\ddot{\boldsymbol{U}}^{\alpha}}} = \underset{I}{\overset{e}{\boldsymbol{F}^{\alpha}}} \tag{5.42}$$

where the matrix $\underset{IJ}{\overset{e}{\boldsymbol{K}^{\alpha\beta}}}$ is the *direct element stiffness matrix*, the matrix $\underset{IJ}{\overset{e}{\boldsymbol{M}^{\alpha\beta}}}$ is the *element mass matrix*, the column vector $\underset{I}{\overset{e}{\boldsymbol{F}^{\alpha}}}$ is the *element force vector* and the column vector $\underset{I}{\overset{e}{\boldsymbol{U}^{\alpha}}} = \left\{\underset{1}{\overset{e}{\boldsymbol{U}^{\alpha I}}}, \underset{2}{\overset{e}{\boldsymbol{U}^{\alpha I}}}, \ldots, \underset{L_e^\alpha+1}{\overset{e}{\boldsymbol{U}^{\alpha I}}}\right\}$ is the vector of the *nodal degrees of freedom* per element ω^e, where $\underset{j}{\overset{e}{\boldsymbol{U}^{\alpha I}}} = \left\{\underset{ij}{\overset{e}{U^{\alpha I}}}, \underset{ij}{\overset{e}{U^{\alpha I}}}, \underset{ij}{\overset{e}{U^{\alpha I}}}\right\} = \left\{\underset{j}{\overset{e}{U^{\alpha I}}}, \underset{j}{\overset{e}{V^{\alpha I}}}, \underset{j}{\overset{e}{W^{\alpha I}}}\right\}$, $I = 1, \ldots, \left(\sum_{\alpha \in \mathcal{M}_i} N_p^\alpha\right)$, $i = 1, \ldots, 3$ and $j = 1, \ldots, L_e^\alpha + 1$.

Equation (5.42) has $2n^e$ unknowns, where

$$n^e = 3\left(\sum_{\alpha \in \mathcal{M}_i} N_p^\alpha\right)(L_e^\alpha + 1) \tag{5.43}$$

Because of the adopted modeling approach, both discretization and modeling errors can be reduced within a certain region of ω_i by selecting, in a hierarchical fashion, the effective number of models from $\mathcal{M}_i$ that are used within that region. Every time a new model α is superimposed on the previous models in certain region, the nodal degrees of freedom of that region are *enriched* by the degrees of freedom of new model. As consequence this will increase the total number of nodal degrees of freedom n^e per element domain ω^e in that region, so other elements where less precision is required should not be enriched is order to keep the computational cost to the minimum required for the analysis.

For example, in the case of the superposition of a FSDT with a linear LWT model displayed in Figure 5-5, the set of available mathematical models in Ω is $\mathcal{M} = \{1, 2, 3\}$. In subdomain ω_2 the subset of available models is $\mathcal{M}_2 = \{1, 2, 3\}$. During normal operation only models 1 and 2 are used, but when discretization and modeling errors need to be reduced then model 3 can be superimposed in ω_2 on models 1 and 2, at the expense of increasing the number of nodal degrees of freedom and consequently the computational efficiency.

The direct element stiffness and element mass matrices can be expressed as follows

$$\begin{aligned}
\underset{IJ}{\overset{e}{\boldsymbol{K}}{}^{\alpha\beta}} &= \begin{bmatrix} \underset{11}{\boldsymbol{K}^{\alpha\beta}_{IJ}} & \underset{12}{\boldsymbol{K}^{\alpha\beta}_{IJ}} & \underset{13}{\boldsymbol{K}^{\alpha\beta}_{IJ}} \\ \underset{21}{\boldsymbol{K}^{\alpha\beta}_{IJ}} & \underset{22}{\boldsymbol{K}^{\alpha\beta}_{IJ}} & \underset{23}{\boldsymbol{K}^{\alpha\beta}_{IJ}} \\ \underset{31}{\boldsymbol{K}^{\alpha\beta}_{IJ}} & \underset{32}{\boldsymbol{K}^{\alpha\beta}_{IJ}} & \underset{33}{\boldsymbol{K}^{\alpha\beta}_{IJ}} \end{bmatrix} \\
\underset{IJ}{\overset{e}{\boldsymbol{M}}{}^{\alpha\beta}} &= \begin{bmatrix} \underset{11}{\boldsymbol{M}^{\alpha\beta}_{IJ}} & \boldsymbol{0} & \boldsymbol{0} \\ \boldsymbol{0} & \underset{22}{\boldsymbol{M}^{\alpha\beta}_{IJ}} & \boldsymbol{0} \\ \boldsymbol{0} & \boldsymbol{0} & \underset{33}{\boldsymbol{M}^{\alpha\beta}_{IJ}} \end{bmatrix}
\end{aligned} \tag{5.44}$$

where $\alpha, \beta \in \mathcal{M}_i$. The direct stiffness matrix is symmetric only in the linear case, while the mass matrix is always symmetric.

Substituting the laminate constitutive equations (5.35) in to the weak forms (5.39) we can express the element stiffness matrix and element mass matrix in terms of the laminate stiffnesses (5.34) as follows

$$\underset{ij}{\boldsymbol{K}^{\alpha\beta}_{IJ}} = f\left(\underset{ij}{A^{\alpha\beta}_{IJ}}, \underset{ij}{\bar{A}^{\alpha\beta}_{IJ}}, \underset{ij}{\bar{\bar{A}}^{\alpha\beta}_{IJ}}, \underset{ij}{B^{\alpha\beta\gamma}_{IJK}}, \underset{ij}{\bar{B}^{\alpha\beta\gamma}_{IJK}}, \underset{ij}{D^{\alpha\beta\gamma\delta}_{IJKL}}\right) \tag{5.45}$$

$$\underset{ii}{\boldsymbol{M}^{\alpha\beta}_{IJ}} = f\left(I^{\alpha\beta}_{IJ}\right) \tag{5.46}$$

where $i, j = 1, 2, 3$.

It's important to note that the diagonal terms in $\underset{IJ}{\overset{e}{\boldsymbol{K}}{}^{\alpha\beta}}$ present *linear and nonlinear self coupling* contributions plus *non linear coupling* contributions from all the other models. The non diagonal terms instead present *linear and non linear coupling* contributions between each two models. This is summarized as follows (dropping indices IJ)

$$\begin{aligned}
\overset{e}{\boldsymbol{K}}_{\alpha\alpha} &= \underset{L}{\overset{e}{\boldsymbol{K}}{}^{\alpha\alpha}} + \underset{NL}{\overset{e}{\boldsymbol{K}}{}^{\alpha\alpha}} + \sum_{\substack{\beta=1 \\ \beta\neq\alpha}}^{M} \underset{NLC}{\overset{e}{\boldsymbol{K}}{}^{\alpha\beta}} \\
\overset{e}{\boldsymbol{K}}_{\alpha\beta} &= \underset{LC}{\overset{e}{\boldsymbol{K}}{}^{\alpha\beta}} + \underset{NLC}{\overset{e}{\boldsymbol{K}}{}^{\alpha\beta}}
\end{aligned} \tag{5.47}$$

Moreover, the general form of the above contributions is independent of any two models being considered. The expressions of the element secant stiffness matrix and element secant stiffness matrix are given in appendix D.

After assembly, the semidiscretized finite element equation can be given in the following form

$$\boldsymbol{K}^{\alpha\beta}_{IJ}\boldsymbol{U}^{\alpha}_{I} + \boldsymbol{M}^{\alpha\beta}_{IJ}\ddot{\boldsymbol{U}}^{\alpha}_{I} = \boldsymbol{F}^{\alpha}_{I} \tag{5.48}$$

where $\alpha, \beta \in \mathcal{M}_i$.

The fully discretized finite element model is obtained using a *time approximation*, e.g. the *Newmark* scheme.

5.4.6 Multiple models compatibility and uniqueness conditions

Certain degrees of freedom (DOF) should be suppressed to ensure compatibility of the total displacement field and uniqueness of the solution of the multiple assumed displacement fields. For this reason additional boundary conditions need to be imposed on top of the *physical* boundary conditions before the finite element equations (5.48) can be solved. The additional boundary conditions are generally referred to [189, 261] as compatibility and uniqueness conditions, and are shown in Figure 5-7.

Compatibility conditions

The total displacement field should be continuous throughout the composite mesh, which is the requirement of *compatibility* or C^0 *continuity*. For this reason, homogeneous essential boundary conditions must be enforced on incompatible regions, setting to zero the DOF of the plate models in those regions. Note that the compatibility conditions are not imposed on boundaries that coincide with physical boundaries, as displayed in Figure 5-7. Here DOF need only to be suppressed in accordance with the physical boundary conditions.

Given two neighboring subdomains ω_i and ω_j, if an assumed displacement field α is in $\mathcal{M}_i$, but not in $\mathcal{M}_j$, then the region $\partial\omega_i \bigcap \partial\omega_j$ is defined to be an *incompatible region.* Homogeneous essential boundary conditions must be enforced on incompatible regions, setting to zero the DOF of model α in those regions. An example is displayed in Figure 5-7 for the case of structured mesh superposition.

Uniqueness conditions

The other issue is the singularity of the assembled stiffness matrix in equation (5.48), which is caused by redundant rigid body modes. In fact there may be more than one set of assumed displacement fields that can be summed to yield the total displacement field, as shown in Figure 5-7 for the case of structured mesh superposition. To guarantee uniqueness of the solution, homogeneous essential boundary conditions must be enforced in coinciding nodes of different mesh levels by setting to zero the redundant DOF. These should be selected between the DOF of the highest level mesh, as shown in Figure 5-7.

For the case of the superposition of a FSDT with a linear LWT model there are five redundant variables that need to be set to zero to permit a unique solution for the remaining variables. Figure 5-8 shows the in-plane deformation $u\left(x,y\right) = u_1\left(x,y\right)$ along a transverse material line $A - B$ for a 4 layer plate. Two variables need to be set

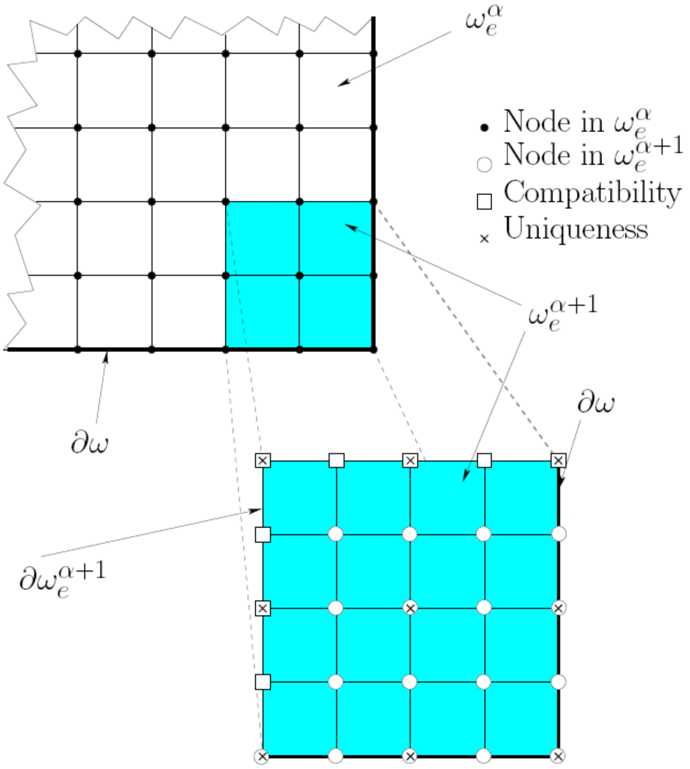

Figure 5-7: Compatibility and uniqueness conditions for the case of structured mesh superposition

to zero. In this case the particular pair of variables is arbitrary [200], and although the same deformation is achieved in 5-8a and 5-8b, the numerical values of the remaining five nonzero values are different.

5.4.7 Calculation of the coupling terms

The coupling terms in equation (5.47) are the result of an integral whose integrands contain products of in-plane interpolation functions defined for different mesh levels. A mapping between the different co-ordinate systems of the overlaid meshes is necessary to perform the numerical integration.

This can be quite complex when unstructured mesh superposition is used. In the case of structured mesh superposition displayed in Figure 5-6, a *top/non-top transformation matrix* [261] can be calculated that allows expressing the interpolation functions of any mesh level $\alpha \in \mathcal{M}_i$ to those of mesh level S_i. A specific form of this matrix exists for any pair of mesh levels considered.

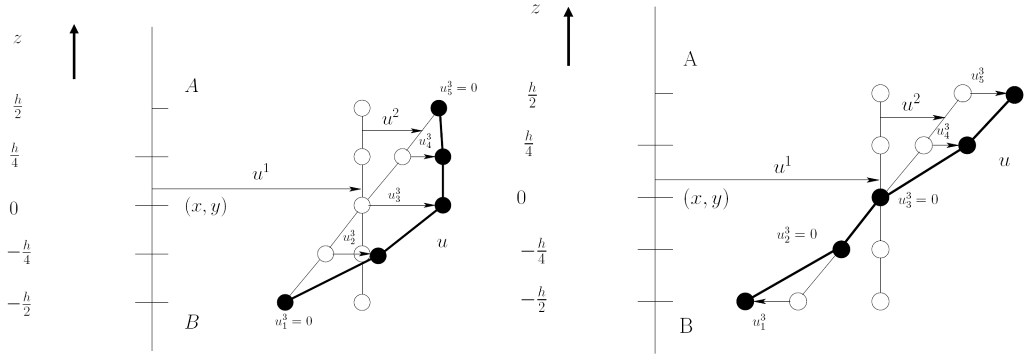

(a) $u_1^3 = u_5^3 = 0$ **(b)** $u_2^3 = u_3^3 = 0$

Figure 5-8: Suppression of redundant in-plane deformations for the case of superposition of FSDT, u^1 and u^2, and linear LWT models, u^3

5.4.8 Inclusion of delaminations

The occurrence of delaminations is common in composite laminates [148, 18], so it is important to incorporate the kinematics of single and multiple delaminations in to the general theory presented here.

For the purpose of the following discussion it is assumed that the domain Ω is crossed by D discontinuities $\partial\Omega_I^d$, where $I = 1, \ldots, D$, between the laminae, i. e. one or more delaminations. As shown in Figure 5-9, the two resulting parts of the domain are called Ω_+^I and Ω_-^I. $\hat{n}_I^d$ is the unit vector along the normal to $\partial\Omega_I^d$ pointing into Ω_+^I. The following relation holds for all discontinuities: $\Omega_-^I \bigcup \Omega_+^I = \Omega$, $\forall I = 1, \ldots, D$.

Furthermore, it is assumed that the delaminated interface $\partial\Omega_I^d$ has coordinate z_I^d. Recalling that $\boldsymbol{x} = (\underset{\sim}{x}, z)$, then $\boldsymbol{x} \in \Omega_+^I$, if $\underset{\sim}{x} \in \omega$ and $z \geq z_I^d$. Otherwise, if $\boldsymbol{x} \in \Omega_-^I$, then $\underset{\sim}{x} \in \omega$ and $z < z_I^d$.

Discontinuous through the thickness displacement fields, such as delaminations, are incorporated in the theoretical framework by performing an extrinsic enrichment of one or more of the assumed displacement fields. This can be achieved when, for the set of nodes that belong to the domain of the discontinuity, the functions $\boldsymbol{F}_I^\alpha$ are multiplied by discontinuous enrichment functions, such as the Heaviside unit step functions [155] defined as follows

$$H_I\left(z - z_I^d\right) = \begin{cases} 1 & \text{if } z \geq z_I^d; \\ 0 & \text{if } z < z_I^d. \end{cases} \tag{5.49}$$

Another possible choice is the Heaviside sign-functions [155].

The additional generalized displacements $\boldsymbol{u}_I^d$ are physically meaningful and they represent jump discontinuities in the displacement components of the total displacement field across the delamination. A cohesive law between laminae is incorporated where

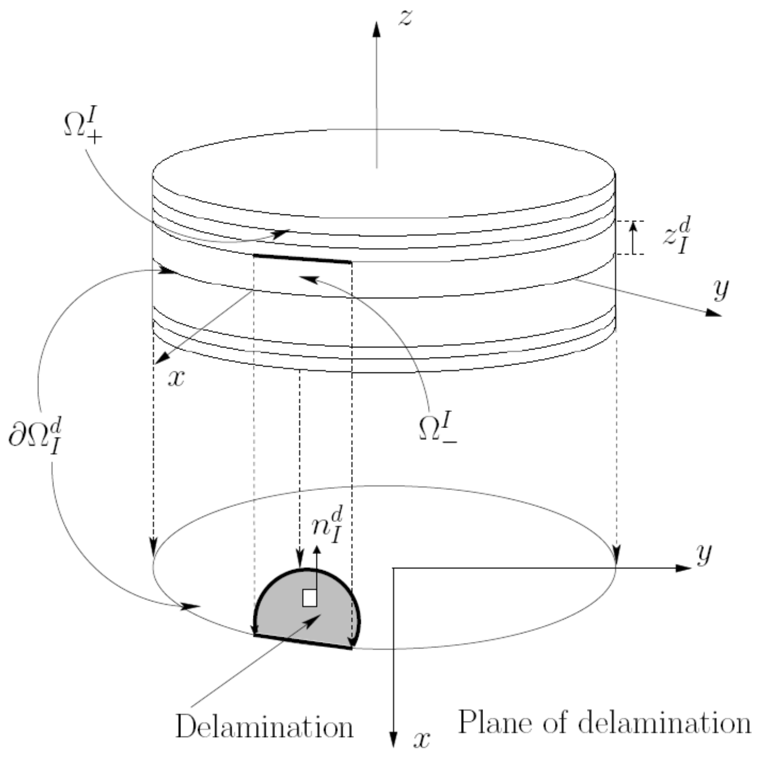

Figure 5-9: The domain Ω is crossed by a delamination $\partial\Omega^d_I$ at coordinate z^d_I

appropriate. This approach is outlined in section 5.4.9.

For example, Figure 5-10 shows the in-plane deformation $u\,(x, y) = u_1\,(x, y)$ along a transverse material line $A - B$ for the case of a 4 layer plate and the superposition of FSDT, linear LWT and delamination models. A single delamination (field $\boldsymbol{u}^4$) occurs at $z = 0$.

5.4.9 Cohesive zone model

We assume that the tractions between layers can be modeled using a *cohesive zone model* (CZM) [166, 245, 40, 65, 256]. Note that only the presence, and not the particular form, of the CZM is assumed.

Considering the the discontinuities $\partial\Omega^d_I$ as an internal boundary condition, the following relationships can be added to the boundary conditions of the problem

$$\hat{n}^d_I \boldsymbol{\sigma} = \boldsymbol{t}^d_I \quad \boldsymbol{x} \in \partial\Omega^d_I \tag{5.50}$$

where $\boldsymbol{t}^d_I$ are the tractions at the internal boundaries $\partial\Omega^d_I$.

In the co-ordinate system aligned with the orientation of the discontinuity, which is displayed in Figure 5-11, the tractions $\boldsymbol{t}^d_I$ are related to the displacement jumps $\boldsymbol{v}^d_I$ via

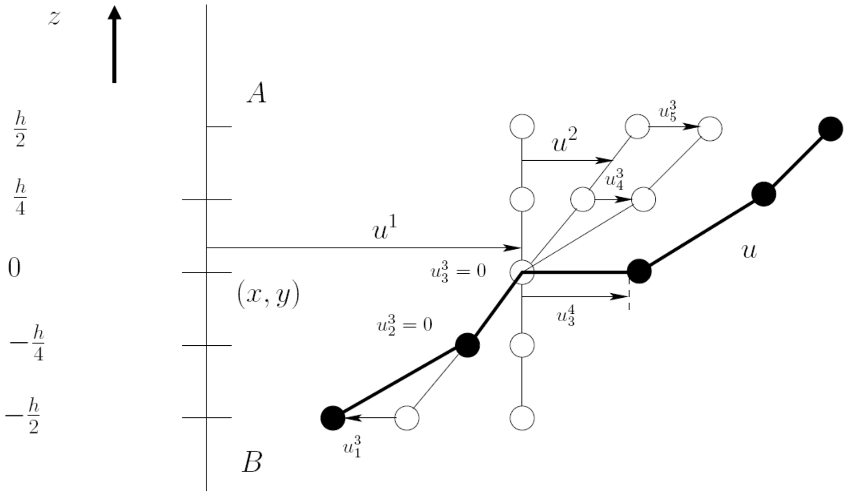

Figure 5-10: In-plane deformation for the case of superposition of FSDT, u^1 and u^2, linear LWT, u^3, and delamination models, u^4

tangent stiffness matrix of the traction-separation law [40]

$$\boldsymbol{t}_I^d = \boldsymbol{T}^d \boldsymbol{v}_I^d \quad \boldsymbol{x} \in \partial\Omega_I^d \tag{5.51}$$

Note that normally in the co-ordinate system aligned with the orientation of the discontinuity the z-direction is chosen to coincide with the direction normal to the discontinuity.

In general, the displacement jumps $\boldsymbol{v}_I^d$ are related to the additional generalized displacements $\boldsymbol{u}_I^d$ via the magnitude of the jump in the step function, which in the present case is equal to one.

$$\boldsymbol{v}_I^d = \boldsymbol{u}_I^d \quad \boldsymbol{x} \in \partial\Omega_I^d \tag{5.52}$$

The tangent stiffness matrix in the global co-ordinate system is equal to

$$\bar{\boldsymbol{T}}^d = \boldsymbol{L}^T \boldsymbol{T}^d \boldsymbol{L} \tag{5.53}$$

where the orthogonal transformation matrix $\boldsymbol{L}$ performs the transformation from the coordinate system aligned to the discontinuity to the global co-ordinate system.

Therefore there is a new contribution δV_{czm} to the virtual work energy given in equation (5.15) performed by cohesive forces amongst the layers, which has the following form

$$\delta V_{czm} = \sum_{I=1}^{D} \left[\int_{\partial\Omega_I^d} \boldsymbol{t}_I^d \cdot \delta \boldsymbol{u}_I^d \right] \mathrm{d}x\mathrm{d}y = \sum_{I=1}^{D} \left[\int_{\Omega_I^d} \left(\bar{T}_{xx}^d U_I^d \delta U_I^d + \bar{T}_{yy}^d V_I^d \delta V_I^d + \bar{T}_{zz}^d W_I^d \delta W_I^d \right) \right] \mathrm{d}x\mathrm{d}y$$

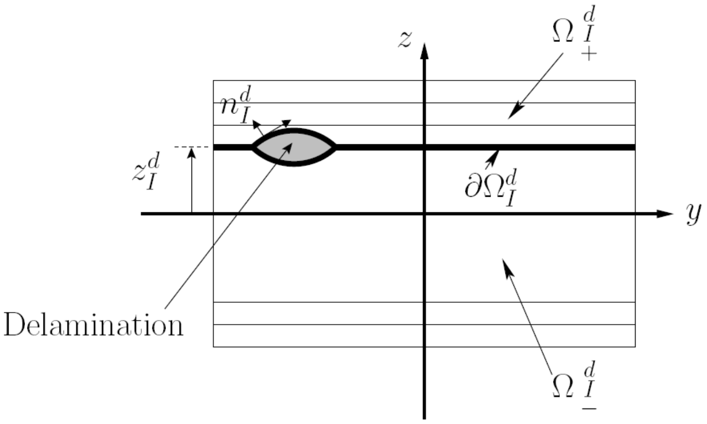

Figure 5-11: Orientation of the discontinuity within the laminate deformed configuration

If tractions between layers are modeled using a CZM, then the force resultants in equations (5.20) can be modified as follows for the delamination field

$$\begin{aligned} \left\{ N^d_{\underset{1}{I}} \quad N^d_{\underset{2}{I}} \right\}^T &= \sum_{k=1}^{N_m} \int_{z_b^{(k)}}^{z_t^{(k)}} \left\{ \sigma_{xx} \quad \sigma_{yy} \right\}^T H_I \mathrm{d}z + \left\{ \bar{T}^d_{xx} \quad \bar{T}^d_{yy} \right\}^T \\ \tilde{N}^d_{\underset{3}{I}} &= \bar{T}^d_{zz} \end{aligned} \tag{5.54}$$

The terms introduced by the cohesive forces in equation (5.54) will have to be taken into account on top of the contributions given in (5.45) when computing the element stiffness and mass matrices for the delamination field.

5.5 Results

5.5.1 Accuracy of the linear analysis

In this section the accuracy of the displacements and stresses calculated by the proposed approach for the case of linear analysis is compared to data presented in literature for plates of different geometries and loading conditions. In particular, the results reported in [42] are used for the comparison because these authors present many different plate models. The 3-D analytical solution is taken from [42].

The second matter that will be addressed is to check that, when applying an enriching plate model to the total domain of a global model, the results are the same as those obtained with the enriching plate model alone.

For ease of comparison, the same acronyms found in [42] are used to describe the plate models used in the following. The structure of the acronyms will be described briefly here. Acronyms for plate models are composed by three digits [42]. The first digit

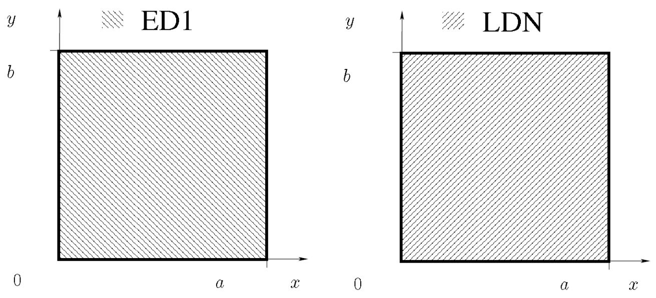

(a) ED1 plate model **(b)** LDN plate model

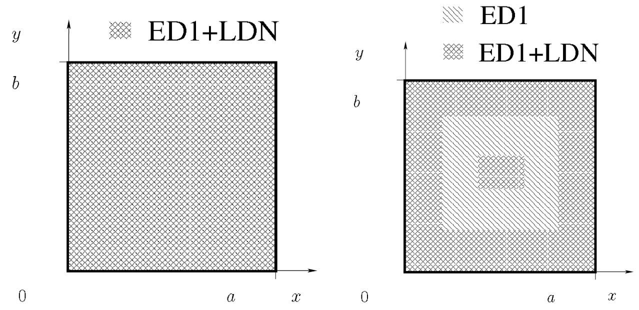

(c) ED1+LDN-full plate model **(d)** ED1+LDN-part plate model

Figure 5-12: Four plate models are used for each test case. This figure represents the domain of the models within the plate. This ranges from the whole plate for models ED1, LDN and ED1+LDN-full to selected areas of the plate for model ED1+LDN-part.

indicates the type of plate model and can assume the values L for *layerwise* and E for *equivalent single layer*. The second digit in the acronym refers to the type of formulation (D for *principle of virtual displacement*; and M for *Reissner mixed variational theorem*) used in the plate model, and although not immediately useful in the following this digit will be used throughout. The third digit is the order of the through-the-thickness (z-axis) approximation function (e.g. *1* for *linear*, *2* for *quadratic*, *3* for *cubic* and *4* for *fourth-order* and so on), which was discussed in section 5.3. For example the acronym *ED1* stands for an equivalent single layer plate model based on the principle of virtual displacement formulation using a linear out-of-plane approximation function. Another example is *LD4*, which is a layerwise plate model based on the principle of virtual displacement formulation using a fourth-order out-of-plane approximation function.

Length and width of the plate are indicated respectively by a and b, while the total thickness of the plate is indicated by h. Again for ease of comparison with [42] in this section the components of the displacement along the x, y and z-axis are defined as u, v and w.

Four different plate models (figure 5-12) will be considered for each test case. The first (in figure 5-12a) is an ED1 plate model used throughout the plate. The second plate model that will be examined is the LDN (or LMN) (see 5-12b), again used throughout

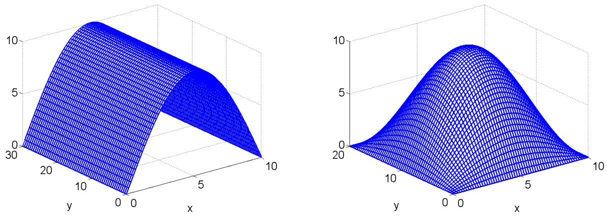

(a) Test case N.1: harmonic distribution of transverse pressure

(b) Test case N.2: bi-harmonic distribution of transverse pressure

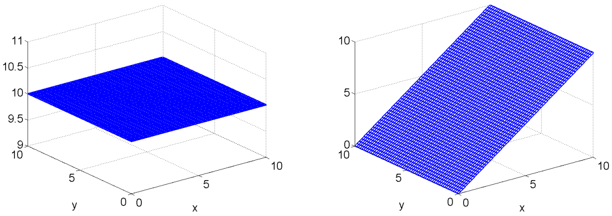

(c) Test case N.3: transverse distribution of constant pressure

(d) Test case N.4: triangular distribution of transverse pressure

Figure 5-13: A different load is applied to the surface of the plate in each of the four test cases considered.

the plate, where the order N of the out-of-plane approximation function will be taken in the range of 1 to 4, depending on the test case under examination. In the third case (indicated with the term *ED1+LDN-full* in subsequent tables and figures) two plate models, ED1 and LDN, are superpositioned throughout the plate (in figure 5-12c), and N again is in the range 1 to 4. In the fourth (indicated with *ED1-LDN-part* in subsequent tables and figures) the superpositioning of the plate models ED1 and LDN is only partial, and the enhancing plate model LDN is used only in the center and sides of the plate, as shown in figure 5-12d.

In summary the first two plate models used here are standard *single* plate models, while the second two are *multiple* plate models. The code was developed in MATLAB.

Only *structured* mesh superpositioning [274] will be considered, i. e. the superpositioning elements fit entirely within the domain of the superpositioned element, which simplifies the programming. Moreover, as a further simplification, the superpositioning elements have the same size as the superpositioned ones, i. e. the two meshes in overlapping regions are identical.

Four different test cases are considered. Each test case has a different kind of load applied to the surface of the plate, as shown in figure 5-13, and a different geometry. Furthermore, each test case will be analyzed for different values of the ratio a/h. The range of values considered for a/h goes from 4 - for thick plates - to 100 - for thin plates.

For symmetrical loads only a quarter of the plate is modeled, as shown in figures

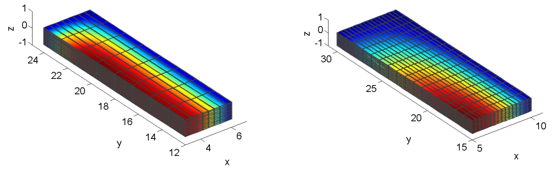

(a) Test case N.1: harmonic distribution of transverse pressure for $a/h = 6$ and plate model LD4

(b) Test case N.2: bi-harmonic distribution of transverse pressure for $a/h = 10$ and plate model LD3

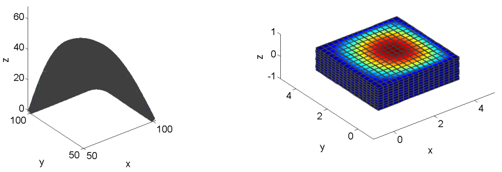

(c) Test case N.3: transverse distribution of constant pressure for $a/h = 100$ and plate model LD1

(d) Test case N.4: triangular distribution of transverse pressure for $a/h = 4$ and plate model LD3

Figure 5-14: Transverse displacement w in each of the four test cases considered for plates with three layers $\left(0^0/90^0/0^0\right)$. In these figures the deformation is scaled by a factor of ten. Note that for symmetrical loads only a quarter of the plate is modeled.

5-13a, 5-13b and 5-13c which display the transverse displacement w for particular values of a/h and particular plate models.

In all test cases simply supported boundary conditions of type *SSSS1* will be used. The notation adopted for specifying the boundary condition is the following. On each edge of the plate the boundary condition is specified with a letter. S stands for *simply supported*, F for *free* and C for *clamped*. The edges are taken in the sequence: $x = 0$, $x = a$, $y = 0$ and and $y = b$. A combination of different boundary conditions is in general possible. Moreover, two types (1 or 2) [200] of simply supported boundary conditions are available. The type is specified for last in the notation. For simply support boundary conditions of type 1 (SSSS1), $u = w = 0$ is imposed on edges $x = 0, a$, while $v = w = 0$ is imposed on edges $y = 0, b$.

Both symmetric $\left(0^0/90^0/0^0\right)$ and anti-symmetric laminates are considered $\left(0^0/90^0/0^0/90^0\right)$: the first kind of laminate will be referred to in the following as $N_I = 3$, while the second as $N_I = 4$. The laminae have equal thickness. All test cases will be studied for the case of symmetric laminate, while only two test cases - the first and the third - will be taken into consideration for the case of anti-symmetric laminate.

The material properties for each lamina used in all test cases are given in equation

$\bar{w}$	$N_I = 3$			
	$a/h = 4$		$a/h = 6$	
	PM	[42]	PM	[42]
3D [181]		2.887		1.635
LD4	2.889	2.887	1.633	1.634
ED1+LD4-full	2.889		1.633	
ED1+LD4-part	2.208		1.300	
ED1	2.091	2.091	1.210	1.209

(a) Test case N.1: harmonic distribution of transverse pressure

$\bar{w}$	$N_I = 3$					
	$a/h = 4$		$a/h = 10$		$a/h = 20$	
	PM	[42]	PM	[42]	PM	[42]
3D [181]		2.820		0.919		0.610
LD3	2.821	2.821	0.919	0.919	0.610	0.609
ED1+LD3-full	2.821		0.919		0.610	
ED1+LD3-part	2.166		0.806		0.586	
ED1	2.051	2.051	0.750	0.750	0.563	0.565

(b) Test case N.2: bi-harmonic distribution of transverse pressure

$\bar{w}$	$N_I = 3$					
	$a/h = 4$		$a/h = 10$		$a/h = 100$	
	PM	[42]	PM	[42]	PM	[42]
LD3	3.0451	3.0446	1.1544	1.1541		0.6713
LD1					0.6704	
ED1+LD3-full	3.0451		1.1544			
ED1+LD1-full					0.6704	
ED1+LD3-part	2.4648		1.0251			
ED1+LD1-part					0.6687	
ED1	2.3346	2.3344	0.9548	0.9546	0.6620	0.6618

(c) Test case N.3: transverse distribution of constant pressure

$\bar{w}$	$N_I = 3$					
	$a/h = 4$		$a/h = 10$		$a/h = 100$	
	PM	[42]	PM	[42]	PM	[42]
LM4		1.5222		0.5771		0.3356
LD3	1.5224		0.5772			
LD1					0.3352	
ED1+LD3-full	1.5224		0.5772			
ED1+LD1-full					0.3352	
ED1+LD3-part	1.2311		0.5116			
ED1+LD1-part					0.3336	
ED1	1.1672	1.1672	0.4774	0.4773	0.3310	0.3310

(d) Test case N.4: triangular distribution of transverse pressure

Table 5.1: Comparison of different plate models against superposition of models for non-dimensional transverse displacement for plates with three layers $\left(0^0/90^0/0^0\right)$.

(5.55).

$$\frac{E_L}{E_T} = 25; \qquad \frac{G_{LT}}{E_T} = 0.5; \qquad \frac{G_{TT}}{E_T} = 0.2; \qquad \nu_{LT} = \nu_{TT} = 0.25 \tag{5.55}$$

Non-dimensional physical properties will be used when comparing the results for different values of a/h and N_I. The non-dimensional transverse displacement $\bar{w}$ is calculated using the formula (5.56), where w is evaluated at $(a/2, b/2, 0)$. The non-dimensional in-plane stress $\bar{\sigma}_{xx}$ is calculated according to formula (5.57), where σ_{xx} is evaluated at $(a/2, b/2, h/2)$. The non-dimensional transverse shear stress $\bar{\sigma}_{xz}$ is calculated according to formula (5.58), where σ_{xz} is evaluated at $(0, b/2, 0)$.

$$\bar{w} = \frac{w 100 E_T h^3}{q_0 a^4} \tag{5.56}$$

$\bar{w}$	$N_I = 4$			
	$a/h = 4$		$a/h = 6$	
	PM	[42]	PM	[42]
3D [181]		4.181		2.556
LD3	4.276	4.180	2.617	2.556
ED1+LD3-full	4.275		2.617	
ED1+LD3-part	3.195		2.114	
ED1	2.996	2.924	1.958	1.917

(a) Test case N.1: harmonic distribution of transverse pressure

$\bar{w}$	$N_I = 4$					
	$a/h = 4$		$a/h = 10$		$a/h = 100$	
	PM	[42]	PM	[42]	PM	[42]
LM4		2.9679		1.1817		0.8123
LD3	2.9679		1.1817		0.8114	
ED1+LD3-full	2.9668		1.1816		0.8114	
ED1+LD3-part	2.2654		1.0773		0.8084	
ED1	2.1095	2.1096	1.0068	1.0068	0.7997	0.7997

(b) Test case N.3: transverse distribution of constant pressure

Table 5.2: Comparison of different plate models against superposition of models for non-dimensional transverse displacement for plates with four layers $\left(0^0/90^0/0^0/90^0\right)$.

$\bar{\sigma}_{xx}$	$N_I = 3$					
	$a/h = 4$		$a/h = 10$		$a/h = 100$	
	PM	[42]	PM	[42]	PM	[42]
LD3	1.1169	1.1174	0.8720	0.8708		0.8083
LD1					0.8090	
ED1+LD4-full	1.1169		0.8720			
ED1+LD1-full					0.8090	
ED1+LD4-part	0.8687		0.8567			
ED1+LD1-part					0.8086	
ED1	0.6665	0.6648	0.7753	0.7733	0.8038	0.8037

(a) Test case N.3: transverse distribution of constant pressure

$\bar{\sigma}_{xx}$	$N_I = 3$					
	$a/h = 4$		$a/h = 10$		$a/h = 100$	
	PM	[42]	PM	[42]	PM	[42]
LM4		0.5592		0.4355		0.4042
LD3	0.5592		0.4364			
LD1					0.4045	
ED1+LD3-full	0.5592		0.4364			
ED1+LD1-full					0.4045	
ED1+LD3-part	0.4352		0.4303			
ED1+LD1-part					0.4040	
ED1	0.3353	0.3324	0.3901	0.3866	0.4020	0.4019

(b) Test case N.4: triangular distribution of transverse pressure

Table 5.3: Comparison of different plate models against superposition of models for non-dimensional in-plane stresses for plates with three layers $\left(0^0/90^0/0^0\right)$.

$$\bar{\sigma}_{xx} = \frac{\sigma_{xx}}{q_0 \left(a/h\right)^2} \tag{5.57}$$

$$\bar{\sigma}_{xz} = \frac{\sigma_{xz}}{q_0 a/h} \tag{5.58}$$

In tables 5.1, 5.2, 5.3, 5.4 the results obtained with the present modeling approach are indicated by the acronym PM standing for *present model.*

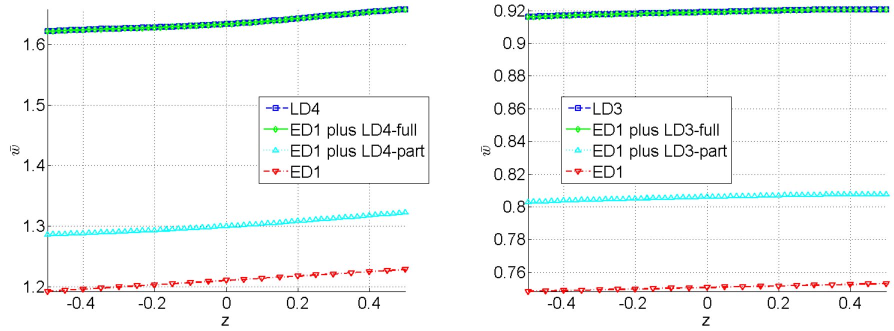

(a) Test case N.1: harmonic distribution of transverse pressure for $a/h = 6$

(b) Test case N.2: bi-harmonic distribution of transverse pressure for $a/h = 10$

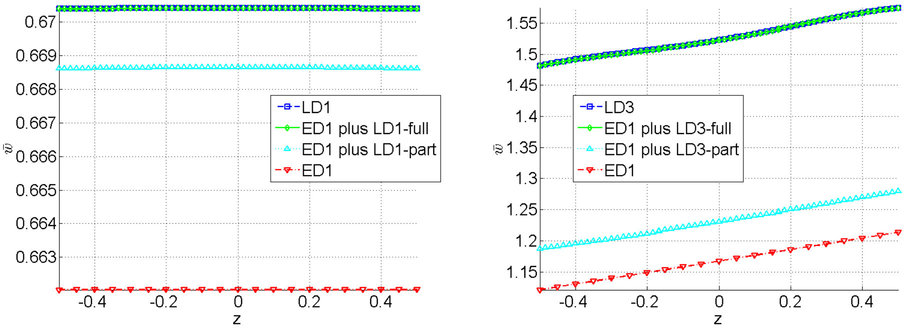

(c) Test case N.3: transverse distribution of constant pressure for $a/h = 100$

(d) Test case N.4: triangular distribution of transverse pressure for $a/h = 4$

Figure 5-15: Comparison of different plate models against superposition of models for non-dimensional transverse displacement for plates with three layers $(0^0/90^0/0^0)$.

Test case N.1: cross-ply plate in cylindrical bending loaded by harmonic distribution of transverse pressure

The harmonic distribution of transverse pressure in (5.59) is applied to the top surface of the plate (see Figure 5-13a) and $b = 3a$.

$$q_z = q_0 \sin\left(\frac{\pi x}{a}\right) \tag{5.59}$$

The results for different a/h configurations are displayed in tables 5.1a (case $N_I = 3$) and 5.2a (case $N_I = 4$). The non-dimensional transverse displacements, in-plane stresses and transverse shear stresses are plotted, respectively, in figures 5-15a, 5-16a and 5-17a for the case of $a/h = 6$.

The results for the present model in tables 5.1a and 5.2a are equivalent to the analytical results in [181] and in good agreement with those previously published in [42].

Moreover, table 5.1a and figures 5-15a, 5-16a and 5-17a show that, as expected, superpositioning the ED1 plate model with an LD4 plate model throughout the plate

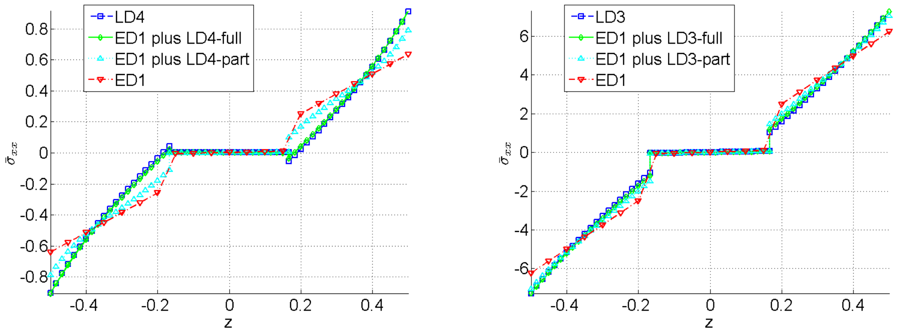

(a) Test case N.1: harmonic distribution of transverse pressure for $a/h = 6$

(b) Test case N.2: bi-harmonic distribution of transverse pressure for $a/h = 10$

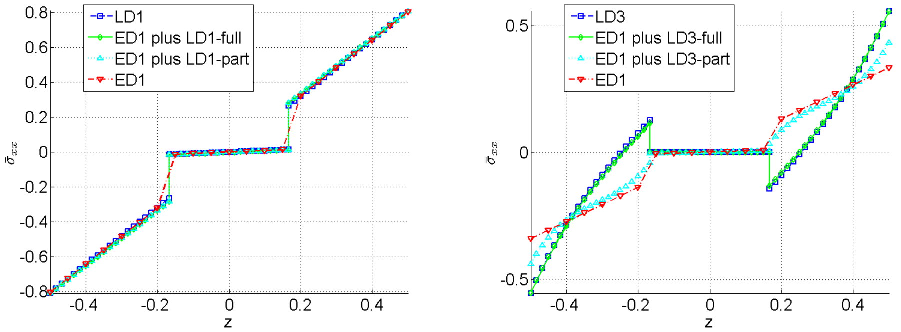

(c) Test case N.3: transverse distribution of constant pressure for $a/h = 100$

(d) Test case N.4: triangular distribution of transverse pressure for $a/h = 4$

Figure 5-16: Comparison of different plate models against superposition of models for non-dimensional in-plane stresses for plates with three layers $(0^0/90^0/0^0)$.

(ED1+LD4-full) generates the same results as those of the LD4 plate model alone. This is confirmed by the results in table 5.2a for the case ED1+LD3-full.

Finally, by superpositioning these two plate models only in the center and the sides of the plate (ED1+LD4-part or ED1+LD3-part) the approximation is improved yielding better results compared to ED1 alone.

Test case N.2: cross-ply plate loaded by bi-harmonic distribution of transverse pressure

The bi-harmonic distribution of transverse pressure in (5.60) is applied to the top-surface of a cross-ply plate (see figure 5-13b) and $b = 2a$.

$$q_z = q_0 \sin\left(\frac{\pi x}{a}\right) \sin\left(\frac{\pi y}{b}\right) \tag{5.60}$$

The results for different a/h configurations are displayed in table 5.1b, while the non-dimensional transverse displacements, in-plane stresses and transverse shear stresses are plotted, respectively, in figures 5-15b, 5-16b and 5-17b for the case of $a/h = 10$.

The results for the present model in tables 5.1b are equivalent to the analytical results in [181] and in good agreement with those previously published in [42].

As for the previous test case, table 5.1b and figures 5-15b, 5-16b and 5-17b show that the results obtained by superpositioning the ED1 plate model with an LD3 plate model throughout the plate, i.e using the plate model ED1+LD3-full are equivalent to those of the LD3 plate model alone. Furthermore, by superpositioning these two plate models only in the center and the sides of the plate (ED1+LD4-part), the approximation again is improved compared to ED1 alone.

Test case N.3: cross-ply plate loaded by transverse distribution of constant pressure

A square plate ($b = a$) is loaded by the transverse distribution of constant pressure in (5.61) (see figure 5-13c).

$$q_z = q_0 \tag{5.61}$$

The results for different a/h configurations are displayed in tables 5.1c (case $N_I = 3$), 5.2b (case $N_I = 4$), 5.3a and 5.4a, while the non-dimensional transverse displacements, in-plane stresses and transverse shear stresses are displayed, respectively, in figures 5-15c, 5-16c and 5-17c for the case of $a/h = 100$.

$\bar{\sigma}_{xz}$	$N_I = 3$					
	$a/h = 4$		$a/h = 10$		$a/h = 100$	
	PM	[42]	PM	[42]	PM	[42]
LD3	0.44675	0.44343	0.63403	0.62784		0.72009
LD1					0.72641	
ED1+LD3-full	0.44675		0.63403			
ED1+LD1-full					0.72641	
ED1+LD3-part	0.30081		0.50739			
ED1+LD1-part					0.72600	
ED1	0.23515	0.64669	0.25853	0.70600	0.26512	0.72096

(a) Test case N.3: transverse distribution of constant pressure

$\bar{\sigma}_{xz}$	$N_I = 3$					
	$a/h = 4$		$a/h = 10$		$a/h = 100$	
	PM	[42]	PM	[42]	PM	[42]
LM4		0.1656		0.2281		0.2499
LD3	0.1667		0.2314			
LD1					0.2524	
ED1+LD3-full	0.1667		0.2314			
ED1+LD1-full					0.2524	
ED1+LD3-part	0.1034		0.1840			
ED1+LD1-part					0.2514	
ED1	0.0759	0.2106	0.0884	0.2394	0.0926	0.2489

(b) Test case N.4: triangular distribution of transverse pressure

Table 5.4: Comparison of different plate models against superposition of models for non-dimensional transverse shear stresses for plates with three layers $\left(0^0/90^0/0^0\right)$.

The results for the present model in tables 5.1c, 5.2b, 5.3a and 5.4a are in good agreement with those previously published in [42], except for the values of non-dimensional transverse shear stresses for plate model ED1 in table 5.4a. By superpositioning the ED1 plate model with an enhancing plate model the approximation is improved, compared to using only the ED1 plate model alone, yielding more accurate results.

Test case N.4: cross-ply square plate loaded by triangular distribution of transverse pressure

The triangular distribution of transverse pressure in (5.62) is applied to the top surface of a square ($b = a$) plate (see figure 5-13d).

$$q_z = q_0 \frac{x}{a} \tag{5.62}$$

The results for different a/h configurations are displayed in tables 5.1d, 5.3b and 5.4b, while the non-dimensional transverse displacements, in-plane stresses and transverse shear stresses are displayed, respectively, in figures 5-15d, 5-16d and 5-17d for the case of $a/h = 4$.

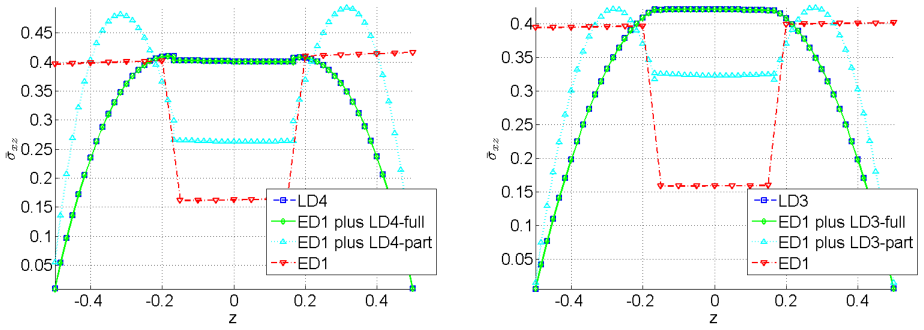

(a) Test case N.1: harmonic distribution of transverse pressure for $a/h = 6$

(b) Test case N.2: bi-harmonic distribution of transverse pressure for $a/h = 10$

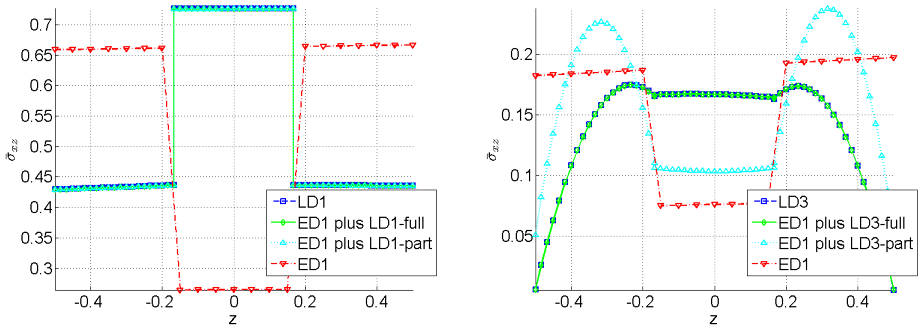

(c) Test case N.3: transverse distribution of constant pressure for $a/h = 100$

(d) Test case N.4: triangular distribution of transverse pressure for $a/h = 4$

Figure 5-17: Comparison of different plate models against superposition of models for non-dimensional transverse shear stresses for plates with three layers $\left(0^0/90^0/0^0\right)$.

The results for the present model in tables 5.1d, 5.3b and 5.4b are in good agreement with those previously published in [42]. As for the previous case there was a discrepancy between the values of the non-dimensional transverse shear stresses for plate model ED1 in table 5.4b.

Also in this case, by superpositioning the ED1 model with an enhancing plate model, the approximation is improved compared to the case of considering ED1 alone.

5.6 Conclusions

In this chapter, a new computational approach for the accurate estimation of interlaminar stresses in thick layered material is presented. The approach combines an extended FEM to a multilevel mesh superposition approach.

First the general theory and then the finite element formulation based on a multilevel mesh superposition method was derived. A cohesive zone model was included in the development.

The results for the multiple plate models demonstrate an improvement in the computed transverse displacements and stresses compared to equivalent single layer plate models used alone. Results are also in excellent agreement with 3-D analytical solutions and show good correlation with those previously published in literature.

The theory presented in this chapter can be extended to incorporate thermal effects, shell structures, mixed variational formulations and multifield problems.

Chapter 6

Conclusions and future work

6.1 Summary of work carried out

The overall objective of this thesis was the experimental-numerical study of the potential use of shape memory alloys (SMA) embedded into woven composite layers for structural energy dissipation. The work carried out to date is summarized here.

In chapter 2 the basic properties of shape memory alloys (SMAs) have been examined. In this chapter the constitutive equations for SMA hybrid composites (SMAHCs) have been discussed, and the impact damage resistance and damage suppression properties of SMAHCs have been reviewed distinguishing between active and passive methods.

In chapter 3 the analytical methods based on the mechanics of materials approach for homogenization of two-dimensional (2-D) woven composites have been critically reviewed. The analytical methods have been compared with the asymptotic expansion homogenization method (AEHM) approach, and anisotropic damage mechanics has been integrated with the AEHM to model failure in this chapter. These methods have been coded in MATLAB and tested against data extracted from the literature.

In chapter 4 the Brinson one-dimensional constitutive model and the Sadjadpour and Bhattacharya three-dimensional (3-D) constitutive model for SMA have been reviewed, and results of these models implemented in MATLAB have been given. The finite element implementation of these models has also been considered. In this chapter a multiscale 3-D constitutive model for SMAHCs based on the AEHM approach has been proposed, and the AEHM macroscopic problem for SMAHCs has been reformulated using Transformation Field Analysis (TFA). Moreover, samples of SMAHCs were manufactured and tested in laboratory, and a comparison of impact testing results for woven and uni-directional SMAHCs has been presented in this chapter.

In chapter 5 the multiple plate models theory for laminated composite plates has been formulated. The accuracy of the linear analysis for the multiple plate models theory has also been reported in this chapter.

This work was carried out between November 2007 and September 2010.

6.2 Original contributions

Original contributions of this thesis are the following:

1. A thorough review of impact damage resistance and damage suppression properties of SMAHCs.
2. The comparison of homogenization methods for 2-D woven composites including analytical methods and the AEHM approach.
3. A theoretical framework for multiscale 3-D constitutive modeling of SMAHCs based on the AEHM approach and TFA.
4. A comparison of the impact testing results for woven and uni-directional SMAHCs.
5. The formulation of the multiple plate models theory for laminated composite plates.

6.3 Scope for future work

There was never any certainty in receiving from the sponsor QinetiQ Limited samples of woven SMAHC, which were finally made available only in July 2010, very late into the research project.

For this reason, from year two of project, more emphasis was placed on developing advanced methodologies for modeling composite laminates giving rise to the methods described in chapter 5. The techniques specific to woven SMAHC discussed in chapter 4 were formalized only theoretically and have not been fully implemented in code.

As a result there is scope for future work, and specifically the following activities are suggested:

1. Coding of the proposed multiscale 3-D constitutive model for SMAHCs.
2. Integration of the multiscale model for SMAHCs with the multiple plate models theory for laminated composite plates.
3. Inclusion of the delamination models discussed in chapter 5 into the multiple plate models software.

Appendix A

Micromechanical models

In the following Sections, m stands for matrix, and f stands for reinforcement fibres, and V_f is the volume fraction of fibre reinforcements, while $V_m = 1 - V_f$ is the volume fraction of the matrix.

A.1 Rule-of-Mixtures

For the rule-of-mixtures the following equations are valid:

$$E_{11}^{sel} = E_{11f}V_f + E_mV_m \tag{A.1}$$

$$E_{22}^{sel} = \frac{E_{22f}E_m}{E_mV_f + E_{22f}V_m} \tag{A.2}$$

$$G_{12}^{sel} = \frac{G_{12f}G_m}{G_mV_f + G_{12f}V_m} \tag{A.3}$$

$$\nu_{12}^{sel} = \nu_{12f}V_f + \nu_mV_m \tag{A.4}$$

A.2 Chamis Model

For the micromechanical model developed by Chamis [43] the following equations are valid

$$E_{11}^{sel} = E_{11f}V_f + E_mV_m \tag{A.5}$$

$$E_{22}^{sel} = \frac{E_m}{1-\sqrt{V_f}\left(1-\frac{E_m}{E_{22f}}\right)} \tag{A.6}$$

$$G_{12}^{sel} = \frac{G_m}{1-\sqrt{V_f}\left(1-\frac{G_m}{G_{12f}}\right)} \tag{A.7}$$

$$G_{23}^{sel} = \frac{G_m}{1-V_f\left(1-\frac{G_m}{G_{23f}}\right)} \tag{A.8}$$

$$\nu_{12}^{sel} = \nu_{12f}V_f + \nu_mV_m \tag{A.9}$$

$$\nu_{23}^{sel} = \nu_{23f}V_f + V_m\left(2\nu_m - \frac{\nu_{12}^{sel}}{E_{11}^{sel}}E_{22}^{sel}\right) \tag{A.10}$$

A.3 Hashin and Rosen Model for Anisotropic Constituents

For the micromechanical model developed by Hashin and Rosen (or *Composite Cylinder Assemblage model (CCA)*) for anisotropic constituents [98] the following equations are valid:

$$E_{11}^{sel} = E_{11f}V_f + E_mV_m + \frac{4\left(\nu_{12f}-\nu_m\right)^2V_fV_m}{\frac{V_m}{k_f}+\frac{V_f}{k_m}+\frac{1}{G_m}} \tag{A.11}$$

$$\nu_{12}^{sel} = \nu_{12f}V_f + \nu_mV_m + \frac{\left(\nu_{12f}-\nu_m\right)\left(\frac{1}{k_m}-\frac{1}{k_f}\right)V_fV_m}{\frac{V_m}{k_f}+\frac{V_f}{k_m}+\frac{1}{G_m}} \tag{A.12}$$

$$G_{12}^{sel} = G_m\frac{G_mV_m + G_{12f}\left(1+V_f\right)}{G_m\left(1+V_f\right)+G_{12f}V_m} \tag{A.13}$$

$$\tag{A.14}$$

where

$$k_f = \frac{E_{11f}E_{22f}}{2E_{11f}\left(1-\nu_{23f}\right)-4\nu_{12f}^2E_{22f}} \tag{A.15}$$

$$k_m = \frac{E_m}{2\left(1-\nu_m-2\nu_m^2\right)} \tag{A.16}$$

If $k_f > k_m$ and $G_{12f} > G_m$

$$G_{23(-)}^{sel} = G_m + \frac{V_f}{\frac{1}{G_{23f} - G_m} + \frac{k_m + 2G_m}{2G_m (k_m + G_m)} V_f} \tag{A.17}$$

$$G_{23(+)}^{sel} = G_m + \frac{1 + (1 + \beta_m) V_f}{\rho - V_f \left(1 + \frac{3\beta_m^2 V_m^2}{\alpha V_f^3 + 1}\right)} \tag{A.18}$$

else

$$G_{23(-)}^{sel} = G_m \frac{1 + (1 + \beta_m) V_f}{\rho - V_f \left(1 + \frac{3\beta_m^2 V_m^2}{\alpha V_f^3 - \beta_m}\right)} \tag{A.19}$$

$$G_{23(+)}^{sel} = G_m \frac{V_f}{\frac{1}{G_{23f} - G_m} + \frac{k_m + 2G_m}{2G_m (k_m + G_m) V_f}} \tag{A.20}$$

where

$$\beta_m = \frac{k_m}{k_m + 2G_m} \tag{A.21}$$

$$\beta_f = \frac{k_f}{k_f + 2G_{23f}} \tag{A.22}$$

$$\gamma = \frac{G_{23f}}{G_m} \tag{A.23}$$

$$\alpha = \frac{\beta_m - \gamma\beta_f}{1 + \gamma\beta_f} \tag{A.24}$$

$$\rho = \frac{\gamma + \beta_m}{\gamma - 1} \tag{A.25}$$

$$E_{22(\pm)}^{sel} = \frac{4G_{23(\pm)}^{sel}}{1 + \left(\frac{G_{23(\pm)}^{sel}}{k}\right)\left(1 + \frac{4k{\nu_{12}^{sel}}^2}{E_{11}^{sel}}\right)} \tag{A.26}$$

$$\nu_{23(\pm)}^{sel} = \left(1 - \frac{G_{23(\pm)}^{sel}}{k}\right) \frac{1 + \frac{4k{\nu_{12}^{sel}}^2}{E_{11}^{sel}}}{1 + \frac{G_{23(\pm)}^{sel}}{k}\left(1 + \frac{4k{\nu_{12}^{sel}}^2}{E_{11}^{sel}}\right)} \tag{A.27}$$

where

$$k = \frac{k_m (k_f + G_m) V_m + k_f (k_m + G_m) V_f}{(k_f + G_m) V_m + (k_m + G_m) V_f} \tag{A.28}$$

A.4 Hashin and Rosen Model for Isotropic Constituents

For the micromechanical model developed by Hashin and Rosen for isotropic constituents [211] (also called *CCA model for isotropic constituents*) the following equations are valid:

$$E_{11}^{sel} = E_f V_f + E_m V_m + \frac{4\left(\nu_f - \nu_m\right)^2 V_f V_m}{\frac{V_m}{k_f} + \frac{V_f}{k_m} + \frac{1}{G_m}} \tag{A.29}$$

$$G_{12}^{sel} = G_m \frac{G_m V_m + G_f\left(1 + V_f\right)}{G_m\left(1 + V_f\right) + G_f V_m} \tag{A.30}$$

$$\nu_{12}^{sel} = \nu_f V_f + \nu_m V_m + \frac{\left(\nu_f - \nu_m\right)\left(\frac{1}{k_m} - \frac{1}{k_f}\right) V_f V_m}{\frac{V_m}{k_f} + \frac{V_f}{k_m} + \frac{1}{G_m}} \tag{A.31}$$

where

$$k_f = \frac{E_f}{2\left(1 - \nu_f - 2\nu_f^2\right)} \tag{A.32}$$

$$k_m = \frac{E_m}{2\left(1 - \nu_m - 2\nu_m^2\right)} \tag{A.33}$$

$$G_{23}^{sel} = G_m \frac{\left(\alpha + \beta_m V_f\right)\left(1 + \rho V_f^3\right) - 3 V_f V_m^2 \beta_m^2}{\left(\alpha - V_f\right)\left(1 + \rho V_f^3\right) - 3 V_f V_m^2 \beta_m^2} \tag{A.34}$$

where

$$\beta_m = \frac{1}{3 - 4\nu_m} \tag{A.35}$$

$$\beta_f = \frac{1}{3 - 4\nu_f} \tag{A.36}$$

$$\gamma = \frac{G_f}{G_m} \tag{A.37}$$

$$\alpha = \frac{\gamma + \beta_m}{\gamma - 1} \tag{A.38}$$

$$\rho = \frac{\beta_m - \gamma\beta_f}{1 + \gamma\beta_f} \tag{A.39}$$

$$E_{22}^{sel} = \frac{4 k G_{23}^{sel}}{k + G_{23}^{sel}\left(1 + \frac{4 k \nu_{12}^{sel\,2}}{E_{11}^{sel}}\right)} \tag{A.40}$$

where

$$k = \frac{k_m k_f + \left(V_f k_f + V_f k_m\right) G_m}{V_m k_f + V_f k_m + G_m} \tag{A.41}$$

$$\nu_{23}^{sel} = \frac{E_{22}^{sel}}{2G_{23}^{sel} - 1} \tag{A.42}$$

Appendix B

Fill and warp fibres transformation matrices

B.1 Transformation Matrix

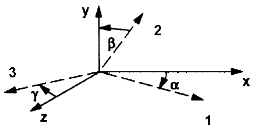

Figure B-1: Principal and global coordinate systems [226]

The stress transformation between the global and local coordinate systems for a composite lamina is given by [226]

$$\begin{Bmatrix} \sigma_1 \\ \sigma_2 \\ \sigma_3 \\ \tau_{23} \\ \tau_{31} \\ \tau_{12} \end{Bmatrix} = [T_\epsilon] \begin{Bmatrix} \sigma_x \\ \sigma_y \\ \sigma_z \\ \tau_{yz} \\ \tau_{zx} \\ \tau_{xy} \end{Bmatrix} \tag{B.1}$$

where transformed stiffness matrix is

$$[T_\epsilon] = \begin{bmatrix} l_1^2 & m_1^2 & n_1^2 & 2m_1n_1 & 2n_1l_1 & 2l_1m_1 \\ l_2^2 & m_2^2 & n_2^2 & 2m_2n_2 & 2n_2l_2 & 2l_2m_2 \\ l_3^2 & m_3^2 & n_3^2 & 2m_3n_3 & 2n_3l_3 & 2l_3m_3 \\ l_2l_3 & m_2m_3 & n_2n_3 & (m_2n_3+m_3n_2) & (l_2n_3+l_3n_2) & (l_2m_3+l_3m_2) \\ l_1l_3 & m_1m_3 & n_1n_3 & (m_1n_3+m_3n_1) & (l_1n_3+l_3n_1) & (l_1m_3+l_3m_1) \\ l_1l_2 & m_1m_2 & n_1n_2 & (m_1n_2+m_2n_1) & (l_1n_2+l_2n_1) & (l_1m_2+l_2m_1) \end{bmatrix} \tag{B.2}$$

and the cosine directors are defined as

$$l_i = \cos{(i,x)} \qquad m_i = \cos{(i,y)} \qquad n_i = \cos{(i,z)} \qquad (i,j = 1,2,3) \tag{B.3}$$

B.2 Fill Fibres Transformation Matrix

For a woven composite lamina two coordinate transformations are necessary [50], and the cosine directors are given by

$$\begin{bmatrix} l_1 & m_1 & n_1 \\ l_2 & m_2 & n_2 \\ l_3 & m_3 & n_3 \end{bmatrix} = \begin{bmatrix} \cos\beta\cos\theta & \cos\beta\sin\theta & \sin\beta \\ -\sin\theta & \cos\theta & 0 \\ -\sin\beta\cos\theta & -\sin\beta\sin\theta & \cos\beta \end{bmatrix} \tag{B.4}$$

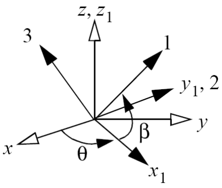

Figure B-2: Coordinate transformations for the woven composite lamina [50]

Because the Fill fibres orientation is along the $x-$axis, imposing in $[T_\epsilon]$ that $\theta = 0$ and $\beta = \theta_F$, the stress transformation matrix, and its inverse, for the Fill strand become

$$\left[T^F\right] = \begin{bmatrix} c_F^2 & 0 & s_F^2 & 0 & 2c_F s_F & 0 \\ 0 & 1 & 0 & 0 & 0 & 0 \\ s_F^2 & 0 & c_F^2 & 0 & -2c_F s_F & 0 \\ 0 & 0 & 0 & c_F & 0 & -s_F \\ -c_F s_F & 0 & c_F s_F & 0 & 2c_F^2 - 1 & 0 \\ 0 & 0 & 0 & s_F & 0 & c_F \end{bmatrix} \tag{B.5}$$

$$\left[T^F\right]^{-1} = \begin{bmatrix} c_F^2 & 0 & s_F^2 & 0 & -2s_F c_F & 0 \\ 0 & 1 & 0 & 0 & 0 & 0 \\ s_F^2 & 0 & c_F^2 & 0 & 2s_F c_F & 0 \\ 0 & 0 & 0 & c_F & 0 & s_F \\ s_F c_F & 0 & -s_F c_F & 0 & 2c_F^2 - 1 & 0 \\ 0 & 0 & 0 & -s_F & 0 & c_F \end{bmatrix} \tag{B.6}$$

where $s_F = \sin(\theta_F)$, $c_F = \cos(\theta_F)$ and the Reuter matrix and its inverse are given by

$$[R] = \begin{bmatrix} 1 & 0 & 0 & 0 & 0 & 0 \\ 0 & 1 & 0 & 0 & 0 & 0 \\ 0 & 0 & 1 & 0 & 0 & 0 \\ 0 & 0 & 0 & 2 & 0 & 0 \\ 0 & 0 & 0 & 0 & 2 & 0 \\ 0 & 0 & 0 & 0 & 0 & 2 \end{bmatrix} \tag{B.7}$$

$$[R]^{-1} = \begin{bmatrix} 1 & 0 & 0 & 0 & 0 & 0 \\ 0 & 1 & 0 & 0 & 0 & 0 \\ 0 & 0 & 1 & 0 & 0 & 0 \\ 0 & 0 & 0 & \frac{1}{2} & 0 & 0 \\ 0 & 0 & 0 & 0 & \frac{1}{2} & 0 \\ 0 & 0 & 0 & 0 & 0 & \frac{1}{2} \end{bmatrix} \tag{B.8}$$

The transformed stiffness matrix for the Fill strand in the global coordinates is

$$\left[\bar{Q}^F\right] = \begin{bmatrix} \bar{Q}^F_{11} & \bar{Q}^F_{12} & \bar{Q}^F_{13} & 0 & \bar{Q}^F_{15} & 0 \\ \bar{Q}^F_{12} & \bar{Q}^F_{22} & \bar{Q}^F_{23} & 0 & \bar{Q}^F_{25} & 0 \\ \bar{Q}^F_{13} & \bar{Q}^F_{23} & \bar{Q}^F_{33} & 0 & \bar{Q}^F_{35} & 0 \\ 0 & 0 & 0 & \bar{Q}^F_{44} & 0 & \bar{Q}^F_{46} \\ \bar{Q}^F_{15} & \bar{Q}^F_{25} & \bar{Q}^F_{35} & 0 & \bar{Q}^F_{55} & 0 \\ 0 & 0 & 0 & \bar{Q}^F_{46} & 0 & \bar{Q}^F_{66} \end{bmatrix} \tag{B.9}$$

where

$$
\begin{aligned}
&\bar{Q}^F_{11} = Q^F_{xx} = c^4_F Q^F_{11} + 2c^2_F s^2_F Q^F_{13} + s^4_F Q^F_{33} + 4s^2_F c^2_F Q^F_{55} \\
&\bar{Q}^F_{12} = Q^F_{xy} = c^2_F Q^F_{12} + s^2_F Q^F_{23} \\
&\bar{Q}^F_{13} = Q^F_{xz} = c^2_F s^2_F Q^F_{11} + c^4_F Q^F_{13} + s^4_F Q^F_{13} + s^2_F c^2_F Q^F_{33} - 4s^2_F c^2_F Q^F_{55} \\
&\bar{Q}^F_{15} = Q^F_{xr} = c^3_F s_F Q^F_{11} - c^3_F s_F Q^F_{13} + s^3_F c_F Q^F_{13} - s^3_F c_F Q^F_{33} - 4s_F c^3_F Q^F_{55} + 2s_F c_F Q^F_{55} \\
&\bar{Q}^F_{22} = Q^F_{yy} = Q^F_{22} \\
&\bar{Q}^F_{23} = Q^F_{yz} = s^2_F Q^F_{12} + c^2_F Q^F_{23} \\
&\bar{Q}^F_{25} = Q^F_{yr} = s_F c_F Q^F_{12} - s_F c_F Q^F_{23} \\
&\bar{Q}^F_{33} = Q^F_{zz} = s^4_F Q^F_{11} + 2c^2_F s^2_F Q^F_{13} + c^4_F Q^F_{33} + 4s^2_F c^2_F Q^F_{55} \\
&\bar{Q}^F_{35} = Q^F_{zr} = s^3_F c_F Q^F_{11} - s^3_F c_F Q^F_{13} + c^3_F s_F Q^F_{13} - c^3_F s_F Q^F_{33} + 4s_F c^3_F Q^F_{55} - 2s_F c_F Q^F_{55} \\
&\bar{Q}^F_{44} = Q^F_{qq} = c^2_F Q^F_{44} + s^2_F Q^F_{66} \\
&\bar{Q}^F_{46} = Q^F_{qs} = -c_F s_F Q^F_{44} + s_F c_F Q^F_{66} \\
&\bar{Q}^F_{55} = Q^F_{rr} = c^2_F s^2_F Q^F_{11} - 2c^2_F s^2_F Q^F_{13} + s^2_F c^2_F Q^F_{33} + 4c^4_F Q^F_{55} - 4c^2_F Q^F_{55} + Q^F_{55} \\
&\bar{Q}^F_{66} = Q^F_{ss} = s^2_F Q^F_{44} + c^2_F Q^F_{66}
\end{aligned}
$$

B.3 Warp Fibres Transformation Matrix

Because the Warp fibres orientation is along the $y-$axis, imposing in $[T_\epsilon]$ that $\theta = \frac{\pi}{2}$ and $\beta = \theta_W$, the stress transformation matrix, and its inverse, for the Warp strand become

$$
[T^W] = \begin{bmatrix}
0 & c^2_W & s^2_W & 2c_W s_W & 0 & 0 \\
1 & 0 & 0 & 0 & 0 & 0 \\
0 & s^2_W & c^2_W & -2c_W s_W & 0 & 0 \\
0 & 0 & 0 & 0 & -c_W & s_W \\
0 & -c_W s_W & c_W s_W & 2c^2_W - 1 & 0 & 0 \\
0 & 0 & 0 & 0 & -s_W & -c_W
\end{bmatrix} \tag{B.10}
$$

$$
[T^W]^{-1} = \begin{bmatrix}
0 & 1 & 0 & 0 & 0 & 0 \\
c^2_W & 0 & s^2_W & 0 & -2c_W s_W & 0 \\
s^2_W & 0 & c^2_W & 0 & 2c_W s_W & 0 \\
c_W s_W & 0 & -c_W s_W & 0 & 2c^2_W - 1 & 0 \\
0 & 0 & 0 & -c_W & 0 & -s_W \\
0 & 0 & 0 & s_W & 0 & -c_W
\end{bmatrix} \tag{B.11}
$$

where $s_W = \sin(\theta_W)$ and $c_W = \cos(\theta_W)$. The transformed stiffness matrix for the Warp strand in the global coordinates is

$$\left[\bar{Q}^W\right] = \begin{bmatrix} \bar{Q}_{11}^W & \bar{Q}_{12}^W & \bar{Q}_{13}^W & \bar{Q}_{14}^W & 0 & 0 \\ \bar{Q}_{12}^W & \bar{Q}_{22}^W & \bar{Q}_{23}^W & \bar{Q}_{24}^W & 0 & 0 \\ \bar{Q}_{13}^W & \bar{Q}_{23}^W & \bar{Q}_{33}^W & \bar{Q}_{34}^W & 0 & 0 \\ \bar{Q}_{14}^W & \bar{Q}_{24}^W & \bar{Q}_{34}^W & \bar{Q}_{44}^W & 0 & 0 \\ 0 & 0 & 0 & 0 & \bar{Q}_{55}^W & \bar{Q}_{56}^W \\ 0 & 0 & 0 & 0 & \bar{Q}_{56}^W & \bar{Q}_{66}^W \end{bmatrix} \tag{B.12}$$

where

$$\begin{aligned}
\bar{Q}_{11}^W &= Q_{xx}^W = Q_{22}^W \\
\bar{Q}_{12}^W &= Q_{xy}^W = c_W^2 Q_{12}^W + s_W^2 Q_{23}^W \\
\bar{Q}_{13}^W &= Q_{xz}^W = s_W^2 Q_{12}^W + c_W^2 Q_{23}^W \\
\bar{Q}_{14}^W &= Q_{xq}^W = s_W c_W Q_{12}^W - s_W c_W Q_{23}^W \\
\bar{Q}_{22}^W &= Q_{yy}^W = c_W^4 Q_{11}^W + 2 c_W^2 s_W^2 Q_{13}^W + s_W^4 Q_{33}^W + 4 s_W^2 c_W^2 Q_{55}^W \\
\bar{Q}_{23}^W &= Q_{yz}^W = c_W^2 s_W^2 Q_{11}^W + c_W^4 Q_{13}^W + s_W^4 Q_{13}^W + s_W^2 c_W^2 Q_{33}^W - 4 s_W^2 c_W^2 Q_{55}^W \\
\bar{Q}_{24}^W &= Q_{yq}^W = c_W^3 s_W Q_{11}^W - c_W^3 s_W Q_{13}^W + s_W^3 c_W Q_{13}^W - s_W^3 c_W Q_{33}^W - 4 s_W c_W^3 Q_{55}^W + 2 s_W c_W Q_{55}^W \\
\bar{Q}_{33}^W &= Q_{zz}^W = s_W^4 Q_{11}^W + 2 c_W^2 s_W^2 Q_{13}^W + c_W^4 Q_{33}^W + 4 s_W^2 c_W^2 Q_{55}^W \\
\bar{Q}_{34}^W &= Q_{zq}^W = s_W^3 c_W Q_{11}^W + c_W^3 s_W Q_{13}^W - s_W^3 c_W Q_{13}^W - s_W c_W^3 Q_{33}^W + 4 s_W c_W^3 Q_{55}^W - 2 s_W c_W Q_{55}^W \\
\bar{Q}_{44}^W &= Q_{qq}^W = c_W^2 s_W^2 Q_{11}^W - 2 c_W^2 s_W^2 Q_{13}^W + s_W^2 c_W^2 Q_{33}^W + 4 c_W^4 Q_{55}^W - 4 c_W^2 Q_{55}^W + Q_{55}^W \\
\bar{Q}_{55}^W &= Q_{rr}^W = c_W^2 Q_{44}^W + s_W^2 Q_{66}^W \\
\bar{Q}_{56}^W &= Q_{rs}^W = -c_W s_W Q_{44}^W + s_W c_W Q_{66}^W \\
\bar{Q}_{66}^W &= Q_{ss}^W = s_W^2 Q_{44}^W + c_W^2 Q_{66}^W
\end{aligned}$$

Appendix C

Numerical implementation of the Brinson model

For the numerical simulation of the Brinson model, the evolution equations are discretized in time using the *Backward Euler* method or *implicit method* by assuming strain and temperature as control variable, and treating the non-linear behavior of the material as a strain-driven, temperature-driven and time-discrete problem.

To develop the solution for the time-discrete model, a suitable *return-mapping* algorithm [178, 225] similar to those in classical elasto-plasticity, such as the elastic predictor-transformation corrector is used. The algorithm known as elastic predictor-transformation corrector return mapping algorithm consists of two stages:

1. The elastic stage aims at determining whether or not phase transformation is to occur, and giving the directions of evolution of transformation in the positive case.
2. The stage of transformation correction to update the transformation strain tensor, the volume fraction of Martensite and the stress tensor, for the total strain found in stage 1. The transformation correction is carried out to correct the stress and transformation strain tensors corresponding to the current state of temperature and total strain.

Given strain ϵ and temperature T at time $(n+1)$, the numerical solution procedure consists in finding the factions of Martensite (ξ_S and ξ_M) at time $(n+1)$ solving a non-linear algebraic system of equations using the multivariate Newton-Raphson method, and then finding the stress σ at time $(n+1)$.

$$\begin{aligned}
\frac{\mathrm{d}\xi_S}{\mathrm{d}t} &= f_1\left(\xi_S, \xi_M, \sigma, T\right) \\
\frac{\mathrm{d}\xi_M}{\mathrm{d}t} &= f_2\left(\xi_S, \xi_M, \sigma, T\right) \\
\frac{\mathrm{d}\sigma}{\mathrm{d}t} &= g\left(\xi_S, \xi_M, \epsilon, T\right)
\end{aligned} \tag{C.1}$$

Using the chain-rule of derivation, equations (C.1) become

$$\frac{\mathrm{d}\xi_S}{\mathrm{d}t} = \dot{\xi}_S = \frac{\partial \xi_S}{\partial \xi_M}\dot{\xi}_M + \frac{\partial \xi_S}{\partial \sigma}\dot{\sigma} + \frac{\partial \xi_S}{\partial T}\dot{T} \tag{C.2}$$

$$\frac{\mathrm{d}\xi_M}{\mathrm{d}t} = \dot{\xi}_M = \frac{\partial \xi_M}{\partial \xi_S}\dot{\xi}_S + \frac{\partial \xi_M}{\partial \sigma}\dot{\sigma} + \frac{\partial \xi_M}{\partial T}\dot{T} \tag{C.3}$$

$$\frac{\mathrm{d}\sigma}{\mathrm{d}t} = \dot{\sigma} = \frac{\partial \sigma}{\partial \xi_S}\dot{\xi}_S + \frac{\partial \sigma}{\partial \xi_M}\dot{\xi}_M + \frac{\partial \sigma}{\partial T}\dot{T} \tag{C.4}$$

Often a model with incremental strains and incremental temperatures can be used in which case the following equation will be very useful

$$\mathrm{d}\sigma = \mathsf{L}\mathrm{d}\epsilon + \Theta \mathrm{d}T \tag{C.5}$$

where L is the *tangent stiffness tensor* and Θ is the *tangent thermal tensor*.

The numerical implementation of the Brinson model for the direct phase transformation to single-variant Martensite for the case $(T > M_s)$ will be given in the following subsections. The implementation for the direct phase transformation to single-variant Martensite for the case $(T < M_s)$ and for the reverse phase transformation of single-variant Martensite into Austenite follow along the same lines.

C.1 Direct phase transformation to single-variant Martensite $(T > M_s)$

C.1.1 Calculation of the values of ξ_S and ξ_M at step $(n + 1)$

Using equation (4.22), equation (C.2) becomes

$$\begin{aligned}
\frac{\partial \xi_S}{\partial \xi_M} &= 0 \\
\frac{\partial \xi_S}{\partial \sigma} &= -\frac{1-\xi_{S0}}{2}\sin\left\{\frac{\pi}{\sigma_s^{CR}-\sigma_f^{CR}}\left[\sigma - \sigma_f^{CR} - C_M\left(T - M_s\right)\right]\right\}\frac{\pi}{\sigma_s^{CR}-\sigma_f^{CR}} = A_1 \\
\frac{\partial \xi_S}{\partial T} &= -\frac{1-\xi_{S0}}{2}\sin\left\{\frac{\pi}{\sigma_s^{CR}-\sigma_f^{CR}}\left[\sigma - \sigma_f^{CR} - C_M\left(T - M_s\right)\right]\right\}C_M = -A_1 C_M \\
\dot{\xi}_S &= A_1\left(\dot{\sigma} - C_M\dot{T}\right)
\end{aligned} \tag{C.6}$$

Using equation (4.23), equation (C.3) becomes

$$\begin{aligned}
\frac{\partial \xi_M}{\partial \xi_S} &= -\frac{\xi_{M0}}{1-\xi_{S0}} = R \\
\frac{\partial \xi_M}{\partial \sigma} &= 0 \\
\frac{\partial \xi_M}{\partial T} &= 0 \\
\dot{\xi}_M &= R\dot{\xi}_S
\end{aligned} \tag{C.7}$$

Using equation (4.17), (4.18) and (4.19), equation (C.4) becomes

$$\begin{aligned}
\sigma &= E\left(\xi\right)\epsilon + \Omega\left(\xi\right)\xi_S + \Theta\left(T - T_0\right) \\
\sigma &= E\left(\xi\right)\left(\epsilon + \epsilon_L \xi_S\right) + \Theta\left(T - T_0\right)
\end{aligned}$$

where

$$E\left(\xi\right) = E_A + \xi\left(E_M - E_A\right) = E_A + \left(\xi_S + \xi_M\right)\left(E_M - E_A\right)$$

$$\begin{aligned}
\frac{\partial \sigma}{\partial \epsilon} &= E\left(\xi\right) \\
\frac{\partial \sigma}{\partial \xi_S} &= \left(E_M - E_A\right)\epsilon - \left(E_M - E_A\right)\epsilon_L \xi_S - E\left(\xi\right)\epsilon_L = E^{\star}\left(\epsilon - \epsilon_L \xi_S\right) - E\left(\xi\right)\epsilon_L = H_1 \\
\frac{\partial \sigma}{\partial \xi_M} &= \left(E_M - E_A\right)\epsilon - \left(E_M - E_A\right)\epsilon_L \xi_S = E^{\star}\left(\epsilon - \epsilon_L \xi_S\right) = H_2 \\
\frac{\partial \sigma}{\partial T} &= \Theta \\
\dot{\sigma} &= E\dot{\epsilon} + H_1\dot{\xi}_S + H_2\dot{\xi}_M + \Theta\dot{T}
\end{aligned} \tag{C.8}$$

where

$$E^{\star} = E_M - E_A \tag{C.9}$$

Now, after substitution of equations (4.19) and (C.8) in equation (C.6), equations (C.6) and (C.7) can be rewritten as follows

$$\begin{cases}
\dot{\xi}_S = A_1\left(\epsilon, \xi_S, \xi_M, T\right)\left[E\left(\xi_S, \xi_M\right)\dot{\epsilon} + H_1\left(\epsilon, \xi_S, \xi_M\right)\dot{\xi}_S + H_2\left(\epsilon, \xi_S\right)\dot{\xi}_M + \Theta\dot{T} - C_M\dot{T}\right] \\
\dot{\xi}_M = R\dot{\xi}_S
\end{cases}$$

$$\begin{cases}
\left(1 - A_1 H_1\right)\dot{\xi}_S - A_1 H_2 \dot{\xi}_M = A_1\left(E\dot{\epsilon} + \left(\Theta - C_M\right)\dot{T}\right) \\
\dot{\xi}_M = R\dot{\xi}_S
\end{cases}$$

$$\begin{cases}
\dot{\xi}_S = \frac{Z_2\left(\dot{\epsilon}, \epsilon, \xi_S, \xi_M, T, \dot{T}\right)}{Z_1\left(\epsilon, \xi_S, \xi_M, T\right)} \\
\dot{\xi}_M = \frac{Z_3\left(\dot{\epsilon}, \epsilon, \xi_S, \xi_M, T, \dot{T}\right)}{Z_1\left(\epsilon, \xi_S, \xi_M, T\right)}
\end{cases} \tag{C.10}$$

where

$$\begin{aligned} Z_1\left(\epsilon,\xi_S,\xi_M,T\right) &= 1 - A_1\left(\epsilon,\xi_S,\xi_M,T\right)\left[H_1\left(\epsilon,\xi_S,\xi_M\right) + H_2\left(\epsilon,\xi_S\right)R\right] \\ Z_2\left(\dot{\epsilon},\epsilon,\xi_S,\xi_M,T,\dot{T}\right) &= A_1\left(\epsilon,\xi_S,\xi_M,T\right)\left[E\left(\xi_S,\xi_M\right)\dot{\epsilon} + \left(\Theta - C_M\right)\dot{T}\right] \\ Z_3\left(\dot{\epsilon},\epsilon,\xi_S,\xi_M,T,\dot{T}\right) &= RZ_2\left(\dot{\epsilon},\epsilon,\xi_S,\xi_M,T,\dot{T}\right) \end{aligned}$$

Now equations (C.10) are discretized in time using the Backward Euler method or implicit method by assuming strain and temperature as control variable

$$\begin{cases} \xi_{S,n+1} - \xi_{S,n} - \Delta t\frac{Z_2\left(\dot{\epsilon}_{n+1},\epsilon_{n+1},\xi_{S,n+1},\xi_{M,n+1},T_{n+1},\dot{T}_{n+1}\right)}{Z_1\left(\epsilon_{n+1},\xi_{S,n+1},\xi_{M,n+1},T_{n+1}\right)} = 0 \\ \xi_{M,n+1} - \xi_{M,n} - \Delta t\frac{Z_3\left(\dot{\epsilon}_{n+1},\epsilon_{n+1},\xi_{S,n+1},\xi_{M,n+1},T,\dot{T}_{n+1}\right)}{Z_1\left(\epsilon_{n+1},\xi_{S,n+1},\xi_{M,n+1},T_{n+1}\right)} = 0 \end{cases}$$

where

$$\dot{\epsilon}_{n+1} = \frac{\epsilon_{n+1}-\epsilon_n}{\Delta t}; \quad \dot{T}_{n+1} = \frac{T_{n+1}-T_n}{\Delta t}$$

The system of equations (C.1.1) is solved using the *Multivariate Newton-Raphson Method*.

Now defining the solution vector as [104]

$$\bar{F}\left(\bar{\xi}_{n+1}\right) = \begin{Bmatrix} F_1\left(\xi_{S,n+1},\xi_{M,n+1}\right) \\ F_2\left(\xi_{S,n+1},\xi_{M,n+1}\right) \end{Bmatrix} = \begin{Bmatrix} \xi_{S,n+1} - \xi_{S,n} - \Delta t\frac{Z_2\left(\dot{\epsilon}_{n+1},\epsilon_{n+1},\xi_{S,n+1},\xi_{M,n+1},T_{n+1},\dot{T}_{n+1}\right)}{Z_1\left(\epsilon_{n+1},\xi_{S,n+1},\xi_{M,n+1},T_{n+1}\right)} \\ \xi_{M,n+1} - \xi_{M,n} - \Delta t\frac{Z_3\left(\dot{\epsilon}_{n+1},\epsilon_{n+1},\xi_{S,n+1},\xi_{M,n+1},T,\dot{T}_{n+1}\right)}{Z_1\left(\epsilon_{n+1},\xi_{S,n+1},\xi_{M,n+1},T_{n+1}\right)} \end{Bmatrix}$$

and the Jacobian matrix as

$$\left[D\bar{F}\left(\bar{\xi}_{n+1}\right)\right] = \begin{bmatrix} \frac{\partial F_1\left(\bar{\xi}_{n+1}\right)}{\partial \xi_{S,n+1}} & \frac{\partial F_1\left(\bar{\xi}_{n+1}\right)}{\partial \xi_{M,n+1}} \\ \frac{\partial F_2\left(\bar{\xi}_{n+1}\right)}{\partial \xi_{S,n+1}} & \frac{\partial F_2\left(\bar{\xi}_{n+1}\right)}{\partial \xi_{M,n+1}} \end{bmatrix}$$

where

$$\begin{aligned} \frac{\partial F_1\left(\bar{\xi}_{n+1}\right)}{\partial \xi_{S,n+1}} &= 1 - \Delta t\frac{\frac{\partial Z_1\left(\bar{\xi}_{n+1}\right)}{\partial \xi_{S,n+1}}Z_2\left(\bar{\xi}_{n+1}\right) - Z_1\left(\bar{\xi}_{n+1}\right)\frac{\partial Z_2\left(\bar{\xi}_{n+1}\right)}{\partial \xi_{S,n+1}}}{Z_1^2\left(\bar{\xi}_{n+1}\right)} \\ \frac{\partial F_1\left(\bar{\xi}_{n+1}\right)}{\partial \xi_{M,n+1}} &= -\Delta t\frac{\frac{\partial Z_1\left(\bar{\xi}_{n+1}\right)}{\partial \xi_{M,n+1}}Z_2\left(\bar{\xi}_{n+1}\right) - Z_1\left(\bar{\xi}_{n+1}\right)\frac{\partial Z_2\left(\bar{\xi}_{n+1}\right)}{\partial \xi_{M,n+1}}}{Z_1^2\left(\bar{\xi}_{n+1}\right)} \\ \frac{\partial F_2\left(\bar{\xi}_{n+1}\right)}{\partial \xi_{S,n+1}} &= -\Delta t\frac{\frac{\partial Z_1\left(\bar{\xi}_{n+1}\right)}{\partial \xi_{S,n+1}}Z_3\left(\bar{\xi}_{n+1}\right) - Z_1\left(\bar{\xi}_{n+1}\right)\frac{\partial Z_3\left(\bar{\xi}_{n+1}\right)}{\partial \xi_{S,n+1}}}{Z_1^2\left(\bar{\xi}_{n+1}\right)} \\ \frac{\partial F_2\left(\bar{\xi}_{n+1}\right)}{\partial \xi_{M,n+1}} &= 1 - \Delta t\frac{\frac{\partial Z_1\left(\bar{\xi}_{n+1}\right)}{\partial \xi_{M,n+1}}Z_3\left(\bar{\xi}_{n+1}\right) - Z_1\left(\bar{\xi}_{n+1}\right)\frac{\partial Z_3\left(\bar{\xi}_{n+1}\right)}{\partial \xi_{M,n+1}}}{Z_1^2\left(\bar{\xi}_{n+1}\right)} \end{aligned}$$

If $\bar{\xi}_{n+1,0}$ is our initial guess, then for the Multivariate Newton-Raphson Method

$$\bar{F}\left(\bar{\xi}_{n+1,0}\right) + \left[D\bar{F}\left(\bar{\xi}_{n+1,0}\right)\right]\left(\bar{x} - \bar{\xi}_{n+1,0}\right) = 0$$

$$\begin{aligned}\left[D\bar{F}\left(\bar{\xi}_{n+1,0}\right)\right]\left(\bar{x} - \bar{\xi}_{n+1,0}\right) &= -\bar{F}\left(\bar{\xi}_{n+1,0}\right)\\ \bar{x} &= \bar{\xi}_{n+1,0} - \left[D\bar{F}\left(\bar{\xi}_{n+1,0}\right)\right]^{-1}\bar{F}\left(\bar{\xi}_{n+1,0}\right)\end{aligned}$$

If $\bar{x} = \bar{\xi}_{n+1,1}$ is our new guess, then we iterate again

$$\left[D\bar{F}\left(\bar{\xi}_{n+1,1}\right)\right]\left(\bar{x} - \bar{\xi}_{n+1,1}\right) = -\bar{F}\left(\bar{\xi}_{n+1,1}\right)$$

until the solution is within the tolerance required.

C.1.2 Calculation of the value of σ at step $(n+1)$

From equation (C.8) we have

$$\sigma_{n+1} = \sigma_n + E\left(\epsilon_{n+1} - \epsilon_n\right) + H_1\left(\xi_{S,n+1} - \xi_{S,n}\right) + H_2\left(\xi_{M,n+1} - \xi_{M,n}\right) + \Theta\left(T_{n+1} - T_n\right)$$

C.1.3 Calculation of the values of the tangent moduli at step $(n+1)$

After substitution of equations (C.6) and (C.7), equation (C.8) can be written as

$$\mathrm{d}\sigma = \frac{E}{L_1}\mathrm{d}\epsilon + \frac{\Theta - A_1 C_M H}{L_1}\mathrm{d}T$$

where

$$\begin{aligned}L_1 &= 1 - A_1 H\\ H &= H_1 + H_2 R = E^{\star}\left(\epsilon - \epsilon_L \xi_S\right)(1 + R) - \epsilon_L E\\ E^{\star} &= E_M - E_A\end{aligned}$$

Appendix D

Element stiffness matrices for the multiple models theory

In this appendix the same notation used in chapter 5 will be adopted except for the fact that symmetries in the laminate stiffnesses will not be exploited.

D.1 Laminate stiffness matrices

The laminate stiffness matrices are defined as follows

$$\boldsymbol{A}_{IJ}^{\alpha\beta} = \begin{bmatrix} \underset{11}{A_{IJ}^{\alpha\beta}} & \underset{12}{A_{IJ}^{\alpha\beta}} & \underset{13}{A_{IJ}^{\alpha\beta}} & 0 & 0 & \underset{16}{A_{IJ}^{\alpha\beta}} \\ \underset{21}{A_{IJ}^{\alpha\beta}} & \underset{22}{A_{IJ}^{\alpha\beta}} & \underset{23}{A_{IJ}^{\alpha\beta}} & 0 & 0 & \underset{26}{A_{IJ}^{\alpha\beta}} \\ \underset{31}{A_{IJ}^{\alpha\beta}} & \underset{32}{A_{IJ}^{\alpha\beta}} & \underset{33}{A_{IJ}^{\alpha\beta}} & 0 & 0 & \underset{36}{A_{IJ}^{\alpha\beta}} \\ 0 & 0 & 0 & \underset{44}{A_{IJ}^{\alpha\beta}} & \underset{45}{A_{IJ}^{\alpha\beta}} & 0 \\ 0 & 0 & 0 & \underset{54}{A_{IJ}^{\alpha\beta}} & \underset{55}{A_{IJ}^{\alpha\beta}} & 0 \\ \underset{61}{A_{IJ}^{\alpha\beta}} & \underset{62}{A_{IJ}^{\alpha\beta}} & \underset{63}{A_{IJ}^{\alpha\beta}} & 0 & 0 & \underset{66}{A_{IJ}^{\alpha\beta}} \end{bmatrix}$$

$$\bar{\boldsymbol{A}}_{IJ}^{\alpha\beta} = \begin{bmatrix} \underset{11}{\bar{A}_{IJ}^{\alpha\beta}} & \underset{12}{\bar{A}_{IJ}^{\alpha\beta}} & \underset{13}{\bar{A}_{IJ}^{\alpha\beta}} & 0 & 0 & \underset{16}{\bar{A}_{IJ}^{\alpha\beta}} \\ \underset{21}{\bar{A}_{IJ}^{\alpha\beta}} & \underset{22}{\bar{A}_{IJ}^{\alpha\beta}} & \underset{23}{\bar{A}_{IJ}^{\alpha\beta}} & 0 & 0 & \underset{26}{\bar{A}_{IJ}^{\alpha\beta}} \\ \underset{31}{\bar{A}_{IJ}^{\alpha\beta}} & \underset{32}{\bar{A}_{IJ}^{\alpha\beta}} & \underset{33}{\bar{A}_{IJ}^{\alpha\beta}} & 0 & 0 & \underset{36}{\bar{A}_{IJ}^{\alpha\beta}} \\ 0 & 0 & 0 & \underset{44}{\bar{A}_{IJ}^{\alpha\beta}} & \underset{45}{\bar{A}_{IJ}^{\alpha\beta}} & 0 \\ 0 & 0 & 0 & \underset{54}{\bar{A}_{IJ}^{\alpha\beta}} & \underset{55}{\bar{A}_{IJ}^{\alpha\beta}} & 0 \\ \underset{61}{\bar{A}_{IJ}^{\alpha\beta}} & \underset{62}{\bar{A}_{IJ}^{\alpha\beta}} & \underset{63}{\bar{A}_{IJ}^{\alpha\beta}} & 0 & 0 & \underset{66}{\bar{A}_{IJ}^{\alpha\beta}} \end{bmatrix}$$

$$\bar{\bar{\boldsymbol{A}}}^{\alpha\beta}_{IJ} = \begin{bmatrix} \underset{11}{\bar{\bar{A}}^{\alpha\beta}_{IJ}} & \underset{12}{\bar{\bar{A}}^{\alpha\beta}_{IJ}} & \underset{13}{\bar{\bar{A}}^{\alpha\beta}_{IJ}} & 0 & 0 & \underset{16}{\bar{\bar{A}}^{\alpha\beta}_{IJ}} \\ \underset{21}{\bar{\bar{A}}^{\alpha\beta}_{IJ}} & \underset{22}{\bar{\bar{A}}^{\alpha\beta}_{IJ}} & \underset{23}{\bar{\bar{A}}^{\alpha\beta}_{IJ}} & 0 & 0 & \underset{26}{\bar{\bar{A}}^{\alpha\beta}_{IJ}} \\ \underset{31}{\bar{\bar{A}}^{\alpha\beta}_{IJ}} & \underset{32}{\bar{\bar{A}}^{\alpha\beta}_{IJ}} & \underset{33}{\bar{\bar{A}}^{\alpha\beta}_{IJ}} & 0 & 0 & \underset{36}{\bar{\bar{A}}^{\alpha\beta}_{IJ}} \\ 0 & 0 & 0 & \underset{44}{\bar{\bar{A}}^{\alpha\beta}_{IJ}} & \underset{45}{\bar{\bar{A}}^{\alpha\beta}_{IJ}} & 0 \\ 0 & 0 & 0 & \underset{54}{\bar{\bar{A}}^{\alpha\beta}_{IJ}} & \underset{55}{\bar{\bar{A}}^{\alpha\beta}_{IJ}} & 0 \\ \underset{61}{\bar{\bar{A}}^{\alpha\beta}_{IJ}} & \underset{62}{\bar{\bar{A}}^{\alpha\beta}_{IJ}} & \underset{63}{\bar{\bar{A}}^{\alpha\beta}_{IJ}} & 0 & 0 & \underset{66}{\bar{\bar{A}}^{\alpha\beta}_{IJ}} \end{bmatrix}$$

$$\bar{\bar{\bar{\boldsymbol{A}}}}^{\alpha\beta}_{IJ} = \begin{bmatrix} \underset{11}{\bar{\bar{\bar{A}}}^{\alpha\beta}_{IJ}} & \underset{12}{\bar{\bar{\bar{A}}}^{\alpha\beta}_{IJ}} & \underset{13}{\bar{\bar{\bar{A}}}^{\alpha\beta}_{IJ}} & 0 & 0 & \underset{16}{\bar{\bar{\bar{A}}}^{\alpha\beta}_{IJ}} \\ \underset{21}{\bar{\bar{\bar{A}}}^{\alpha\beta}_{IJ}} & \underset{22}{\bar{\bar{\bar{A}}}^{\alpha\beta}_{IJ}} & \underset{23}{\bar{\bar{\bar{A}}}^{\alpha\beta}_{IJ}} & 0 & 0 & \underset{26}{\bar{\bar{\bar{A}}}^{\alpha\beta}_{IJ}} \\ \underset{31}{\bar{\bar{\bar{A}}}^{\alpha\beta}_{IJ}} & \underset{32}{\bar{\bar{\bar{A}}}^{\alpha\beta}_{IJ}} & \underset{33}{\bar{\bar{\bar{A}}}^{\alpha\beta}_{IJ}} & 0 & 0 & \underset{36}{\bar{\bar{\bar{A}}}^{\alpha\beta}_{IJ}} \\ 0 & 0 & 0 & \underset{44}{\bar{\bar{\bar{A}}}^{\alpha\beta}_{IJ}} & \underset{45}{\bar{\bar{\bar{A}}}^{\alpha\beta}_{IJ}} & 0 \\ 0 & 0 & 0 & \underset{54}{\bar{\bar{\bar{A}}}^{\alpha\beta}_{IJ}} & \underset{55}{\bar{\bar{\bar{A}}}^{\alpha\beta}_{IJ}} & 0 \\ \underset{61}{\bar{\bar{\bar{A}}}^{\alpha\beta}_{IJ}} & \underset{62}{\bar{\bar{\bar{A}}}^{\alpha\beta}_{IJ}} & \underset{63}{\bar{\bar{\bar{A}}}^{\alpha\beta}_{IJ}} & 0 & 0 & \underset{66}{\bar{\bar{\bar{A}}}^{\alpha\beta}_{IJ}} \end{bmatrix}$$

$$\boldsymbol{B}^{\alpha\beta\gamma}_{IJK} = \begin{bmatrix} \underset{11}{B^{\alpha\beta\gamma}_{IJK}} & \underset{12}{B^{\alpha\beta\gamma}_{IJK}} & \underset{13}{B^{\alpha\beta\gamma}_{IJK}} & 0 & 0 & \underset{16}{B^{\alpha\beta\gamma}_{IJK}} \\ \underset{21}{B^{\alpha\beta\gamma}_{IJK}} & \underset{22}{B^{\alpha\beta\gamma}_{IJK}} & \underset{23}{B^{\alpha\beta\gamma}_{IJK}} & 0 & 0 & \underset{26}{B^{\alpha\beta\gamma}_{IJK}} \\ \underset{31}{B^{\alpha\beta\gamma}_{IJK}} & \underset{32}{B^{\alpha\beta\gamma}_{IJK}} & \underset{33}{B^{\alpha\beta\gamma}_{IJK}} & 0 & 0 & \underset{36}{B^{\alpha\beta\gamma}_{IJK}} \\ 0 & 0 & 0 & \underset{44}{B^{\alpha\beta\gamma}_{IJK}} & \underset{45}{B^{\alpha\beta\gamma}_{IJK}} & 0 \\ 0 & 0 & 0 & \underset{54}{B^{\alpha\beta\gamma}_{IJK}} & \underset{55}{B^{\alpha\beta\gamma}_{IJK}} & 0 \\ \underset{61}{B^{\alpha\beta\gamma}_{IJK}} & \underset{62}{B^{\alpha\beta\gamma}_{IJK}} & \underset{63}{B^{\alpha\beta\gamma}_{IJK}} & 0 & 0 & \underset{66}{B^{\alpha\beta\gamma}_{IJK}} \end{bmatrix}$$

$$\bar{\boldsymbol{B}}^{\alpha\beta\gamma}_{IJK} = \begin{bmatrix} \underset{11}{\bar{B}^{\alpha\beta\gamma}_{IJK}} & \underset{12}{\bar{B}^{\alpha\beta\gamma}_{IJK}} & \underset{13}{\bar{B}^{\alpha\beta\gamma}_{IJK}} & 0 & 0 & \underset{16}{\bar{B}^{\alpha\beta\gamma}_{IJK}} \\ \underset{21}{\bar{B}^{\alpha\beta\gamma}_{IJK}} & \underset{22}{\bar{B}^{\alpha\beta\gamma}_{IJK}} & \underset{23}{\bar{B}^{\alpha\beta\gamma}_{IJK}} & 0 & 0 & \underset{26}{\bar{B}^{\alpha\beta\gamma}_{IJK}} \\ \underset{31}{\bar{B}^{\alpha\beta\gamma}_{IJK}} & \underset{32}{\bar{B}^{\alpha\beta\gamma}_{IJK}} & \underset{33}{\bar{B}^{\alpha\beta\gamma}_{IJK}} & 0 & 0 & \underset{36}{\bar{B}^{\alpha\beta\gamma}_{IJK}} \\ 0 & 0 & 0 & \underset{44}{\bar{B}^{\alpha\beta\gamma}_{IJK}} & \underset{45}{\bar{B}^{\alpha\beta\gamma}_{IJK}} & 0 \\ 0 & 0 & 0 & \underset{54}{\bar{B}^{\alpha\beta\gamma}_{IJK}} & \underset{55}{\bar{B}^{\alpha\beta\gamma}_{IJK}} & 0 \\ \underset{61}{\bar{B}^{\alpha\beta\gamma}_{IJK}} & \underset{62}{\bar{B}^{\alpha\beta\gamma}_{IJK}} & \underset{63}{\bar{B}^{\alpha\beta\gamma}_{IJK}} & 0 & 0 & \underset{66}{\bar{B}^{\alpha\beta\gamma}_{IJK}} \end{bmatrix}$$

$$\bar{\bar{\bar{\boldsymbol{B}}}}^{\alpha\beta\gamma}_{IJK} = \begin{bmatrix} \underset{11}{\bar{\bar{\bar{B}}}^{\alpha\beta\gamma}_{IJK}} & \underset{12}{\bar{\bar{\bar{B}}}^{\alpha\beta\gamma}_{IJK}} & \underset{13}{\bar{\bar{\bar{B}}}^{\alpha\beta\gamma}_{IJK}} & 0 & 0 & \underset{16}{\bar{\bar{\bar{B}}}^{\alpha\beta\gamma}_{IJK}} \\ \underset{21}{\bar{\bar{\bar{B}}}^{\alpha\beta\gamma}_{IJK}} & \underset{22}{\bar{\bar{\bar{B}}}^{\alpha\beta\gamma}_{IJK}} & \underset{23}{\bar{\bar{\bar{B}}}^{\alpha\beta\gamma}_{IJK}} & 0 & 0 & \underset{26}{\bar{\bar{\bar{B}}}^{\alpha\beta\gamma}_{IJK}} \\ \underset{31}{\bar{\bar{\bar{B}}}^{\alpha\beta\gamma}_{IJK}} & \underset{32}{\bar{\bar{\bar{B}}}^{\alpha\beta\gamma}_{IJK}} & \underset{33}{\bar{\bar{\bar{B}}}^{\alpha\beta\gamma}_{IJK}} & 0 & 0 & \underset{36}{\bar{\bar{\bar{B}}}^{\alpha\beta\gamma}_{IJK}} \\ 0 & 0 & 0 & \underset{44}{\bar{\bar{\bar{B}}}^{\alpha\beta\gamma}_{IJK}} & \underset{45}{\bar{\bar{\bar{B}}}^{\alpha\beta\gamma}_{IJK}} & 0 \\ 0 & 0 & 0 & \underset{54}{\bar{\bar{\bar{B}}}^{\alpha\beta\gamma}_{IJK}} & \underset{55}{\bar{\bar{\bar{B}}}^{\alpha\beta\gamma}_{IJK}} & 0 \\ \underset{61}{\bar{\bar{\bar{B}}}^{\alpha\beta\gamma}_{IJK}} & \underset{62}{\bar{\bar{\bar{B}}}^{\alpha\beta\gamma}_{IJK}} & \underset{63}{\bar{\bar{\bar{B}}}^{\alpha\beta\gamma}_{IJK}} & 0 & 0 & \underset{66}{\bar{\bar{\bar{B}}}^{\alpha\beta\gamma}_{IJK}} \end{bmatrix}$$

$$\boldsymbol{D}^{\alpha\beta\gamma\delta}_{IJKL} = \begin{bmatrix} \underset{11}{D^{\alpha\beta\gamma\delta}_{IJKL}} & \underset{12}{D^{\alpha\beta\gamma\delta}_{IJKL}} & \underset{13}{D^{\alpha\beta\gamma\delta}_{IJKL}} & 0 & 0 & \underset{16}{D^{\alpha\beta\gamma\delta}_{IJKL}} \\ \underset{21}{D^{\alpha\beta\gamma\delta}_{IJKL}} & \underset{22}{D^{\alpha\beta\gamma\delta}_{IJKL}} & \underset{23}{D^{\alpha\beta\gamma\delta}_{IJKL}} & 0 & 0 & \underset{26}{D^{\alpha\beta\gamma\delta}_{IJKL}} \\ \underset{31}{D^{\alpha\beta\gamma\delta}_{IJKL}} & \underset{32}{D^{\alpha\beta\gamma\delta}_{IJKL}} & \underset{33}{D^{\alpha\beta\gamma\delta}_{IJKL}} & 0 & 0 & \underset{36}{D^{\alpha\beta\gamma\delta}_{IJKL}} \\ 0 & 0 & 0 & \underset{44}{D^{\alpha\beta\gamma\delta}_{IJKL}} & \underset{45}{D^{\alpha\beta\gamma\delta}_{IJKL}} & 0 \\ 0 & 0 & 0 & \underset{54}{D^{\alpha\beta\gamma\delta}_{IJ}} & \underset{55}{D^{\alpha\beta\gamma\delta}_{IJ}} & 0 \\ \underset{61}{D^{\alpha\beta\gamma\delta}_{IJKL}} & \underset{62}{D^{\alpha\beta\gamma\delta}_{IJKL}} & \underset{63}{D^{\alpha\beta\gamma\delta}_{IJKL}} & 0 & 0 & \underset{66}{D^{\alpha\beta\gamma\delta}_{IJKL}} \end{bmatrix}$$

where

$$\begin{aligned}
\underset{ij}{A^{\alpha\beta}_{IJ}} &= \sum_{k=1}^{N_m} \int_{z_b^{(k)}}^{z_t^{(k)}} \bar{C}_{ij}^{(k)} F_I^{\alpha} F_J^{\beta} \mathrm{d}z \\
\underset{ij}{\bar{A}^{\alpha\beta}_{IJ}} &= \sum_{k=1}^{N_m} \int_{z_b^{(k)}}^{z_t^{(k)}} \bar{C}_{ij}^{(k)} F_I^{\alpha} \frac{\mathrm{d}F_J^{\beta}}{\mathrm{d}z} \mathrm{d}z \\
\underset{ij}{\bar{\bar{A}}^{\alpha\beta}_{IJ}} &= \sum_{k=1}^{N_m} \int_{z_b^{(k)}}^{z_t^{(k)}} \bar{C}_{ij}^{(k)} \frac{\mathrm{d}F_I^{\alpha}}{\mathrm{d}z} F_J^{\beta} \mathrm{d}z \\
\underset{ij}{\bar{\bar{\bar{A}}}^{\alpha\beta}_{IJ}} &= \sum_{k=1}^{N_m} \int_{z_b^{(k)}}^{z_t^{(k)}} \bar{C}_{ij}^{(k)} \frac{\mathrm{d}F_I^{\alpha}}{\mathrm{d}z} \frac{\mathrm{d}F_J^{\beta}}{\mathrm{d}z} \mathrm{d}z \\
\underset{ij}{B^{\alpha\beta\gamma}_{IJK}} &= \sum_{k=1}^{N_m} \int_{z_b^{(k)}}^{z_t^{(k)}} \bar{C}_{ij}^{(k)} F_I^{\alpha} F_J^{\beta} F_K^{\gamma} \mathrm{d}z \\
\underset{ij}{\bar{B}^{\alpha\beta\gamma}_{IJK}} &= \sum_{k=1}^{N_m} \int_{z_b^{(k)}}^{z_t^{(k)}} \bar{C}_{ij}^{(k)} F_I^{\alpha} F_J^{\beta} \frac{\mathrm{d}F_K^{\gamma}}{\mathrm{d}z} \mathrm{d}z \\
\underset{ij}{\bar{\bar{B}}^{\alpha\beta\gamma}_{IJK}} &= \sum_{k=1}^{N_m} \int_{z_b^{(k)}}^{z_t^{(k)}} \bar{C}_{ij}^{(k)} \frac{\mathrm{d}F_I^{\alpha}}{\mathrm{d}z} F_J^{\beta} F_K^{\gamma} \mathrm{d}z \\
\underset{ij}{D^{\alpha\beta\gamma\delta}_{IJKL}} &= \sum_{k=1}^{N_m} \int_{z_b^{(k)}}^{z_t^{(k)}} \bar{C}_{ij}^{(k)} F_I^{\alpha} F_J^{\beta} F_K^{\gamma} F_L^{\delta} \mathrm{d}z
\end{aligned}$$

D.2 Element secant stiffness matrix

The expression for the element secant stiffness matrix is

$$\boldsymbol{K}^{\alpha\beta}_{IJ} = \underset{L}{\boldsymbol{K}^{\alpha\beta}_{IJ}} + \underset{NL}{\boldsymbol{K}^{\alpha\beta}_{IJ}} \tag{D.1}$$

where, defining the *transpose operator* as T, the element linear stiffness matrix $\boldsymbol{K}_L$ for models $\alpha\beta$ and interfaces IJ is

$$\underset{L}{\boldsymbol{K}^{\alpha\beta}_{IJ}} = (\boldsymbol{L}_b)^T \boldsymbol{A}^{\alpha\beta}_{IJ} \boldsymbol{L}_b + (\boldsymbol{L}_b)^T \bar{\boldsymbol{A}}^{\alpha\beta}_{IJ} \boldsymbol{L}_m + (\boldsymbol{L}_m)^T \bar{\bar{\boldsymbol{A}}}^{\alpha\beta}_{IJ} \boldsymbol{L}_b + (\boldsymbol{L}_m)^T \bar{\bar{\bar{\boldsymbol{A}}}}^{\alpha\beta}_{IJ} \boldsymbol{L}_m,$$

the element nonlinear stiffness matrix $\boldsymbol{K}_{NL}$ for models $\alpha\beta$ and interfaces IJ is

$$\begin{aligned}
\boldsymbol{K}^{\alpha\beta}_{\underset{NL}{IJ}} =& \sum_{\gamma=1}^{M}\sum_{K=1}^{N} \left(\boldsymbol{L}_b\right)^T \boldsymbol{B}^{\alpha\beta\gamma}_{IJK} \boldsymbol{L}^{\gamma}_{\underset{\theta}{K}} + \sum_{\gamma=1}^{M}\sum_{K=1}^{N} \left(\boldsymbol{L}_m\right)^T \bar{\bar{\bar{\boldsymbol{B}}}}^{\alpha\beta\gamma}_{IJK} \boldsymbol{L}^{\gamma}_{\underset{\theta}{K}} \\
&+ \sum_{\gamma=1}^{M}\sum_{K=1}^{N} 2\left(\boldsymbol{L}^{\gamma}_{\underset{\theta}{K}}\right)^T \boldsymbol{B}^{\alpha\beta\gamma}_{IJK} \boldsymbol{L}_b + \sum_{\gamma=1}^{M}\sum_{K=1}^{N} 2\left(\boldsymbol{L}^{\gamma}_{\underset{\theta}{K}}\right)^T \bar{\boldsymbol{B}}^{\alpha\beta\gamma}_{IJK} \boldsymbol{L}_m \\
&+ \sum_{\gamma=1}^{M}\sum_{\delta=1}^{M}\sum_{K=1}^{N}\sum_{L=1}^{N} 2\left(\boldsymbol{L}^{\gamma}_{\underset{\theta}{K}}\right)^T \boldsymbol{D}^{\alpha\beta\gamma\delta}_{IJKL} \boldsymbol{L}^{\delta}_{\underset{\theta}{L}},
\end{aligned}$$

and

$$\boldsymbol{L}_{b(6\times 3m)} = \begin{bmatrix} \frac{\partial\psi_i}{\partial x} & 0 & 0 \\ 0 & \frac{\partial\psi_i}{\partial y} & 0 \\ 0 & 0 & 0 \\ 0 & 0 & \frac{\partial\psi_i}{\partial y} \\ 0 & 0 & \frac{\partial\psi_i}{\partial x} \\ \frac{\partial\psi_i}{\partial y} & \frac{\partial\psi_i}{\partial x} & 0 \end{bmatrix},$$

$$\boldsymbol{L}_{m(6\times 3m)} = \begin{bmatrix} 0 & 0 & 0 \\ 0 & 0 & 0 \\ 0 & 0 & \psi_i \\ 0 & \psi_i & 0 \\ \psi_i & 0 & 0 \\ 0 & 0 & 0 \end{bmatrix},$$

$$\boldsymbol{L}^{\beta}_{\underset{\theta\,(6\times 3m)}{J}} = \frac{1}{2}\begin{bmatrix} 0 & 0 & \frac{\partial w^{\beta}_J}{\partial x}\frac{\partial\psi_i}{\partial x} \\ 0 & 0 & \frac{\partial w^{\beta}_J}{\partial y}\frac{\partial\psi_i}{\partial y} \\ 0 & 0 & 0 \\ 0 & 0 & 0 \\ 0 & 0 & 0 \\ 0 & 0 & \frac{\partial w^{\beta}_J}{\partial x}\frac{\partial\psi_i}{\partial y} + \frac{\partial w^{\beta}_J}{\partial y}\frac{\partial\psi_i}{\partial x} \end{bmatrix},$$

and M, N, m and ψ_i are, respectively, the number of models, number of interfaces, number of nodes and the shape functions of the element.

D.3 Element tangent stiffness matrix

The expression for the element tangent stiffness matrix is

$$\boldsymbol{T}^{\alpha\beta}_{IJ} = \boldsymbol{K}^{\alpha\beta}_{IJ} + \frac{\partial \boldsymbol{K}^{\alpha\beta}_{IJ}}{\partial \boldsymbol{\Delta}^{\beta}_{J}} \boldsymbol{\Delta}^{\alpha}_{I} \tag{D.2}$$

where

$$
\frac{\partial \boldsymbol{K}_{IJ}^{\alpha\beta}}{\partial \boldsymbol{\Delta}_{J}^{\beta}}_{(3\times3)\times(1\times3)} = \left\{ \boldsymbol{0}_{(3\times3)} \right.
$$

$$
\begin{aligned}
&\boldsymbol{0}_{(3\times3)} \\
&\left[\sum_{\gamma=1}^{M} \sum_{K=1}^{N} \left(\boldsymbol{L}_b\right)^T \boldsymbol{B}_{IKJ}^{\alpha\gamma\beta} \frac{\partial \boldsymbol{L}_{\underset{\theta}{K}}^{\gamma}}{\partial w_K^{\gamma}} + \sum_{\gamma=1}^{M} \sum_{K=1}^{N} \left(\boldsymbol{L}_m\right)^T \bar{\bar{\bar{\boldsymbol{B}}}}_{IKJ}^{\alpha\gamma\beta} \frac{\partial \boldsymbol{L}_{\underset{\theta}{K}}^{\gamma}}{\partial w_K^{\gamma}} \right. \\
&+ \sum_{\gamma=1}^{M} \sum_{K=1}^{N} 2 \frac{\partial \left(\boldsymbol{L}_{\underset{\theta}{K}}^{\gamma}\right)^T}{\partial w_K^{\gamma}} \boldsymbol{B}_{IKJ}^{\alpha\gamma\beta} \boldsymbol{L}_b + \sum_{\gamma=1}^{M} \sum_{K=1}^{N} 2 \frac{\partial \left(\boldsymbol{L}_{\underset{\theta}{K}}^{\gamma}\right)^T}{\partial w_K^{\gamma}} \bar{\boldsymbol{B}}_{IKJ}^{\alpha\gamma\beta} \boldsymbol{L}_m \\
&\left. \left. + \sum_{\gamma=1}^{M} \sum_{\delta=1}^{M} \sum_{K=1}^{N} \sum_{L=1}^{N} 2 \frac{\partial \left(\boldsymbol{L}_{\underset{\theta}{K}}^{\gamma}\right)^T}{\partial w_K^{\gamma}} \boldsymbol{D}_{IKJL}^{\alpha\gamma\beta\delta} \boldsymbol{L}_{\underset{\theta}{L}}^{\delta} \right]_{(3\times3)} \right\}
\end{aligned}
$$

and

$$
\boldsymbol{\Delta}_{I\,(3\times1)}^{\alpha} = \left\{ u_I^{\alpha} \quad v_I^{\alpha} \quad w_I^{\alpha} \right\}^T
$$

Bibliography

[1] Ricardo L. Actis, Barna A. Szabo, and Christoph Schwab. Hierarchic models for laminated plates and shells. *Computer Methods in Applied Mechanics and Engineering*, 172(1-4):79 – 107, 1999.

[2] VR Aitharaju and RC Averill. Three-dimensional properties of woven-fabric composites. *Composites Science and Technology*, 59(12):1901–1911, 1999.

[3] R. Akkerman. Laminate mechanics for balanced woven fabrics. *Composites Part B: Engineering*, 37(2-3):108–116, 2006.

[4] M. Amano, Y. Okabe, and N. Takeda. Evaluation of Crack Suppression Effect of TiNi SMA Foil Embedded in CFRP Cross-Ply Laminates with Embedded Small-Diameter FBG Sensor. *JSME International Journal Series A*, 48(4):443–450, 2005.

[5] M. Amano, I. Taketa, M. Kobayashi, T. Ogisu, Y. Okabe, and N. Takeda. Evaluation of the damage suppression effect of Ti-Ni shape memory alloy foils embedded in carbon fiber reinforced plastic laminates. *Advanced Composite Materials*, 14(1):43–61, 2005.

[6] S.L. Angioni, A. Visrolia, and M. Meo. A hierarchical multiple plate models theory for laminated composites including delamination and geometrical nonlinear effects. *Composite Structures*, 93(2):780 – 791, 2011.

[7] S. Araki, H. Ono, and K. Saito. Fracture Mechanics-Micromechanical Analysis of Crack Closure Mechanism for Intelligent Material Containing TiNi Fibers (2nd Report, Numerical Calculation of Stress Intensity Factor in the Process. *JSME International Journal-Series A-Solid Mechanics and Material Engineering*, 45(3):356–362, 2002.

[8] S. Araki, H. Ono, and K. Saito. Papers-Fracture Mechanics-Micromechanical Analysis of Crack Closure Mechanism for Intelligent Material Containing TiNi Fibers (1st Report, Modeling of Crack Closure Mechanism and Analysis of. *JSME International Journal-Series A-Solid Mechanics and Material Engineering*, 45(2):208–216, 2002.

[9] F. Auricchio and J. Lubliner. A uniaxial model for shape-memory alloys. *International Journal of Solids and Structures*, 34(27):3601–3618, 1997.

[10] F. Auricchio and L. Petrini. Improvements and algorithmical considerations on a recent three-dimensional model describing stress-induced solid phase transformations. *International Journal for numerical methods in engineering*, 55(11):1255–1284, 2002.

[11] F. Auricchio and L. Petrini. A three-dimensional model describing stress-temperature induced solid phase transformations: solution algorithm and boundary value problems. *International Journal for Numerical Methods in Engineering*, 61(6):807–836, 2004.

[12] F. Auricchio and E. Sacco. A one-dimensional model for superelastic shape-memory alloys with different elastic properties between austenite and martensite. *International Journal of Non-Linear Mechanics*, 32(6):1101–1114, 1997.

[13] F. Auricchio, R.L. Taylor, and J. Lubliner. Shape-memory alloys: macromodelling and numerical simulations of the superelastic behavior. *Computer methods in applied mechanics and engineering*, 146(3-4):281–312, 1997.

[14] B.S. Balapgol, K.M. Bajoria, and S.A. Kulkarni. A two-dimensional finite element analysis of a shape memory alloy laminated composite plate. *Smart Materials and Structures*, 15:1009, 2006.

[15] E. J. Barbero. *On a Generalized Laminated Plate Theory with Application to Bending Vibration and Delamination Buckling*. PhD thesis, Virginia Polytechnic Institute and State University, Blacksburg, VA, Oct. 1989.

[16] E. J. Barbero and J. N. Reddy. Nonlinear analysis of composite laminates using a generalized laminated plate theory. *AIAA Journal*, 28:1987–1994, November 1990.

[17] E. J. Barbero and J. N. Reddy. Modeling of delamination in composite laminates using a layer-wise plate theory. *International Journal of Solids and Structures*, 28(3):373 – 388, 1991.

[18] E. Barbieri and M. Meo. A meshfree penalty-based approach to delamination in composites. *Composites Science and Technology*, 69(13):2169–2177, 2009.

[19] J. Bayandor, RS Thomson, ML Scott, MQ Nguyen, and DJ Elder. Investigation of impact and damage tolerance in advanced aerospace composite structures. *International Journal of Crashworthiness*, 8(3):297–306, 2003.

[20] T. Belytschko, R. Gracie, G. Ventura, S. Ogata, Y. Umeno, M. Kohyama, J. LLorca, T. Zohdi, H. Böhm, V. Tvergaard, et al. A review of extended/generalized finite element methods for material modeling. In *Proceedings of the 7th World Congress of Computational Mechanics on Computational Bridging of Length Scales in Complex Materials*, volume 20, page 21, 2006.

[21] T. Belytschko, K.W. Liu, and B. Moran. *Nonlinear Finite Element Analysis for Continua and Structures.* John Wiley & Sons, New York, 2000.

[22] A. Bensoussan, J.L. Lions, and G. Papanicolaou. *Asymptotic analysis for periodic structures.* North Holland, 1978.

[23] S.A. Berggren, D. Lukkassen, A. Meidell, and L. Simula. Some methods for calculating stiffness properties of periodic structures. *Applications of Mathematics*, 48(2):97–110, 2003.

[24] S. Bhandarkar, RK Agarwal, and A. Dasgupta. Micromechanical Simulation of Thermo-Mechanical and Thermal Properties of Woven-Fabric Composites. *Computer Aided Design in Composite Material Technology. III*, pages 547–558, 1992.

[25] K. Bhattacharya. *Microstructure of martensite: Why it forms and how it gives rise to the shape-memory effect.* Oxford University Press, USA, 2003.

[26] K. Bhattacharya and R.V. Kohn. Elastic Energy Minimization and the Recoverable Strains of Polycrystalline Shape-Memory Materials. *Archive for Rational Mechanics and Analysis*, 139(2):99–180, 1997.

[27] K. Bhattacharya and A. Sadjadpour. A micromechanics-inspired constitutive model for shape-memory alloys. *Smart Materials and Structures*, 16(5):1751–1765, 2007.

[28] D. Bollas, P. Pappas, J. Parthenios, and C. Galiotis. Stress generation by shape memory alloy wires embedded in polymer composites. *Acta Materialia*, 55(16):5489–5499, 2007.

[29] F. Boussu, G. Bailleul, JL Petitniot, and H. Vinchon. Development of shape memory alloy fabrics for composite structures, AUTEX Res J 2 (2002). *View Record in Scopus— Cited By in Scopus (5)*, pages 1–7, 2002.

[30] J.G. Boyd and D.C. Lagoudas. A thermodynamical constitutive model for shape memory materials. Part I. The monolithic shape memory alloy. *International Journal of Plasticity*, 12(6):805, 1996.

[31] J.G. Boyd and D.C. Lagoudas. A thermodynamical constitutive model for shape memory materials. Part II. The SMA composite material. *International Journal of Plasticity*, 12(7):843–874, 1996.

[32] V. Brailovski, S. Prokoshkin, P. Terriault, and F. Trochu. *Shape memory alloys: fundamentals, modeling and applications.* Universite du Qúebec, Ecole de Technologie Superieure, National Library of Canada, 2003.

[33] LC Brinson. One-dimensional constitutive behavior of shape memory alloys: thermomechanical derivation with non-constant material functions and redefined martensite internal variable. *Journal of Intelligent Material Systems and Structures*, 4(2):229, 1993.

[34] L.C. Brinson, D. Burton, and X. Gao. SMA hybrid composites: self-healing, self-stiffening, and shape control simulations. In *International Congress on Theoretical and Applied Mechanics, Warsaw, Poland (Aug. 15–19, 2004)*, 2004.

[35] LC Brinson and MS Huang. Simplifications and comparisons of shape memory alloy constitutive models. *Journal of Intelligent Material Systems and Structures(USA)*, 7(1):108–114, 1996.

[36] LC Brinson and R. Lammering. Finite element analysis of the behavior of shape memory alloys and their applications. *International journal of Solids and Structures*, 30(23):3261–3280, 1993.

[37] WJ Buehler, JV Gilfrich, and RC Wiley. Effect of low-temperature phase changes on the mechanical properties of alloys near composition TiNi. *Journal of Applied Physics*, 34:1475, 1963.

[38] DS Burton, X. Gao, and LC Brinson. Finite element simulation of a self-healing shape memory alloy composite. *Mechanics of Materials*, 38(5-6):525–537, 2006.

[39] J. Byström, N. Jekabsons, and J. Varna. An evaluation of different models for prediction of elastic properties of woven composites. *Composites Part B: Engineering*, 31(1):7–20, 2000.

[40] P.P. Camanho, CG Davila, and MF De Moura. Numerical simulation of mixed-mode progressive delamination in composite materials. *Journal of composite materials*, 37(16):1415, 2003.

[41] E. Carrera. Evaluation of layerwise mixed theories for laminated plates analysis. *AIAA Journal*, 36(5):830–839, May 1998.

[42] E. Carrera and A. Ciuffreda. A unified formulation to assess theories of multilayered plates for various bending problems. *Composite Structures*, 69:271–293, 2005.

[43] CC Chamis. Simplified composite micromechanics equations for strength, fracture toughness, impact resistance and environmental effects, 1984.

[44] CC Chamis. Simplified composite micromechanics equations of hygral, thermal, and mechanical properties. *Sampe Quarterly*, 15:14–23, 1984.

[45] R. Chandra, S. P. Singh, and K. Gupta. Micromechanical damping models for fiber-reinforced composites: a comparative study. *Composites Part A: Applied Science and Manufacturing*, 33(6):787 – 796, 2002.

[46] L. Chandrasekaran and A. D. Foreman. Composite materials, 2006.

[47] Y.C. Chen and D.C. Lagoudas. Impact induced phase transformation in shape memory alloys. *Journal of the Mechanics and Physics of Solids*, 48(2):275–300, 2000.

[48] JR Cho and J.T. Oden. Priori error estimations of hp-finite element approximations for hierarchical models of plate- and shell-like structures. *Computer Methods in Applied Mechanics and Engineering*, 132(1):135–177, 1996.

[49] I. Chopra. Review of state of art of smart structures and integrated systems. *AIAA journal*, 40(11):2145–2187, 2002.

[50] N. Chretien. Numerical constitutive models of woven and braided textile structural composites, unpublished msc thesis, faculty of aerospace engineering, virginia polytechnic institute and state university, blacksburg, virginia. 2002.

[51] J.H. Chung, J.S. Heo, and J.J. Lee. Implementation strategy for the dual transformation region in the Brinson SMA constitutive model. *Smart Materials and Structures*, 16:N1, 2007.

[52] Peter W. Chung, Kumar K. Tamma, and Raju R. Namburu. A finite element thermo-viscoelastic creep approach for heterogeneous structures with dissipative correctors. *Finite Elements in Analysis and Design*, 36(3-4):279 – 313, 2000.

[53] P.W. Chung and K.K. Tamma. Woven fabric compositesdevelopments in engineering bounds, homogenization and applications. *International Journal for Numerical Methods in Engineering*, 45(12):1757–1790, 1999.

[54] P.W. Chung, K.K. Tamma, and R.R. Namburu. A micro/macro homogenization approach for viscoelastic creep analysis with dissipative correctors for heterogeneous woven-fabric layered media. *Composites science and technology*, 60(12-13):2233–2253, 2000.

[55] P.W. Chung, K.K. Tamma, and R.R. Namburu. Asymptotic expansion homogenization for heterogeneous media: computational issues and applications. *Composites Part A: Applied Science and Manufacturing*, 32(9):1291–1301, 2001.

[56] P.W. Chung, K.K. Tamma, and R.R. Namburu. A computational approach for multi-scale analysis of heterogeneous elasto-plastic media subjected to short duration loads. *International journal for numerical methods in engineering*, 59(6):825–848, 2004.

[57] P.G. Ciarlet. A justification of the von Karman equations. *Archive for Rational Mechanics and Analysis*, 73(4):349–389, 1980.

[58] JP Cordebois and F. Sidoroff. Damage induced elastic anisotropy. In *colloque Euromech*, volume 115, pages 761–774, 1979.

[59] MA Crisfield and G. Alfano. Adaptive hierarchical enrichment for delamination fracture using a decohesive zone model. *International Journal for Numerical Methods in Engineering*, 54(9):1369–1390, 2002.

[60] JJ Crookston, AC Long, and IA Jones. A summary review of mechanical properties prediction methods for textile reinforced polymer composites. *Proceedings of the Institution of Mechanical Engineers, Part L: Journal of Materials: Design and Applications*, 219(2):91–109, 2005.

[61] J. Pinho da Cruz, J.A. Oliveira, and F. Teixeira-Dias. Asymptotic homogenisation in linear elasticity. part i: Mathematical formulation and finite element modelling. *Computational Materials Science*, 45(4):1073 – 1080, 2009.

[62] F. Daghia. *Active fibre-reinforced composites with embedded shape memory alloys.* PhD thesis, Department of Civil Engineering and Archiecture, University of Bologna, Bologna, Italy, 2008.

[63] A. Dasgupta, RK Agarwal, and SM Bhandarkar. Three-dimensional modeling of woven-fabric composites for effective thermo-mechanical and thermal properties. *Composites Science and Technology*, 56(3):209–223, 1996.

[64] M. Dauge, E. Faou, and Z. Yosibash. Plates and shells: Asymptotic expansions and hierarchical models. *Encyclopedia of computational mechanics*, 1:199–236, 2004.

[65] R. de Borst, M.A. Gutiérrez, G.N. Wells, J.J.C. Remmers, and H. Askes. Cohesive-zone models, higher-order continuum theories and reliability methods for computational failure analysis. *International Journal for Numerical Methods in Engineering*, 60(1):289–315, 2004.

[66] S. De la Flor, C. Urbina, and F. Ferrando. Constitutive model of shape memory alloys: Theoretical formulation and experimental validation. *Materials Science and Engineering: A*, 427(1-2):112–122, 2006.

[67] L. Demasi. Refined multilayered plate elements based on Murakami zig–zag functions. *Composite Structures*, 70(3):308–316, 2005.

[68] M.V. Donadon, B.G. Falzon, L. Iannucci, and J.M. Hodgkinson. A 3-D micromechanical model for predicting the elastic behaviour of woven laminates. *Composites Science and Technology*, 67(11-12):2467–2477, 2007.

[69] J. Dong and M. Feng. Asymptotic expansion homogenization for simulating progressive damage of 3D braided composites. *Composite Structures*, 92(4):873–882, 2010.

[70] TW Duerig, KN Melton, D. Stockel, and CM Wayman. *Engineering aspects of shape memory alloys.* Butterworth-Heinemann, Reed Books Services Ltd, P. O. Box 5, Rushden, Northants, NN 10 9 YX, UK, 1990. 499, 1990.

[71] F. Dunne and N. Petrinic. *Introduction to computational plasticity.* Oxford University Press, USA, 2005.

[72] G.J. Dvorak. Transformation field analysis of inelastic composite materials. *Proceedings of the Royal Society of London. Series A: Mathematical and Physical Sciences*, 437(1900):311, 1992.

[73] GJ Dvorak and YA Bahei-El-Din. A bimodal plasticity theory of fibrous composite materials. *Acta mechanica*, 69(1):219–241, 1987.

[74] GJ Dvorak, YA Bahel-el Din, Y. Macheret, and CH Liu. An experimental study of elastic-plastic behavior of a fibrous boron-aluminum composite. *Journal of the Mechanics and Physics of Solids*, 36(6):655–687, 1988.

[75] G.J. Dvorak and Y. Benveniste. On transformation strains and uniform fields in multiphase elastic media. *Proceedings of the Royal Society of London. Series A: Mathematical and Physical Sciences*, 437(1900):291, 1992.

[76] G.J. Dvorak and MS Rao. Axisymmetric plasticity theory of fibrous composites* 1. *International Journal of Engineering Science*, 14(4):361–373, 1976.

[77] T.E. Dye. An experimental investigation of the behavior of nitinol. Master's thesis, Virginia Tech, Blacksburg, VA, 1990.

[78] R.L. Ellis. *Ballistic Impact Resistance of Graphite Epoxy Composites with Shape Memory Alloy and Extended Chain Polyethylene Spectra Hybrid Components.* PhD thesis, Virginia Polytechnic Institute and State University, 1996.

[79] R.L. Ellis, F. Lalande, H. Jia, and C.A. Rogers. Ballistic impact resistance of SMA and spectra hybrid graphite composites. *Journal of Reinforced Plastics and Composites*, 17(2):147, 1998.

[80] J. Epps and R. Chandra. Shape memory alloy actuation for active tuning of composite beams. *Smart Materials and Structures*, 6:251, 1997.

[81] MG Faulkner, JJ Amalraj, and A. Bhattacharyya. Experimental determination of thermal and electrical properties of Ni-Ti shape memory wires. *Smart Materials and Structures*, 9(5):632–639, 2000.

[82] J. Fish. Hierarchical modelling of discontinuous fields. *Communications in Applied Numerical Methods*, 8(7):443 – 453, 1992.

[83] J. Fish. The s-version of the finite element method. *Computers & structures*, 43(3):539–547, 1992.

[84] J. Fish and R. Guttal. The s-version of finite element method for laminated composites. *International Journal for Numerical Methods in Engineering*, 39(21):3641 – 3662, 1996.

[85] J. Fish and S. Markolefas. Adaptive s-method in linear elastostatics. In *AIAA/ASME/ASCE/AHS/ASC Structures, Structural Dynamics and Materials Conference, 33 rd, Dallas, TX*, pages 313–316, 1992.

[86] J. Fish and S. Markolefas. The s-version of the finite element method for multilayer laminates. *International Journal for Numerical Methods in Engineering*, 33(5):1081–1105, 1992.

[87] J. Fish, S. Markolefas, R. Guttal, and P. Nayak. On adaptive multilevel superposition of finite element meshes for linear elastostatics. *Applied Numerical Mathematics*, 14(1-3):135–164, 1994.

[88] J. Fish, K. Shek, M. Pandheeradi, and M.S. Shephard. Computational plasticity for composite structures based on mathematical homogenization: Theory and practice. *Computer Methods in Applied Mechanics and Engineering*, 148(1-2):53–73, 1997.

[89] A.D. Foreman, T. Nensi, C.B. Meeks, and P.T. Curtis. An integrated system for improved damage resistance and lightning strike protection in composite structures. In *16th International Conference on Composite Materials, Kyoto, Japan*, 2007.

[90] X. Gao, D. Burton, T.L. Turner, and L.C. Brinson. Finite element analysis of adaptive-stiffening and shape-control SMA hybrid composites. *Journal of Engineering Materials and Technology*, 128:285, 2006.

[91] X. Gao, R. Qiao, and L.C. Brinson. Phase diagram kinetics for shape memory alloys: a robust finite element implementation. *Smart Materials and Structures*, 16:2102, 2007.

[92] MM Ghomshei, N. Tabandeh, A. Ghazavi, and F. Gordaninejad. Nonlinear transient response of a thick composite beam with shape memory alloy layers. *Composites Part B: Engineering*, 36(1):9–24, 2005.

[93] R.F. Gibson. *Principles of composite material mechanics.* McGraw-Hill New York, 1994.

[94] R. Gilat and J. Aboudi. Dynamic response of active composite plates: shape memory alloy fibers in polymeric/metallic matrices. *International journal of solids and structures*, 41(20):5717–5731, 2004.

[95] R. Gilat and J. Aboudi. Thermal buckling of activated shape memory reinforced laminated plates. *Smart Materials and Structures*, 15:829, 2006.

[96] E. Greenhalgh and M. Hiley. The assessment of novel materials and processes for the impact tolerant design of stiffened composite aerospace structures. *Composites Part A*, 34(2):151–161, 2003.

[97] D.J. Hartl and D.C. Lagoudas. Aerospace applications of shape memory alloys. *Proceedings of the Institution of Mechanical Engineers, Part G: Journal of Aerospace Engineering*, 221(4):535–552, 2007.

[98] Z. Hashin. *Theory of fiber reinforced materials.* National Aeronautics and Space Administration, 1972.

[99] H. Herzog and E. Jacquet. From a shape memory alloys model implementation to a composite behavior. *Computational materials science*, 39(2):365–375, 2007.

[100] R. Hill. Theory of mechanical properties of fibre-strengthened materials: I. Elastic behaviour. *Journal of the Mechanics and Physics of Solids*, 12(4):199–212, 1964.

[101] M.J. Hinton, AS Kaddour, and P.D. Soden. *Failure criteria in fibre reinforced polymer composites: the world-wide failure exercise.* Elsevier Science, 2004.

[102] O. Hoffman. The brittle strength of orthotropic materials. *Journal of Composite Materials*, 1(2):200, 1967.

[103] Z.M. Huang and S. Ramakrishna. Micromechanical modeling approaches for the stiffness and strength of knitted fabric composites: a review and comparative study. *Composites Part A*, 31(5):479–501, 2000.

[104] J H Hubbard and B B Hubbard. *Vector Calculus, Linear Algebra, and Differential Forms: A Unified Approach.* Prentice Hall, Upper Saddle River, NJ, 2nd edition, 2002.

[105] T. Ishikawa and T.W. Chou. Elastic behavior of woven hybrid composites. *Journal of Composite Materials*, 16(1):2, 1982.

[106] T. Ishikawa and T.W. Chou. Stiffness and strength behaviour of woven fabric composites. *Journal of Materials Science*, 17(11):3211–3220, 1982.

[107] Y. Ivshin and T.J. Pence. A thermomechanical model for a one variant shape memory material. *Journal of Intelligent Material Systems and Structures*, 5(4):455, 1994.

[108] BK Jang and T. Kishi. Adhesive strength between TiNi fibers embedded in CFRP composites. *Materials Letters*, 59(11):1338–1341, 2005.

[109] B.K. Jang and T. Kishi. Thermomechanical response of TiNi fiber-impregnated CFRP composites. *Materials Letters*, 59(19-20):2472–2475, 2005.

[110] B.K. Jang and T. Kishi. Mechanical properties of TiNi fiber impregnated CFRP composites. *Materials Letters*, 60(4):518–521, 2006.

[111] B.K. Jang, Y. Xu, R. Oishi, H. Nagai, H. Yoshida, Y. Akimune, K. Otsuka, and T. Kishi. Thermomechanical characterization and development of SMA-embedded CFRP composites with self-damage control. In *Proceedings of SPIE*, volume 4699, page 182, 2002.

[112] C.S. Jarali, S. Raja, and AR Upadhya. Micro-mechanical behaviors of SMA composite materials under hygro-thermo-elastic strain fields. *International Journal of Solids and Structures*, 45(9):2399–2419, 2008.

[113] H. Jia. Impact Damage Resistance of Shape Memory Alloy Hybrid Composite Structures. Master's thesis, Faculty of Mechanical Engineering, Virginia Polytechnic Institute and State University, Blacksburg, VA, 1998.

[114] H. Jia, F. Lalande, and C.A. Rogers. Modeling of strain energy absorption in superelastic shape memory alloys. In *Proceedings of SPIE*, volume 3039, page 548, 1997.

[115] K. Jonnalagadda, G.E. Kline, and N.R. Sottos. Local displacements and load transfer in shape memory alloy composites. *Experimental Mechanics*, 37(1):78–86, 1997.

[116] P. Kanouté, D.P. Boso, J.L. Chaboche, and B.A. Schrefler. Multiscale Methods for Composites: A Review. *Archives of Computational Methods in Engineering*, 16(1):31–75, 2009.

[117] M. Kawai. Effects of matrix inelasticity on the overall hysteretic behavior of TiNi-SMA fiber composites. *International Journal of Plasticity*, 16(3-4):263–282, 2000.

[118] M.R. Kessler. Self-healing: a new paradigm in materials design. *Proceedings of the Institution of Mechanical Engineers, Part G: Journal of Aerospace Engineering*, 221(4):479–495, 2007.

[119] SMR Khalili, A. Shokuhfar, F. Ashenai Ghasemi, and K. Malekzadeh. Dynamic Response of Smart Hybrid Composite Plate Subjected to Low-Velocity Impact. *Journal of Composite Materials*, 41(19):2347, 2007.

[120] SMR Khalili, A. Shokuhfar, and F.A. Ghasemi. Effect of smart stiffening procedure on low-velocity impact response of smart structures. *Journal of Materials Processing Tech.*, 190(1-3):142–152, 2007.

[121] SMR Khalili, A. Shokuhfar, K. Malekzadeh, and F. Ashenai Ghasemi. Low-velocity impact response of active thin-walled hybrid composite structures embedded with SMA wires. *Thin-Walled Structures*, 45(9):799–808, 2007.

[122] T.C. Kiesling. *Impact failure modes of graphite epoxy composites with embedded superelastic nitinol.* PhD thesis, Faculty of Mechanical Engineering, Virginia Polytechnic Institute and State University, 1995.

[123] TC Kiesling, Z. Chaudhry, JSN Paine, and C. Rogers. Impact failure modes of thin graphite epoxy composites embedded with superelastic nitinol. In *AIAA/ASME/ASCE/AHS/ASC Structures, Structural Dynamics, and Materials Conference and Exhibit, 37 th, Salt Lake City, UT*, pages 1448–1457, 1996.

[124] H. Kimura, Y. Akiniwa, K. Tanaka, H. Tanaka, and Y. Okumura. Smart structure for suppression of mode I and II crack propagation in CFRP laminates by shape memory alloy TiNi actuator. *International Journal of Fatigue*, 28(10):1147–1153, 2006.

[125] KSC Kuang and WJ Cantwell. The use of plastic optical fibres and shape memory alloys for damage assessment and damping control in composite materials. *Measurement Science and Technology*, 14(8):1305–1313, 2003.

[126] D.C. Lagoudas. *Shape Memory Alloys: Modeling and Engineering Applications.* Springer Verlag, 2008.

[127] D.C. Lagoudas, Z. Bo, and M.A. Qidwai. A unified thermodynamic constitutive model for SMA and finite element analysis of active metal matrix composites. *Mechanics of Advanced Materials and Structures*, 3(2):153–179, 1996.

[128] D.C. Lagoudas, P.B. Entchev, P. Popov, E. Patoor, L.C. Brinson, and X. Gao. Shape memory alloys, Part II: Modeling of polycrystals. *Mechanics of Materials*, 38(5-6):430–462, 2006.

[129] E.A.D. Lamers. *Shape distortions in fabric reinforced composite products due to processing induced fibre reorientation.* PhD thesis, University of Twente, 2004.

[130] K. Lau, H. Ling, and L. Zhou. Low velocity impact on shape memory alloy stitched composite plates. *Smart Materials and Structures*, 13(2):364–370, 2004.

[131] JK Lee and M. Taya. Strengthening mechanism of shape memory alloy reinforced metal matrix composite. *Scripta materialia*, 51(5):443–448, 2004.

[132] S.H. Lee, J.H. Song, Y.C. Yoon, G. Zi, and T. Belytschko. Combined extended and superimposed finite element method for cracks. *Int. J. Numer. Methods Eng*, 59(8):1119–1136, 2004.

[133] C. Liang and CA Rogers. One-dimensional thermomechanical constitutive relations for shape memory material J. Intell. *Mater. Syst. Struct*, 1:207–34, 1990.

[134] H.C. Lin, S.K. Wu, and M.T. Yeh. Damping characteristics of TiNi shape memory alloys. *Metallurgical and Materials Transactions A*, 24(10):2189–2194, 1993.

[135] R. Liu and DY Li. Indentation behaviour and wear resistance of pseudoelastic Ti-Ni alloy. *Materials Science and Technology*, 16(3):328–332, 2000.

[136] Y. Liu and SP Galvin. Criteria for pseudoelasticity in near-equiatomic NiTi shape memory alloys. *Acta materialia*, 45(11):4431–4439, 1997.

[137] S.V. Lomov, D.S. Ivanov, I. Verpoest, M. Zako, T. Kurashiki, H. Nakai, and S. Hirosawa. Meso-FE modelling of textile composites: Road map, data flow and algorithms. *Composites Science and Technology*, 67(9):1870–1891, 2007.

[138] ZK Lu and GJ Weng. A two-level micromechanical theory for a shape-memory alloy reinforced composite. *International Journal of Plasticity*, 16(10-11):1289–1307, 2000.

[139] D. Lukkassen, L.E. Persson, and P. Wall. Some engineering and mathematical aspects on the homogenization method. *Composites Engineering*, 5:519–519, 1995.

[140] Lawrence E. Malvern. *Introduction to the Mechanics of a Continuous Medium.* Series in Engineering of the Physical Sciences. Prentice-Hall, Inc., Englewood Cliffs, New Jersey, 1969.

[141] S. Marfia. Micro-macro analysis of shape memory alloy composites. *International Journal of Solids and Structures*, 42(13):3677–3699, 2005.

[142] S. Marfia and E. Sacco. Micromechanics and Homogenization of SMA-wire-reinforced Materials. *Journal of applied mechanics*, 72:259, 2005.

[143] A. Masuda, Q.Q. Ni, A. Sone, R.X. Zhang, and T. Yamamura. Preliminary characterization and modeling of SMA-based textile composites. In *Society of Photo-Optical Instrumentation Engineers (SPIE) Conference Series*, volume 5383, pages 94–102, 2004.

[144] T. Matsuda, Y. Nimiya, N. Ohno, and M. Tokuda. Elastic-viscoplastic behavior of plain-woven GFRP laminates: Homogenization using a reduced domain of analysis. *Composite structures*, 79(4):493–500, 2007.

[145] T. Matsuda, N. Ohno, H. Tanaka, and T. Shimizu. Homogenized in-plane elastic-viscoplastic behavior of long fiber-reinforced laminates. *JSME International Journal Series A*, 45(4):538–544, 2002.

[146] J.M. McNaney, V. Imbeni, Y. Jung, P. Papadopoulos, and RO Ritchie. An experimental study of the superelastic effect in a shape-memory Nitinol alloy under biaxial loading. *Mechanics of Materials*, 35(10):969–986, 2003.

[147] JM Melenk and I. Babuška. The partition of unity finite element method: basic theory and applications. *Computer methods in applied mechanics and engineering*, 139(1-4):289–314, 1996.

[148] M Meo, F Achard, and M Grassi. Finite Element Modeling of Bridging Micro-mechanics in Through-thickness Reinforced Composite Laminates. *Composite Structures*, 71(71):383–387, 2005.

[149] M. Meo, E. Antonucci, P. Duclaux, and M. Giordano. Finite element simulation of low velocity impact on shape memory alloy composite plates. *Composite Structures*, 71(3-4):337–342, 2005.

[150] YJE Meziere, JCF Millett, and NK Bourne. Equation of state and mechanical response of NiTi during one-dimensional shock loading. *Journal of Applied Physics*, 100:033513, 2006.

[151] V. Michaud. Can shape memory alloy composites be smart? *Scripta materialia*, 50(2):249–253, 2004.

[152] J.C. Michel and P. Suquet. Nonuniform transformation field analysis. *international Journal of Solids and Structures*, 40(25):6937–6955, 2003.

[153] S. Miyazaki and K. Otsuka. Development of shape memory alloys. *ISIJ International*, 29(5):353–377, 1989.

[154] S.P. Mizar. *Thermomechanical characterization of NiTiNOL and NiTiNOL based structures using ACES methodology.* PhD thesis, Worcester Polytechnic Institute, 2005.

[155] S. Mohammadi. *Extended finite element method.* Oxford: Blackwell Publishing, 2008.

[156] P. M. Mohite and C. S. Upadhyay. Region-by-region modeling of laminated composite plates. *Computers & Structures*, 85:1808–1827, 2007.

[157] H. M. Mourad, T. O. Williams, and F. L. Addessio. Finite element analysis of inelastic laminated plates using a global-local formulation with delamination. *Computer Methods in Applied Mechanics and Engineering*, 198:542–554, 2008.

[158] AP Mouritz. Review of z-pinned composite laminates. *Composites Part A*, 38(12):2383–2397, 2007.

[159] AP Mouritz, MK Bannister, PJ Falzon, and KH Leong. Review of applications for advanced three-dimensional fibre textile composites. *Composites Part A*, 30(12):1445–1461, 1999.

[160] AP Mouritz, KH Leong, and I. Herszberg. A review of the effect of stitching on the in-plane mechanical properties of fibre-reinforced polymer composites. *Composites Part A*, 28(12):979–991, 1997.

[161] S. Murakami. Mechanical modeling of material damage. *Journal of Applied Mechanics*, 55:280, 1988.

[162] G. Murasawa, K. Tohgo, and H. Ishii. Deformation Behavior of NiTi/Polymer Shape Memory Alloy Composites-Experimental Verifications. *Journal of Composite Materials*, 38(5):399, 2004.

[163] G. Murasawa, K. Tohgo, and H. Ishii. The effect of fiber volume fraction and aspect ratio on the creation of internal stress in the matrix and deformation for short-fiber shape memory alloy composite. *Smart Materials and Structures*, 15(1):33, 2006.

[164] NK Naik and VK Ganesh. An analytical method for plain weave fabric composites. *Composites(UK)*, 26(4):281–289, 1995.

[165] NK Naik and E. Sridevi. An analytical method for thermoelastic analysis of 3D orthogonal interlock woven composites. *Journal of reinforced plastics and composites*, 21(13):1149, 2002.

[166] A. Needleman. A continuum model for void nucleation by inclusion debonding. *Journal of Applied Mechanics*, 54:525, 1987.

[167] S. Nemat-Nasser and W.G. Guo. Superelastic and cyclic response of NiTi SMA at various strain rates and temperatures. *Mechanics of Materials*, 38(5-6):463–474, 2006.

[168] S. Nemat-Nasser, Y. Su, W.G. Guo, and J. Isaacs. Experimental characterization and micromechanical modeling of superelastic response of a porous NiTi shape-memory alloy. *Journal of the Mechanics and Physics of Solids*, 53(10):2320–2346, 2005.

[169] Q.Q. Ni, R. Zhang, T. Natsuki, and M. Iwamoto. Stiffness and vibration characteristics of SMA/ER3 composites with shape memory alloy short fibers. *Composite Structures*, 79(4):501–507, 2007.

[170] S. Ogihara, S. Kobayashi, and N. Takeda. Effect of embedded SMA fibers on the damage progress in composite laminate. *Journal of Materials Science Letters*, 20(12):1139–1141, 2001.

[171] S. Ogihara and T. Uehara. Mechanical properties of SMA fiber/epoxy composite. *Journal of Materials Science Letters*, 22(9):683–685, 2003.

[172] T. Ogisu, N. Ando, J. Takaki, T. Okabe, and N. Takeda. Improved surface treatment of SMA foils and damage suppression of SMA-foil embedded CFRP laminates. *Journal of Intelligent Material Systems and Structures*, 12(4):265, 2001.

[173] T. Ogisu, M. Shimanuki, S. Kiyoshima, J. Takaki, and N. Takeda. Damage suppression in CFRP laminates using embedded shape memory alloy foils. *Advanced Composite Materials*, 13(1):27–42, 2004.

[174] T. Ogisu, M. Shimanuki, S. Kiyoshima, J. Takaki, I. Taketa, and N. Takeda. Damage behavior analysis of smart composites with embedded pre-strained SMA foils. *Smart Materials and Structures*, 15(1):41, 2006.

[175] T. Ogisu, M. Shimanuki, S. Kiyoshima, and N. Takeda. A Basic Study of CFRP Laminates with Embedded Prestrained SMA Foils for Aircraft Structures. *Journal of Intelligent Material Systems and Structures*, 16(2):175, 2005.

[176] N. Ohno, X. Wu, and T. Matsuda. Homogenized properties of elastic-viscoplastic composites with periodic internal structures. *International Journal of Mechanical Sciences*, 42(8):1519–1536, 2000.

[177] JA Oliveira et al. Asymptotic homogenisation in linear elasticity. Part II: Finite element procedures and multiscale applications. *Computational Materials Science*, 45(4):1081–1096, 2009.

[178] M. Ortiz and JC Simo. An analysis of a new class of integration algorithms for elastoplastic constitutive relations. *International Journal for Numerical Methods in Engineering*, 23(3):353–366, 1986.

[179] C. Oskay and J. Fish. Eigendeformation-based reduced order homogenization for failure analysis of heterogeneous materials. *Computer Methods in Applied Mechanics and Engineering*, 196(7):1216–1243, 2007.

[180] K. Otsuka and C.M. Wayman. *Shape memory materials*. Cambridge University Press Cambridge, UK, 1998.

[181] NJ Pagano. Exact solutions for composite laminates in cylindrical bending. *Journal of Composite Materials*, 3(3):398, 1969.

[182] J.S. Paine and C.A. Rogers. Improved impact damage resistance in adaptive shape memory alloy hybrid composite materials. In *Proceedings of SPIE*, volume 2190, page 402, 1994.

[183] JSN Paine and C. Rogers. High velocity impact response of composites with surface bonded nitinol-SMA hybrid layers. In *36 th AIAA/ASME/ASCE/AHS/ASC Structures, Structural Dynamics, and Materials Conference and AIAA/ASME Adaptive Structures Forum. Part 3*, pages 2084–2094, 1995.

[184] J.S.N. Paine and C.A. Rogers. Low velocity perforating impact response of shape memory alloy hybrid composite materials. *American Society of Mechanical Engineers. Aerospace Division. Publication AD.*, 45:75–84, 1994.

[185] J.S.N. Paine and C.A. Rogers. The response of SMA hybrid composite materials to low velocity impact. *Journal of Intelligent Material Systems and Structures*, 5(4):530, 1994.

[186] J.S.N. Paine and C.A. Rogers. Observations of the Drop-weight Impact Response of Composites with Surface Bonded Nitinol Layers. In *Proceedings of the ASME Materials Division: presented at the 1995 ASME International Mechanical Engineering Congress and Exposition, November 12-17, 1995, San Francisco, California*, volume 10, page 381. American Society of Mechanical Engineers, 1995.

[187] J.S.N. Paine and C.A. Rogers. Shape memory alloys for damage resistant composite structures. *Active materials and smart structures*, pages 353–371, 1995.

[188] A. Paiva and M.A. Savi. An overview of constitutive models for shape memory alloys. *Mathematical Problems in Engineering*, 2006:1–30, 2006.

[189] J.W. Park, J.W. Hwang, and Y.H. Kim. Efficient finite element analysis using mesh superposition technique. *Finite Elements in Analysis & Design*, 39(7):619–638, 2003.

[190] J. Parthenios, GC Psarras, and C. Galiotis. Adaptive composites incorporating shape memory alloy wires. Part 2: development of internal recovery stresses as a function of activation temperature. *Composites Part A*, 32(12):1735–1747, 2001.

[191] E. Patoor, D.C. Lagoudas, P.B. Entchev, L.C. Brinson, and X. Gao. Shape memory alloys, Part I: General properties and modeling of single crystals. *Mechanics of materials*, 38(5-6):391–429, 2006.

[192] M.J. Pindera, H. Khatam, A.S. Drago, and Y. Bansal. Micromechanics of spatially uniform heterogeneous media: A critical review and emerging approaches. *Composites Part B: Engineering*, 40(5):349–378, 2009.

[193] P. Popov. *Constitutive modelling of shape memory alloys and upscaling of deformable porous media.* PhD thesis, Texas A&M University, 2005.

[194] P. Popov and D.C. Lagoudas. A 3-D constitutive model for shape memory alloys incorporating pseudoelasticity and detwinning of self-accommodated martensite. *International Journal of Plasticity*, 23(10-11):1679–1720, 2007.

[195] H. Prahlad and I. Chopra. Comparative evaluation of shape memory alloy constitutive models with experimental data. *Journal of Intelligent Material Systems and Structures*, 12(6):383, 2001.

[196] GC Psarras, J. Parthenios, and C. Galiotis. Adaptive composites incorporating shape memory alloy wires Part I Probing the internal stress and temperature distributions with a laser Raman sensor. *Journal of Materials Science*, 36(3):535–546, 2001.

[197] J. N. Reddy and D. H. Robbins. *Computational Modelling of Damage and Failures in Composite Laminates.* John Wiley & Sons, Ltd, 2004.

[198] J. N. Reddy and D. H. Robbins Jr. Theories and computational models for composite laminates. *Applied Mechanics Reviews*, 47(6):147–169, June 1994.

[199] J.N. Reddy. *An introduction to nonlinear finite element analysis.* Oxford University Press, USA, 2004.

[200] J.N. Reddy. *Mechanics of laminated composite plates and shells: theory and analysis.* CRC, 2004.

[201] S.R. Reid and G. Zhou. *Impact behaviour of fibre-reinforced composite materials and structures.* CRC, 2000.

[202] MOW Richardson and MJ Wisheart. Review of low-velocity impact properties of composite materials. *Composites Part A*, 27(12):1123–1131, 1996.

[203] D. H. Robbins Jr. and J. N. Reddy. Variable kinematic modelling of laminated composite plates. *International Journal for Numerical Methods in Engineering*, 39:2283–2317, 1996.

[204] CA Rogers, C. Liang, and J. Jia. Behavior of shape memory alloy reinforced composite plates, Part 1: model formulation and control concepts. In *Proceedings of the 30th Structures, Structural Dynamics and Materials Conference*, pages 3–5, 1989.

[205] CA Rogers, C. Liang, and S. Li. Active damage control of hybrid material systems using induced strain actuator. In *AIAA/ASME/ASCE/AHS/ASC Structures, Structural Dynamics, and Materials Conference, 32 nd, Baltimore, MD*, pages 1190–1203, 1991.

[206] CA Rogers and HH Robertshaw. Shape memory alloy reinforced composites. *Engineering Science Preprints*, 25, 1988.

[207] CA Rogers and HH Robertshaw. Development of a Novel Smart Material. *Designers in action, 1985-1991: case studies in mechanical engineering design*, page 71, 1992.

[208] J.H. Roh and J.H. Kim. Hybrid smart composite plate under low velocity impact. *Composite Structures*, 56(2):175–182, 2002.

[209] J.H. Roh and J.H. Kim. Adaptability of hybrid smart composite plate under low velocity impact. *Composites Part B*, 34(2):117–125, 2003.

[210] K. Rohwer, S. Friedrichs, and C. Wehmeyer. Analyzing laminated structures from fibre-reinforced composite material-an assessment. *Technische Mechanik*, 25(1):59–79, 2005.

[211] BW Rosen. Thermomechanical properties of fibrous composites. *Proceedings of the Royal Society of London. Series A, Mathematical and Physical Sciences*, 319(1536):79–94, 1970.

[212] A. Sadjadpour and K. Bhattacharya. A micromechanics inspired constitutive model for shape-memory alloys: the one-dimensional case. *Smart Materials and Structures*, 16:S51, 2007.

[213] E. Sánchez-Palencia. *Non-homogeneous media and vibration theory.* Springer-Verlag, 1980.

[214] S. Sarip. Stress analysis of laminated composite plates with embedded shape memory alloy using finite element method. Technical report, Universiti Teknologi Malaysia, 2006. (Unpublished).

[215] C. Schwab. *Hierarchic modelling in mechanics in Wavelets, Multilevel Methods and Elliptic PDEs.* Oxford University Press, 1997.

[216] D. Scida, Z. Aboura, ML Benzeggagh, and E. Bocherens. Prediction of the elastic behaviour of hybrid and non-hybrid woven composites. *Composites Science and Technology*, 57(12):1727–1740, 1998.

[217] D. Scida, Z. Aboura, ML Benzeggagh, and E. Bocherens. A micromechanics model for 3D elasticity and failure of woven-fibre composite materials. *Composites Science and Technology*, 59(4):505–517, 1999.

[218] MY Serry, WA Moussa, and DW Raboud. Finite-element modeling of shape memory alloy components in smart structures, part II: Application on shape-memory-alloy-embedded smart composite for self-damage control. In *MEMS, NANO and Smart Systems, 2003. Proceedings. International Conference on*, pages 423–429, 2003.

[219] MY Serry, WA Moussa, and DW Raboud. Finite element investigation of the behavior of SMA damage-control smart system. *Smart Materials and Structures*, 16(1):71, 2007.

[220] MY Serry, DW Raboud, and WA Moussa. Finite-element modeling of shape memory alloy components in smart structures, part I: Non-linear coupled field finite element procedure. In *MEMS, NANO and Smart Systems, 2003. Proceedings. International Conference on*, pages 15–21, 2003.

[221] K. Shek. *Finite Deformation Plasticity for Composite Structures: Computational Models and Adaptive Strategies.* PhD thesis, School Mechanical Engineering Institution RPI, 1997.

[222] A. Shimamoto, T. Azakami, and T. Oguchi. Reduction ofK I andK II by the shape-memory effect in a TiNi shape-memory fiber-reinforced epoxy matrix composite. *Experimental Mechanics*, 43(1):77–82, 2003.

[223] A. Shimamoto, H. Ohkawara, and F. Nogata. Enhancement of mechanical strength by shape memory effect in TiNi fiber-reinforced composites. *Engineering fracture mechanics*, 71(4-6):737–746, 2004.

[224] A. Shimamoto, HY Zhao, and H. Abé. Fatigue crack propagation and local crack-tip strain behavior in TiNi shape memory fiber reinforced composite. *International Journal of Fatigue*, 26(5):533–542, 2004.

[225] J.C. Simo and T.J.R. Hughes. *Computational inelasticity.* Springer Verlag, 1998.

[226] G.H. Staab. *Laminar composites.* Butterworth-Heinemann, 1999.

[227] Z. Su, H. Mai, M. Lu, and L. Ye. Thermo-mechanical behaviour of shape memory alloy reinforced composite laminate (Ni-Ti/glass-fibre/epoxy). *Composite structures*, 47(1-4):705–710, 1999.

[228] Q.P. Sun and K.C. Hwang. Micromechanics modelling for the constitutive behavior of polycrystalline shape memory alloys–I. Derivation of general relations. *Journal of the Mechanics and Physics of Solids*, 41(1):1–17, 1993.

[229] SS Sun, G. Sun, F. Han, and JS Wu. Thermoviscoelastic analysis for a polymeric composite plate with embedded shape memory alloy wires. *Composite Structures*, 58(2):295–302, 2002.

[230] SS Sun, G. Sun, and JS Wu. Thermo-viscoelastic bending analysis of a shape memory alloy hybrid epoxy beam. *Smart Materials and Structures*, 11:970, 2002.

[231] N. Takano, Y. Uetsuji, Y. Kashiwagi, and M. Zako. Hierarchical modelling of textile composite materials and structures by the homogenization method. *Modelling and Simulation in Materials Science and Engineering*, 7:207, 1999.

[232] N. Takeda, S. Minakuchi, and Y. Okabe. Smart Composite Sandwich Structures for Future Aerospace Application-Damage Detection and Suppression-: a Review. *Journal of Solid Mechanics and Materials Engineering*, 1(1):3–17, 2007.

[233] I. Taketa, M. Amano, M. Kobayashi, T. Ogisu, Y. Okabe, and N. Takeda. Modeling of thermo-mechanical behavior of Ti-Ni shape memory alloy foils embedded in carbon fiber reinforced plastic laminates. *Advanced Composite Materials*, 14(1):25–42, 2005.

[234] P. Tan, L. Tong, and G. P. Steven. Modelling for predicting the mechanical properties of textile composites–a review. *Composites Part A: Applied Science and Manufacturing*, 28(11):903 – 922, 1997.

[235] K. Tanaka. A thermomechanical sketch of shape memory effect: one-dimensional tensile behavior. *Res Mech.*, 18(3):251–263, 1986.

[236] K. Terada and N. Kikuchi. Nonlinear homogenization method for practical applications. *computational methods in micromechanics. Amer Soc Mech Eng, AMD.*, 212:1–16, 1995.

[237] SP Thompson and J. Loughlan. Enhancing the post-buckling response of a composite panel structure utilising shape memory alloy actuators–a smart structural concept. *Composite Structures*, 51(1):21–36, 2001.

[238] L. Tong, A.P. Mouritz, and M.K. Bannister. *3D fibre reinforced polymer composites.* Elsevier Science Ltd, 2002.

[239] S.W. Tsai and E.M. Wu. A general theory of strength for anisotropic materials. *Journal of composite materials*, 5(1):58, 1971.

[240] K.A. Tsoi, J. Schrooten, and R. Stalmans. Part I. Thermomechanical characteristics of shape memory alloys. *Materials Science & Engineering A*, 368(1-2):286–298, 2004.

[241] K.A. Tsoi, J. Schrooten, Y. Zheng, and R. Stalmans. Part II. Thermomechanical characteristics of shape memory alloy composites. *Materials Science & Engineering A*, 368(1-2):299–310, 2004.

[242] KA Tsoi, R. Stalmans, and J. Schrooten. Transformational behaviour of constrained shape memory alloys. *Acta Materialia*, 50(14):3535–3544, 2002.

[243] K.A. Tsoi, R. Stalmans, J. Schrooten, M. Wevers, and Y.W. Mai. Impact damage behaviour of shape memory alloy composites. *Materials Science & Engineering A*, 342(1-2):207–215, 2003.

[244] T.L. Turner. *Thermomechanical Response of Shape Memory Alloy Hybrid Composites.* PhD thesis, National Aeronautics and Space Administration, Langley Research Center, Hampton, VA, USA, 2000.

[245] V. Tvergaard. Effect of fibre debonding in a whisker-reinforced metal. *Materials Science and Engineering: A*, 125(2):203 – 213, 1990.

[246] R.R. Valisetty, P.W. Chung, and R.R. Namburu. Scalable computing for the transient elasto-plastic impact analysis of composite armor using the homogenization method. *Computers & structures*, 84(1-2):49–60, 2005.

[247] A. Vigliotti. Finite Element Implementation of a Multivariant Shape Memory Alloy Model. *Journal of Intelligent Material Systems and Structures*, 21(7):685, 2010.

[248] ZG Wei, R. Sandstrom, and S. Miyazaki. Shape-memory materials and hybrid composites for smart systems: Part I Shape-memory materials. *Journal of Materials Science*, 33(15):3743–3762, 1998.

[249] ZG Wei, R. Sandstrom, and S. Miyazaki. Shape memory materials and hybrid composites for smart systems: Part II Shape-memory hybrid composites. *Journal of Materials Science*, 33(15):3763–3783, 1998.

[250] ZG Wei, CY Tang, and WB Lee. Design and fabrication of intelligent composites based on shape memory alloys. *Journal of materials processing technology*, 69(1-3):68–74, 1997.

[251] J.D. Whitcomb. Three dimensional stress analysis of plain weave composites. In *Composite materials: fatigue and fracture: a symposium sponsored by ASTM Committee D-30 on High Modulus Fibers and Their Composites, Dallas, TX, 24-25 Oct. 1984*, page 417. ASTM, 1991.

[252] S. Wijskamp. *Shape distortions in composites forming.* PhD thesis, University of Twente, 2005.

[253] T. O. Williams. A generalized multilength scale nonlinear composite plate theory with delamination. *International Journal of Solids and Structures*, 36:3015–3050, 1999.

[254] X. Wu and N. Ohno. A homogenization theory for time-dependentnonlinear composites with periodic internal structures. *International journal of solids and structures*, 36(33):4991–5012, 1999.

[255] CL Xie, M. Hailat, X. Wu, G. Newaz, M. Taya, and B. Raju. Development of Short Fiber-Reinforced NiTi/ Al6061 Composite. *Journal of Engineering Materials and Technology*, 129:69, 2007.

[256] D. Xie and A.M. Waas. Discrete cohesive zone model for mixed-mode fracture using finite element analysis. *Engineering Fracture Mechanics*, 73(13):1783–1796, 2006.

[257] Z. Xu, K. Ang, and Q. Wang. A Study of Interaction between Embedded SMA Fibers and Host Material. *Mechanics of Advanced Materials and Structures*, 13(1):33–42, 2006.

[258] Y. Yamada, M. Taya, and R. Watanabe. Strenghtening of metal matrix composite by shape memory effect. *Materials transactions- JIM*, 34(3):254–260, 1993.

[259] S. Yi and S. Gao. Fracture toughening mechanism of shape memory alloys due to martensite transformation. *International Journal of Solids and Structures*, 37(38):5315–5327, 2000.

[260] S. Yi, S. Gao, and L. Shen. Fracture toughening mechanism of shape memory alloys under mixed-mode loading due to martensite transformation. *International Journal of Solids and Structures*, 38(24-25):4463–4476, 2001.

[261] Z. Yue and DH Robbins. Adaptive superposition of finite element meshes in non-linear transient solid mechanics problems. *International Journal for Numerical Methods in Engineering*, 72(9):1063–1094, 2007.

[262] AJ Zak, MP Cartmell, WM Ostachowicz, and M. Wiercigroch. One-dimensional shape memory alloy models for use with reinforced composite structures. *Smart Materials and Structures*, 12:338, 2003.

[263] M. Zako and Y. Uetsuji. On the damage behavior of fiber reinforced composite materials. *International Journal of damage mechanics*, 11(2):187, 2002.

[264] M. Zako, Y. Uetsuji, and T. Kurashiki. Finite element analysis of damaged woven fabric composite materials. *Composites science and technology*, 63(3-4):507–516, 2003.

[265] R. Zhang, Q.Q. Ni, A. Masuda, T. Yamamura, and M. Iwamoto. Vibration characteristics of laminated composite plates with embedded shape memory alloys. *Composite structures*, 74(4):389–398, 2006.

[266] R. Zhang, Q.Q. Ni, T. Natsuki, and M. Iwamoto. Mechanical properties of composites filled with SMA particles and short fibers. *Composite Structures*, 79(1):90–96, 2007.

[267] W. Zhang, J. Kim, and N. Koratkar. Energy-absorbent composites featuring embedded shape memory alloys. *Smart Materials and Structures*, 12(4):642–646, 2003.

[268] Y. Zhang and Y.P. Zhao. A discussion on modeling shape memory alloy embedded in a composite laminate as axial force and elastic foundation. *Materials & Design*, 28(3):1016–1020, 2007.

[269] Y. Zhang and Y.P. Zhao. A study of composite beam with shape memory alloy arbitrarily embedded under thermal and mechanical loadings. *Materials & Design*, 28(3):1096–1115, 2007.

[270] Y. Zhao, M. Taya, Y. Kang, and A. Kawasaki. Compression behavior of porous NiTi shape memory alloy. *Acta Materialia*, 53(2):337–343, 2005.

[271] Y. Zheng, L. Cui, D. Zhu, and D. Yang. The constrained phase transformation of prestrained TiNi fibers embedded in metal matrix smart composite. *Materials Letters*, 43(3):91–96, 2000.

[272] YJ Zheng, LS Cui, and J. Schrooten. Basic design guidelines for SMA/epoxy smart composites. *Materials Science & Engineering A*, 390(1-2):139–143, 2005.

[273] Y.J. Zheng, J. Schrooten, K.A. Tsoi, and P. Šittner. Qualitative and quantitative evaluation of the interface in activated shape memory alloy composites. *Experimental Mechanics*, 43(2):194–200, 2003.

[274] OC Zienkiewicz and R.L. Taylor. *The finite element method for solid and structural mechanics*. Butterworth-Heinemann, 2005.